

Imperial College London
Department of Electrical and Electronic Engineering

Remote sensing methods for biodiversity monitoring with emphasis on vegetation height estimation and habitat classification

Zisis Petrou

October 2014

Submitted in part fulfilment of the requirements for the degree of
Doctor of Philosophy in Electrical and Electronic Engineering of Imperial
College London
and the Diploma of Imperial College London

Declaration

I declare that the work in this dissertation is my own, and all references are indicated as such and have been appropriately cited.

Zisis Petrou

Copyright Declaration

The copyright of this thesis rests with the author and is made available under a Creative Commons Attribution Non-Commercial No Derivatives license. Researchers are free to copy, distribute or transmit the thesis on the condition that they attribute it, that they do not use it for commercial purposes and that they do not alter, transform or build upon it. For any reuse or redistribution, researchers must make clear to others the license terms of this work.

List of publications

1. Z. I. Petrou, I. Manakos, T. Stathaki, “Remote sensing for biodiversity monitoring: A review of methods for biodiversity indicator extraction and assessment of progress towards international targets,” *Biodiversity and Conservation*, 2015. Under review.
2. Z. I. Petrou, I. Manakos, T. Stathaki, C. A. Mùcher, and M. Adamo, “Discrimination of vegetation height categories with passive satellite sensor imagery using texture analysis,” *IEEE Journal of Selected Topics in Applied Earth Observation and Remote Sensing*, 2015. In press.
3. Z. I. Petrou, V. Kosmidou, I. Manakos, T. Stathaki, M. Adamo, C. Tarantino, V. Tomaselli, P. Blonda, and M. Petrou, “A rule-based classification methodology to handle uncertainty in habitat mapping employing evidential reasoning and fuzzy logic,” *Pattern Recognition Letters*, vol. 48, pp. 24–33, Oct. 2014.
4. Z. I. Petrou, T. Stathaki, I. Manakos, M. Adamo, C. Tarantino, and P. Blonda, “Land cover to habitat map conversion using remote sensing data: a supervised learning approach,” in *IEEE International Geoscience and Remote Sensing Symposium*, Quebec City, 13–18 Jul. 2014, pp. 4683–4686.
5. Z. I. Petrou, I. Manakos, T. Stathaki, C. Tarantino, M. Adamo, and P. Blonda, “A vegetation height classification approach based on texture analysis of a single VHR image,” in *Proceedings of the 35th International Symposium on Remote Sensing of Environment, IOP Conference Series: Earth and Environmental Science*, vol. 17, 2014, 012210, doi:10.1088/1755-1315/17/1/012210.
6. Z. I. Petrou, C. Tarantino, M. Adamo, P. Blonda, and M. Petrou, “Estimation of vegetation height through satellite image texture anal-

- ysis,” in *International Archives of the Photogrammetry, Remote Sensing and Spatial Information Sciences*, vol. XXXIX-B8, Melbourne, 2012, pp. 321–326.
7. Z. I. Petrou and M. Petrou, “A review of remote sensing methods for biodiversity assessment and bioindicator extraction,” in *Proceedings of the 2nd International Conference on Space Technology*, IEEE, Athens, 15–17 Sep. 2011, DOI: 10.1109/ICSpT.2011.6064679.
 8. Z. I. Petrou, I. Manakos, T. Stathaki, C. Tarantino, M. Adamo, and P. Blonda, “Canopy height estimation through the use of texture analysis of a very high resolution satellite image,” Poster presentation at the *4th Advanced Training Course in Land Remote Sensing*, ESA, Athens, 1–5 Jul. 2013.

Relevant publications

9. R. Lucas, P. Blonda, P. Bunting, G. Jones, J. Inglada, M. Arias, V. Kosmidou, Z. I. Petrou, I. Manakos, M. Adamo, R. Charnock, C. Tarantino, C. A. Mùcher, R. Jongman, H. Kramer, D. Arvor, J.P. Honrado, and Paola Mairota, “The Earth Observation Data for Habitat Monitoring (EODHaM) System,” *International Journal of Applied Earth Observation and Geoinformation*, vol. 37, pp. 17–28, May 2015.
10. C. A. Mùcher, L. Roupioz, H. Kramer, M. M. B. Bogers, R. H. G. Jongman, R. M. Lucas, V. Kosmidou, Z. I. Petrou, I. Manakos, E. Padoa-Schioppa, M. Adamo, and P. Blonda., “Synergy of Airborne LiDAR and Wordldview-2 satellite imagery for land cover and habitat mapping: a BIOSOS-EODHAM case study for the Netherlands,” *International Journal of Applied Earth Observation and Geoinformation*, vol. 37, pp. 48–55, May 2015.
11. M. Adamo, C. Tarantino, V. Tomaselli, V. Kosmidou, Z. I. Petrou, I. Manakos, R. M. Lucas, C. A. Mùcher, G. Veronico, C. Marangi, V. De Pasquale, and P. Blonda, “Expert knowledge for translating land cover/use maps to General Habitat Categories (GHC),” *Landscape Ecology*, vol. 29, no. 6, pp. 1045–1067, Jul. 2014.

12. V. Kosmidou, Z. I. Petrou, R. G. H. Bunce, C. A. Múcher, R.H.G. Jongman, M.M. Bogers, R.M. Lucas, V. Tomaselli, P. Blonda, E. Padoa-Schioppa, I. Manakos, and M. Petrou, “Harmonization of the Land Cover Classification System (LCCS) with the General Habitat Categories (GHC) classification system,” *Ecological Indicators*, vol. 36, pp. 290–300, Jan. 2014.
13. C. A. Múcher, L. Roupioz, H. Kramer, M. Wolters, M. Bogers, R. Lucas, P. Bunting, Z. I. Petrou, V. Kosmidou, I. Manakos, E. Padoa-Schioppa, G.F. Ficetola, A. Bonardi, M. Adamo, and P. Blonda, “LIDAR as a valuable information source for habitat mapping,” in *GLForum conference*, Salzburg, 2–5 Jul. 2013, pp. 520–523.
14. M. Adamo, C. Tarantino, V. Kosmidou, Z. I. Petrou, I. Manakos, V. Tomaselli, R. Lucas, C. A. Múcher, and P. Blonda, “Disambiguation rules based on earth observation data for land cover to habitat map translation: a case study,” in *GLForum conference*, Salzburg, 2–5 Jul. 2013, pp. 487–491.
15. R. Lucas, G. Jones, P. Bunting, V. Kosmidou, Z. I. Petrou, J. Inglada, M. Adamo, C. A. Múcher, and D. Arvor, “Land cover and habitat classification from earth observation data: A new approach from BIO_SOS,” in *GLForum conference*, Salzburg, 2–5 Jul. 2013, pp. 516–519.
16. M. Adamo, C. Tarantino, V. Kosmidou, Z. I. Petrou, I. Manakos, R. M. Lucas, V. Tomaselli, C. A. Múcher, and P. Blonda, “Land cover to habitat map translation: Disambiguation rules based on earth observation data,” in *IEEE International Geoscience and Remote Sensing Symposium*, IEEE, Melbourne, 2013. pp. 3817–3820.

Awards

- Best Paper Award for a young professional under 35, for the paper entitled “A review of Remote Sensing methods for Biodiversity assessment and Bioindicator extraction,” at the 2nd International Conference on Space Technology, Athens, 15-17 Sep. 2011.

Abstract

Biodiversity is a principal factor for ecosystem stability and functioning, and the need for its protection has been identified as imperative globally. Remote sensing can contribute to timely and accurate monitoring of various elements related to biodiversity, but knowledge gap with user communities hinders its widespread operational use. This study advances biodiversity monitoring through earth observation data by initially identifying, reviewing, and proposing state-of-the-art remote sensing methods which can be used for the extraction of a number of widely adopted indicators of global biodiversity assessment. Then, a cost and resource effective approach is proposed for vegetation height estimation, using satellite imagery from very high resolution passive sensors. A number of texture features are extracted, based on local variance, entropy, and local binary patterns, and processed through several data processing, dimensionality reduction, and classification techniques. The approach manages to discriminate six vegetation height categories, useful for ecological studies, with accuracies over 90%. Thus, it offers an effective approach for landscape analysis, and habitat and land use monitoring, extending previous approaches as far as the range of height and vegetation species, synergies of multi-date imagery, data processing, and resource economy are regarded. Finally, two approaches are introduced to advance the state of the art in habitat classification using remote sensing data and pre-existing land cover information. The first proposes a methodology to express land cover information as numerical features and a supervised classification framework, automating the previous labour- and time-consuming rule-based approach used as reference. The second advances the state of the art incorporating Dempster-Shafer evidential theory and fuzzy sets, and proves successful in handling uncertainties from missing data or vague rules and offering wide user defined parameterization potential. Both approaches outperform the reference study in classification accuracy, proving promising for biodiversity monitoring, ecosystem preservation, and sus-

tainability management tasks.

Acknowledgements

I was honoured to be Prof. Maria Petrou's student during the first two years of this research work. Her restless guidance, support, and lively engagement, by even equation solving on paper in our meetings, pushed the limits of ideal supervision higher and will continue inspiring my future endeavours. I am grateful to Dr. Tania Stathaki and Dr. Ioannis Manakos for taking over as supervisors of this thesis and offering their continuous help and invaluable contribution.

Most of all, I am indebted to my family, Ioannis, Maria, Apostolos, Evdokia, Apostolos, Stamos, and Evdokia, for the privilege of their presence, support, encouragement, and love that extend far beyond the timeline of these studies. I wish to thank my friends for the precious moments and Katerina for making this journey more meaningful and enjoyable.

To dad

Contents

1. Introduction	30
1.1. Motivation	30
1.1.1. Biodiversity monitoring and remote sensing	30
1.1.2. Vegetation height estimation and remote sensing	32
1.1.3. Habitat mapping and remote sensing	33
1.1.4. Objectives	34
1.2. Contributions	35
1.3. Organization of the thesis	37
2. Remote sensing for biodiversity monitoring	39
2.1. Targets and indicators	39
2.2. Remote sensing capacity for CBD indicator extraction	40
2.2.1. Trends in extent, condition and vulnerability of ecosystems, biomes and habitats	47
2.2.2. Trends in abundance, distribution and extinction risk of species	53
2.2.3. Trends in pressures from unsustainable agriculture, forestry, fisheries and aquaculture	55
2.2.4. Trends in pressures from habitat conversion, pollution, invasive species, and climate change	58
2.2.5. Trends in distribution, condition and sustainability of ecosystem services for equitable human well-being	59
2.2.6. Trends in coverage, condition, representativeness and effectiveness of protected areas and other area-based approaches	61
2.3. Conclusions and future considerations	62

3. Vegetation height estimation through texture analysis	67
3.1. State of the art and open issues in height estimation using remote sensing	67
3.2. Study area and data	70
3.3. Texture features	73
3.3.1. Local Variance	74
3.3.2. Local Entropy	76
3.3.3. Local Entropy Ratio	77
3.3.4. Local Binary Patterns	77
3.4. Data processing and classification	79
3.4.1. Handling of indefinite values	79
3.4.2. Outlier removal	80
3.4.3. Data normalization	81
3.4.4. Data transformation for dimensionality reduction . . .	82
3.4.5. Feature selection	82
3.4.6. Classification	83
3.4.7. Result evaluation	84
3.5. Results and Discussion	84
3.5.1. Experiments with the full feature set	85
3.5.2. Experiments with feature subsets	93
3.6. Conclusions	100
4. Habitat classification with supervised learning	104
4.1. Formulation of the habitat classification problem	104
4.2. Classification taxonomy definitions, study areas, and data . .	107
4.2.1. LCCS and GHC taxonomy definitions	107
4.2.2. Le Cesine, Italy	108
4.2.3. Lago Salso, Italy	111
4.3. Feature extraction	111
4.3.1. Data features	111
4.3.2. LCCS class features	114
4.4. Results and discussion	117
4.4.1. Le Cesine	117
4.4.2. Lago Salso	120
4.4.3. Transferability from Le Cesine to Lago Salso	123
4.5. Conclusions	126

5. Habitat classification with evidential reasoning and fuzzy logic	129
5.1. Dempster–Shafer theory for uncertainty handling	129
5.2. Methods	131
5.2.1. Dempster–Shafer theory principles	131
5.2.2. Fuzzification methods	135
5.3. Experimental setup	141
5.3.1. Classification process	141
5.3.2. Classifier implementations	142
5.3.3. Final class selection	143
5.3.4. Fusion of classifiers	145
5.3.5. Transferability evaluation	146
5.3.6. Classification accuracy evaluation	146
5.4. Results and discussion	147
5.4.1. Le Cesine study area	147
5.4.2. Transferability to Lago Salso study area	162
5.4.3. Comparison with the supervised learning approach . .	172
5.5. Conclusions	176
6. Thesis summary, conclusions, and future research	178
6.1. Summary	178
6.2. Conclusions	180
6.3. Future research	182
Bibliography	184
Appendices	227
A. Methods for CBD indicator extraction	227
A.1. Abbreviations in Tables A.1–A.6	227
A.2. Tables with methods for CBD headline indicator extraction .	232
A.2.1. Trends in extent, condition and vulnerability of ecosys- tems, biomes and habitats	232
A.2.2. Trends in abundance, distribution and extinction risk of species	237
A.2.3. Trends in pressures from unsustainable agriculture, forestry, fisheries and aquaculture	241

A.2.4. Trends in pressures from habitat conversion, pollution, invasive species, climate change, overexploitation and underlying drivers	244
A.2.5. Trends in distribution, condition and sustainability of ecosystem services for equitable human well-being . .	245
A.2.6. Trends in coverage, condition, representativeness and effectiveness of protected areas and other area-based approaches	247
B. Available data for the study areas	248
B.1. Ederheide and Ginkelse heide, The Netherlands	248
B.2. Le Cesine, Italy	251
B.3. Lago Salso, Italy	253

List of Tables

2.1. Aichi targets that can be monitored through RS data, and the associated CBD headline indicators and EBV classes. . .	41
2.2. Accuracy evaluation measures used throughout the thesis. . .	42
2.3. Acronyms and characteristics of multispectral / hyperspectral, SAR, and (satellite) lidar sensors used in CBD headline indicator extraction related studies.	43
3.1. Problem statement of Chapter 3.	70
3.2. The 24 texture features calculated from each band of the satellite images.	75
3.3. Confusion matrix from classification on the full June image set following listwise deletion, using AdaBoost.M1 with J48 as base classifier. Rows represent the reference classes, whereas columns the predicted ones. Producer's (PA), user's (UA) and overall accuracies, as well as the kappa coefficient, are reported.	90
3.4. Individual features achieving the highest 10 classification accuracies, with the respective kappa coefficients, using the Random Forest classifier.	95
3.5. Feature selection methods with the highest ratios of classification accuracies to the number of selected features, for the cases where features from the June, September and both images were selected. For each method, the overall accuracy (OA) and the selected features are shown. The Random Forest classifier was used.	100

3.6.	Confusion matrix from classification following the CB feature selection method in the feature set of both images, (a) showing all six GHC classes, and (b) merging low shrubs of 0.05–0.6 m and tree classes. Rows represent the reference classes, whereas columns the predicted ones. Producer’s (PA), user’s (UA) and overall accuracies, as well as the kappa coefficient, are reported. The Random Forest classifier was used.	101
4.1.	Problem statement of Chapter 4.	106
4.2.	The 8 main LCCS classes.	108
4.3.	The 5 main GHC categories and the principal classes.	109
4.4.	Features representing the LCCS class names and attributes and the assigned numerical values.	115
4.5.	Classification accuracies for combinations of datasets and feature sets in Le Cesine. The total number of features of each set is written in parentheses. The best results from each feature set are highlighted.	119
4.6.	Confusion matrix from classification of the ‘Main + lidar’ feature set with the Bagging classifier with J48 in Le Cesine. The rows represent the ground truth data, whereas the columns the classified objects.	121
4.7.	Classification accuracies for combinations of datasets and feature sets in Lago Salso. The total number of features of each set is written in parentheses. The best accuracies for each feature set are highlighted.	122
4.8.	Confusion matrix from classification of the ‘Main + QB texture’ feature set with the Bagging classifier with J48 in Lago Salso. The rows represent the ground truth data, whereas the columns the classified objects.	124
4.9.	Classification accuracies (%) applying classifiers trained with data from Le Cesine to Lago Salso, for combinations of datasets and feature sets. The total number of features of each set is written in parentheses. The best accuracies for each feature set are highlighted.	125

4.10. Confusion matrix from classification of the ‘Main + LTBP4 NIR’ feature set with the AdaBoost.M1 classifier with REP-Tree in Lago Salso, using the respective feature set from Le Cesine for training. The rows represent the ground truth data, whereas the columns the classified objects.	127
5.1. Problem statement of Chapter 5.	131
5.2. Maximum classification accuracies (%) achieved by the crisp and the fuzzy classifiers for implementations without and with lidar data for Le Cesine, under interpretations tolerant to and penalizing incorrect classes in multiple ones, as well as the averaging interpretation of the two.	153
5.3. Comparison of results applying crisp classification and fuzzy classification with less strict rule outcomes under the availability of lidar data, for each class. The number of ground truth samples, together with the absolute correct classifications of the two methods under penalizing commission errors are given, for each GHC class. The percentage of correct classifications is also shown in the last columns.	155
5.4. Classes returned by DS fuzzy F1 classifiers with the sum of belief and plausibility and 0.9 threshold value as selection parameters, in case lidar are considered either missing (A1) or available (B1).	158
5.5. Average classification accuracies (%) following different selection criteria, for implementations ignoring (A) or using (B) lidar data.	158
5.6. Classes returned by DS fuzzy F5 classifier with implementation B2 and belief as selection criterion, for threshold values 0.1 and 0.9.	160
5.7. Classification accuracies (%) achieved by the fusion of classifiers for each implementation (A1, A2, B1, B2) and fuzzification method (F0–F6), under the interpretation penalizing multiple classes. In parenthesis, the accuracy of the maximum individual classifier of each case is reported.	162

5.8.	Maximum classification accuracies (%) achieved by the crisp and the fuzzy classifiers for implementations without and with lidar data, under interpretations tolerant to and penalizing incorrect classes in multiple ones, as well as the averaging interpretation of the two.	168
5.9.	Results of one of the best performing classifier under the interpretation penalizing commission errors, for each class. The classifier applies fuzzification method F1 with less strict rule outcomes ignoring lidar data, maximum belief as selection criterion and threshold value 0.1. The number of ground truth samples, together with the absolute correct classifications of the method under this interpretation are given, for each GHC class. The percentage of correct classifications is also shown in the last column.	175
A.1.	Methods studying different parameters related to the CBD headline indicator measuring trends in extent, condition and vulnerability of ecosystems, biomes and habitats.	232
A.2.	Methods studying different parameters related to the CBD headline indicator measuring trends in abundance, distribution, and extinction risk of species.	237
A.3.	Methods studying different parameters related to the CBD headline indicator measuring trends in pressures from unsustainable agriculture, forestry, fisheries and aquaculture. . . .	241
A.4.	Methods studying different parameters related to the CBD headline indicator measuring trends in pressures from habitat conversion, pollution, invasive species, climate change, overexploitation and underlying drivers.	244
A.5.	Methods studying different parameters related to the CBD headline indicator measuring trends in distribution, condition and sustainability of ecosystem services for equitable human well-being.	245
A.6.	Methods studying different parameters related to the CBD headline indicator measuring trends in coverage, condition, representativeness and effectiveness of protected areas and other area-based approaches.	247

List of Figures

3.1. Flow chart of the overall methodology proposed for vegetation height estimation.	71
3.2. The study area in the Netherlands. The WorldView-2 images from June 2011 (top) and September 2011 (bottom) are depicted in true colour (Red, Green, Blue bands), overlaid by the segment lines from the topographic land cover/use map. .	72
3.3. Average height for each object of interest based on the CHM. ‘Other’ indicates objects of different classes than the GHC studied ones.	85
3.4. The best classification accuracies acquired for certain data processing methods, indicated by a number of capital letters. Feat: exclusion of texture features having at least one indefinite value; Obj: exclusion of objects having at least one indefinite value; Norm: zero-mean normalization; MI: multiple imputation with the Amelia II method; OR: outlier removal with the Mahalanobis distance-based box plot method.	86
3.5. Kappa coefficients of the data processing methods shown in Fig. 3.4.	89
3.6. Height classification after listwise deletion in the full June image dataset, using AdaBoost.M1 with J48 as base classifier. ‘Excluded’ indicates the removed objects by listwise deletion, whereas ‘Other’ shows classes different than the studied ones and cloud masked areas. The percentage of the objects classified to each class over the total number of classified objects is shown in parenthesis.	91

3.7.	Average classification accuracies achieved from the various classifiers, over the different datasets shown in Fig. 3.4. RT: REPTree; RF: Random Forest; A-RT: AdaBoost.M1 with REPTree; A-J48: AdaBoost.M1 with J48; B-RT: Bagging with REPTree; B-J48: Bagging with J48; SVM-M: SVM with logistic models.	92
3.8.	The best classification accuracies achieved with different dimensionality reduction approaches, reducing to 5 features the datasets after listwise deletion ('Obj'). Methods: Full: Full dataset; PCA: Principal Component Analysis; LPP: Locality Preserving Projections; NPE: Neighborhood Preserving Embedding; Isomap: isometric feature mapping; LDA: Linear Discriminant Analysis.	94
3.9.	Classification accuracies and kappa coefficient values achieved employing all features of a band, for each band of the June and September image, using the Random Forest classifier. Bands: coastal (1), blue (2), green (3), yellow (4), red (5), red-edge (6), NIR1 (7), NIR2 (8).	97
3.10.	Classification accuracies achieved employing the features selected through different approaches for filter feature selection and the respective number of selected features, for the selected features of (a) the June image, (b) the September image, (c) the union of those two selected sets and (d) the features selected from the ones of both images. The Random Forest classifier was used. Feature selection methods: correlation-based evaluation with best-first (RB) and Linear Forward Selection (RL), consistency-based evaluation with best-first (CB) and Linear Forward Selection (CL).	98
4.1.	Flow chart of the overall methodology proposed for supervised habitat classification.	107
4.2.	Le Cesine study site, Apulia region, Italy. Worldview-2 image from October 2010 in (a) true colour, overlaid by the segment boundaries delineated in the LCCS map. In addition, the (b) Blue, (c) Red, and (d) NIR-1 bands are drawn.	110

4.3.	Lago Salso study site, Apulia region, Italy. Worldview-2 image from 2010 in true colour, overlaid by the segment boundaries delineated in the LCCS map. In addition, the (b) Blue, (c) Red, and (d) NIR-1 bands are drawn.	112
5.1.	The proposed fuzzification methods: (a) Membership functions with constant slopes (methods F1–F5); (b) F2 (red), F4 (green), and F5 (blue) methods in case of small distance thresholds; and (c) membership functions with variable slopes (method F6).	138
5.2.	The 28 classifier versions, resulting from the combination of the four implementations and the F0–F6 fuzzification methods.	144
5.3.	Classification accuracies (%) for all DS fuzzy classifiers for Le Cesine study area, based on (a) tolerance to the existence of the correct class in the returned event, or (b) penalizing incorrect classes on a multiple class event. Columns represent the fuzzification measures (F0–F6) for each implementation (A1, A2, B1, B2) of the classifier (Figure 5.2), whereas rows the different minimum threshold values for single classes (0.1–0.9) for each selection criterion (<i>bel</i> , <i>pls</i> , or combination). . .	148
5.4.	Average accuracies (%) of the two classification interpretations of Fig. 5.3 for Le Cesine study area. Columns represent the fuzzification measures (F0–F6) for each implementation (A1, A2, B1, B2) of the classifier (Figure 5.2), whereas rows the different minimum threshold values for single classes (0.1–0.9) for each selection criterion (<i>bel</i> , <i>pls</i> , or combination). . .	150
5.5.	Normalized difference of the two main classification interpretations for Le Cesine study area. Only the upper quartile classifiers under both interpretations, for each A and B implementations, are selected. Columns represent the fuzzification measures (F0–F6) for each implementation (A1, A2, B1, B2) of the classifier (Figure 5.2), whereas rows the different minimum threshold values for single classes (0.1–0.9) for each selection criterion (<i>bel</i> , <i>pls</i> , or combination).	151

5.6.	GHC map resulting from the best performing fuzzy DS classifier under penalizing multiple class and averaging interpretations (a) and GHC validated classes (b) for Le Cesine. . . .	154
5.7.	Classification accuracies (%) for all DS fuzzy classifiers for Lago Salso study area, based on (a) tolerance to the existence of the correct class in the returned event, or (b) penalizing incorrect classes on a multiple class event. Columns represent the fuzzification measures (F0–F6) for each implementation (A1, A2, B1, B2) of the classifier (Figure 5.2), whereas rows the different minimum threshold values for single classes (0.1–0.9) for each selection criterion (<i>bel</i> , <i>pls</i> , or combination). . . .	163
5.8.	Average accuracies (%) of the two classification interpretations of Fig. 5.7 for Lago Salso study area. Columns represent the fuzzification measures (F0–F6) for each implementation (A1, A2, B1, B2) of the classifier (Figure 5.2), whereas rows the different minimum threshold values for single classes (0.1–0.9) for each selection criterion (<i>bel</i> , <i>pls</i> , or combination). . . .	164
5.9.	Normalized difference of the two main classification interpretations for Lago Salso study area. Only the upper quartile classifiers under both interpretations are selected. Columns represent the fuzzification measures (F0–F6) for each implementation (A1, A2, B1, B2) of the classifier (Figure 5.2), whereas rows the different minimum threshold values for single classes (0.1–0.9) for each selection criterion (<i>bel</i> , <i>pls</i> , or combination).	165
5.10.	Correlation between the classifier results for Le Cesine and Lago Salso, based on results shown in Fig. 5.3 and 5.7. Fig. 5.3a and 5.7a are crossed (a) column per column or (b) row per row; the same is repeated for Fig. 5.3b and 5.7b. (c) The accuracies of the classifiers applied in the two sites are also provided in a scatter diagram.	166
5.11.	GHC map resulting from the best performing fuzzy DS classifier under the averaging interpretation (a) and GHC validated classes (b) for Lago Salso.	170

B.1. The WorldView-2 image for the Dutch study area from June 2011, in true colour.	248
B.2. The WorldView-2 image for the Dutch study area from September 2011, in true colour.	249
B.3. The Canopy Height Model for the Dutch study area.	249
B.4. The Land Cover map for the Dutch study area.	250
B.5. The QuickBird image for Le Cesine study area from June 2009, in true colour.	251
B.6. The WorldView-2 image for Le Cesine study area from October 2010, in true colour.	251
B.7. LCCS map of Le Cesine site and validation points.	252
B.8. The WorldView-2 image for Lago Salso study area from June 2010, in true colour.	253
B.9. The WorldView-2 image for Lago Salso study area from February 2011, in true colour.	253
B.10.LCCS map of Lago Salso site and validation points.	254

List of Acronyms

A-J48	AdaBoost.M1 with J48 as basis classifier
A-J48	AdaBoost.M1 with REPTree as basis classifier
ALI	Advanced Land Imager
ALS	Airborne Laser Scanning
ANN	Artificial Neural Networks
ANN-D	ANN with decay in the learning rate
AQU	Aquatic (SPV)
ART	Artificial (URB)
ASAR	Advanced SAR
ASTER	Advanced Spaceborne Thermal Emission and Reflection Radiometer
AVHRR	Advanced Very High Resolution Radiometer
AVIRIS	Airborne Visible / Infrared Imaging Spectrometer
AVNIR-2	Advanced Visible and Near Infrared Radiometer type 2
AWiFS	Advanced Wide Field Sensor
B-J48	Bagging with J48 as basis classifier
B-J48	Bagging with REPTree as basis classifier
BOU	Boulders (SPV)
BTBR	Bi-temporal band ratio
CART	Classification And Regression Tree
CASI	Compact Airborne Spectrographic Imager
CBD	Convention on Biological Diversity
CFS	Correlation-based Feature Selector

CHE	Caespitose hemicryptophytes (HER)
CIR	Colour infrared
CMFDA	Continuous Monitoring of Forest Disturbance Algorithm
CON	Coniferous
CRO	Herbaceous crops (CUL)
CRY	Cryptogams (HER)
CUL	Cultivated
DCH	Dwarf chamaephytes (TRS)
DDI	Diameter Differentiation Index
DEC	Deciduous
DEM	Digital Elevation Model
DESDynI	Deformation, Ecosystem Structure and Dynamics of Ice
DGVI	Derivative Greenness Vegetation Index
DN	Digital Number
DR	Dimensionality Reduction
DS	Dempster–Shafer (theory)
DTM	Digital Terrain Models
EAR	Earth (SPV)
EBV	Essential Biodiversity Variables
EHY	Emergent hydrophytes (HER)
EO-1	Earth Observing 1
ERS-2	European Remote Sensing Satellite 2
ETM+	Enhanced Thematic Mapper Plus
EU	European Union
EVI	Enhanced Vegetation Index
EVR	Evergreen
ExG _M	Excess Green Index
FAO	Food and Agriculture Organization
FPH	Forest phanerophytes (TRS)

GAM	Generalized Additive Models
GAMLSS	Generalized Additive Models for Location, Scale and Shape
GC	Gini Coefficient
GCP	Ground Control Points
GEO	Geophytes (HER)
GEO BON	Group on Earth Observations Biodiversity Observation Network
GHC	General Habitat Categories
GI	Greenness Index
GLCM	Gray Level Co-occurrence Matrix
GPH	Mega phanerophytes (TRS)
GPP	Gross Primary Productivity
GRA	Herbaceous (URB)
GRV	Gravel (SPV)
HCH	Herbaceous chamaephytes (HER)
HEL	Helophytes (HER)
HER	Herbaceous vegetation
HRG	High Resolution Geometric
HRVIR	High-Resolution Visible and Infrared
ICE	Ice / snow (SPV)
ICESat II	Ice Cloud and land Elevation Satellite II
IIC	Integral Index of Connectivity
IRMI	Iterative Robust Model-based Imputation
J48	J48 implementation of C4.5 tree classifier
LAI	Leaf Area Index
LBP	Local Binary Patterns
LC	Land Cover
LC/LU	Land Cover / Land Use
LCCS	Land Cover Classification System

LDA	Linear Discriminant Analysis
LE	Local Variance
LH	Local Entropy
LHE	Leafy hemicryptophytes (HER)
LHR	Local Entropy Ratio
LISS-III	Linear Imaging Self Scanning Sensor 3
LPH	Low phanerophytes (TRS)
LPP	Locality Preserving Projections
LTBP	Local Binary Patterns with range
LTP	Local Ternary Patterns
LUCAS	Land Use/Cover Area frame statistical Survey
MEA	Millennium Ecosystem Assessment
MERIS	Medium Resolution Imaging Spectrometer
MESMA	Multiple Endmember Spectral Mixture Analysis
MIVIS	Multispectral Infrared and Visible Imaging Spectrometer
MLC	Maximum Likelihood Classifier
MODIS	Moderate Resolution Imaging Spectroradiometer
MPH	Mid phanerophytes (TRS)
MSS	Multispectral Scanner
NDVI	Normalized Difference Vegetation Index
NDWI	Normalized Difference Water Index
NIR	Near infrared
NLE	Non-leafy evergreen
NON	Non-vegetated (URB)
NPE	Neighborhood Preserving Embedding
OA	Overall Accuracy
OBIA	Object Based Image Analysis
OHM	Object Height Model
OMI	Ozone Monitoring Instrument

OSAVI	Optimized Soil-Adjusted Vegetation Index
PA	Producer's Accuracy
PALSAR	Phased Array type L-band Synthetic Aperture Radar
PCA	Principal Component Analysis
PolInSAR	Polarimetric SAR Interferometry
PRI	Photochemical Reflectance Index
PVI	Perpendicular Vegetation Index
QB	QuickBird
QDA	Quadratic Discriminant Analysis
QP	Quadratic Programming
RDA	Regularized Discriminant Analysis
REDD+	Reducing Emissions from Deforestation and Forest Degradation
REIP	Red-Edge Inflection Point
RF	Random Forest
RMSE	root mean square error
ROC	Bare rocks (SPV)
ROSIS	Reflective Optics System Imaging Spectrometer
RT	REPTree (reduced-error pruning) classifier
SAM	Spectral Angle Mapper
SAN	Sand (SPV)
SAR	Synthetic Aperture Radar
SCH	Shrubby chamaephytes (TRS)
SDA	Stepwise Discriminant Analysis
SDD	Secchi Disk Depth
SDDBH	Standard Deviation of Diameter at Breast Height
SEA	Sea (SPV)
SeaWiFS	Sea-Viewing Wide Field-of-View Sensor
SHY	Submerged hydrophytes (HER)
SID	Spectral Information Divergence

SMO	Sequential Minimal Optimization
SPA	Bare ground (CUL)
SPV	Sparsely vegetated
STO	Stones (SPV)
SVM	Support Vector Machines
SVM-M	SVM with fitting logistic models to the output
TCT	Tasseled Cap Transformation
THE	Therophytes (HER)
TID	Tidal (SPV)
TM	Thematic Mapper
TOA	Top-of-Atmosphere (reflectance)
TPH	Tall phanerophytes (TRS)
TRE	Woody (URB)
TRMM/TMI	Tropical Rainfall Measuring Mission's Microwave Imager
TRS	Trees and Shrubs
UA	User's Accuracy
UN	United Nations
UNEP	UN Environment Programme
URB	Urban
VEG	Vegetables (URB)
VHR	Very High Resolution
WI	Water Index
WiFS	Wide Field Sensor
WOC	Woody crops (CUL)
WV-2	WorldView-2

1. Introduction

1.1. Motivation

1.1.1. Biodiversity monitoring and remote sensing

Biodiversity, i.e. the variety of plant and animal life in the world or in a particular habitat [1], is a key issue in ecosystem stability and functioning, severely affecting human society and health [2, 3]. It is a complex notion, difficult to measure and express in a simple manner [4, 5]. Various indicators are broadly used as means to assess status and trends of different aspects of biodiversity, measure pressures and threats, and quantify biodiversity loss at the level of genes, populations, species, or ecosystems [6–8]. Several sets of such biodiversity indicators, have been proposed by different organizations, scientific groups, and policy makers worldwide to achieve monitoring in a reliable and repeatable way [7, 9–13]. They can be measured directly or calculated using mathematical and statistical models, and they may be defined to have a global, regional, or local applicability. Among the most widely adopted indicators are the ones proposed by the United Nations (UN) Convention on Biological Diversity (CBD), aiming at monitoring the progress towards the achievement of defined targets, at global scale [14, 15]. Further efforts include the definition of more directly measured variables, to enhance indicator extraction, such as the Essential Biodiversity Variables (EBV), proposed by the Group on Earth Observations Biodiversity Observation Network (GEO BON) [16]. The importance of biodiversity indicators and EBVs lies in the concise information they provide to the scientific and policy making communities on the status and trends of a variety of biodiversity related characteristics, such as the extent and condition of particular ecosystems and habitats; the abundance and distribution of selected species; or the pressures from pollution, climate change, and unsustainable agriculture and forestry. They are used as proxies to indicate the progress towards globally or locally defined targets for biodiversity preservation, e.g. reduc-

tion of loss of habitats and their degradation and fragmentation; restoration of ecosystems that provide essential services for health and well-being; and identification of invasive alien species. Thus, accurate and timely estimation of indicators has a significant impact in early warning for the need of restoration or mitigation actions to sensitive or endangered areas.

The imperative need for biodiversity protection and preservation has been highlighted during the last years [17], with the UN declaring 2010 as the International Year of Biodiversity and 2010–2020 as the Decade on Biodiversity. Following the realization that the targets for halting biodiversity loss by 2010 were not met [6, 18], CBD and the European Union (EU) updated their mitigation strategies towards 2020 [19, 20]. CBD adopted the Strategic Plan for Biodiversity 2011–2020 and set the so-called Aichi Biodiversity Targets [19], as criteria of achieving the defined goals by 2020.

Although the most accurate way of measuring certain aspects of biodiversity, such as the distribution and population of plant and animal species, is by in-situ campaigns, in many cases, such approaches are proven particularly cost or time demanding, and for some areas, difficult or even impossible [21, 22]. Remote sensing (RS) data, on the contrary, derived from airborne or satellite sensors, have been increasingly employed in biodiversity monitoring studies [4, 23–25]. Offering the capability of constant, repetitive, and cost-effective monitoring of large areas, RS data can provide precious information nearly impossible to be acquired solely by field assessment [26]. Numerous studies using RS data to measure biodiversity-related properties have been presented in the literature, covering a broad range of applications, study areas and employed data and methods.

The majority of these studies are rarely explicitly connected to any of the widely adopted biodiversity indicators, e.g. those proposed by CBD, that could be extracted through them, directly or indirectly. Instead, on the one hand, a variety of indicators have been proposed and used by individual RS studies, resulting in numerous incompatible monitoring systems [9]. On the other hand, despite the increasing availability of RS data, the connection between entities measured by remote sensing and indicators required by the biodiversity, management, and policy-making communities has still been poor [27]. Thus, identification of high performing RS approaches and establishment of a link to a common set of indicators widely adopted by the user community would be highly beneficial for their extraction and the

minimization of this knowledge gap.

1.1.2. Vegetation height estimation and remote sensing

Among variables related to biodiversity monitoring, vegetation height is a fundamental biophysical and structural parameter, useful additionally to a number of relevant ecological and environmental studies and applications, such as conservation planning and biomass estimation [24,28,29]. The mean tree height of a stand has been identified as one of the most important stand characteristics for forest planning tasks [30], with a root mean squared error (RMSE) below 1 m being adequate for forest inventory studies in certain areas [31]. Furthermore, high-resolution maps of canopy height are important as means to improve aboveground biomass and carbon stock estimation, used as proxies to model future climate change, and also to measure carbon fluxes and emission reduction in the framework of national and international strategies [32]. In addition, vegetation height constitutes a basic element for landscape analysis tasks and a discriminatory feature for class characterization in various land cover and habitat taxonomies [33,34]. Precise estimation leads to correct classification of certain land cover types and habitats based on their height range, enhancing the monitoring of their extent and condition, the detection of changes, and their conservation and management.

Satellite and airborne sensors have been increasingly used for the estimation of vegetation height during the last decades, as time-, cost-, and labour-efficient alternatives to field measurements. Aerial and spaceborne active sensors (i.e. sensors transmitting signals and receiving the reflected, refracted, or scattered ones), namely lidar and Synthetic Aperture Radar (SAR) sensors, have been proven particularly effective in retrieving vegetation structural information [35–37]. However, their cost per unit area can be prohibitively high [38]; in addition, a number of two or more images of the same area may be required.

Less cost and resource demanding approaches have been sought in the use of passive satellite sensors, mainly of high spatial resolution, applying regression analysis to model vegetation height using image spectral properties [39] or, more effectively, texture features [40,41]. However, although such methods achieved results indicating the potential of texture analysis

on data from passive sensors in vegetation height estimation, certain limitations can be spotted. The majority of these studies have been restricted to trees with heights of several metres and of a specific vegetation type each time, e.g. coniferous, or even a specific species. In addition, remote sensing data from only one date have been employed in each study, neglecting to evaluate the proposed method in different time of the year or study synergies of data from multiple dates. Furthermore, potential improvements from data processing techniques after the extraction of features, e.g. dimensionality reduction or imputation of missing values, have rarely been examined. Such shortcomings of previous studies are attempted to be addressed by the present work.

1.1.3. Habitat mapping and remote sensing

The term ‘habitat’ describes the place and the type of environment in which an organism normally occurs [42]. Different definitions have been suggested, with Bunce *et al.* [43] recently defining habitat as “an element of the land surface that can be consistently defined spatially in the field in order to define the principal environments in which organisms live.” Thus, mapping of habitats and their changes has been identified as significant stepping stone for biodiversity and ecosystem monitoring, as well as conservation planning and landscape sustainability management [43–45]. Highlighting the importance of habitat monitoring, halving the loss of habitats by 2020 has been defined as one of the 20 Aichi targets for global biodiversity preservation, whereas indicators for habitat extent, condition, and pressures have been included in the updated biodiversity strategies of CBD and EU [19,20]. Robust estimates on habitat status and changes have been used in national rural policy strategies [43].

The extraction of habitat maps with RS data has mainly been performed using directly the available imagery [46–48]. However, direct mapping of habitats has been challenging, whereas the majority of RS methods have focused on the simpler mapping of land cover (LC) categories [23]. The latter are defined as “the observed (bio)physical description of the earth’s surface” [42], and therefore, are more straightforward to monitor through RS data. Furthermore, land cover and land use (LC/LU) maps have been extensively produced during the last years, at regional or national scales, as

minimum approximations to the increasingly, often due to legal obligations, required habitat maps [49].

Therefore, the extraction of habitat maps through the conversion of existing LC maps, using RS data, seems a promising alternative to direct habitat mapping from RS imagery. However, it has still been poorly investigated and mainly restricted to theoretical analyses [50, 51]. Although such conversion was limited by discrepancies in definitions of LC and habitat classes, and requirements of richer information for the mapping of the latter, Adamo *et al.* [52, 53] recently presented a rule-based expert system to delineate habitats using LC maps and Very High Resolution (VHR) satellite data.

The method identified a number of habitat classes using a variety of RS derived features and respective classification rules defined by expert ecologists. Although relatively high accuracies were achieved, certain shortcomings of the method can be spotted. On the one hand, features were selected empirically by the experts, whereas rules and the associated thresholds were based on expertise and repetitive trial-and-error experimentation. Such task involves labour and time consuming fine-tuning of threshold values through numerous iterations, while the number of total different evaluated combinations of values remains limited. On the other hand, no counteraction is provided in case of missing information or inaccuracies caused by noisy input data or vague expert rules. Such problems are common in remote sensing applications, where data considered necessary may be unavailable for certain study areas, or be afflicted by noise during different stages from acquisition to processing, such as image registration, quantization, or topographic and atmospheric correction. Approaches addressing these limitations are expected to provide more robust solutions and improve the habitat classification.

1.1.4. Objectives

Following the previous discussion, the main objectives of the thesis can be summarized as:

- To identify and review high performing remote sensing approaches and their connection to a common widely adopted set of biodiversity indicators, namely the CBD indicators, supporting their extraction

and the decrease of the knowledge gap between the remote sensing and the ecology, conservation biology, site manager, and policy making communities.

- To offer a cost and resource effective approach to vegetation height estimation, by the use of single passive sensor images, and to address shortcomings of previous methods limited to specific types of vegetation, restricted height ranges, single-date imagery, and small use of data processing techniques.
- To implement effective and robust methodologies for the conversion of land cover to habitat maps with the use of RS data, (i) by automating the classification process and (ii) handling uncertainties, in order to increase the classification accuracy and the transferability of the methods to different study areas.

1.2. Contributions

With regards to the defined objectives, the main contributions of the thesis can be summarized as follows:

- The Aichi targets that can be monitored through RS data are recognized, by identifying the CBD biodiversity indicators and EBV that can be extracted using such data. Then, a wide number of recent state-of-the-art remote sensing methods are identified in the literature, reviewed, and proposed to be adopted for the calculation of CBD headline indicators and the further monitoring of the progress towards the achievement of the Aichi Targets, at a global level. The methods are evaluated based on their outcomes and the achieved accuracies, when appropriate, and the best performing ones are identified. Capacity and limitations of the methods are discussed, and future directions are proposed.
- A framework to estimate vegetation height through texture analysis of very high resolution (VHR) passive sensor imagery is proposed. An object-based approach is followed and a number of features are suggested, based on local variance, entropy, and local binary patterns. The extracted features are used to delineate a number of height

classes representing specific habitats. A wide range of algorithms for data processing and classification are employed and evaluated, including handling of missing values, outlier removal, data normalization, dimensionality reduction with data transformation and feature selection, and various supervised classifiers. Contrary to previous studies, synergies of data from two dates are additionally tested, whereas the classified objects are of various vegetation types and of heights ranging from less than 5 cm to several tens of metres.

- Two approaches for LC map conversion to habitats using VHR imagery are proposed, to counteract limitations of the expert rule-based classifier by Adamo *et al.* [52, 53]. The approaches are applied in two areas each, to evaluate their generalization performance and their transferability in various study sites.
 - a) The first one is a supervised learning approach, where extracted feature values are used to train high performing classifiers and automatically provide classification rules. A methodology to express LC names/codes (string variables) as numerical values (interval-scaled variables) is proposed, allowing land cover classes to be fed as input to the classifier, while characterizing inter- and intra-class variabilities. Texture features, proposed in the height estimation framework, are also extracted and evaluated as surrogates of features derived from lidar data in the habitat classification process. A number of different supervised classifiers are employed and evaluated.
 - b) The second proposed approach is based on the use of evidential reasoning, in particular the Dempster–Shafer (DS) theory [54, 55], as a means to allow handling of uncertainty and enhance information fusion. Building on the expert rules of [52, 53], a number of fuzzification methods, to counteract noise in data or inaccurate rule thresholds, are proposed and coupled with the DS classifier. In addition, a framework allowing the classifier to select multiple classes, when not enough data are available to strongly support the selection of a single habitat class, is proposed, whereas extensive evaluation of criteria for class selection and user-dependent decision making is provided.

1.3. Organization of the thesis

The thesis is organized as follows. The present Chapter 1 serves as introduction, outlining the scope, the major objectives, and the contributions of the presented research work. It also provides an overview of the thesis structure.

Chapter 2 identifies the Aichi targets and the respective CBD headline indicators and EBV that can be measured through remote sensing. For each CBD indicator, covering a wide range of fields, RS methods that can be used for the monitoring of a number of related properties are reviewed, as far as the employed data, algorithms, final products, and achieved accuracies are regarded. Finally, advantages and limitations of RS in monitoring different aspects of biodiversity are discussed, and future research directions are proposed.

In Chapter 3, the proposed framework for estimation of vegetation height is reported. Following a brief presentation of the study area and the available data, the proposed texture features are described. The algorithms used to process the derived texture features, including handling of missing data, outlier removal, data normalization, and dimensionality reduction through feature selection and data transformation, are presented, together with a number of classifiers used for their evaluation. Particular focus is given on feature selection methods, as means to identify best performing feature subsets. Images from two dates, representing different vegetation status periods, are employed and evaluated both individually and in synergy.

Chapter 4 presents the proposed approach for land cover to habitat map conversion with supervised learning. The two study areas and the related available data are briefly introduced. The methodology to represent the classes of the LC map as numerical values is then described. Evaluation of the feature sets used by Adamo *et al.* [52, 53], as well as of other feature combinations, is performed for two study areas, under different supervised classifiers. To test the generalization performance of the methodology, additional experiments are performed training the classifiers with data from the one study area and testing them in the other.

In Chapter 5, the proposed classification framework for LC to habitat conversion based on the Dempster–Shafer theory and fuzzy logic is described. A brief overview on the main notions of DS theory is initially provided, fol-

lowed by the description of the different fuzzification methods proposed. As in [52, 53], classifiers (i) considering and (ii) neglecting the availability of lidar data, as sources of height information, are developed. The classification framework is thoroughly evaluated under the use of all different fuzzification methods, and compared with crisp classification results, i.e. with no fuzzification, similar to [52, 53]. An extensive number of parameters for the final class selection, using flexibility to different user preferences, are tested and their outcomes are discussed. Combination of the results from individual classifiers through the use of Dempster rule of combination [55] is also tested. Evaluation of the approach is performed for both the area which the expert rules were originally derived for and a second area used to test its generalization performance and transferability to other sites. Comparison with the results from the supervised classification framework is finally performed.

Chapter 6 summarizes the main outcomes of the thesis, in relation with the defined objectives, and provides concluding remarks. In addition, potential extents of the developed methodologies and future research directions based on the presented work are discussed.

Appendix A draws the tables with the sorting and characteristics of the remote sensing methods discussed in Chapter 2. Appendix B presents the available data for each study area discussed in the thesis, including satellite imagery, land cover maps, and object height models derived from lidar data.

2. Remote sensing for biodiversity monitoring

2.1. Targets and indicators

CBD initially suggested a set of biodiversity indicators aiming at monitoring the progress of biodiversity conservation achievements by 2010, the so-called 2010 Biodiversity Target [10]. The biodiversity indicators were defined in a way to be globally applicable and organized in seven focal areas, trying to incorporate issues ranging from conservation and sustainable use of biodiversity, to social considerations dependent upon the maintenance of biodiversity. Following the failure of meeting the 2010 targets [6], new indicators were proposed, as well as an updated organization of the biodiversity indicators under 12 headline indicators [15]. The headline indicators were associated with the 20 Aichi Targets and meant to monitor the progress towards their achievement [19]. A number of specific indicators may be grouped under each headline indicator [15].

Upon demand by CBD, the Group on Earth Observations Biodiversity Observation Network (GEO BON) attempted to assess the adequacy of global observation systems for biodiversity monitoring, mainly as far as information needs are regarded, for the achievement of the Aichi targets [56]. Although numerous existing observation systems were identified, the need for further development, expansion and financial resource flow was recognized for the global completion of most targets. Acknowledging the lack [57] and envisaging the development of a global, harmonized system to observe biodiversity [58], a set of candidate Essential Biodiversity Variables (EBV) were suggested [16]. The aim of EBV is to define a minimum set of essential measurements and act as an intermediate layer between primary observations (e.g. RS data) and biodiversity indicators, facilitating the extraction of the latter. They are organized in six main classes, the particular EBV

being under development [16].

Remote sensing, as provenly a valuable tool in monitoring of biodiversity-related variables, is expected to contribute immensely in monitoring the progress of certain Aichi targets. Such monitoring will become feasible by the extraction and update of the respective CBD biodiversity indicators, or related EBV. Table 2.1 identifies the CBD headline indicators that can be extracted through RS data, and based on them, identifies and presents the Aichi targets whose progress may be monitored using remote sensing. The respective EBV classes measurable through RS are also depicted. The table does not depict the full network of associations and secondary inter-relations; e.g. expansion of sustainable forestry may also be an indicator of pollution reduction or species extinction prevention. However, the primary associations between indications and target achievements are reported.

2.2. Remote sensing capacity for CBD indicator extraction

A review of the most recent approaches in biodiversity monitoring and their link to the CBD headline indicators that can be measured by space- or air-borne sensors, as identified in Table 2.1, is provided in this section. Extending previous studies focusing on policy-makers and identifying the principal role of RS data in CBD indicator extraction [27], the present work focuses not only on the potential of various RS data, but also on the data processing and mapping algorithms employed.

A variety of measures have been employed to evaluate the accuracy of the methods, depending on the characteristics of each method and the nature of the problem. Table 2.2 provides the definition of the accuracy evaluation measures used in this chapter and throughout the thesis.

Although a direct comparison of methods, even among ones measuring similar variables, is rarely possible, due to differences in numerous parameters, an indicative sorting of the methods is attempted for each measured entity category. The sorting is mainly based on reported accuracies, taking into account the number of employed classes, in classification problems. In cases where accuracies are provided in different evaluation metrics among the approaches of the same category, e.g. as a mixture of classification accu-

Table 2.1.: Aichi targets that can be monitored through RS data, and the associated CBD headline indicators and EBV classes.

Aichi targets	CBD headline indicators	EBV classes
(4) Sustainable production and consumption	(4) Pressures practices ¹ (5) Pressures various ²	Species populations
(5) Reduction of habitat loss, fragmentation and degradation	(1) Extent ³ (4) Pressures practices (5) Pressures various	Species populations Ecosystem function Ecosystem structure
(6) Sustainable exploitation of marine resources	(4) Pressures practices	Species populations
(7) Sustainable management of agriculture, aquaculture and forestry areas	(4) Pressures practices	Species populations Ecosystem structure
(8) Pollution reduction	(5) Pressures various	Species populations Community composition Ecosystem function
(9) Invasive alien species control	(2) Species ⁴ (5) Pressures various	Species populations
(10) Protection of vulnerable ecosystems	(5) Pressures various	Species populations Community composition Ecosystem structure
(11) Conservation and protection of important areas	(11) Protected areas ⁵	Species populations Ecosystem structure
(12) Preventing extinction of threatened species	(2) Species	Species populations
(14) Safeguarding ecosystems with essential services	(6) Services ⁶ (11) Protected areas	Species populations Community composition Ecosystem function Ecosystem structure
(15) Enhancing ecosystem resilience	(6) Services (11) Protected areas	Species populations Species traits Ecosystem structure

¹Trends in pressures from unsustainable agriculture, forestry, fisheries and aquaculture

²Trends in pressures from habitat conversion, pollution, invasive species, climate change, overexploitation and underlying drivers

³Trends in extent, condition and vulnerability of ecosystems, biomes and habitats

⁴Trends in abundance, distribution and extinction risk of species

⁵Trends in coverage, condition, representativeness and effectiveness of protected areas and other area-based approaches

⁶Trends in distribution, condition and sustainability of ecosystem services for equitable human well-being

Table 2.2.: Accuracy evaluation measures used throughout the thesis.

Metric	Definition	Symbols
Overall accuracy	$OA \equiv \frac{NC}{N}$	NC : number of correctly classified samples; N : total number of samples
Producer's accuracy (for class A)	$PA_A \equiv \frac{NC_A}{NO_A}$	NC_A : Correctly classified samples to class A ; NO_A : total observed samples of class A
Omission error (for class A)	$EO_A \equiv 1 - PA_A$	
User's accuracy (for class A)	$UA_A \equiv \frac{NC_A}{NP_A}$	NC_A : Correctly classified samples to class A ; NP_A : total samples classified to class A
Commission error (for class A)	$EC_A \equiv 1 - UA_A$	
Cohen's kappa coefficient	$\kappa \equiv \frac{P_o - P_c}{1 - P_c}$	P_o : proportion of agreement between classified and observed samples $\equiv OA$; P_c : proportion of expected agreement by chance, $P_c = \sum_{i=1}^C (NO_i/N)(NP_i/N)$, C : number of classes, NO_i , NP_i , N defined as above
Pearson's correlation coefficient	$r \equiv \frac{\sum_{i=1}^N (f_i - \bar{f})(y_i - \bar{y})}{\sqrt{\sum_{i=1}^N (f_i - \bar{f})^2} \sqrt{\sum_{i=1}^N (y_i - \bar{y})^2}}$	y_i : observed values; f_i : model predicted values; $\bar{y} \equiv \sum_{i=1}^N y_i/N$; $\bar{f} \equiv \sum_{i=1}^N f_i/N$; N : number of samples
Coefficient of determination	$R^2 \equiv 1 - \frac{\sum_{i=1}^N (y_i - f_i)^2}{\sum_{i=1}^N (y_i - \bar{y})^2}$	y_i , f_i , \bar{y} , N defined as above
Adjusted R^2	$\bar{R}^2 \equiv R^2 - (1 - R^2) \frac{D}{N - D - 1}$	N : number of samples; D : number of explanatory variables in the regression model
Root mean square error	$RMSE = \sqrt{\frac{1}{N} \sum_{i=1}^N (y_i - f_i)^2}$	y_i , f_i , N defined as above
Absolute (standard) error	$E = \frac{1}{N} \sum_{i=1}^N y_i - f_i $	y_i , f_i , N defined as above
Relative (standard) error	$E_r = \frac{1}{N} \sum_{i=1}^N \frac{ y_i - f_i }{y_i}$	y_i , f_i , N defined as above

racies, root mean square errors (RMSE), coefficient of determination (R^2) values, etc., the provided sorting is indicative, not conveying any comparative information. An indisputable comparison of the methods would only be possible if experiments were conducted under the same conditions, datasets,

and study areas, which is highly unlikely in RS applications; however, the attempted sorting may convey useful information on the efficiency of certain sensors or algorithmic approaches and their comparative advantages over others, and provide guidelines to research, monitoring, and policy-making communities on future applications.

A large number of satellite and aerial sensors are employed in the studies discussed in the next paragraphs. Table 2.3 presents a list of the sensors and some of their properties as derived from the respective studies, including their spatial resolution, number of bands, cost, and their acronyms as used in the tables of the following paragraphs. Both space- and airborne sensors are listed, ranging from passive multispectral and hyperspectral to active SAR and lidar sensors. Due to their large number, airborne lidar sensors and digital cameras are not included in the table. Sensors with large archive of data distributed at no cost, are indicated as ‘free’, even though new acquisitions or certain products may be commercially available. In addition, the CBD headline indicators where these sensors are involved, based on the discussion in the next paragraphs, are depicted. As a note, the CBD headline indicator on protected area monitoring (CBD 11) is under-represented in Table 2.3, since several methods conducted in or applicable to protected areas are discussed under other related indicators, such as ecosystem extent (CBD 1), or species diversity (CBD 2).

Table 2.3.: Acronyms and characteristics of multispectral / hyperspectral, SAR, and (satellite) lidar sensors used in CBD headline indicator extraction related studies.

Acronym	Sensor	Spatial resolution (m)	Bands	Cost	CBD
Multispectral / Hyperspectral					
ADS40	airborne	0.2	4	yes	(1) Extent ⁷
AHS-160	airborne	2.4	63	yes	(11) Prot. areas
AISA	airborne (AISA Eagle)	2-2.5	272	yes	(1) Extent
ALI	EO-1 ALI	30	9	free	(1) Extent, (6) Services
ASTER	Terra ASTER	15, 30, 90	14	free	All
AVHRR	TIROS-N, NOAA-7, NOAA-15 AVHRR	≈1100	6	free	(1) Extent, (2) Species, (6) Services
AVIRIS	airborne	3.5–4	224	yes	(5) Press. various

Continued on next page...

⁷Abbreviations of CBD headline indicators are given in Table 2.1

Table 2.3 – continued

Acronym	Sensor	Spatial resolution (m)	Bands	Cost	CBD
AVNIR-2	ALOS AVNIR-2	10	4	yes	(1) Extent, (4) Press. practices
AWIFS	IRS-P6 AWIFS	56	4	yes	(1) Extent
CAO-Alpha	airborne	0.56–1.2	24, 72	yes	(2) Species
CASI	airborne	1–3	15,36, 72	yes	(1) Extent, (2) Species, (4) Press. practices, (11) Prot. areas
DuncanTech	airborne	0.2	3	yes	(4) Press. practices
CHRIS	PROBA-1 CHRIS	17, 34	18, 62	free	(1) Extent
DMC Z/I	airborne	2	4	yes	(4) Press. practices
ETM+	Landsat-7 ETM+	30	8	free	All
GE-1	GeoEye-1	≈1–2	4	yes	(1) Extent
GS	airborne (Geospatial Systems)	0.2	3	yes	(4) Press. practices
HJ	HJ-1A/1B	30	4	yes	(5) Press. various
HRG	SPOT-5 HRG	10, 20	4	yes	(1) Extent, (4) Press. practices
HRVIR	SPOT-4 HRVIR	10, 20	4	yes	(4) Press. practices
HYDICE	airborne	1.6	210	yes	(2) Species
HyMap	airborne	3–5	126, 128	yes	(2) Species, (4) Press. practices
Hyperion	EO-1 Hyperion	30	220	free	(1) Extent, (2) Species, (4) Press. practices
IKONOS	IKONOS	1, 4	4	yes	(1) Extent, (2) Species, (4) Press. practices
LISS-III	IRS-P6 / IRS-1C/1D LISS-III	20–25	4	yes	(1) Extent, (4) Press. practices, (6) Services
LISS-II	IRS-1B LISS-II	36.25	4	yes	(4) Press. practices
MERIS	ENVISAT MERIS	300	15	free	(6) Services
MIVIS	airborne	3	102	yes	(1) Extent
MODIS	Terra / Aqua MODIS	250, 500, 1000	36	free	All
MP39	airborne (Leica MP 39)	0.25	3	yes	(4) Press. practices
MSS	Landsat 1–5	60–80	4–5	free	(1) Extent

Continued on next page...

Table 2.3 – continued

Acronym	Sensor	Spatial resolution (m)	Bands	Cost	CBD
OMI	Aura	13000×24000	740	free	(5) Press. various
QB	QuickBird 2	0.6, ≈2.4	4	yes	(1) Extent, (2) Species, (4) Press. practices, (6) Services
REye	RapidEye	6.5	5	yes	(4) Press. practices
ROSIS	airborne	1	115	yes	(1) Extent
SeaWiFS	SeaStar SeaWiFS	1100, 4500, 9000	8	free	(2) Species, (6) Services
Sentinel-2 ⁸	Sentinel-2 MSI	10, 20, 60	13	free	(4) Press. practices
SSat	SumbandilaSat	6.25	6	yes	(1) Extent
TCAMP	airborne (ThermaCAMP40)	1	1	yes	(4) Press. practices
TM	Landsat-5 TM	30	7	free	All
TMI	TRMM/TMI	5000–72000	5	free	(2) Species
TSys	airborne (Toposys GmbH)	0.4	4	yes	(6) Services
VEN μ S ⁸	VEN μ S VSSC	5.3	12	yes	(4) Press. practices
VGT	SPOT–VEGETATION	1000	4	free	(2) Species
WiFS	IRS-1D WiFS	180–188	2	yes	(1) Extent
WV-2	WorldView-2	≈0.5, ≈2	8	yes	(1) Extent, (2) Species
SAR					
ASAR	ENVISAT ASAR	30	1 (C)	free	(1) Extent, (5) Press. various, (6) Services
BioSAR	airborne	30×300	1 (80–120 MHz)	yes	(4) Press. practices
ERS	ERS-1/2 AMI (SAR)	6–30	1 (C)	free	(1) Extent, (5) Press. various
JERS-1 SAR	JERS-1 SAR	12.5–18	1 (L)	free	(1) Extent
PALSAR	ALOS PALSAR	≈30–50	1 (L)	yes	(1) Extent, (11) Prot. areas
RSAT-1	RADARSAT-1	≈30–50	1 (C)	yes	(5) Press. various
RSAT-2	RADARSAT-2	≈30–50	1 (C)	yes	(1) Extent
SIR-C	Space Shuttle SIR-C	≈30	2 (C, L)	free	(2) Species
TDX	TanDEM-X	12	1 (X)	yes	(4) Press. practices

Continued on next page...

⁸upcoming sensors, whose data have been simulated

Table 2.3 – continued

Acronym	Sensor	Spatial resolution (m)	Bands	Cost	CBD
TSX	TerraSAR-X	18.5–40	1 (X)	yes	(4) Press. practices
GLAS	ICESat GLAS	Lidar 40 times/s, 70 m footprint, 172 m interval	2 (532 nm, 1064 nm)	free	(4) Press. practices, (6) Services

Although not explicitly mentioned in the following sections, a significant degree of preparation, i.e. pre-processing, of the RS data is required before their actual use in each study. The required pre-processing steps are highly dependent on the type of sensor, the quality of data and conditions they were captured, and the specific application. The main categories of pre-processing usually include (i) geometric and (ii) radiometric correction [59]. Geometric correction is applied to reduce distortions from variations in the altitude or velocity of the sensor platform, panoramic distortion, earth curvature, atmospheric refraction, or relief displacement [60]. Most studies, especially ones using multiple data that need to co-align, apply at least georeferencing of image data, appropriately placing the images to a map projection; in case a Digital Elevation Model (DEM) or appropriate Ground Control Points (GCP) with elevation information are available, orthorectification [61] can also be performed, additionally correcting distortions due to topographic variation. Image resampling techniques are used to perform geometric correction, including nearest-neighbour resampling, bilinear interpolation, or cubic convolution [59].

Radiometric effects are caused by a variety of factors, including changes in scene illumination, atmospheric conditions, viewing geometry, and instrument response characteristics [60]. Some of these effects, e.g. from viewing geometry, are more intense for airborne than satellite data, whereas the opposite may happen for some others, e.g. from atmospheric conditions. Optical data pixels are usually initially expressed as Digital Numbers (DN), i.e. integer values with no physical meaning. In applications where data related with physical properties on the ground are required, DNs are converted to absolute radiance values, using sensor related calibration information. In other applications, e.g. performing spectral-based change detection, this

conversion is not adequate and a further conversion to Top-Of-Atmosphere or even surface reflectance values, eliminating atmospheric effects, is necessary. As a note, the latter corrections are usually not necessary for SAR data, since they are largely unaffected by the atmosphere. As an indicative example of RS data assumptions and requirements in certain studies, the following conditions ideally need to hold for the optical data for spectral-based change detection [59]: (i) acquired from the same or inter-calibrated sensors and the same time of day and look angle; (ii) acquired during the same season, for inter-annual studies; (iii) well co-registered with accuracies up to 0.2 of a pixel; (iv) free of cloud; (v) corrected to Top-Of-Atmosphere, or preferably, surface reflectance; and (vi) under same surrounding conditions influencing the signal, e.g. soil moisture.

2.2.1. Trends in extent, condition and vulnerability of ecosystems, biomes and habitats

Remote sensing data have been effectively used in various mapping applications, ranging from mixed land cover (LC) [62,63] and habitat [42] tasks, to mapping of specific target areas, e.g. forests [64] and wetlands [65], addressing different elements of the related CBD headline indicator. Trends may be extracted through the use of time series of data or extracted products. Among the cited methods, several use time series of RS data; others use single-date imagery, although their expansion to studying trends is straightforward if data time series are available. Methods studying LC and habitat mapping, of both terrestrial and aquatic biomes, provide direct information on the extent and condition of selected areas, whereas methods studying ecosystem degradation or deforestation, and fragmentation or connectivity offer valuable input to ecosystem condition and, even, vulnerability assessments.

Table A.1 in Appendix A lists selected state-of-the-art studies, indicatively sorted based on their best reported accuracies, when available. The studies are organized under: (1) terrestrial mapping, including (1a) forests, (1b) generic vegetation, such as grasslands, savannas, heathlands, and steppes, and (1c) mixed LC and habitats; (2) ecosystem degradation and deforestation; (3) ecosystem fragmentation and connectivity; and (4) aquatic mapping, including (4a) freshwater and (4b) marine and coastal biomes.

For each study, the principal sensor data are listed (‘RS data’ column), without including any ancillary data, such as GIS or thematic layers, or elevation models. In addition, the ‘Feature extraction’ column lists the algorithms used for extraction of features, such as spectral, texture, or image segments, as well as employed variables, whereas classification and regression techniques are listed under the ‘Mapping methods’ column. The final product of each method is also provided, together with the respective best achieved accuracies. The methods described below can be employed to monitor progress to Aichi target 5 (Table 2.1), on the reduction of habitat loss, fragmentation and degradation.

A. Terrestrial mapping

Landsat data, including the Multispectral Scanner (MSS), Thematic Mapper (TM), and Enhanced Thematic Mapper Plus (ETM+) sensors, have been among the most widely used and efficient sources for numerous terrestrial mapping applications, including habitat classification [47,66], LC mapping of tropical areas [67], savannas [68], grasslands [69], or forests [70,71], and change detection [72,73]. Other optical data included: (i) the similar spatial resolution Advanced Spaceborne Thermal Emission and Reflection Radiometer (ASTER) [46,74] and (ii) Linear Imaging Self Scanning Sensor 3 (LISS-III) [46]; the higher resolution (iii) Advanced Visible and Near Infrared Radiometer type 2 (AVNIR-2) [75] and (iv) High Resolution Geometric (HRG) instrument [46]; and the very high resolution (v) QuickBird and (vi) WorldView-2 [52,53] sensors, with significant contributions in habitat and LC mapping. Although of lower spatial resolution, data time series from the Moderate Resolution Imaging Spectroradiometer (MODIS) have proven successful in mapping dry savanna vegetation, capturing phenological properties with inter-annual classification average user’s (UA) and producer’s (PA) accuracies reaching 94.86% and 97.73% for 12 classes, respectively [76]. Hyperspectral data features have shown high potential in discriminating among different vegetation types [77–79]. On the other hand, besides their ability in providing vegetation structure information, as discussed in next paragraphs, active data have been increasingly used in mapping applications. Phased Array type L-band Synthetic Aperture Radar (PALSAR) and RADARSAT-2 data have provided high

mapping potential in LC mapping and forest characterization, used either individually [80–82] or in synergy with optical data [75, 83]. In a study by Vaglio Laurin *et al.* [75], PALSAR coupled with AVNIR-2 identified 8 LC classes in a tropical rainforest and fragmented area with accuracy 97.5%, outperforming PALSAR synergy with Landsat TM. In addition, Airborne Laser Scanning (ALS), i.e. airborne lidar, data proved particularly effective in forest delineation in upper timberline and fragmented forests in Austria, reaching 96% detection accuracy [84].

Apart from cases where new classification and change detection schemes were proposed [70, 72], most studied approaches have employed widely used, mainly supervised, classifiers. Support Vector Machines (SVM) have been among the most widely used and highly performing ones. In a Natura 2000 heathland characterization study [79], SVM outperformed Random Forest (RF) and AdaBoost tree ensemble classifiers by around 4.5% in experiments involving 18 features from a hyperspectral image for 537 samples in 10 classes. Interestingly, with the addition of more features, resulting in three times the number of the initial ones, the performance of RF and AdaBoost reached the one of SVM, whereas the latter remained the same; this indicated that SVM classifier was more sensitive to the Hughes phenomenon, resulting in decrease of classifier performance when the number of features is high compared with the number of training samples [85]. In other studies, SVM outperformed k -nearest neighbour (k -NN), binary Classification And Regression Tree (CART), and Maximum Likelihood Classifier (MLC) [66, 67]. The latter has outperformed Spectral Angle Mapper (SAM) and Spectral Information Divergence (SID) classifiers in a study by Forzieri *et al.* [77]. Artificial Neural Networks (ANN) have shown advantages over SVM, SAM, or MLC in different studies [75, 78]. It is worth noting, however, that ANN implementation proved incapable to build a model when 165 features were employed in [78], probably due to the very complicated network of nodes resulting in such case; on the contrary, SVM and SAM classifiers could handle this size of feature sets and perform the classification. The highest performing classifiers among the ones discussed above will be used in the classification tasks of Chapters 3 and 4.

As far as mapping elements are concerned, it seems that object based image analysis (OBIA) and classification approaches have been gaining space over pixel based approaches [86–88], especially in applications using very

high resolution data (with spatial resolution finer than 3 m). Characteristic examples include habitat mapping applications, e.g. [46, 52, 53]. However, object based classification has proven more effective than pixel based also in some cases where data with coarser resolution were used, e.g. the delineation of forest clear cuts with Landsat data, using polygon shape parameters and context with other classes, besides traditional spectral features [89]. In general, multiple reasons favour the use of object based analysis over pixel-based approaches, particularly for mapping applications. The large spectral variabilities within habitats may create inaccurate classifications and salt and pepper effects under pixel-based approaches for images of very high spatial resolution, proving them inappropriate for habitat classification [47, 90, 91]. Furthermore, pixel-based approaches prohibit the extraction of spatial, contextual, and topological features, such as object area or adjacency to other objects of specific class, that are valuable for certain classification tasks, as will be evident in the next chapters of this thesis, where object based approaches are developed.

B. Degradation / deforestation

Satellite data have been considered as the only efficient and realistic means to monitor deforestation and forest degradation in a timely manner [92]. Data time series are necessary to detect deforestation in space and time and assess deforestation rates. Landsat data have been the primary sources of information in studies monitoring forest disturbance [93–100], mainly due to the long archive, spectral and spatial resolution properties, and the free availability of data. Tasseled Cap Transformation (TCT) indices from Landsat near-annual time series, evaluated under trajectory-based change detection methods, resulted in identifying forest disturbances within 22 years with overall accuracy (OA) 95.72% [93]. The Continuous Monitoring of Forest Disturbance Algorithm (CMFDA) has been proposed to take advantage of the full Landsat archive of an area and provide timely forest disturbance monitoring, by even predicting unseen Landsat pixel reflectance values [95]. Although highly accurate disturbance maps may be extracted, a period of more than one month is required to confidently detect changes, expected to be more in areas with low Landsat imagery coverage. Thus, future fusion with similar sensors that have shown consistent results, e.g. HRG [101], or

sensors with higher temporal resolution is expected to be crucial for global near real time deforestation monitoring. Wider availability of free satellite data, at least from government agencies, should be a policy makers' priority [102].

Other employed data include the passive Advanced Very High Resolution Radiometer (AVHRR) [103], Advanced Wide Field Sensor (AWiFS), and MODIS [104] sensors, as well as active PALSAR time series [105,106]. The latter, providing the ability of cloud unobstructed monitoring, may have comparative advantages in highly cloud covered area, such as tropical rainforests.

C. Fragmentation / connectivity

Fragmentation and connectivity may constitute significant factors that affect biodiversity, the former isolating living species areas, whereas the latter allowing the invasion of alien or destructive species. Despite the common notion, Fahrig [107] argued that fragmentation per se may have also positive effects on biodiversity and should be clearly distinguished by habitat loss, whereas Kindlmann and Burel [108] suggested that connectivity should be assessed both in landscape and organism (functional) diversions, allowing different degrees of connectivity to be defined for different species within the same landscape.

Numerous landscape measures have been proposed to assess fragmentation or connectivity, at the patch or landscape level, whose estimation is based on LC or habitat map monitoring, or change assessment. Among the most widely adopted measures for fragmentation are the ones implemented in the FRAGSTATS software [109], having been estimated using Landsat [110–114], IKONOS-2, GeoEye-1 [115], QuickBird, ASTER [113], or Wide Field Sensor (WiFS) [114] imagery. Variogram analysis has also been employed to assess forest heterogeneity [116]. In addition, a number of indices have been used to assess connectivity, e.g. in forested areas, including the Integral Index of Connectivity (IIC) [112] and the Equivalent Connected Area Index [117].

A direct comparison of the efficiency of the different measures in describing the degree of fragmentation or connectivity is not straightforward [118]. A number of criteria have been suggested by Saura and Pascual-Hortal [119],

where the proposed Probability of Connectivity index was acknowledged as the only satisfying all defined requirements. Plexida *et al.* [120] identified Patch Density, Area-Weighted Mean Fractal Dimension Index, and Patch Cohesion Index as the most suitable measures to describe landscape patterns in different scales, whereas fragmentation indices have been evaluated on their sensitivity to scale by García-Gorro and Saura [114].

D. Aquatic mapping

Airborne lidar data have been extensively used in aquatic area mapping studies, including wetland inundation below the forest canopy [121], upland swamp boundary detection [122], and river [123] or tidal [124–126] water mapping, based on their point cloud or full waveform properties and their ability in extracting accurate DEMs. In addition, L-band and C-band SAR data have been effectively used in wetland and mangrove characterization studies [127–130].

Regarding passive sensors, Belluco *et al.* [131] evaluated a range of multispectral and hyperspectral sensors, namely the airborne Reflective Optics System Imaging Spectrometer (ROSIS), Compact Airborne Spectrographic Imager (CASI), and Multispectral Infrared and Visible Imaging Spectrometer (MOVIS), and the satellite QuickBird and IKONOS-2 sensors, in salt-marsh vegetation mapping. It was found that hyperspectral ROSIS and CASI slightly outperformed the multispectral ones, whereas MLC consistently provided superior classification accuracies to SAM and K-means classifiers. Minimum Noise Fraction (MinNF) and band averaging performed better than Principal Component Analysis (PCA) in feature dimensionality reduction. In another study, hyperspectral Hyperion data outperformed the same or higher spatial resolution data of Advanced Land Imager (ALI), Landsat TM, and IKONOS in seagrass habitat mapping [132]. Both studies confirmed the advantages of dense spectral information for wetland mapping, with the former additionally highlighting the even greater importance of high spatial resolution data. Thus, the existence of future high spatial resolution hyperspectral satellite sensors, in addition to the only existing coarser resolution Hyperion, would highly benefit timely wetland monitoring and characterization. Airborne optical cameras have been used for upland swamp [133] and wetland [134] mapping, coarser resolution Landsat data

being shown insufficient if used alone, for the latter application. Super-resolution techniques have been proposed to improve mapping tasks, such as representation of lakes using satellite data time series, halftoning, and morphological filtering [135], and may find future applications in relevant applications.

2.2.2. Trends in abundance, distribution and extinction risk of species

Abundance and distribution of species constitute a core part of biodiversity. The respective CBD headline indicator encompasses both plant and animal species. Table A.2 lists a number of recent studies where RS data have been successfully employed to study species distribution and abundance, either through direct monitoring or through proxy variables. The methods are organized under: (1) plant species, including (1a) alien and (1b) indigenous species; and (2) animals, including (2a) birds, (2b) fishes, (2c) mammals, and (2d) invertebrates. The methods are connected to Aichi targets 9 and 12 (Table 2.1), on monitoring invasive and threatened species, respectively.

A. Plant species

Scale has been reported as one of the core issues in species monitoring, where the spatial resolution of the remote sensor is crucial [136]. As rule of thumb, it has been suggested that the optimal spatial resolution of the sensor is two to five times smaller than the monitored object, in order to provide an effective trade-off between within-object and between-object variance [26]. In line with this notion, some of the best performing studies in alien and invasive species detection have been based in fine resolution data (pixel size ≤ 30 m), either aerial [137–142] or satellite [143–145]. Dorigo *et al.* [137] extracted a bi-temporal band ratio (BTBR) and a number of Haralick texture features from bi-seasonal digital orthophotos and successfully detected *Fallopia japonica*, one of the world’s worst invasive alien species, with up to 90.3% PA and 98.1% UA. Similar results were achieved neglecting the near infrared (NIR) band one of the photos had, suggesting the applicability of the method also in cases where only true color photos are available.

Hyperspectral data have shown increased performance in species mapping applications during the last years [146] and have been widely employed

[139, 141, 142, 147–153]. Thenkabail *et al.* [154] demonstrated the use of hyperspectral data by simulating the bands of Hyperion with a hand-held spectroradiometer to discriminate vegetation and agricultural crops. Use of PCA, lambda-lambda R^2 models, stepwise discriminant analysis (SDA), and derivative greenness vegetation indices (DGVI), identified 22 optimal bands that resulted in classification of five weed species with 97% OA.

Féret and Asner [147] evaluated the performance of a number of parametric and non-parametric classifiers, including SVM, ANN, k -NN, and Linear (LDA), Quadratic (QDA), and Regularized Discriminant Analysis (RDA), in tropical tree species discrimination; RDA achieved the best performance when small training sample sets were used, whereas SVM in larger ones. In the same study, object-based classification outperformed pixel-based, with both providing inferior accuracies to majority-class rule classification, where an object is classified to the class where the majority of its pixels are classified. In another study using airborne hyperspectral data, and combining them with digital photos, application of MinNF and SAM, successfully mapped invasive *Phragmites australis* with 93% PA and 96% UA, whereas linear spectral unmixing was employed to find the fractional cover of *P. australis* in mixed pixels [139]. Among other sensors, ALS data have shown high potential in discriminating wetland vegetation species [155].

B. Animal species

Whereas the monitoring of the distribution and abundance of animal species is crucial for biodiversity assessment and species interrelations, e.g. with invasive animal species [156], direct observation is rarely possible, and mainly restricted in large mammals with the use of VHR sensors. As an example, WorldView-2 data, and particularly a thresholding classifier using the Coastal band (400–450 nm), detected whales with up to 84.6% PA and 76.3% UA [157]. However, the most common way to estimate distribution of animal species, including mammals, birds, fishes, or invertebrates, has been to model it based on proxies, such as spectral or structural properties [158–161], habitat suitability [162–164], or detection of colonies [165, 166].

Suarez-Seoane *et al.* [158] demonstrated the ability of AVHRR, combined with topographic and GIS data, to model the occurrence of three agricultural steppe birds in Spain, using PCA and Generalized Additive

Models (GAM). Other studies included Landsat imagery, either individually [159, 162] or in synergy with SAR data [167], to derive forest parameters and relate them with species distribution. The fusion of structure variables extracted by lidar data with spectral information appears beneficial for avian species distribution assessment and has been applied in some studies [160, 168]. Based on the notion that the 3D structure of coral reef fish habitat intensely affects their communities, acoustic data have been used in synergy with VHR IKONOS-2 to correlate abundance of different species with habitat characterization and topographic features [161, 169]. Active data, i.e. ALS, have also been used for the extraction of lidar derived parameters and modelling the presence of invertebrates spider [170] and beetle [171]. Other passive data, such as MODIS [163, 172], VEGETATION [173], Landsat [174, 175], or Tropical Rainfall Measuring Mission’s Microwave Imager (TRMM/TMI) and Sea-Viewing Wide Field-of-View Sensor (SeaWiFS) [176], have been used in different animal abundance modelling studies with satisfactory accuracies.

2.2.3. Trends in pressures from unsustainable agriculture, forestry, fisheries and aquaculture

Pressures from unsustainable management in agricultural, forest, and aquatic areas may be inferred up to a degree by remote sensing methods. Most of the research studies have focused on forestry applications, concentrated on biomass and forest structural parameters, supporting United Nations (UN) Reducing Emissions from Deforestation and Forest Degradation (REDD+) activities [177], whereas pressures from unsustainable agriculture may be inferred mainly from changes in Land Use (LU), irrigation strategies, or nitrogen concentration. Pressures from unsustainable fisheries and aquaculture have not been extensively studied through RS data per se, but can be deduced up to a degree from monitoring fish distribution and abundance, or pollution in aquatic areas. Table A.3 lists a number of high performing recent methodologies that can be used to monitor agriculture and forestry management unsustainable practices. Monitoring of Aichi targets 4, 5, 6, and 7 (Table 2.1) can benefit from the discussed methods.

A. Unsustainable agriculture

Studies revealing pressures from unsustainable agriculture practices have mainly focused on effects from irrigation strategies [178–180], nitrogen treatment [181–183], and crop characterization [184–186]. Structural properties of the studied areas are less revealing than spectral properties for these tasks, therefore passive multispectral or hyperspectral data have mainly been used.

LISS-II data time series have been proven useful in extracting a number of ground salinity indices [178]. Following the LU mapping of the studied area, salinity affected soils of different degree were identified as crucial tool for irrigation management. The forthcoming superspectral VEN μ S and Sentinel-2 sensors have been evaluated by Herrmann *et al.* [187] in estimating Leaf Area Index (LAI) of wheat and potato crops, simulated by a field spectrometer. It was found that both sensors are promising in performing as well as a hyperspectral sensor, whereas the calculated Red-Edge Inflection Point (REIP) index, using their four red-edge bands, was proven more consistent than NDVI.

Multispectral data with large extent coverage and high revisit time have been preferred in capturing crop area characteristics. Different methodologies employing Landsat TM / ETM+ and MODIS data have been evaluated in cropping intensity mapping in smallholder farms, in different spatial scales [186]. Thresholding Landsat-derived NDVI values outperformed three MODIS based methodologies in almost all scales for both winter and summer periods, with hierarchical training method being the best among the MODIS ones. In a recent study, Zhong *et al.* [184] showed that phenological metrics extracted by TM / ETM+ time series can map corn and soybean more accurately than spectral features in cross-year classifications, i.e. when the training and test features correspond to different cropping years. Mapping of abandoned agriculture has also been proven feasible by MODIS time series [185], demonstrating MODIS capacity for large extent monitoring.

B. Unsustainable forestry

Structure-based indicators have been suggested as core elements for planning sustainable forest management [12]. Active sensors, including mainly lidar data, have been proven the most effective sources of forest structure

information, [188–190]. Besides the usually employed first pulse and statistical point height metrics, last pulse and individual tree-based features have shown increased accuracy in approximating tree height, diameter at breast height and stem volume in a boreal managed forest [189]. However, although the omission errors in tree detection are reduced, the commission errors are increased; therefore, a synergy of first and last pulse data is expected to combine the benefits of the former in detecting non-overlapping trees and of the latter in overlapping ones. Besides satellite lidar data [35, 191], the synergy of TanDEM-X and TerraSAR-X, as the first source of spaceborne single-pass polarimetric SAR interferometry (PolInSAR) data, has been proven particularly promising for future height estimation applications. Kugler *et al.* [192] evaluated single polarization data with ancillary Digital Terrain Models (DTM) and reached correlations with lidar derived height data up to $R^2 = 0.98$, while using solely dual polarization data resulted in $R^2 = 0.86$. In general, as rule of thumb, 25–30 m SAR spatial resolution or 25 m lidar footprint diameter have been proposed as required to capture vegetation structure for biodiversity monitoring [24]. Other promising alternatives to active data have included the use of multispectral or hyperspectral data, mainly using neighbourhood statistics, spectral indices, or texture features [40, 41, 193, 194], the latter being more thoroughly discussed in Chapter 3.

Additional parameters assessing forest sustainability have been measured by RS studies. Nichol and Sarker [195] recently presented a study where texture feature ratios extracted from AVNIR-2 and HRG data, were successfully employed in modelling biomass with multiple regression with up to $R^2 = 0.939$. Lidar, SAR, and even Landsat data have also been employed in biomass estimation studies [177, 196–199]. Stem volume and basal area have been approximated through a synergy of ALS with airborne colour infrared (CIR) and AVNIR-2 data [200]. In another study, Ozdemir and Karnieli [201] used WorldView-2 data and texture analysis to approximate a number of additional parameters, including Standard Deviation of Diameter at Breast Height (SDDBH), Gini Coefficient (GC), and Diameter Differentiation Index (DDI). ETM+ data have outperformed the higher spatial resolution but lower spectral information IKONOS and SPOT-4 High-Resolution Visible and Infrared sensors (HRVIR) in LAI estimation [202], with ALS data being reported as high performing alternatives [203]. Finally,

managed forest disturbances, due to logging activities, have been monitored with Landsat time series [204], whereas the use of VHR imagery in logging trail detection has been demonstrated with RapidEye data [205].

2.2.4. Trends in pressures from habitat conversion, pollution, invasive species, and climate change

As aforementioned, habitat mapping and conversion from one category to another has been extensively studied and pressures can be inferred from methods discussed in Section 2.2.1. Furthermore, numerous studies on species invasion detection, pressures and effects have successfully employed RS data, as mentioned in Section 2.2.2. This paragraph focuses on studies that can be used to address the detection of pressures from climate change and pollution. Table A.4 lists recently proposed state-of-the-art methodologies, mainly related to the monitoring of Aichi targets 4, 5, 8, 9, and 10 (Table 2.1).

Climate change has been recognized as severe factor affecting biodiversity in different scales and can influence species phenology, physiology, or range [206]. RS data have high capacity in monitoring species range, extent, and distribution, as mentioned in previous sections, whereas the task of assessing physiological changes, response, and adaptivity to new conditions seems more challenging. SPOT-4 and SPOT-5 VEGETATION data time series have been proven efficient in detecting variations in leaf phenology of a deciduous broadleaved forest in different elevations, based on the extraction of a five year perpendicular vegetation index (PVI) and the use of a temporal unmixing method [207]. A number of indices from MODIS or Landsat data, including Enhanced Vegetation Index (EVI), Normalized Difference Vegetation Index (NDVI), Excess Green Index (ExG_M), and Normalized Difference Water Index (NDWI), have been evaluated in several studies [208–210]. The optimized soil-adjusted vegetation index (OSAVI), calculated from MODIS data, showed higher consistency than NDVI and EVI in characterizing Gross Primary Productivity (GPP) and in evergreen needleleaved forests, and its broader use has been suggested [211]. In general, phenology monitoring in deciduous broadleaved forests has been proven more feasible than in needleleaved forests or savannas. Correlation of RS estimates with systematic field observations of phenology of multi-layer canopy is expected to further

improve relevant RS derived land surface models [212].

Detection of various pollution sources has been achieved, up to one degree, by RS methods. Oil spills have been one of the most widely monitored sources, although there is a notion that RS data can only complement rather than fully replace airborne observations, due to the particularities of oil spills [213]. SAR data have been extensively used for oil spill detection in oceans, because of their all weather and illumination condition monitoring, wide coverage, and the capability in separating oil from the surrounding water area, under low or moderate wind [214], where oil surface appears significantly smoother. ENVISAT Advanced SAR (ASAR) data have been used with an adaptive thresholding algorithm to almost perfectly label oil spill pixels in Iberian Peninsula [215]. Other recent studies have employed C-band RADARSAT-1 [216] and European Remote Sensing Satellite 2 (ERS-2) SAR data [217], but also the use of hyperspectral Airborne Visible / Infrared Imaging Spectrometer (AVIRIS) data [218]. Besides oil spills, studies have been conducted to detect non-point source pollution, identified as a core arising issue in water environmental protection [219], such as total nitrogen, total phosphorous, ammonia nitrogen ($\text{NH}_4\text{-N}$) and chemical oxygen demand (COD_{Cr}) with multispectral HJ-1A and HJ-1B data [220]. Furthermore, ozone injury to coniferous forest [221] and urban ground-level nitrogen dioxide (NO_2) [222] have been assessed using Ozone Monitoring Instrument (OMI) and airborne hyperspectral data, respectively.

2.2.5. Trends in distribution, condition and sustainability of ecosystem services for equitable human well-being

Ecosystem services seem to have declined significantly during the last years [223], and the need for monitoring and sustainable management has been prominent. A usual categorization of ecosystem services, following the Millennium Ecosystem Assessment (MEA) classification, identifies four categories: provisioning (e.g. food, raw materials), regulating (e.g. carbon storage), habitat (e.g. maintenance of genetic diversity), and cultural (e.g. tourism) [224]. Provisioning and regulating services have been widely studied with RS data [225]; habitat services have been assessed mainly as far as their presence and condition are regarded, as discussed in previous sections, whereas cultural services are relatively more challenging to be monitored

by RS data. Table A.5 lists a number of methods that can be used to assess ecosystem services and address the related CBD headline indicator. Focus is given on (i) provisioning (food, raw materials, water) and (ii) regulating (carbon storage, pest control) services. The discussed methods are mainly relevant with the Aichi targets 14 and 15 (Table 2.1), on monitoring ecosystem services and resilience, respectively.

A. Provisioning services

A number of studies have been presented assessing services of food, raw material, and water provisioning, using a variety of data. Through a data assimilation algorithm, MODIS LAI product and extracted vegetation indices of NDVI and EVI were able to forecast crop yield, using only a partial year of data, with relative deviations from reference data less than 3.5% [226]. Passive MODIS, AVHRR, and Medium Resolution Imaging Spectrometer (MERIS), as well as active ASAR data have been used in further studies to estimate wheat or maize yield with relative differences less than 11% [227–230]. On the other hand, lidar data, either airborne [231–233] or spaceborne [234], have been the primary sources to estimate timber volume. Jaskierniak *et al.* [231] proposed the use of mixture models with distributions based on Generalized Additive Models for Location, Scale and Shape (GAMLSS) with airborne lidar data, to capture the complexity of a eucalyptus native forest; correlation with observed stand volume and basal area values reached $R^2 = 0.88$ and $R^2 = 0.89$, respectively.

On the contrary, mainly passive sensors, have been employed to assess water quality, clarity, and turbidity in related studies, including Landsat [235–237], Earth Observing 1 (EO-1) ALI [238], and SeaWiFS [239]. As a characteristic example, a 20 year archive of Landsat data has proven effective in providing correlations with field-measured Secchi Disk Depths (SDD) up to $R^2 = 0.96$, to characterize water clarity in Minnesota lakes, USA [235].

B. Regulating services

Carbon storage and pest control constitute regulating services in whose estimation RS data can have a notable contribution. Hyperspectral AVIRIS data have been used for the derivation of NDVI, Photochemical Reflectance Index (PRI), and water content indices, and the extraction of carbon and

water flux maps in a semi-arid area [240]. Regression analysis demonstrated accuracies with adjusted R^2 values up to 0.96 and 0.94 for net carbon and water fluxes, respectively. Airborne lidar derived measures [241] and QuickBird and ASTER spectral, texture, and transformation features [242] have also been used to assess carbon stocks. As far as pest control is regarded, several studies have been presented detecting defoliation and other effects, which may be used as means to infer the resistance of a study area to pest attack. Multispectral or hyperspectral data have mainly been employed to detect affected areas. Time series of VHR multispectral or panchromatic data have been proposed as successful tool for site managers to evaluate pine beetle red attack over time [243]; QuickBird time series and extracted red-to-green band ratios, lead to true positive accuracies 89–93% for three studied years. Spectral properties of MODIS, AVIRIS, and Landsat data, together with regression analysis, have been used to assess gypsy moth defoliation [244], decline in emerald ash borer-infested areas [245], and mortality of lodgepole pine to bark beetle attack [246].

2.2.6. Trends in coverage, condition, representativeness and effectiveness of protected areas and other area-based approaches

The number of protected areas worldwide are estimated around 133 000, being increased by 400% since the 1970's and covering approximately 13.9% and 3.2% of the terrestrial and marine environment, respectively [6, 23, 247]. Although delineation of protected areas offers an indicator of conservation status, these statistics per se can poorly describe the condition within the protected areas and the effectiveness of the conservation management practices [23]. RS data can offer valuable input in monitoring of both the protected sites and their surrounding areas, since the condition, changes, and pressures of the latter closely, or even equally, affect the former [248]. Different parameters may well be assessed by RS methods discussed in previous sections, e.g. LC or habitat extent, fragmentation, and degradation (Section 2.2.1), species invasion or distribution and abundance (Section 2.2.2), or pressures from unsustainable forestry (Section 2.2.3), with the additional potential requirement of higher temporal coverage for timely monitoring. Table A.6 lists a number of methods used to provide conservation assess-

ment and management guidelines, as indicative examples on how RS methods can be employed to address needs of the related CBD headline indicator. Methods reported in this paragraph, as well as related methods from previous ones, are linked mainly to the related Aichi targets 11, 14, and 15, as noted in Table 2.1.

ASTER derived vegetation indices have been used in synergy with species richness and topographic and climatic variables to characterize vegetation structure and model the spatial variation in woody species richness in a protected temperate forest in Chile [249]. Developed models predicted future tree species richness, identified gaps in current conservation strategies and suggested the creation of new protected areas. Using Multiple End-member Spectral Mixture Analysis (MESMA) in Airborne Hyperspectral line-Scanner radiometer (AHS-160) data, Delalieux *et al.* [250] delineated three heather age classes in a Natura 2000 site with OA around 86%, as contribution to conservation management of natural heathlands. Airborne multispectral CASI and lidar data have been employed for mapping of protected cork oak forests and characterization of habitat condition as high, medium, and low [251].

SAR data have also shown increased potential as tools for conservation monitoring and planning. TerraSAR-X time series have successfully identified swath events in protected semi-natural grasslands within 11-day intervals [252], whereas changes in PALSAR backscatter data have mapped coastline retreat and health degradation in a large mangrove forest [253].

2.3. Conclusions and future considerations

The wide range of methods presented demonstrate the latest advancements and the potential of remote sensing data in monitoring various biodiversity related characteristics. These methods have been linked to the respective CBD headline indicators, in an attempt to indicate methodologies that can be adopted for the constant monitoring of the progress towards the Aichi targets. Such linkage has rarely been attempted in the past and intends to reduce the gap of communication and information sharing between the remote sensing and the ecology, conservation biology, site manager, and policy making communities, which has also been identified by previous studies [23, 247, 254].

Despite the wide availability of RS data, their full potential has not yet been exploited in operational tasks [255], mainly because of the technical challenges in handling such data by non-experts. Thus, a more effective two-way communication and know-how exchange between the related communities is required to fundamentally assist timely and large area biodiversity monitoring. An additional burden to wider RS data utilization remains the cost of certain RS products, including mainly airborne or very high resolution satellite ones. Free provision of RS data, as has been proposed for certain applications [102], and more systematic use of already free ones, e.g. Landsat, EO-1 Hyperion, and the upcoming Sentinels, is expected to boost the use of RS data and improve early and timely monitoring. Finally, a lack of standardization for each indicator [27] restricts a closer connection between user requirements and RS potential and the wide adoption of robust methodologies for indicator extraction. The creation of a large scale database of RS data from different bio-geographic regions and of different spatial, spectral, and temporal characteristics would benefit the development, evaluation, and selection of methodologies to provide accurate biodiversity indicators in a consistent, harmonised, and standardized manner.

A wide number of the discussed methods were assisted by or relied on ancillary in-situ information, including field measurements, elevation models, and GIS thematic layers. In many applications, including invasion ecology, phenology, and ecosystem services [146, 225], in-situ data are indispensable for modelling, calibration, training, or validation of the developed RS approaches. Thus, lack of in-situ data of high quality, or data collected in inconsistent manner under different sources, periods, or methods, may severely limit the quality of RS products [4, 63]. Therefore, collection of in-situ data needs to be harmonized at least within a specific task or study, whereas the expansion or initialization of large scale national or international field data collection initiatives, e.g. the Land Use/Cover Area frame statistical Survey (LUCAS) [256], will be crucial steps for RS and in-situ operational integration. Further integration is expected to benefit from the creation of a large scale knowledge base of in-situ spectral observations, that will enhance correlation with various types of RS data and modelling applications.

Active sensor data have been increasingly contributing to vegetation struc-

ture related applications, including quantification of tree height, stem volume, basal area, or biomass. Although lidar data have been proven effective sources for vertical forest structure characterization, certain restrictions limit their repeated applicability, including high costs [40], technical challenges [23], and restricted understanding on interactions between lidar beams and vegetation [190]. High costs are mainly related to the necessity of airborne campaigns, under the limited availability of satellite lidar data. Upcoming missions, such as the Ice Cloud and land Elevation Satellite II (ICESat II) and Deformation, Ecosystem Structure and Dynamics of Ice (DESDynI) missions [257], are expected to provide lower cost coverage with similar performance to aerial surveys. Further training of ecologists and site managers on the use of lidar data, and further research on beam properties and interactions with, especially multi-layer, vegetation are expected to be beneficial for wider applicability. On the other hand, SAR data in vegetation structure studies have been mainly restricted by temporal decorrelation limitations, especially in high biomass forests [190]. Missions such as the Tandem-X and TerraSAR-X platforms, in synergy forming a single-pass polarimetric interferometer, are expected to counteract temporal decorrelation; in addition, new missions, such as the recently launched Sentinel-1, are expected to provide free high resolution data for further applications. Furthermore, high performing filtering algorithms can be used to reduce SAR image speckle noise [258–260]. Synergies of lidar/SAR data remain a promising field for future research [24].

Hyperspectral data have shown high potential in species discrimination and vegetation mapping applications. The higher spectral content than multispectral or active sensors has been able to capture species heterogeneity and be used as effective tool in plant invasion studies [146], wetland mapping [65], and in areas of high habitat and species diversity [23]. Spectral mixture analysis has been widely employed to take advantage of the high spectral information for species discrimination [139, 148, 250], where robust endmember extraction and anomaly detection algorithms [261–264] can be beneficial for further applications. A limitation for the wider use of hyperspectral data seems to be the restricted availability of such satellite sensors, necessitating aerial surveys, that often result in higher spatial resolution data. In particular, satellite data from Hyperion, although having shown better discrimination ability than multispectral or VHR sensors [131, 132],

have limited spatial resolution compared with aerial surveys. Finally, technical challenges faced by the large amount of data are expected to be reduced with increasing research and further experimentation on feature selection and dimensionality reduction algorithms.

Multispectral data hold a large potential in numerous mapping and conservation planning applications. Sensors such as Landsat and MODIS have been extensively used in deforestation and vegetation phenology studies, or other applications requiring time series analysis and a large archive. The free availability of products and their spectral properties have been beneficial for the wide use in a number of monitoring tasks. VHR sensors, such as QuickBird and IKONOS, have been employed to surpass the spatial resolution limitations of the former sensors, although with the expense of more restricted spectral content. They have been particularly effective in applications requiring detailed spatial monitoring, e.g. studies of fragmentation [113, 115], whereas providing promising results in habitat mapping and height estimation through texture analysis, as demonstrated in recent studies [41, 52, 53] and will be shown more explicitly in the following chapters. VHR sensors like WorldView-2 and the newly launched WorldView-3, carrying more spectral information than QuickBird or IKONOS, especially in the short-wave infrared part, appear promising in future biodiversity monitoring studies. However, the problem of limited monitoring capacity in cloud covered areas, such as the tropics [4], or in no illumination conditions, remains for optical sensors in general, thus synergies with active data constitute a field of continuous research.

A large spectrum of algorithms has been employed for processing and mapping applications. Although the existence of a universally best performing classifier in all mapping tasks is highly unlikely, support vector machines and artificial neural network classifiers have been widely used and outperformed other classifiers in comparative studies [67, 78, 79, 147]. Research on high performing generic or task oriented classifiers is an ongoing process. Object based image analysis, originated by the development of segmentation approaches [86] and including contextual information to classification tasks, has outperformed pixel-based classifications in numerous applications [147]. This approach has encouraged the use of, development of, and current research on a number of segmentation (multi-temporal, multi-spectral, multi-resolution) and feature generation approaches, includ-

ing neighbourhood statistics and texture measures. The use of hyperspectral data, backscatter coefficients, and large number of generated spectral or texture features, in both pixel- or object-based approaches, has necessitated the use of feature selection and dimensionality reduction algorithms [265]. Principal component analysis and minimum noise fraction have been among the most widely used ones [131, 194, 195, 221], with the selection of the most appropriate among those and others depending on the specific application. A large number of such high performing processing and classification algorithms will be employed in the developed methodologies, discussed in more detail, and evaluated in the next chapters of the thesis.

As has been recognised, fusion of both active and passive data sources are promising [23], but also a great challenge for future research tasks [190, 266]. Wider use of existing and upcoming remote sensing data in operational tasks, integration with high performing algorithms, and broader dissemination of research outcomes, will enhance the robustness and extent of biodiversity monitoring and the assessment of the progress towards the achievement of the established preservation targets, at a global scale.

3. Vegetation height estimation through texture analysis

3.1. State of the art and open issues in height estimation using remote sensing

Vegetation height is a crucial parameter in several applications related to biodiversity monitoring, including land cover and habitat landscape analysis and biomass estimation [24, 28, 33, 34]. The use of remote sensing data in vegetation height estimation studies has increased during the last years. As discussed in Section 2.2.3, lidar sensors have been proven the most accurate remote sensing sources for retrieving vegetation structural information [188–190], performing similarly well in both aerial and spaceborne platforms [257]. Lidar data have been extensively used for height estimation both individually [35, 37, 189, 267] and in synergy with data from other active or passive sensors [31, 268, 269]; however, their cost per unit area can be significantly high [38]. Active sensor alternatives mainly include the use of SAR interferometry [36, 192, 270, 271] or radargrammetry [272, 273], where a number of two or more images of the same area need to be acquired and processed.

Less cost and resource demanding approaches have been sought in the use of passive satellite sensors, usually applying regression analysis to model vegetation height based on spectral intensity or texture features. For instance, band digital number values of Landsat ETM+ and IKONOS images were directly related to height of Sitka spruce plantations through linear models in [38], achieving R^2 values up to 0.87 and residuals within the range ± 2 m, acceptable for forest management purposes. Anderson *et al.* [39] used spectral indices calculated from Landsat imagery, namely Normalized Difference Water Index (NDWI) and Optimized Soil Adjusted Vegetation Index (OSAVI), to estimate corn and soybean height.

Texture features, including Gray Level Co-occurrence Matrix (GLCM) statistics (Haralick features) [274], Markov random fields [275], or wavelet transforms [276], have been widely employed in passive remote sensing. In vegetation height estimation in particular, simple texture features, including the mean [277] and the standard deviation [278] of band reflectance values within a moving 3×3 pixel window, have been employed for the approximation of the canopy height of coniferous trees. Similar features have been calculated by Wolter *et al.* [40] from SPOT-5 (Satellite Pour l’Observation de la Terre (French)—Satellite for Earth Observation) images to characterize tree height in hardwood and coniferous forests; separate regression analyses for each type provided satisfactory predictions, however no single function was found to provide accurate results for both forest types. GLCM texture features calculated from IKONOS-2 imagery have been related to height of oak, beech, and spruce trees with R^2 values of up to 0.76 through univariate linear regression models [41]. Since R^2 values—although providing useful indication on the amount of data variability explained by a model—do not provide sufficient proof of model fit, the predictor significance, residuals, and the relative standard error of the height model were additionally examined. The predictors were found statistically significant (p value < 0.01), whereas the residuals followed normal distribution, thus, supporting goodness of fit; in addition, the standard error E_r was 10%, less than the 15–20% typical forest inventory error for stand management planning purposes [279]. In the same study [41], when reflectance data were used instead of texture, the model accuracy was significantly lower, with R^2 values between 0.3 and 0.66, demonstrating the advantage of the use of texture features over simple reflectance data. In a different approach, an object-based height estimation method in multiple scales was proposed by Chen *et al.* [280], where spectral and texture features and shadow fraction were extracted from a QuickBird image for each object; compared with pixel-based analysis, more accurate estimations were achieved, in most scales.

In this chapter, an object-based approach is proposed to characterize the height of a mixture of tree, shrub, and heath vegetation species, based on texture analysis of very high resolution (VHR) imagery. A number of texture features are proposed, most of which new to height estimation studies. Texture features are preferred over simple reflectance data, on the one hand, due to their superior performance in vegetation height applications [41], and

on the other hand, due to their ability to differentiate among spatial patterns of objects with different vegetation structure, instead of providing averaging reflectance values; the latter would be preferable in tasks such as estimation of vegetation cover over bare ground. With the objective to provide a valuable contribution to habitat monitoring applications, the problem is formulated as a classification—rather than regression—task, where height classes able to discriminate among different habitat categories with similar spectral characteristics are adopted and directly extracted. In particular, the recently introduced General Habitat Categories (GHC) [34] are used as the reference habitat mapping framework based on which the studied height classes are defined. GHC have been proposed as a practical and transmissible framework for habitat surveillance and monitoring, based on life forms. Recording of vegetation structure is a key element in GHC methodology, facilitating the interaction with land cover categories and enhancing habitat mapping through remote sensing observations [51]. In particular, seven height classes are defined in GHC as the main characteristic to discriminate among different Tree and Shrub (TRS) species, namely: (i) dwarf shrubs below 0.05 m (Dwarf chamaephytes — DCH); (ii) undershrubs 0.05–0.3 m (Shrubby chamaephytes — SCH); (iii) low shrubs, buds between 0.3–0.6 m (Low phanerophytes — LPH); (iv) mid shrubs, buds between 0.6–2 m (Mid phanerophytes — MPH); (v) tall shrubs, buds between 2–5 m (Tall phanerophytes — TPH); (vi) trees between 5–40 m (Forest phanerophytes — FPH); and (vii) trees over 40 m (Mega phanerophytes — GPH).

Whereas the majority of the previously discussed height estimation studies focused on tree species with heights of several metres, the proposed approach is extended to a range of less than 5 cm to some tens of metres. Furthermore, a variety of vegetation types are involved, ranging from deciduous and coniferous trees to shrubs and heathland. Images corresponding to both the peak of productivity and the decline of the vegetative period are included, for comparative study. Thorough analysis of the potential of the proposed features for height estimation is performed through a variety of data processing and classification techniques. Classification accuracy to the GHC classes is evaluated both in terms of overall accuracy and kappa coefficient. Besides the evaluation of individual features, research extends to the assessment of feature synergies and the identification of high performing combinations, in order to suggest specific features from both images that

Table 3.1.: Problem statement of Chapter 3.

- **Objective:** Classification of landscape objects of a mixed vegetated area to height classes related to habitats.
- **Input:** (i) Very high resolution multispectral satellite images from the peak and the decline of vegetative period; (ii) land cover map of the area, to delineate objects and mask out irrelevant parts of the area; (iii) Canopy Height Model from lidar data used for validation.
- **Methodology:** (i) Extraction of texture features from the satellite images used for classification; (ii) employment of a number of data processing and supervised classification techniques; (iii) evaluation of individual features and images, as well as identification of highly performing synergies.
- **Output:** Classification of vegetation objects to GHC classes indicating different height categories.
- **Evaluation measures:** (i) Overall, Producer's, and User's accuracies; (ii) kappa coefficient.

provide accurate vegetation height discrimination, with reduced processing time and resource requirements in both feature extraction and classification. Table 3.1 summarizes the statement of the problem being addressed, whereas Fig. 3.1 provides a flow chart of the overall methodology described in this chapter.

3.2. Study area and data

The study area is part of the Ederheide and Ginkelse heide, centred at latitude 52°01'34"N and longitude 5°43'03"E. It is located in the east of the Netherlands near the city of Ede and covers 16 km² (Fig. 3.2). It lies within the National Park and Natura 2000 protected site Veluwe and is included on the heathland Ginkelse area. It is part of the largest end moraine in the Netherlands originating from the penultimate glacial period, constituted by sand dune areas alternated with heathlands and dry forests, and mold by a long history of intensive land use [281]. Besides dry heathland vegetation, the area consists mainly of grassland, herbaceous and shrub vegetation, and forest, whereas small areas of open sand are also present.

Two WorldView-2 multispectral images of the area have been used. One corresponds to the maximum of biomass (peak flush), captured on June 3, 2011, whereas the other to the end of the vegetative period (post flush),

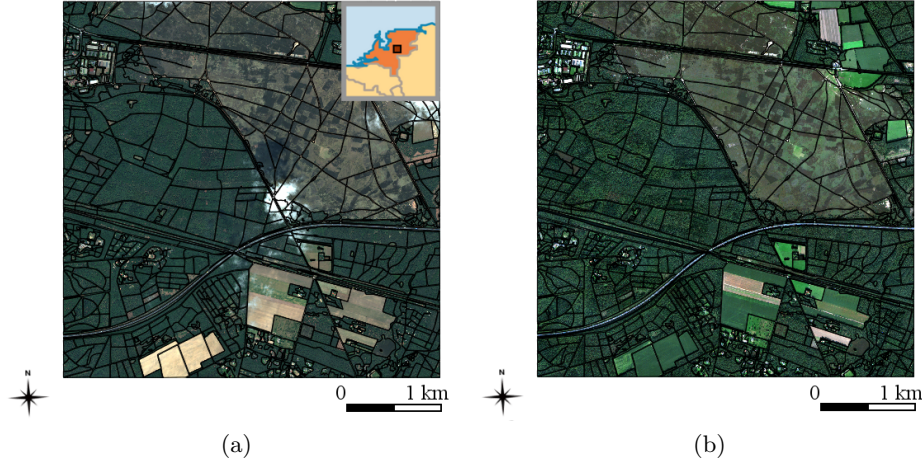


Figure 3.2.: The study area in the Netherlands. The WorldView-2 images from June 2011 (top) and September 2011 (bottom) are depicted in true colour (Red, Green, Blue bands), overlaid by the segment lines from the topographic land cover/use map.

of interest for this study. Data were obtained from the sixth version of the Dutch National Land Use database (Landelijk Grondgebruiksbestand Nederland – LGN6), produced by the integration of satellite images (e.g. Landsat) collected in 2007–2008 with Dutch topographical maps (Top10vector) and databases of geographical data and natural areas [282]. Since the delineation of objects with high spatial accuracy is a prerequisite to enable the calculation of height information from texture analysis in the proposed methodology, the vector based Top10vector maps were used instead of the 25 m resolution grid based LGN6 product. Besides, the LC classes defined in Top10vector, although broader than in LGN6, where higher differentiation in agricultural crops is provided, were appropriate for the scope of this study.

A Canopy Height Model (CHM) has been employed as reference data for the validation of the approach, derived from lidar data, as described in [283, 284]. The original lidar data from the AHN-2 database (actual height model of the Netherlands) used in this study were acquired in spring 2010 by Fugro Aerial Mapping BV, minimizing the effects of leaves on the estimation of the CHM. The average number of points per square meter

were approximately 15, whereas the absolute height accuracy for a single point was approximately 3 cm. After processing the lidar data to extract a height value for each point [283] and removing points with extremely high values representing electric wires or flying birds, the lidar point clouds were rasterized to a grid by assigning to each $1\text{ m} \times 1\text{ m}$ grid cell (pixel) the maximum height value of the respective (around 15) lidar points [284]. The CHM was then rescaled to pixels of $2\text{ m} \times 2\text{ m}$, by averaging the four $1\text{ m} \times 1\text{ m}$ previous pixels included to each new one, to meet the resolution of the satellite imagery.

The provided LCLU map of the area is used as segmentation layer that splits the satellite images into objects. Among the LC classes of the map, objects representing (i) tree nursery, (ii) deciduous, (iii) coniferous, and (iv) mixed forest, and (v) heath vegetation are selected, as vegetated objects with invariant height during the period between the lidar and WorldView-2 data acquisitions, in order to ensure evaluation consistency. The remaining objects of non-vegetated (e.g. sand) or vegetated with variant height (e.g. grassland, cropland) classes are masked out and excluded from the process. All available data, i.e. the two WorldView-2 images, the CHM, and the LC map are shown in Appendix B.

Cloud contaminated pixels in the satellite images are identified through a simple threshold technique, similar to [285], using the coastal band. A threshold value is defined experimentally, through visual inspection of the cloud-contaminated June image, and pixels with reflectance values above this threshold are identified as clouds. A similar cloud mask is not created for the September image too, since the latter was captured in clear-sky conditions.

3.3. Texture features

A number of texture features are calculated per selected object, for each individual band of the satellite images. Although the panchromatic band of VHR data is usually employed in texture analysis tasks [40,41], such data were not available in this study and solely the multispectral bands were used instead.

A number of 24 texture features are calculated for each object per image band to characterize intra-object variability and heterogeneity (Table 3.2).

For a specific feature, a texture value is calculated for each pixel of an object, based on the values of its surrounding pixels within a square moving window of predefined size. The average of the calculated values of the pixels is considered as the value of the object for the specific texture feature and image band. The process is repeated for every selected object and all features and bands. For the WorldView-2 images, pixels previously identified as clouds are excluded from the analysis. For both those images, the same pixels are masked out, although the September one has no cloud contamination, in order to avoid inconsistencies in texture parameters and permit further comparative or synergistic analysis between the images. A detailed description of the extracted features follows.

3.3.1. Local Variance

Around each pixel of an object, a small square area is considered, defined by the selected size of the moving window. The variance of the intensity values of the pixels within the area, for the image band under consideration, is calculated and assigned to the central pixel. The extracted values of all pixels of the object are then averaged to constitute the object value. Windows of 3×3 and 5×5 pixels have been employed for the calculation of local variance features, to take advantage of the high image resolution, and capture and express local variations in as much detail as possible. Under the current image resolution, the selected windows, covering areas of $6 \times 6 \text{ m}^2$ and $10 \times 10 \text{ m}^2$, appear small enough to capture variations within the same habitat and restrict edge effects with neighbouring ones, and large enough to avoid expressing variability within the same plant, e.g. a large tree. In case images of higher resolution were available, e.g. airborne ones, larger windows—in pixels—might be more preferable, keeping the physical size of the covered areas similar—in m^2 ; on the contrary, in case of coarser images, even windows of the smallest size possible, are expected to provide feature of less discriminatory power than the present ones. As a note on the feature computational complexity, for each central pixel surrounded by a window of $n \times n$ pixels, the only possible loop might involve the n^2 operations required to calculate the difference between each pixel and the mean pixel value in the window. Thus, complexity of $\mathcal{O}(n^2)$ can be considered; however, parallel execution of the operations may reduce this upper limit, depending

Table 3.2.: The 24 texture features calculated from each band of the satellite images.

Feature	Window (pixels)	Parameters
Local Variance		
LE1	3×3	
LE2	5×5	
Local Entropy		
LH1	9×9	image band scaled to $[0, 255]$
LH2	9×9	window discretized in 8 values
LH3	9×9	object discretized in 8 values
LH4	3×3	image band scaled to $[0, 255]$
LH5	3×3	window discretized in 8 values
LH6	3×3	object discretized in 8 values
Local Entropy Ratio		
LHR1	9×9 (13×13)	include inner pixels
LHR2	9×9 (21×21)	include inner pixels
LHR3	9×9 (13×13)	exclude inner pixels
LHR4	9×9 (21×21)	exclude inner pixels
Local Binary Patterns		
LBP1	radius 1	rotation invariant
LBP2	radius 1	rotation variant
LBP3	radius 2	rotation invariant
LBP4	radius 2	rotation variant
Local Ternary Patterns		
LTP1	radius 1	rotation invariant
LTP2	radius 1	rotation variant
LTP3	radius 2	rotation invariant
LTP4	radius 2	rotation variant
Local Binary Patterns variation		
LTBP1	radius 1	rotation invariant
LTBP2	radius 1	rotation variant
LTBP3	radius 2	rotation invariant
LTBP4	radius 2	rotation variant

on computational environment and memory access.

3.3.2. Local Entropy

Entropy, initially used in information theory as measure of randomness [286, 287], can offer an indication of variability and heterogeneity of an object. Within a square window, local entropy is calculated as

$$LH(c) = - \sum_{i=1}^k p(i) \log_2 (p(i)), \quad (3.1)$$

where k stands for the total number of different pixel values within the window and $p(i)$ indicates the frequency of appearance of value i , i.e. the ratio of the number of pixels with value i to the total number of pixels in the window, and assigned to the central pixel of the window, c . In a moving window of $n \times n$ pixels, n^2 pixels are serially searched to identify the k distinct values. It is $k \leq n^2$, thus a maximum of n^2 iterations are required for entropy calculation based on the formula above. Therefore, $\mathcal{O}(n^2)$ can be considered as the complexity of the calculation of entropy for each moving window in an object.

Pixel intensities of the images are expressed as float numbers. In such case, insignificant value fluctuations, potentially by noise affliction, would be considered as different values and could result in unwanted or indifferent outcome entropy values. As a countermeasure, scaling of pixel intensity values is applied, three alternative ways being tested: (i) The entire image band is scaled to integer values in the range $[0, 255]$; (ii) the values of the pixels of a specific object are discretized in 8 values; and (iii) the values of the pixels within each window are discretized in 8 values. Moving windows of 3×3 and 9×9 pixels are tested as trade-off cases, the former aiming at capturing small spatial extent variations, whereas the latter at providing wider variety of discrete values. Windows of this size, including 9 and 81 pixels, respectively, are expected to provide non-robust features under the first case of image scaling to 256 values. Surprisingly, entropy calculated with a 3×3 pixel moving window was proven the most effective among features with other windows in a recent habitat classification study, using imagery of the same resolution to the present study [53]. A possible explanation is the existence of high spatial correlations within the image, especially after the scaling to 256 values, which resulted in a histogram of very few distinct values, e.g. two to four, within each moving window, making the

results by the entropy feature sensible. This reported outcome triggers the extraction of feature with parameters of case (i) in this study, for evaluation and comparison with the theoretically more robust parameters of cases (ii) and (iii) mentioned above.

3.3.3. Local Entropy Ratio

The ratio of the entropy values (LHR) of two concentric windows is extracted, aiming at characterizing relative variations within a small area compared with its surrounding one. For each pixel, two concentric windows are formed and local entropy value is calculated for each. For each pixel, c , LHR is defined as the ratio of the entropy value of the smaller inner window, $LH_{in}(c)$, to the entropy value of the larger outer one, $LH_{out}(c)$,

$$LHR(c) = \frac{LH_{in}(c)}{LH_{out}(c)}. \quad (3.2)$$

Entropy values are calculated following the approach of scaling image bands to $[0, 255]$ integer values. Two variations of LHR calculation are tested: in the former, the pixels of the smaller window are included in the calculations of the entropy of the larger one surrounding it, whereas in the latter, they are excluded to enhance the extraction of more independent values. Windows of 9×9 pixels are used as the small ones, as the size favouring the largest variability between the ones used in Section 3.3.2 for LH, whereas 13×13 and 21×21 are tested as the large windows, as indicative example sizes to study the effects of almost doubling the area and each dimension of the initial window, respectively.

3.3.4. Local Binary Patterns

Local Binary Patterns (LBP) [288] are calculated by comparing the intensity value of a pixel with the values of its surrounding ones in a circle of predefined radius, measured in pixels. Image bands are scaled to integer values in the range $[0, 255]$, prior to calculation. Starting from the pixel on the left of the central one and moving in a circular clockwise order, each pixel is flagged with value 1 in case its intensity value is larger than the one of the central pixel, or 0 otherwise, and a binary number of 1 and 0 values is formed. This number, converted to decimal, is assigned to the central pixel.

A rotation invariant variation of the feature is also calculated, by considering every surrounding pixel in the circle as the starting point, calculating the respective binary and, sequentially, decimal numbers, and assigning the largest one to the central pixel. As can be noticed, 0 binary values may arise both in homogeneous areas, with equal intensity values between the central and the surrounding pixels, and in heterogeneous areas, in cases where the intensity values of the surrounding pixels are smaller than the values of the central one.

As countermeasure for this confusion, two variations of the feature are tested, defining a range d in intensity values. In the first variation, local ternary patterns (LTP) [289] are extracted. Surrounding pixels with values within the range $\pm d$ compared with the central pixel are flagged with value 1, whereas pixels with values smaller than the central pixel value by more than d are flagged with 0, otherwise with 2. Values in the ternary system are created, i.e. with number 3 as basis, and converted to decimals. In the second variation (LTBP), surrounding pixels with values within the $\pm d$ range compared with the central pixel, are flagged with value 0, otherwise with 1, no matter whether they are larger or smaller than the central value. The introduction of range d in LTP and LTBP variations attempts to reduce unwanted effects caused by small variations in neighbouring values due to noise affliction, compared with LBP features. In the experiments described below, d was conservatively defined as 0.5% of the difference between the maximum and minimum band values, in order to interpret as noise and handle minimum differences of 1 in the scale of [0,255]. Larger values of d could be applied, although under a higher risk of misinterpreting actual band value variations as noise.

As a note, homogeneous areas are expected to have smaller values than heterogeneous ones in LBP and LTBP features, whereas they will tend to have values between the two extremes in LTP, since more intermediate values of 1 are expected to be found in the ternary numbers in homogeneous areas. Radii of 1 and 2 pixels away from the central pixel have been tested for each feature, together with both the rotation variant and invariant approaches. Considering a moving window of $n \times n$ pixels ($n \equiv 2r + 1$, where r the defined circle radius), less than $4n$ pixels (the pixels of the square enclosing the circle around the central pixel) are compared with the central one, for the extraction of the binary or ternary numbers. Thus, the complexity

of the calculation of LBP-based features can be considered $\mathcal{O}(n)$. Although theoretically faster than the variance or entropy features, the practical difference in computational time is negligible, or even favourable to the latter features, due to the very small size of moving windows/circles used.

3.4. Data processing and classification

3.4.1. Handling of indefinite values

In order to restrict the calculation of texture measures to the area of each individual object and avoid influences and biases from neighbouring objects, all pixels considered for the calculation of the texture features, both central and those belonging in the defined surrounding windows, are required to belong to the specific object under consideration. In case this requirement is not fulfilled for a calculated feature, its value remains indefinite. This results in objects with indefinite values in certain texture features (e.g. LHR), whose calculation requires surrounding windows larger than the dimensions of the object, or all texture features, when one of the dimensions of the object is restricted to solely one or two pixels. As an initial step prior to the classification to a height category, small objects with all their texture values indefinite are excluded, since no information for the classification is available.

For objects with partially missing information, where only some of their texture values are indefinite, three distinct approaches are followed: (i) exclusion of the features with missing data from the classification process for all objects; (ii) exclusion of the objects with missing data; or (iii) imputation (filling in) of the missing data with approximated values. The first approach has the advantage of computational simplicity, but the remaining feature set may have significantly less discriminatory power than the entire set. The second approach, known as listwise deletion, case deletion or complete-case analysis [290], although similarly little time and processing demanding, it may bias or affect the representativeness of the results. The latter is supported by the fact that the assumption that missingness is not related to the observed and missing variables, i.e. missing-completely-at-random (MCAR) assumption [291], is not valid for the missing data. For instance, objects with missing values in features calculated with 9×9 pixel moving

windows (e.g. LH1), will certainly have missing values in features with 13×13 pixel windows (e.g. LHR1), even though their values per se are completely independent. In addition, listwise deletion reduces the number of finally classified objects.

Three approaches for data imputation are evaluated, namely hot deck imputation [292], Amelia II [293], and Iterative Robust Model-based Imputation (IRMI) [294]. Hot deck imputation, drawing values from an unconditional distribution, where the missing data are filled in by randomly selected values among the observed ones, for each feature, preserves the variability of the values, but may distort a number of measures of association among variables, such as inter-correlations [290]. The two multiple imputation techniques, Amelia II, based on the assumption that the values are drawn from a multivariate normal distribution, and IRMI are employed to counteract this drawback. From each technique, five complete sets, including the values of all features from every image band, are created, averaged into one set to be used in the classification process. Rubin [295] estimated that the efficiency of a data set where m imputations are performed, compared with one of infinite imputations, is $(1 + \lambda/m)^{-1}$, where λ stands for the ratio of the number of missing values to the total number of values in the data set. In the present study, the ratio of missing data to the complete data is 0.0832. Therefore, five imputations have been selected as a good trade-off between efficiency and processing time, since, according to the formula proposed by Rubin, efficiency of around 98.32% is achieved.

3.4.2. Outlier removal

Having a complete data set, particularly after performing imputation of indefinite values, it may be essential to introduce a check mechanism for detection of outliers, i.e. objects which appear to be inconsistent with the remaining objects of the site, based on their texture feature values [296]. Among the variety of proposed approaches for the detection of outliers in different applications [297–300], an effective and conceptually simple box plot approach [301] is tested, detecting values in a large distance from the median value, for each texture feature; objects with such extreme values are considered outliers and removed. In particular, the interquartile range, DQ , is calculated, as the distance between the upper, $Q3$, and lower, $Q1$,

quartiles, $DQ = Q3 - Q1$, and values, v , that lie 1.5 times the interquartile range lower or higher than the lower and higher quartile, respectively, i.e. $v < Q1 - 1.5DQ$ or $v > Q3 + 1.5DQ$, are considered outliers. Further experiments are conducted using (i) box plot for multivariate data based on Mahalanobis distance [302], (ii) an adjusted box plot approach considering a measure of skewness of the distribution, termed medcouple [303,304], and (iii) modified Z-scores [305].

3.4.3. Data normalization

Since the range of values may vary among the different texture features—e.g. some values of LTP may be ten orders of magnitude larger than some values of local variance—, appropriate normalization of the data may prove effective to prevent texture features with larger values from having higher impact than ones with smaller values during the classification process. The linear (i) zero-mean and (ii) scaling to the range of $[0, 1]$, and the non-linear softmax scaling feature normalization approaches [306] are tested, applied per feature for each image. In zero-mean normalization, the normalized values of a feature X are calculated as

$$Z_i = \frac{X_i - \mu}{\sigma}, \quad (3.3)$$

where μ and σ stand for the mean and standard deviation of the initial observed values X_i of feature X , $i = 1, \dots, N$. Under scaling to the range of $[0, 1]$, feature values are calculated as

$$M_i = \frac{X_i - X_{min}}{X_{max} - X_{min}}, \quad (3.4)$$

where X_{min} and X_{max} represent the minimum and maximum values of feature X , respectively. Softmax scaling is performed by inserting the zero-mean normalized values Z_i derived by (3.3) in a sigmoid function, the new feature values being calculated as

$$S_i = \frac{1}{1 + e^{-Z_i}}. \quad (3.5)$$

3.4.4. Data transformation for dimensionality reduction

Apart from using all texture features during the classification, a number of data transformation approaches for dimensionality reduction (DR) are tested to transform the original data and reduce the number of final features used for each object. DR is used to remove information redundancies and notably reduce memory requirements and processing time during the classification process, without significant loss of the original information. Several popular data transformation approaches in remote sensing applications are evaluated, mainly unsupervised DR methods, taking under consideration solely the feature data space and not the involved classes, such as Principal Component Analysis (PCA) [307–309], Locality Preserving Projections (LPP) [310], Neighborhood Preserving Embedding (NPE) [311, 312], and Isomap (isometric feature mapping) [313]. In addition, Fisher’s Linear Discriminant Analysis (LDA) [314] is tested, as supervised approach, to reduce dimensionality based on a class separability criterion. Using label information, LDA is expected to perform better than the unsupervised approaches.

3.4.5. Feature selection

Whereas data transformation requires the extraction of all texture features to perform dimensionality reduction and reduce the classification complexity, feature selection aims at identifying a subset of high performing features that will reduce the processing cost of both feature extraction and classification processes. Filter approaches are followed in this study, where feature selection is based on an optimality criterion independent of the classification scheme applied, rather than wrapper approaches—where the classifier employed in the learning process is also used (wrapped) during the feature selection—, in order to allow flexibility in the classifier selection, as well as avoid the generally higher computational cost of wrapper approaches [315].

During the feature selection process, a number of feature subsets of the original set are evaluated and the one that better satisfies the optimality criterion is selected, with the aim to remove irrelevant and redundant information. Several approaches have been proposed for both the evaluation and search methods of the feature sets [316]. In this study, a correlation- and a consistency-based criteria are tested for the evaluation of the subsets. The former, Correlation-based Feature Selector (CFS) [317], favours the selec-

tion of feature sets with high correlation with the class (label) variable and low inter-correlation between each pair of features. The latter assigns an inconsistency rate to each considered feature set [318], based on the degree objects with similar feature values belong to different classes, favouring the most consistent sets. As far as the search method is concerned, instead of conducting exhaustive search among the $2^{192} - 1$ non-empty feature sets for the June and September datasets and $2^{384} - 1$ sets for the image synergy dataset, two heuristic approaches are tested, searching for the optimum subset among a restricted number of evaluated ones. In particular, (i) best-first [317,319] and (ii) fixed-width Linear Forward Selection [320] employing Sequential Floating Forward Selection [321] search methods are applied.

3.4.6. Classification

Classification is performed on object basis. Each object, i.e. each segment on the LC map, is characterized by a vector of texture feature values. For each feature, the average value of the pixels belonging to the object of interest is considered. Since the classification is based on the texture feature values, objects which have at least one texture feature assigned to them (i.e. not all values are indefinite) are classified to one of the seven GHC height categories reported in Section 3.1. Supervised classification is performed, using the texture values as the classification features, and the height classes derived by averaging the reference CHM values of the pixels of each object as label classes.

A number of classifiers are applied to test the discriminatory potential of the extracted features. Classifiers based on decision trees and support vector machines (SVM) [316], are employed due to their extensive use and reported accuracy in various remote sensing applications [322–326]. Two basic decision tree implementations, namely an implementation of C4.5 algorithm introduced in [327], J48, and a reduced-error pruning implementation [316], REPTree, are used as individual classifiers. In addition, Random Forests [328], Bagging [329], and AdaBoost.M1 [330] approaches are employed as ensemble tree classifiers to reduce the generalization error and improve the classification performance of the individual ones. After experimentation, 50, 100, and 20 trees were found as good trade-off numbers between accuracy and time complexity for the Random Forest, Bagging,

and AdaBoost.M1 ensembles, respectively. J48 and REPTree are used as base classifiers in Bagging and AdaBoost.M1 implementations. In addition, two classifiers based on SVM with linear kernel, with and without fitting logistic models to the output [331,332], are also tested.

3.4.7. Result evaluation

During all experiments in this study, 10-fold cross-validation was employed to evaluate the classification results, as one of the most widely used approaches [329,333–335], suggested over holdout, bootstrap, and cross-validation with different numbers of folds [336]. In particular, stratified 10-fold cross-validation was applied, as the variant of the method that provides more consistent results over repetitive evaluations [316]. Under this approach, the object dataset is randomly split in 10 non-overlapping parts (folds), each fold trying to reflect the proportion of each class that the full dataset has, i.e. containing around one tenth of the objects from each class. Then, the classification is run ten times, each one using a different fold for testing and the rest nine for training, i.e. every object is used for testing exactly once. The final evaluation of the classifier is computed by averaging the performances of the individual ten extracted classifiers. To ensure consistency among results and allow comparison of methods, feature sets, and classifiers, the same folds were created for all experiments involving the same number of objects.

3.5. Results and Discussion

In the experiments of this study, vegetation height estimation is directly related to habitat mapping requirements. In particular, the height classes defined in the GHC taxonomy [34] as the main characteristic to discriminate among different Tree and Shrub (TRS) species, are used, as presented in Section 3.1. For each object, i.e. each segment on the LC map, the average vegetation height is calculated, from the values of its pixels in the CHM used as reference layer. The calculated height is mapped to the respective height class and the latter is assigned to the object. Fig. 3.3 depicts the average height for each object belonging to the GHC categories (Section 3.1).

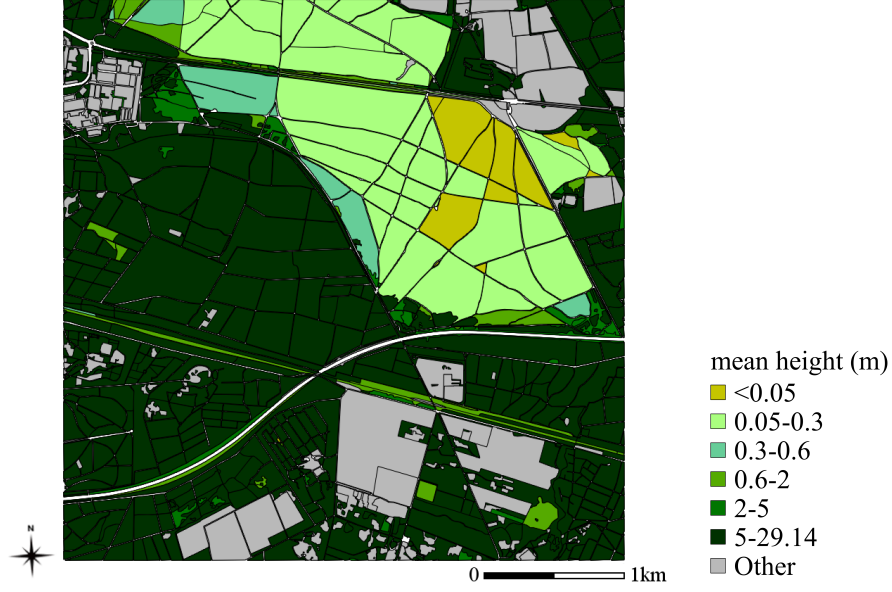


Figure 3.3.: Average height for each object of interest based on the CHM. ‘Other’ indicates objects of different classes than the GHC studied ones.

Following the extraction of features and the exclusion of objects having all their feature values indefinite, several experiments were conducted, including the different datasets created by the feature extraction and data processing approaches discussed in the previous section. The initial number of objects, excluding the ones having all their values indefinite, were 877, including: (i) 26 DCH, (ii) 59 SCH, (iii) 10 LPH, (iv) 43 MPH, (v) 68 TPH, and (vi) 671 FPH objects. As expected for the specific study site, no GPH objects (with trees over 40 m) were found. In cases where either outlier removal or listwise deletion was applied, the number of remaining objects was reduced; however, an adequate number of objects from each aforementioned height class remained in the final set.

3.5.1. Experiments with the full feature set

A. Classification accuracy

Fig. 3.4 draws the highest overall classification accuracies (OA) achieved, from any classifier, for datasets derived by applying different combinations of the data processing methods discussed previously. Data generated from

(i) solely the June, (ii) solely the September, and (iii) both images were evaluated. Overall classification accuracy represents the percentage of objects correctly classified among the total number of objects in the dataset. Amelia II, box plot using the Mahalanobis distance and zero-mean methods are displayed in Fig. 3.4 as indicative examples of value imputation, outlier removal, and data normalization, respectively.

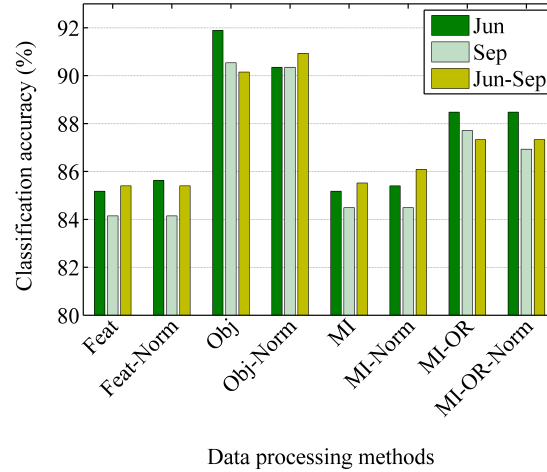


Figure 3.4.: The best classification accuracies acquired for certain data processing methods, indicated by a number of capital letters. Feat: exclusion of texture features having at least one indefinite value; Obj: exclusion of objects having at least one indefinite value; Norm: zero-mean normalization; MI: multiple imputation with the Amelia II method; OR: outlier removal with the Mahalanobis distance-based box plot method.

As readily seen, the proposed texture features lead to successful discrimination of the 6 vegetation height categories with accuracies starting from around 84% and approximating 92%. The results demonstrate the ability of the proposed texture measures applied in VHR optical imagery in acting as surrogates of principal sources of vegetation height information, such as in-situ or lidar data. The lowest accuracies were observed in datasets including all 877 objects ('Feat', 'Feat-Norm', 'MI', and 'MI-Norm' datasets), whereas the highest ones in cases where listwise deletion was applied in objects with at least one indefinite value ('Obj' and 'Obj-Norm' datasets). Excluded objects in the latter case were ones with dimensions smaller than a 21×21 pixel window, the largest surrounding window employed in the texture analysis

features. This result indicates that objects of satisfactory extent favour the extraction of more discriminatory features than small objects, making the latter more difficult to classify.

The set of features extracted from the June image seems to offer higher discriminatory capabilities than the one from the September image (Fig. 3.4). Evaluating the differences between features from the June and the respective ones from the September image for the listwise deletion ('Obj') datasets, through paired-sample T-tests [337], it was found that pairwise differences were statistically significant at the 5% level for 180 out of the total 192 features. When features from both images were used in synergy (Jun-Sep), the classification accuracy was higher than the September image, in most cases. However, in half the cases, it was lower than the June image, indicating the existence of high correlations among the features, confusing or overfitting the classifier and training it in too much detail that its generalization performance was decreased.

Comparing the different data processing approaches, imputation of indefinite values had a small positive effect in accuracy, compared with a simple exclusion of texture features with indefinite values. Considering that after the exclusion of such features, the remaining data correspond to features calculated using a 3×3 pixel surrounding window (larger windows return indefinite values for small objects), it is inferred that significantly localized variations of texture are proven crucial for vegetation height characterization. This conclusion encourages the systematic use of VHR imagery to vegetation height estimation applications. Although results from imputation using Amelia II are drawn, IRMI and hotdeck imputation approaches were also tested, the former providing similar results, whereas the latter slightly inferior.

Data normalization seems to provide insignificant influence in classification performance, in general, compared with the respective approaches where it was not used. All normalization techniques described in the previous section were tested, providing comparable classification results.

On the contrary, outlier removal methods seem to provide added value to the classification process, improving the achieved accuracies by around 2.5%, compared with the respective methods where outliers were not removed, under the expense of discarding around 70 objects considered as outliers. All outlier detection methods discussed in the previous paragraph provided

similar results to the ones through the box plot with Mahalanobis distance shown.

Cohen’s kappa coefficient, κ , has been extensively used in remote sensing literature as measure of accuracy of a classifier, or more precisely, to compare the achieved results with a random classification [113,205,250,338]. Although originally proposed to assess the degree of actual agreement among experts, or classifiers in a similar sense, compared with their random agreement [339], it has been extended to evaluate classifiers against the ground truth observed values, as an indication of randomness. κ is defined as

$$\kappa \equiv \frac{P_o - P_c}{1 - P_c}, \quad (3.6)$$

where P_o stands for the proportion of agreement between classified and observed objects, i.e. the overall accuracy of the classifier; P_c represents the proportion of the expected agreement by chance, calculated as

$$P_c = \sum_{i=1}^C \frac{NO_i NP_i}{N^2}, \quad (3.7)$$

where C stands for the number of different classes, NO_i the total observed objects of class i , NP_i the total objects classified to class i , and N the total number of objects. Fig. 3.5 draws κ for the classification attempts reported in Fig. 3.4, to demonstrate the degree each classification result assimilates a random classification. Values of 1 indicate perfect classifications, 0 values random ones, whereas negative values classifications where results worse than random classifications are acquired. Kappa coefficient provides an indication on whether the classifiers are biased by the significantly larger number of FPH objects compared to the other height categories. For instance, in the theoretical case all objects were classified as FPH, the overall accuracy would range between 76.51% and 80.69% based on the number of FPH objects over the total ones, under the different data processing approaches. However, in that case, the value of κ would be very low, equal to 0, as inferred from (3.6), highlighting the biased results. On the contrary, the observed values of κ , ranging higher than 0.5 in general, indicate that the majority of the class assignments, excluding correct assignments due to chance, are correct [339]; in other words, such values indicate ‘moderate’

($0.41 \leq \kappa \leq 0.60$) or ‘substantial’ ($0.61 \leq \kappa \leq 0.80$) agreement between the observed and predicted classes, according to Landis and Koch [340].

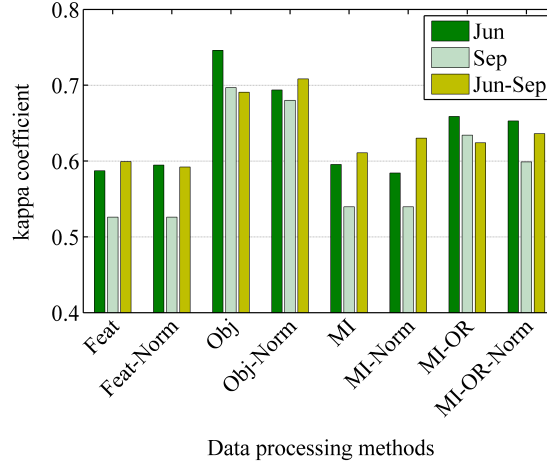


Figure 3.5.: Kappa coefficients of the data processing methods shown in Fig. 3.4.

Table 3.3 presents the confusion matrix for the best classification results achieved with the June image dataset after listwise deletion (‘Obj’ in Fig. 3.4). AdaBoost.M1 was used with J48 as the base tree classifier. As noticed, most of the GHC classes were identified with high user’s and producer’s accuracies (i.e., low commission and omission errors, respectively). Exceptions were the LPH class objects of limited number that remained undetected and the low producer’s accuracy for the TPH class. The results seem to be skewed by the domination of the FPH classes, significantly outnumbering the other classes. In fact, almost all FPH classes were classified correctly (99.04% PA), whereas bias towards this majority class was noticed for objects of the closest in height category of TPH, resulting in 96.06% UA. It is worth noting that the number of LPH objects (7) are less than the number of formed folds in the cross-validation process (10). This implies that three folds have no LPH object. It is statistically preferable to have representation of each class in every object. However, useful conclusions on classifier performance can still be extracted from its ability to avoid false negatives, as in the case where a fold without LPH objects is used as the testing fold during the iterative process of cross-validation. In the particular example, the classifier failed to correctly identify any LPH

object, whereas erroneously labelled as LPH two SCH objects.

Table 3.3.: Confusion matrix from classification on the full June image set following listwise deletion, using AdaBoost.M1 with J48 as base classifier. Rows represent the reference classes, whereas columns the predicted ones. Producer’s (PA), user’s (UA) and overall accuracies, as well as the kappa coefficient, are reported.

	DCH	SCH	LPH	MPH	TPH	FPH	Sum	PA(%)
DCH	7	4					11	63.64
SCH	3	34	2	1			40	85
LPH	1	4		2			7	0
MPH		1		16	1	4	22	72.73
TPH				2	5	13	20	25
FPH			1	2	1	414	418	99.04
Sum	11	43	3	23	7	431	518	
UA(%)	63.64	79.09	0	69.57	71.43	96.06		
Overall accuracy (%): 91.89					Kappa coefficient: 0.746			

Fig. 3.6 visualizes the classification results by listwise deletion in the study area. As noted previously, it can be seen that the objects removed (‘Excluded’) were the ones with smaller dimensions than the minimum required for the calculation of certain texture features (e.g. LHR). Comparison with the object heights extracted by the CHM (Fig. 3.3), demonstrates the high classification accuracy achieved, both in large and small area objects. As a note, cloud contaminated pixels were excluded from the classification, and together with classes different than the studied ones, are noted as ‘Other’ classes.

B. Classifier performance

Regarding the performance of the employed classifiers, Random Forests (RF) outperformed, in most cases, the rest of the classifiers. Fig. 3.7 depicts the average classification accuracies achieved by the tested classifiers, over the different datasets drawn in Fig. 3.4, for the cases where features from the individual images and their synergy were used. Among the decision trees, ensemble classifiers, i.e. RF, Bagging and AdaBoost.M1, where multiple trees are generated, provided better results than the single J48 and REP-Tree classifiers, whereas SVM with logistic models to the output showed

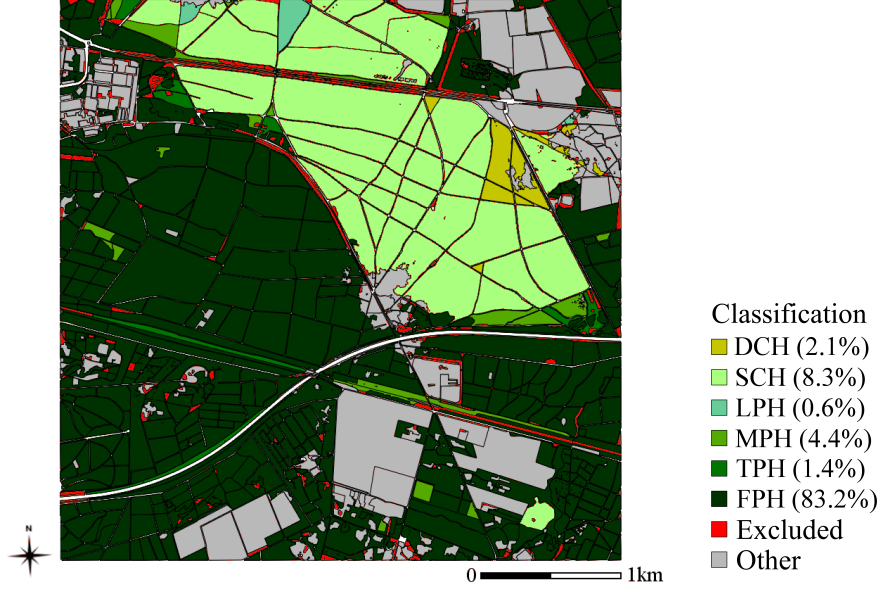


Figure 3.6.: Height classification after listwise deletion in the full June image dataset, using AdaBoost.M1 with J48 as base classifier. ‘Excluded’ indicates the removed objects by listwise deletion, whereas ‘Other’ shows classes different than the studied ones and cloud masked areas. The percentage of the objects classified to each class over the total number of classified objects is shown in parenthesis.

inferior performance than the other SVM classifier. The overall high accuracies from all classifiers verify the effectiveness and discriminatory power of the selected features for height estimation. In compliance with Fig. 3.4 outcomes, the June image provided, in general, higher performing datasets than the September one, whereas their combination had similar performance to the June image.

Although more complex and time expensive classifiers provided superior results, simple classifiers, as the REPTree, still provided high accuracies and may be preferred in similar applications when time and processing efficiency is critical. In particular, the REPTree classifier, involving a fast reduced-error pruning approach, has time complexity $\mathcal{O}(mn \log n)$, where n stands for the number of samples (i.e. objects in this study) and m for the number of attributes (features) [316]. The more complicated pruning by subtree raising used in J48 increases its complexity to $\mathcal{O}(mn \log n) + \mathcal{O}(n(\log n)^2)$ [316].

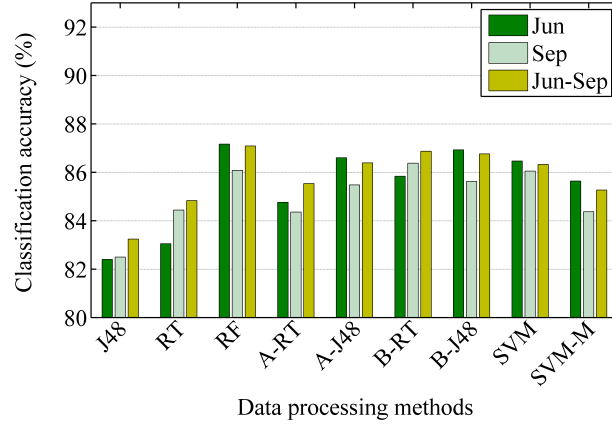


Figure 3.7.: Average classification accuracies achieved from the various classifiers, over the different datasets shown in Fig. 3.4. RT: REPTree; RF: Random Forest; A-RT: AdaBoost.M1 with REPTree; A-J48: AdaBoost.M1 with J48; B-RT: Bagging with REPTree; B-J48: Bagging with J48; SVM-M: SVM with logistic models.

The complexity of the AdaBoost.M1 ensemble classifiers is calculated by multiplying the complexity of the basis classifiers (J48 or REPTree) by the number of derived trees, t . Similarly for the Bagging classifiers, although the bootstrap aggregation performed to select the training set before the construction of each tree slightly increases the computational time; in addition, further computation time was added by the larger number of constructed trees for Bagging than AdaBoost.M1, namely 100 over 20, that resulted in around five times slower execution than AdaBoost.M1. Among the ensemble tree methods, Random Forest was the fastest, with estimated complexity around $\mathcal{O}(tn \log n \log m)$, since $\log m + 1$ features are considered to split each node in this study, instead of m used in J48 and REPTree classifiers. The complexity of SVM, mainly with non linear kernels, is usually estimated around $\mathcal{O}(n^2)$ or $\mathcal{O}(n^3)$, as requesting to solve a quadratic programming (QP) optimization problem [341, 342]; however, implementations involving linear time have also been proven feasible [343]. In this study, SVM classifiers with linear kernels and using the Sequential Minimal Optimization (SMO) [331] are employed, resulting in practical computational time in these experiments between AdaBoost.M1 and Bagging. As inferred from Fig. 3.7 and this discussion, the RF classifier shows the highest ratio of accuracy to computational time, compared with the rest classifiers used.

C. Data transformation

The application of dimensionality reduction through data transformation techniques was evaluated for all datasets. It was observed that intense compression of information can be achieved with insignificant loss, or even increase, in performance. Fig. 3.8 presents the classification accuracies achieved by the different methods when 5 features were held for each method, compared with the full feature set, for the datasets after listwise deletion ('Obj'). The evaluated unsupervised DR techniques (PCA, LPP, NPE, Isomap), although optimizing different criteria, showed similar performance. In fact, insignificant losses of accuracy of about 2-3% are observed, compared with the results from the original datasets including all features, whereas the number of features used in the classification was substantially reduced to 5, from 192 (24 features from each of the 8 bands) for the single images and 384 for their synergy, i.e. by up to 98.7%. Such methods apply DR using only the statistical properties of the feature space. Adding label information, using a supervised DR approach, in particular LDA, higher classification accuracies were achieved, reaching even perfect separability. Although such results seem hardly achievable in generalized and broader datasets, since LDA is trained to maximize class separability for the specific dataset, they indicate the high potential discriminatory power of the calculated texture features for all classes, under proper transformation. The results by all DR methods indicate that the intrinsic dimensionality of the datasets is notably lower than the full feature sets, thus significant improvements in the complexity and processing time of the employed classifier can be achieved through dimensionality reduction. The DR approaches had similar performance compared with the respective full feature set, for all other datasets not shown in Fig. 3.8, that involve exclusion of indefinite features, multiple imputation, outlier removal, or data normalization.

3.5.2. Experiments with feature subsets

A number of experiments were conducted to evaluate the performance of (i) each individual feature, (ii) the features of each individual band, and (iii) the features from the applied feature selection methods. During the experiments described here, the dataset arising from the simple listwise deletion was selected, to study the effectiveness of the actual feature values upon

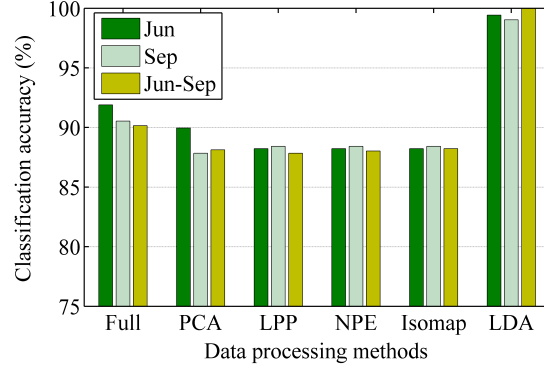


Figure 3.8.: The best classification accuracies achieved with different dimensionality reduction approaches, reducing to 5 features the datasets after listwise deletion (‘Obj’). Methods: Full: Full dataset; PCA: Principal Component Analysis; LPP: Locality Preserving Projections; NPE: Neighborhood Preserving Embedding; Isomap: isometric feature mapping; LDA: Linear Discriminant Analysis.

their extraction, without any data processing applied. After excluding objects with indefinite feature values, 518 remained, including: (i) 11 DCH, (ii) 40 SCH, (iii) 7 LPH, (iv) 22 MPH, (v) 20 TPH, and (vi) 418 FPH objects. RF classifier was selected for all experiments, as the one providing the best accuracy results in the specific dataset and one of the most consistent and best performing classifiers in all datasets (Fig. 3.7). Classification was evaluated under 10-fold cross-validation.

A. Evaluation of individual features

Initially, classification was performed using each of the 384 calculated features, 24 from each band of each image, individually, in order to identify the ones with the best discriminatory power. Table 3.4 lists the features achieving the 10 highest classification accuracies. Almost the same features appear in the respective list with the highest kappa coefficient values, since classification and kappa coefficient values are highly correlated, with the latter two of Table 3.4 being replaced by the LTBP2 ($\kappa = 0.494$, OA = 82.63%) and LTBP3 ($\kappa = 0.487$, OA = 82.63%) features calculated in the red-edge and the red band of the September image, respectively. The highest classification accuracy achieved using an individual feature was 84.36%,

solely around 6% less than the one where all 384 features were employed (Fig. 3.4). This small difference may be an indication of the high degree of correlation among the features, but also the high discriminatory potential of the individual features.

Table 3.4.: Individual features achieving the highest 10 classification accuracies, with the respective kappa coefficients, using the Random Forest classifier.

Rank	Feature	Band	Accuracy (%)	kappa
1	LH4	NIR1 (Sep)	84.36	0.53
2	LTBP1	Red (Sep)	83.98	0.523
3	LH5	Blue (Jun)	83.98	0.513
4	LTBP2	Yellow (Sep)	83.59	0.521
5	LTP2	Yellow (Sep)	83.59	0.519
6	LH4	Yellow (Sep)	83.4	0.514
7	LH4	Red (Sep)	83.2	0.496
8	LTBP3	NIR2 (Sep)	83.01	0.501
9	LTBP4	NIR1 (Jun)	82.82	0.481
10	LH4	NIR2 (Sep)	82.82	0.478

Local entropy features and the features based on the variation of local binary patterns seem to dominate the list. In addition, more features calculated from the September image appear in the tables than the June image, although the June full dataset has outperformed, in general, the September one (Fig. 3.4, 3.5, and 3.7). A potential explanation to this observation is that, whereas individual features extracted from the September image have more discriminatory power than the June ones, they are more correlated, restricting the performance improvements when used in synergy.

It is noteworthy that Table 3.4 is dominated by features extracted using small moving windows, of size 3×3 and 5×5 pixels, or radii 1 and 2, respectively (Table 3.2). This result demonstrates that features that express localized texture variations captured in a small spatial extent may provide more discriminatory capabilities in height estimation than ones that consider variations over a larger extent. This outcome further supports the beneficial use of very high resolution imagery in such tasks, in comparison with coarser resolution alternatives.

The observed advantage of features extracted with small moving windows,

over features with large ones, supports the selection for per pixel calculation of values and their averaging over each object. On the contrary, potential calculation of a single value over each object, e.g. as in [280], would be expected to perform closer to the calculation with large moving windows, or poorer. As far as individual features are regarded, the proposed use of local binary pattern based features seems encouraging for their broad use in height estimation studies through texture analysis, together with entropy based features calculated with 3×3 moving window.

The lowest classification accuracy observed was restricted to 63% (LTP3 feature from the June green band), with a kappa coefficient of -0.048 , implying a bias towards the more populated class of forest phanerophytes (FPH). No clear indication on the most appropriate bands for feature extraction may be supported from the results in Table 3.4, since diversity in employed bands appears in the highest ranking places.

B. Evaluation of individual bands

Fig. 3.9 draws the classification accuracies achieved when all features extracted from a single band were considered, for each band. The classification accuracies range from 84.17% to 90.35%. Following the expectations, the results from the synergies of features involved were significantly better than the ones from the individual features, discussed in the previous paragraph. The bands of the September image provided measures that consistently outperformed the ones of the June image. Combined with the observation that when the entire set of features from all bands of the June image was employed the results surpassed the respective ones from the September image (Fig. 3.4, 3.5 and 3.7), the existence of high correlation among the bands of the September image may be inferred, resulting in insignificant improvement of the discriminatory power for combined September bands, since they contain similar information.

The features from the red-edge band provided the best results among the bands of the June image, reaching accuracies of around 88%. On the other hand, NIR2 band of the September image seems to provide the most discriminatory features, slightly outperforming the red, yellow, red-edge, green, and NIR1 bands. It is noteworthy that all these bands achieved better results than the red-edge band of the June image. In addition, high

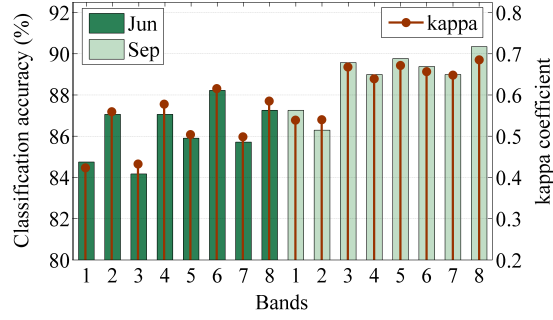


Figure 3.9.: Classification accuracies and kappa coefficient values achieved employing all features of a band, for each band of the June and September image, using the Random Forest classifier. Bands: coastal (1), blue (2), green (3), yellow (4), red (5), red-edge (6), NIR1 (7), NIR2 (8).

performing bands, such as NIR2 for the June image or yellow, red-edge, and NIR2 for the September one, may indicate an advantage of the use of WorldView-2 imagery for height estimation, compared with spectrally poorer high resolution imagery used in past studies, e.g. IKONOS [38, 41], QuickBird [280] or Spot-5 [40]. Overall, texture analysis performed solely in one band of a satellite image can provide results comparable to the ones achieved by exploiting all image bands, using around 8 (one image) or 16 (two images) times less processing time and memory requirements.

C. Evaluation of selected feature sets

All possible combinations of the evaluation and search methods of Section 3.4.5 were tested for the selection of features through filter approach, i.e. correlation-based evaluation with best-first (RB) and Linear Forward Selection (RL), as well as consistency-based evaluation with best-first (CB) and Linear Forward Selection (CL). The methods were applied to three different datasets, including all features from the June, September, and both images. The results are drawn in Fig. 3.10.

Four different groups of sets of selected features were used for the classification: features selected from (i) the June image (Fig. 3.10a), (ii) the September image (Fig. 3.10b), (iii) the union of selected features in (i) and (ii) (Fig. 3.10c) and (iv) the complete feature set of both images (Fig. 3.10d). Besides the classification accuracy, in order to provide an indication of the

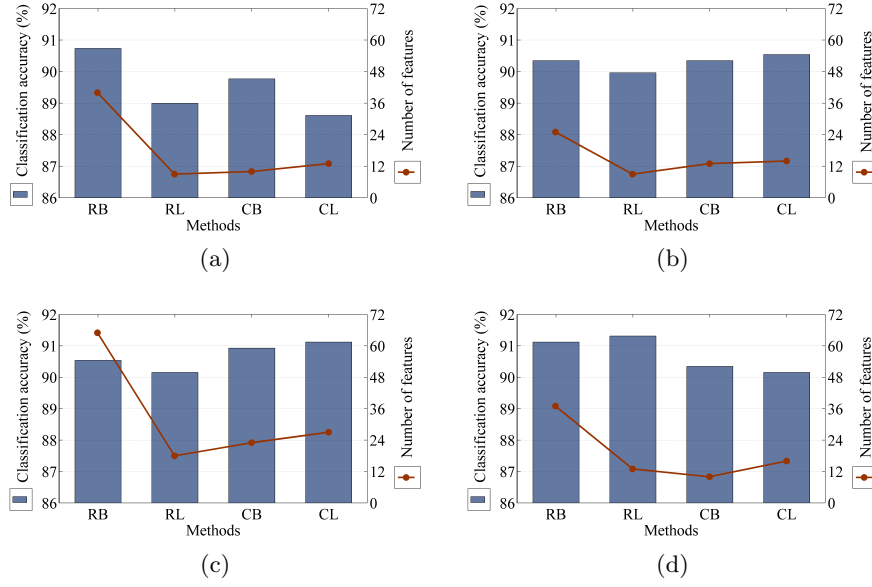


Figure 3.10.: Classification accuracies achieved employing the features selected through different approaches for filter feature selection and the respective number of selected features, for the selected features of (a) the June image, (b) the September image, (c) the union of those two selected sets and (d) the features selected from the ones of both images. The Random Forest classifier was used. Feature selection methods: correlation-based evaluation with best-first (RB) and Linear Forward Selection (RL), consistency-based evaluation with best-first (CB) and Linear Forward Selection (CL).

efficiency of the feature selection approaches, as far as the expected advantages in computation cost reduction are regarded, the number of selected features is additionally depicted.

Fig. 3.10 demonstrates the overall advantageous effects from the use of a feature selection approach. In all tested approaches, significant reduction of the initial feature set was achieved, together with high classification accuracies, ranging from over 88% to almost 92%. Combinations of features selected by the proposed methods clearly outperformed the accuracies of individual features (Table 3.4), and in most cases, the best performing individual bands (Fig. 3.9), using a smaller number of features. Even further, selection of 13 out of 384 features from both images, i.e. 3.4% of the features, under the RL method (Fig. 3.10d), outperformed the accuracy of the

full June-September feature set (‘Obj’ in Fig. 3.4).

When the selected features from the June and September images were used together (Fig. 3.10c), the number of features increased significantly, for each selection approach, as the sum of the features from the two images, without, however, proportionally increasing the achieved classification accuracies, an indication of significant correlation among the selected feature sets from the two images. Applying feature selection to the total number of features of the June and September image (Fig. 3.10d) resulted in overall comparable performance to the previous case, although with the use of significantly less features. It is noteworthy that since filter feature selection does not intend to improve classification per se, but to reduce redundant information, the selected features from an individual image may provide better results than ones from both images (e.g. CL approaches in Fig. 3.10b and 3.10d). A method that aims specifically at optimizing the classification results, e.g. a wrapper method, may select features that further improve the performance of the synergy of images, although being computationally more expensive in general and tied to a specific classifier and classification task.

The number of selected features significantly affects the complexity of the classifier and the classification time, which may be crucial factors in certain applications. Table 3.5 lists the approaches with the highest ratios of accuracy to the number of features, for the cases where features from the June, September and both images were selected. As seen, extraction of solely 9 or 10 features may result in classification accuracies almost as high as employing the full set of 192 or 384 features, while reducing the processing cost in both feature extraction and classification processes.

As observed from Table 3.5, the selected features are not in general among the top-performing individual ones, shown in Table 3.4. However, being relatively uncorrelated, they contain supplementary information that seems to improve the performance of the classifier and prevents its overfitting. It is noteworthy that in the highest performing feature set shown, extracted from the June image, features from all the proposed types are included (namely LE, LH, LHR, LBP, LTP, and LTBP). This indicates that, despite the low performance of some feature types when used individually, they may all contain uncorrelated supplementary information that enhances classification when they are used in synergy.

Table 3.5.: Feature selection methods with the highest ratios of classification accuracies to the number of selected features, for the cases where features from the June, September and both images were selected. For each method, the overall accuracy (OA) and the selected features are shown. The Random Forest classifier was used.

Image	Method	OA(%)	Selected features
June	RL	89	9: LHR3(1), LE1(5), LH5(6), LBP2(6), LTP2(6), LE1(7), LTBP1(7), LTBP2(7), LTP1(8)
Sep	RL	89.96	9: LH2(1), LTP1(4), LH4(6), LH5(6), LTP2(6), LTBP1(6), LE1(8), LTP2(8) LTBP3(8)
June + Sep	CB	90.35	10: LH6(J1), LH4(J2), LH5(J2), LTBP2(J3), LBP2(J5), LE2(J7), LBP1(S3), LH6(S5), LH1(S6), LH2(S7)

Among the approaches of Table 3.5, the CB method applied in the features of both images provided the highest ratio of overall accuracy to number of features. The confusion matrix of the classification is shown in Table 3.6, the rows and columns presenting the reference and predicted classes, respectively.

Table 3.6 demonstrates the results for all six GHC classes, being characterized by different vegetation height. SCH (0.05–0.3 m), MPH (0.6–2 m), and FPH (5–40 m) were the classes with the highest precision and recall accuracies, whereas the classifier did not achieve to detect any of the LPH objects. Although the number of FPH objects were significantly higher than the other objects, only a small bias of the classifier towards this class is observed, resulting in misclassification of some objects of the previous TPH height class as FPH.

3.6. Conclusions

Texture features based on local variance, entropy and binary patterns, calculated from very high resolution passive sensor imagery, proved particularly effective in discriminating among different vegetation height categories. Features from two vegetation productivity periods were evaluated,

Table 3.6.: Confusion matrix from classification following the CB feature selection method in the feature set of both images, (a) showing all six GHC classes, and (b) merging low shrubs of 0.05–0.6 m and tree classes. Rows represent the reference classes, whereas columns the predicted ones. Producer’s (PA), user’s (UA) and overall accuracies, as well as the kappa coefficient, are reported. The Random Forest classifier was used.

	DCH	SCH	LPH	MPH	TPH	FPH	Sum	PA(%)
DCH	4	5	1			1	11	36.36
SCH	4	34		2			40	85
LPH	1	3		3			7	0
MPH		3		14	4	1	22	63.63
TPH				3	1	16	20	5
FPH				2	1	415	418	99.28
Sum	9	45	1	24	6	433	518	
UA(%)	44.44	75.56	0	58.33	16.67	95.84		
Overall accuracy (%): 90.35					Kappa coefficient: 0.694			

both individually and in synergy. Extending the diversity and height range of species of previous studies employing texture analysis—focusing, for instance, on coniferous [40, 278] and hardwood [40] forests, or oak, beech and spruce trees [41], of several metres high—, different vegetation species were assessed in this study, including heathland, trees and shrubs, and various height categories, ranging from less than 5 cm to some tens of metres, supporting the extensive use of the proposed features in cost-effective height estimation applications.

Thorough evaluation of different data processing techniques to further enhance classification was performed: whereas data imputation and normalization had little effect in feature discriminatory power, removal of outliers and listwise deletion of objects with missing information resulted in higher classification accuracies; the latter method indicated that objects of larger extent, not being removed, were more likely to provide more discriminatory features than smaller objects. High accuracies were achieved under different classifiers, with ensemble decision tree ones and SVM outperforming the single trees. Data transformation revealed that data compression of about up to 98.7% may be applied to the full feature set, reducing the classifier complexity, with an insignificant loss, or even increase, in accuracy.

Feature subset selection through filter methods proved that time and processing cost reduction could be extended to both classification and feature extraction. A selected subset with a number of features less than 3% of the features of the full set was able to provide similar classification accuracies, whereas larger subsets could even outperform the full feature sets. Images from both vegetative periods provided similarly discriminatory features, alternating in performance within the different data processing techniques.

Among the proposed texture features, the local entropy features (LH) and the features based on the variation of local binary patterns (LTBP) have resulted in the highest classification accuracies, when considered individually. Both types of features were extracted with moving windows of 3×3 (LH4, LH5, LTBP1, LTBP2) and 5×5 (LTBP3, LTBP4) pixels, proven advantageous over features calculated with larger windows (i.e. LH1–LH3 and LHR of 9×9 pixels or larger windows); this implicitly suggests the advantages brought by the use of very high resolution images (WorldView-2) over coarser resolution ones used in previous studies (e.g. Landsat, SPOT). Expressing interrelations with neighbouring pixels, local entropy and binary patterns proved more effective than the simpler local variance features, even though having similarly small windows. In addition, the modifications proposed by LTBP features over LBP and LTP seem to be advantageous. However, despite their differences in individual performance, the features of all types appear to provide useful or complementary information that can prove beneficial in similar classification tasks, as shown by the high accuracy achieved from the selection of features from all types, as described in Table 3.5.

It is noteworthy that in the area studied, around 80% of the objects belong to a single class, namely forest phanerophytes (FPH). Although cross-validation was employed to ensure every class was present in both the training and testing datasets, the large number of FPH objects obstructs a reliable evaluation of the classifiers. The evaluation of the confusion matrices showed that there was a bias towards the FPH class, however almost exclusively from the immediately shorter TPH class. The calculated kappa coefficient values showed results far from chance, indicating that this bias was limited and the other classes were only slightly affected. A further interesting dimension for future research might be the use of a binary classifier to identify each class against all others.

The degree that this approach can be generalized in different geographical areas or species is still to be investigated. The study area includes a mixture of vegetation types, such as dry heathland, grassland, herbaceous and shrub vegetation, and forest, as well as a variety of plant species (e.g. *Calluna vulgaris*, *Pinus sylvestris*, *Fagus sylvatica*, *Betula pendula*, to name a few) from different height categories. Being effective in such a complex area supports the expectation that the algorithm can be applicable in other areas, especially of similar climatic conditions or with similar vegetation species. Furthermore, the proposed features have been applied to a Mediterranean coastal area with a complex of lagoons, numerous channels, marshes, and humid grasslands, with different species, such as thermo-mediterranean and pre-desert scrubs, in a preliminary study to evaluate their ability in discriminating between LPH/MPH and TPH classes [344]. The features were calculated from a QuickBird satellite image of 2 m spatial resolution with four bands (namely blue, green, red, and NIR), for each band. It was found that LPH/MPH and TPH classes had statistically significant differences to the 5% confidence level, for most features. These preliminary results are encouraging indications that the method can be generalized in different geographical areas and vegetation species, and discriminatory features can be extracted by different sensors as well. Consideration of multiple areas in future research activities could further investigate how species-dependent the features are or how they are affected by the growing stage of a single species.

Overall, the proposed approach does not intend to replace data sources offering more dense and accurate height information, such as the lidar derived CHM used as reference. The object based classification analysis followed provides coarser spatial resolution and value range than lidar can offer. Using lidar, applications requiring much more detailed information (e.g., surface roughness for wind erosion modelling, forest carbon stock assessment) are better satisfied. However, resulting in classification accuracies of up to over 90%, the proposed texture analysis features seem capable of enhancing vegetation height characterization for studies like habitat monitoring and land use mapping. In these, or similar, cases, VHR imagery may act as a cost-effective surrogate of more expensive and resource demanding approaches.

4. Habitat classification with supervised learning

4.1. Formulation of the habitat classification problem

Habitats and their changes constitute significant indicators for biodiversity monitoring, ecosystem preservation, and sustainability management, thus their mapping attracts the interest of various organizations and management authorities worldwide [43–45]. Habitat mapping with remote sensing data and methods is increasingly used due to their advantages in large area coverage, time and cost efficiency [26].

Most classification approaches have used directly the RS imagery and available ancillary information, such as cadastral and urban layers or digital elevation models [46–48, 345]. However, compared with land cover mapping, direct connection of spectral information to habitats is more challenging, requiring field data and expert interpretation [23]. Due to the larger availability of land cover maps and their more straightforward extraction, habitat classification through the conversion of the former seems a promising alternative, still mainly restricted to theoretical analyses [49–51].

Tomaselli *et al.* [49] compared a number of LC classification schemes and identified the Land Cover Classification System (LCCS) [33] as the most related one to habitats. A following study by Kosmidou *et al.* [51] provided a theoretical framework to map LCCS classes with General Habitat Categories (GHC) [34], confirming the similarities of the two taxonomies but also the fact that a conversion from one to the other is not straightforward. Several one-to-many mapping relationships were identified, together with discrepancies in definitions, and therefore, supplementary sources of information were deemed necessary for more accurate classification.

Based on these outcomes, Adamo *et al.* [52, 53] employed VHR satellite

imagery and presented a classification approach based on rules provided by expert ecologists. In more detail, WorldView-2 images of 2 m spatial resolution and a LC map expressed in the LCCS taxonomy were employed for two coastal Natura 2000 protected sites in Italy, namely Le Cesine and Lago Salso. Using the objects delineated by the LCCS map, a number of spectral, topological, morphological, lidar, and texture features were extracted from the two-date images. They included spectral indices for the presence of vegetation and water; object area and shape indices; estimated adjacency of the object of interest to objects of certain LC or habitat classes; height estimation features extracted from available lidar data; and local entropy texture to substitute lidar features, when the latter were considered missing. Based on the theoretical mapping rules by Kosmidou *et al.* [51] and the laborious work by expert ecologists, a large number of rules and thresholds were developed to extract GHC classes from the LCCS map and the aforementioned features in Le Cesine site. Rules for both considering lidar features and substituting them with the texture feature were developed. The classification system achieved overall accuracies of around 69% when applied to Le Cesine, which it was developed for, and 66% when applied to Lago Salso, for several GHC classes.

Although achieving relatively high accuracies for certain habitat classes, two main limitations of the method can be identified:

- (i) On the one hand, the employed features were empirically selected by the experts, whereas the specific rules and the associated thresholds were based on expertise and repetitive trial-and-error experimentation. This task involves labour and time consuming fine-tuning of threshold values through iterative experiments, while keeping the number of total different evaluated combinations of values limited.
- (ii) On the other hand, the use of crisp rules severely restricts the robustness of the approach to noise afflicted data or inaccurate rule thresholds and its transferability to different sites, i.e. its generalization performance. In addition, for the latter issue, no flexibility is provided in case required data are unavailable for certain areas, a problem often faced in remote sensing studies.

To counteract these limitations, two habitat classification approaches are proposed in the present and the following chapter, building on the approach

Table 4.1.: Problem statement of Chapter 4.

- **Objective:** Habitat classification of landscape objects with automated and fast training using supervised classifiers, and evaluation of method transferability to different sites. Comparison with state-of-the-art approach in [52, 53].
- **Input:** (i) Very high resolution multispectral satellite images from two study areas; (ii) land cover map of the area to delineate objects and provide LCCS class features assisting habitat classification; (iii) Canopy Height Model from lidar data.
- **Methodology:** (i) Extraction of spectral, morphological, topological, and lidar features, for classification; (ii) extraction of a number of features characterizing LCCS classes; (iii) classification using different feature sets and supervised classifiers.
- **Output:** Classification of study areas in GHC habitat classes, (i) for each individual area and (ii) using one area as training site and the other as testing.
- **Evaluation measures:** (i) Overall, Producer's, and User's accuracies; (ii) kappa coefficient.

presented by Adamo *et al.* [52, 53]. The goal of the classifiers is to propose effective schemes that overcome the aforementioned limitations. They use as input (i) a LC map expressed in the LCCS taxonomy, (ii) satellite images of very high spatial resolution, and (iii) lidar data, when available; their output is a map of habitat classes according to the GHC taxonomy.

In this chapter, a supervised learning framework is proposed to automatically train a number of classifiers and select the classification criteria in a labour and time efficient manner. Apart from the labelled objects used for training, no prior information is inserted to the classifier in the form of rules or constraints. An approach to convert the LCCS classes to interval-scaled variables, in order to be directly usable by a supervised classifier, is suggested. The approach is evaluated in two study sites individually. In addition, models derived from one site are tested to the other, as an indication of the generalization performance of the approach. Table 4.1 summarizes the statement of the problem being addressed in this chapter.

In Chapter 5, a classification framework using evidential reasoning and fuzzy logic is proposed, to deal with uncertainties created by unavailable information, noise afflicted data, and inaccurate rule thresholds provided by the experts. Unlike the previous case, prior knowledge is introduced to the

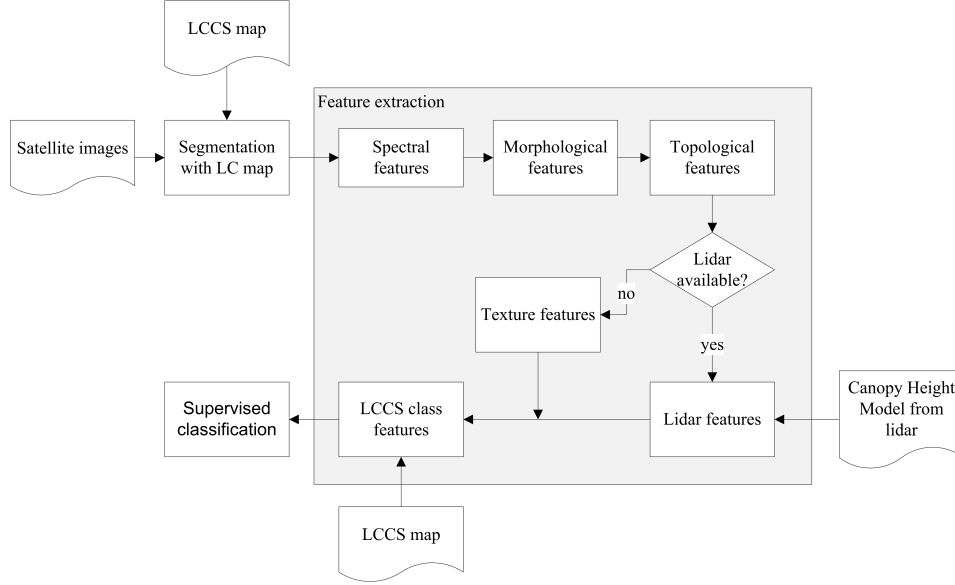


Figure 4.1.: Flow chart of the overall methodology proposed for supervised habitat classification.

classifier in the form of preliminary rules provided by experts, as in [51–53], and processed. The approach is evaluated in the two aforementioned study sites: the one site is which the rule set was originally provided for by the experts, whereas the other is used to test the generalization performance and transferability of the approach to different areas.

Fig. 4.1 provides a flow chart of the overall methodology described in this chapter.

4.2. Classification taxonomy definitions, study areas, and data

4.2.1. LCCS and GHC taxonomy definitions

The LC taxonomy used as proxy for the habitat classification is the Land Cover Classification System (LCCS), proposed by the United Nations (UN) Food and Agriculture Organization (FAO) and the UN Environment Programme (UNEP) [33]. The LCCS taxonomy has been proposed as a generic framework able to describe adequately any LC class globally, whereas the use of life form definitions makes it the closest LC taxonomy to habitats [49].

LCCS classes are organized in eight main categories, depending on whether the area element of interest is (i) vegetated or not, (ii) aquatic or terrestrial, and (iii) managed or artificial or (semi-)natural (Table 4.2). Classes are further refined with the inclusion of additional qualifiers describing various properties, such as life form (e.g. woody or herbaceous vegetation), vegetation coverage, leaf type and phenology (e.g. broadleaved, evergreen, deciduous), canopy height, and surface aspect (e.g. roads, railways, bare rock) [33].

Table 4.2.: The 8 main LCCS classes.

Vegetation	Surface	Management
A. Vegetated	A1. Terrestrial	A11. Cultivated and managed areas
		A12. (Semi-)natural vegetation
	A2. Aquatic or regularly flooded	A23. Cultivated aquatic areas
		A24. (Semi-)natural aquatic vegetation
B. Non-vegetated	B1. Terrestrial	B15. Artificial surfaces
		B16. Bare areas
	B2. Aquatic or regularly flooded	B27. Artificial water bodies, snow, and ice
		B28. Natural water bodies, snow, and ice

In this study, as in [51–53], habitats are expressed in the recently developed General Habitat Categories (GHC) [34]. GHC taxonomy is defined to provide a practical, transmissible and reproducible procedure for habitat monitoring and is highly relevant to the LCCS taxonomy, since they are both based on life forms and include similar attribute definitions. GHC classes are organized in five main categories, namely: i) urban (URB), ii) cultivated (CUL), iii) sparsely vegetated (SPV), iv) trees and shrubs (TRS), and v) herbaceous vegetation (HER). Various classes belong in each category, based on life or non-life forms present in a studied area element, leaf properties, height of canopy, and other properties, comprising a total of around 160 classes [346]. The classes were initially defined to link in-situ and remote sensing observations, thus facilitating their extraction through data derived from satellite or airborne sensors. The main categories and the principal classes of each are reported in Table 4.3.

4.2.2. Le Cesine, Italy

The first study area where the methods of the present and the following chapters are applied is Le Cesine site, centred at latitude 40°21'N and lon-

Table 4.3.: The 5 main GHC categories and the principal classes.

Main Category	Classes
Urban / Constructed (URB)	Artificial (ART)
	Non-vegetated (NON)
	Vegetables (VEG)
	Woody (TRE)
	Herbaceous (GRA)
Cultivated (CUL)	Bare ground (SPA)
	Herbaceous crops (CRO)
	Woody crops (WOC)
Sparsely Vegetated (SPV)	Sea (SEA)
	Tidal (TID)
	Aquatic (AQU)
	Ice / snow (ICE)
	Bare rocks (ROC)
	Boulders (BOU)
	Stones (STO)
	Gravel (GRV)
	Sand (SAN)
	Earth (EAR)
Herbaceous (HER)	Submerged hydrophytes (SHY)
	Emergent hydrophytes (EHY)
	Helophytes (HEL)
	Leafy hemicryptophytes (LHE)
	Caespitose hemicryptophytes (CHE)
	Therophytes (THE)
	Geophytes (GEO)
	Cryptogams (CRY)
	Herbaceous chamaephytes (HCH)
Trees and Scrubs (TRS)	Dwarf chamaephytes (DCH)
	Shrubby chamaephytes (SCH)
	Low phanerophytes (LPH)
	Mid phanerophytes (MPH)
	Tall phanerophytes (TPH)
	Forest phanerophytes (FPH)
	Mega phanerophytes (GPH)

gitude 18°20'35"E, and located in Apulia region, south eastern Italy (Fig. 4.2). It is one of the oldest protected sites in the region, belonging to the Natura 2000 network and covering an area of approximately 3.48 km². It consists of a variety of habitats within agricultural, semi-natural and natural areas, including two extended coastal lagoons, numerous channels, marshes and humid grasslands. Helophytic, halophilous and dry thero-phytic vegetation species alternate, creating interesting mosaics and includ-

ing species such as *Cladium mariscus*, *Pinus halepensis*, *Quercus ilex*, and *Erica forskalii*.

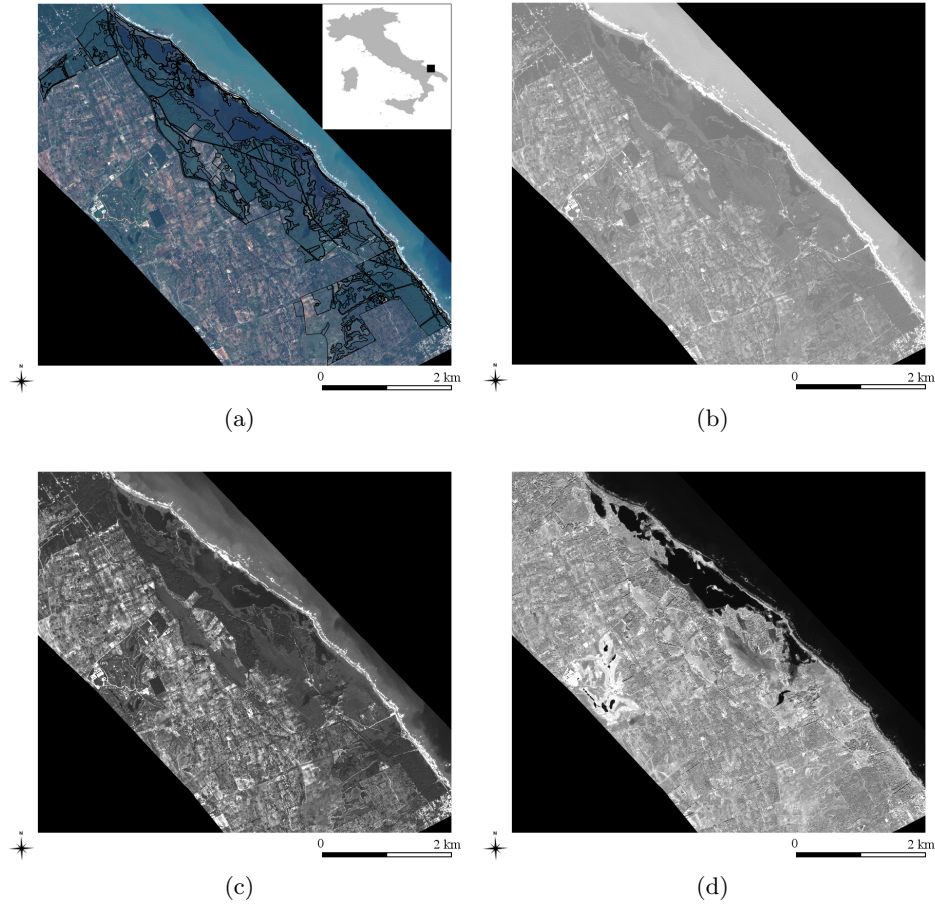


Figure 4.2.: Le Cesine study site, Apulia region, Italy. Worldview-2 image from October 2010 in (a) true colour, overlaid by the segment boundaries delineated in the LCCS map. In addition, the (b) Blue, (c) Red, and (d) NIR-1 bands are drawn.

The principal data used in the classification process include a LCCS map (Fig. B.7 in Appendix B), validated through field campaigns in 2008–2009, and two multispectral optical satellite images with 2 m spatial resolution: a QuickBird (QB) captured in June 2009 and a Worldview-2 (WV-2) in October 2010, both georeferenced, co-registered, orthorectified, and calibrated in Top-of-Atmosphere (TOA) reflectance values. The QB image includes four optical bands, namely blue (450–520 nm), green (520–600 nm), red (630–

690 nm), and near-infrared (NIR) (760–900 nm), whereas the WV-2 image has 8 bands, as detailed in Section 3.2. Fig. 4.2 shows the WV-2 image in true colour, as well as the blue, red, and NIR-1 bands, sensitive to water and vegetation and used in the extraction of relevant spectral indices, as shown in Section 4.3.1. In addition, an Object Height Model (OHM), derived from lidar data from spring 2009, is used as primary source of vegetation height information.

4.2.3. Lago Salso, Italy

The second study area, Lago Salso, is a protected Natura 2000 site centred at latitude $41^{\circ}33'36''\text{N}$ and longitude $15^{\circ}52'20''\text{E}$, and similarly to Le Cesine, is located in the Apulia region, south eastern Italy (Fig. 4.3). It lies in the Gargano National Park at a distance of around 300 km from Le Cesine. A wetland occupies the main part of Lago Salso, characterized by both brackish water and freshwater. In the northern part, the area is adjacent to salt marshes, with shrub and halophilous annual vegetation and salty soils.

Similar data to the ones of Le Cesine are available for Lago Salso study site. The satellite data include two WorldView-2 images from different seasons, acquired in June 2010 and February 2011. As in the previous case, both images were georeferenced, co-registered, orthorectified, and calibrated in TOA reflectance values. Fig. 4.3 shows the WV-2 image from June 2010 in true colour, as well as the blue, red, and NIR-1 bands. A LCCS map validated through field campaigns in 2011–2012 is used as basis for the habitat classification (Fig. B.10 in Appendix B). An OHM was also available from lidar acquisitions during spring 2009.

4.3. Feature extraction

4.3.1. Data features

An object-based approach was followed for the classification, considering as objects the patches delineated in the LCCS maps. The rationale behind this selection over a pixel-based approach is multiple. Pixel-based approaches have proven inappropriate for habitat classification for images of very high spatial resolution—as the ones in this study—because of the large spectral variabilities within habitats which create inaccurate classifications and salt

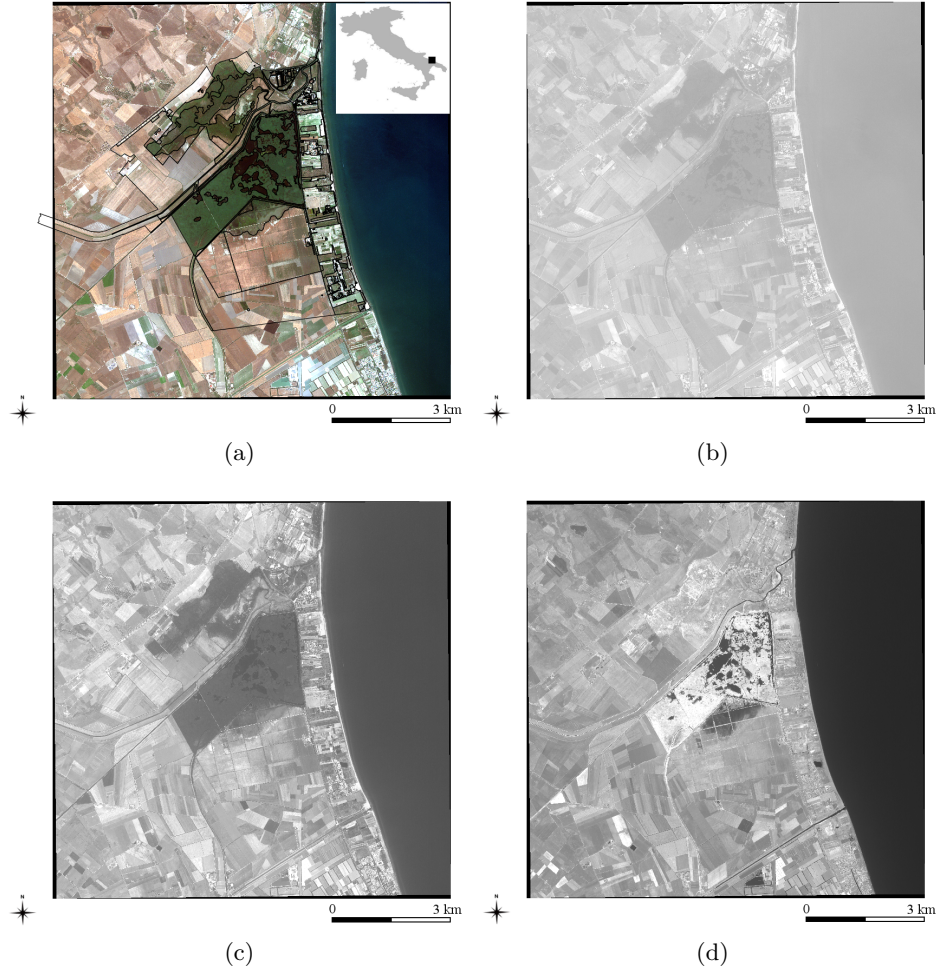


Figure 4.3.: Lago Salso study site, Apulia region, Italy. Worldview-2 image from 2010 in true colour, overlaid by the segment boundaries delineated in the LCCS map. In addition, the (b) Blue, (c) Red, and (d) NIR-1 bands are drawn.

and pepper effects [47, 90, 91]. Furthermore, pixel-based approaches prohibit the extraction of spatial and topological features, such as object area or adjacency to other objects of specific class, that are valuable for certain classification tasks, as in the present study. Finally, an object-based approach is chosen to allow direct comparison of the proposed classifiers with the state-of-the-art habitat classifiers of interest, i.e. [52, 53]. A number of features were extracted for each object from the available data, based on expert knowledge, as described in [53]. The features included spectral,

morphological, and topological characteristics. In addition, features using the OHM extracted from the lidar data were calculated. In particular, the extracted features included:

Spectral features:

- (D1) A greenness index (GI), as index for the presence of vegetation, was calculated in a per pixel basis and then averaged for each object as

$$GI = \frac{r_{green}}{r_{red}}, \quad (4.1)$$

where r_{green} and r_{red} indicate the reflectances in green and red band, respectively.

- (D2) A water index (WI), as index for the presence of water, was similarly calculated as

$$WI = \frac{r_{blue}}{r_{NIR}}, \quad (4.2)$$

where r_{blue} and r_{NIR} indicate the reflectances in blue and NIR band, respectively.

- (D3) The percentage of vegetated pixels within an object. A vegetation mask was extracted by thresholding GI feature (D1). Pixels with $D1 > 1$ were considered as vegetation, whereas with $D1 \leq 1$ as non-vegetated ones.

For Le Cesine site, based on expert knowledge, the WorldView-2 October image was used for the extraction of GI and WI. Since image from this season was not available for Lago Salso, these features were extracted from both June and February available images, and alternately used and evaluated. NIR1 band reflectances were used for the extraction of WI.

Morphological features:

- (D4) Object area, calculated as the number of pixels of each object.
- (D5) The ratio of object perimeter to the perimeter of the smallest rectangle enclosing the object, as a measure of how ragged an object is.

Topological features:

- (D6) Percentage of object pixels adjacent to artificial or non vegetated urban areas, i.e. LCCS class B15.
- (D7) Percentage of object pixels adjacent to submerged hydrophytes (SHY). This rule was originally defined to be executed as part of the sequential rules of the rule-based classification, considering the habitat SHY classes already extracted. Since the present approach requires such information a priori, the membership of each pixel to the SHY class is initially approximated as (i) $1/n$, where n is the number of all possible classes of a pixel, in case SHY is among the possible classes based on its LCCS class and the theoretical mapping in [51], and (ii) 0, in case SHY is not one of the possible classes. Then, the feature value is calculated as

$$D7 = \frac{\sum_{i=1}^N m_{SHY}(i)}{N} 100, \quad (4.3)$$

where $m_{SHY}(i)$ stands for the membership of pixel i in class SHY and N for the total number of pixels (of different objects) adjacent to the object of interest.

Lidar features:

- (D8) Percentage of pixels higher than 0.6 m within an object.
- (D9) Mean vegetation height, using the mask derived with feature (D1).

As surrogate features, to substitute lidar data in cases where the latter are unavailable due to cost or accessibility restrictions, texture analysis measures, as discussed in Chapter 3, are also extracted for each object. To have a common framework for comparison between the two study sites, only the features from the common date of acquisition, i.e. June, are calculated. In addition, for testing purposes, the mean band reflectance values of all images are also extracted for each object, per image band.

4.3.2. LCCS class features

The LCCS class name and attributes of each object, derived from the LCCS map, were originally expressed as LCCS codes [33], (i.e. character/string

variables). In order to facilitate their use by a supervised classifier in a straightforward manner together with the previously extracted features, an approach to generate numerical features from the LCCS codes is proposed. A number of 21 features are defined, presented in detail in Table 4.4, each one representing a specific object property. In particular, one feature (feature L1) is defined to represent the main LCCS class, whereas the rest ones to describe the attributes related to each class, such as life form, leaf phenology, or canopy height (codes are defined in [33]). A numerical value is assigned to each potential code of each feature.

Table 4.4.: Features representing the LCCS class names and attributes and the assigned numerical values.

Class	Feature	Type	Nominal value: property (LCCS code)
all	L1	LCCS class	1: cultiv. & managed (A11); 2: (semi-)nat. terr. veg (A12); 3: cult. aquat. (A23); 4: (semi-)nat. aquat. veg (A24); 5: artif. ter. (B15); 6: bare areas (B16); 7: art. waterbodies (B27); 8: inland waterbodies (B28)
A11	L2	life form	10: trees (A1); 20: shrubs (A2); 30: herbaceous (A3); 31: graminoids (A4); 32: non-graminoids (A5); 40: urban veg. (A6); 41: parks (A11); 42: parkland (A12); 43: lawns (A13)
	L3	leaf type	1: broadleaved (A7); 2: needleleaved (A8)
	L4	leaf phenology	1: evergreen (A9); 2: deciduous (A10)
	L5	cultivation type	1: plantation (W7); 2: orchard (W8)
A12	L6	life form	10: woody (A1); 11: trees (A3); 12: shrubs (A4); 20: herbaceous (A2); 21: forbs (A5); 22: graminoids (A6); 30: lichens/mosses (A7); 31: lichens (A8); 32: mosses (A9)
	L7	height (m)	100: >3 (B2); 110: >14 (B5); 120: 7–14 (B6); 130: 3–7 (B7); 200: 0.3–5 (B3); 210: 0.5–5 (B14); 211: 2–5 (B8); 212: 0.5–2 (B9); 220: <0.5 (B10); 300: 0.03–3 (B4); 310: 0.3–3 (B15); 311: 0.8–3 (B11); 312: 0.3–0.8 (B12); 320: 0.03–0.3 (B13)
	L8	leaf type	1: broadleaved (D1); 2: needleleaved (D2); 3: aphyllous (D3)
	L9	leaf phenology	1: evergreen (E1); 2: deciduous (E2)
	L10	plant cycle	1: annual (E6); 2: perennial (E7)
A23	L11	life form	1: graminoids (A1); 2: non-graminoids (A2); 3: woody (A3)
A24	L12	life form	10: woody (A1); 11: trees (A3); 12: shrubs (A4); 20: herbaceous (A2); 21: forbs (A5); 22: graminoids (A6); 30: lichens/mosses (A7); 31: lichens (A10); 32: mosses (A11)
	L13	mobility	1: rooted (A8); 2: free floating (A9)

Continued on next page...

Table 4.4 – continued

Class	Feature	Type	Nominal value: property (LCCS code)
	L14	height (m)	100 : >3 (B2); 110 : >14 (B5); 120 : 7–14 (B6); 130 : 3–7 (B7); 200 : 0.3–5 (B3); 210 : 0.5–5 (B14); 211 : 2–5 (B8); 212 : 0.5–2 (B9); 220 : <0.5 (B10); 300 : 0.03–3 (B4); 310 : 0.3–3 (B15); 311 : 0.8–3 (B11); 312 : 0.3–0.8 (B12); 320 : 0.03–0.3 (B13)
B15	L15	surface aspect	1000 : built up (A1); 1100 : linear (A3); 1110 : roads (A7); 1111 : paved (A8); 1112 : unpaved (A9); 1120 : railways (A10); 1130 : comm. lines/pipelines (A11); 1200 : non-linear (A4); 1210 : industrial area (A12); 1220 : urban areas (A13); 2000 : non built up (A2); 2100 : waste dump (A5); 2200 : extraction sites (A6)
	L16	density	1 : high (A14); 2 : medium (A15); 3 : low (A16); 4 : scattered (A17)
B16	L17	surface aspect	100 : consolidated (A1); 110 : bare rock and coarse fragments (A3); 111 : bare rock (A7); 112 : gravel/stones/boulders (A8); 120 : hardpans (A4); 121 : ironpan/laterite (A9); 122 : petrocalcic (A10); 123 : petrogypsic (A11); 200 : unconsolidated (A2)
	L18	coarse fragments	1 : gravel (A14); 2 : stones (A15); 3 : boulders (A16)
	L19	composition	1 : stony (5–40%) (A12); 2 : very stony (40–80%) (A13)
B27	L20	physical status	10 : water (A1); 11 : flowing water (A4); 12 : standing water (A5); 20 : snow (A2); 30 : ice (A3); 31 : moving ice (A6); 32 : stationary ice (A7)
B28	L21	physical status	10 : water (A1); 11 : flowing water (A4); 12 : standing water (A5); 20 : snow (A2); 30 : ice (A3); 31 : moving ice (A6); 32 : stationary ice (A7)

In order to express inter- and intra-class variabilities, in consistency with the LCCS definitions [33], a hierarchical approach in value assignment is followed. A number of digits equal to the number of hierarchical layers are used for each feature, with the first digits representing the higher layers and the last the lowest ones. Therefore, small distance numerical values are assigned to codes expressing similar properties—belonging in the same higher layers, and vice versa. As an indicative example, values ‘1111’ and ‘1112’ were selected to describe paved and unpaved roads (feature L15), respectively, both belonging in the ‘built up’, ‘linear’, and ‘roads’ higher hierarchical layers, whereas the very distinct values ‘1000’ and ‘2000’ are assigned to describe the more dissimilar categories of ‘built up’ and ‘non built’ up areas, respectively. The value ‘0’ is assigned by default to the features non-applicable for a specific object, i.e. features characterizing different LCCS classes to the one of the object (e.g. features L6–L21 for

objects of class A11). Following this approach, LCCS class names and attributes can be directly introduced in a supervised classifier as ordinary interval-scaled features.

It can be noted that this approach could be ineffective in discriminating among classes of different layers, yet with very proximal values, e.g. ‘1999’ and ‘2000’. However, this case is not practically possible for the particular application, since the highest possible value of any secondary layer is ‘3’, making it always closer to the core value of the hierarchical layer it belongs (Table 4.4). Although not directly applicable in applications where these conditions do not hold, the specific method was selected here due to its simplicity and effectiveness, as shown in the next section.

4.4. Results and discussion

The efficiency of the selected features in discriminating among the potential habitat classes was evaluated through a number of different supervised classifiers. The same classifiers used in the experiments described in Chapter 3 were employed, namely J48 and REPTree (RT) tree classifiers, random forests (RF), bagging with J48 (B-J48) and REPTree (B-RT), AdaBoost.M1 with J48 (A-J48) and REPTree (A-RT) as basis, and two implementations of SVM with linear kernel, with (SVM-M) and without (SVM) fitting logistic models to the output. In addition, two artificial neural network classifiers with (ANN-D) and without (ANN) decay in the learning rate were used [316]. In all experiments, 10-fold cross validation was used to evaluate the classification results.

4.4.1. Le Cesine

A set of 250 objects was available for the evaluation of the method for Le Cesine, based on the validation points extracted through a field campaign (Fig. B.7). The objects belong in 14 different GHC classes, including all GHC main categories apart from the sparsely vegetated (SPV) one. A series of experiments were conducted, involving a different number of features. In particular, the first set (‘Main’) included the features D1–D7, as described in Section 4.3.1 and used in [52]. A second set (‘Main + lidar’) involved the inclusion of the two lidar-derived features D8 and D9, also used in

[52]. In order to evaluate the potential of texture analysis in surrogating lidar information, texture features were also added to the ‘Main’ set. In particular, the best performing individual sets of the June image in Section 3.5.2, namely LH5 in the blue band and LTBP4 in the NIR band were included separately (‘Main + LH5’ and ‘Main + LTBP4’ sets) and together (‘Main + LH5 + LTBP4’). In addition, a set with all June QuickBird image derived texture features was created (‘Main + QB texture’), June image being preferred to allow compatibility with experiments on Lago Salso site described below. For the few validation points falling outside the QuickBird image boundaries, default texture values of 0 were assigned to the respective objects.

Table 4.5 shows the classification accuracies achieved by applying the selected supervised classifiers to the evaluated feature sets. Among the employed classifiers, the Bagging ensemble using J48 trees as base classifier, showed the highest performance consistently for all sets, with other tree classifiers, namely B-RT, A-J48, and RF, following. The feature set employing lidar information provided the highest accuracies, both in average for all classifiers and in particular with B-J48, equal to 86%. Whereas the ‘Main’ feature set provided accuracies up to 81.2%, the inclusion of the LH5 texture feature further increased the performance up to 81.6%. Furthermore, the feature set including all texture features from the June image provided accuracies up to 82.4%. The latter two results give an indication of the discriminatory potential of the derived texture features, as surrogates of lidar data. The kappa values of the reported classifications ranged from 0.544 to 0.835. Some further features have been experimentally added to the ‘Main + lidar’ sets, including the mean reflectance at each band and the object perimeter, causing no increase or even decreasing the classifier performance.

The proposed approach seems to clearly outperform the results from the crisp knowledge-based classification framework described by Adamo *et al.* [52, 53], where accuracies of 69.9% are reported. The latter approach appears to discriminate a larger number of categories by considering four separate classes for each tree and shrub (TRS) initial class, based on four leaf phenological categories, i.e. (i) deciduous (DEC), (ii) evergreen (EVR), (iii) non-leafy evergreen (NLE), and (iv) coniferous evergreen (CON/EVR). However, this further categorization is inherited by and solely attributed

Table 4.5.: Classification accuracies for combinations of datasets and feature sets in Le Cesine. The total number of features of each set is written in parentheses. The best results from each feature set are highlighted.

	Main (28)	Main + lidar (30)	Main + LH5 blue (29)	Main + LTBP4 NIR (29)	Main + LH5 + LTBP4 (30)	Main + QB texture (124)	Average
J48	75.6	83.6	75.2	75.2	74.8	78.8	77.2
RT	73.2	80.0	75.2	73.2	74.4	70.4	74.4
RF	80.8	81.6	78.4	80.0	78.8	76.4	79.3
A-RT	76.8	82.8	76.0	76.8	75.6	73.2	76.9
A-J48	79.2	84.0	78.0	78.0	77.2	81.2	79.6
B-RT	80.0	84.4	79.2	78.8	78.0	80.4	80.1
B-J48	81.2	86.0	81.6	80.8	80.0	82.4	82.0
SVM	72.4	76.0	74.8	74.0	74.0	75.6	74.5
SVM-M	79.2	82.4	79.6	80.4	78.4	72.0	78.7
ANN	73.6	78.4	72.4	72.4	76.0	74.0	74.5
ANN-D	63.2	63.6	62.8	63.2	63.2	68.4	64.1
Average	75.9	80.3	75.7	75.7	75.5	75.7	76.5

to the object LCCS class name, and applied as a post-classification step. Thus, considering merging of the phenological classes in [52, 53] would result in a similar number of final GHC classes to the ones in the present study with no significant change in the reported accuracy of 69.9%, since misclassifications among the different classes of TRS (as well as the rest of the classes) are expected to remain. Therefore, comparison of the present study with [52, 53] can be considered feasible, since similar conditions and data are applied. The current approach seems to achieve notably higher classification accuracies, in a more automated manner.

The computational complexity of the supervised classifiers is defined as discussed in Section 3.5.1.B. In particular, REPTree showed the lowest computational time, whereas the ANN classifiers the highest, the latter being more sensitive to increase of the feature space size than the rest of the classifiers. In any case, the practical computational time for the training of all supervised classifiers, ranging from seconds to a few minutes, is significantly lower than the trial-and-error manual extraction or rules and thresholds by experts in [52, 53], requiring laborious work of several days or even months.

In Table 4.6, the confusion matrix for the best classification result, with the ‘Main + lidar’ set, is shown. As noticed, perfect discrimination has

been achieved for certain classes for both producer’s and user’s accuracies, namely for cultivated herbaceous (CRO) and woody (WOC) crops, caespitose hemicryptophytes (CHE), and therophytes (THE) or geophytes (GEO). The latter classes were not possible to be discriminated and are provided as a complex class (‘THE or GEO’) in the validated object set. Most classes reached PA and UA values of over 75%, whereas the lowest values were due to the misclassification of the one only urban non-vegetated (NON) object as urban artificial (ART). In general, kappa coefficient of 0.835 was achieved, indicating an ‘almost perfect’ classification, according to [340].

4.4.2. Lago Salso

For Lago Salso, a less numerous set of 59 objects was validated through field campaign and used in the classification process. However, the set included 15 GHC classes from all main GHC categories. The same feature sets as for Le Cesine site were extracted (Section 4.4.1), with the results shown in Table 4.7. The GI (D1) and WI (D2) features were calculated from the October image in Le Cesine, but such image was not available for Lago Salso. Thus, both June and February images were used instead, with the feature sets including the D1 and D2 features from the former image consistently outperforming the ones from the latter; the former sets are shown in Table 4.7. As previously, B-J48 classifier outperformed the rest ones in most experiments. The performance of the ANN classifier with decay in the learning rate was notably low, indicating that the generic parameterization used was not appropriate and a more targeted one to the specific problem might be required.

As in Le Cesine study area, the proposed approach seems to outperform the accuracies of 66.1% reported in [53]. It is noteworthy that the best classification accuracy (OA 88.1%) was achieved by the feature set employing all texture features equivalent to the QuickBird image (‘Main + QB texture’), namely from the blue, green, red, and NIR1 bands of the June WorldView-2 image of Lago Salso, outperforming the set including the lidar features. In fact, the latter set showed the lowest average performance of all sets, indicating that the lidar feature values provided little discriminatory information. Besides the texture features common to the QuickBird bands

Table 4.6.: Confusion matrix from classification of the ‘Main + lidar’ feature set with the Bagging classifier with J48 in Le Cesium. The rows represent the ground truth data, whereas the columns the classified objects.

[illegible]

of Le Cesine, the features from the rest of the WorldView-2 bands were included, although in most cases providing inferior results. Finally, it can be noticed that same classification accuracies are achieved for different features with a specific classifier. This seems to be attributed, up to a degree, to the small size of objects that restricts the training combinations, and also to the ‘dominance’ of certain features compared to others. For instance, features L1, L2, L5, L6, L10, L12, L16, and D2 are the only ones selected by the J48 tree classifier from all feature sets in the five first columns of Table 4.7; choosing the same features and forming the same binary decisions for all these sets result to the same classification accuracies.

Table 4.7.: Classification accuracies for combinations of datasets and feature sets in Lago Salso. The total number of features of each set is written in parentheses. The best accuracies for each feature set are highlighted.

	Main (28)	Main + lidar (30)	Main + LH5 blue (29)	Main + LTBP4 NIR (29)	Main + LH5 + LTBP4 (30)	Main + QB texture (124)	Average
J48	83.1	83.1	83.1	83.1	83.1	86.4	83.6
RT	66.1	62.7	66.1	62.7	62.7	61.0	63.6
RF	81.4	78.0	78.0	76.3	81.4	71.2	77.7
A-RT	76.3	71.2	76.3	67.8	66.1	66.1	70.6
A-J48	83.1	83.1	83.1	83.1	83.1	86.4	83.6
B-RT	74.6	72.9	76.3	72.9	72.9	72.9	73.7
B-J48	86.4	86.4	86.4	86.4	86.4	88.1	86.7
SVM	67.8	62.7	62.7	69.4	66.1	76.3	67.5
SVM-M	72.9	72.9	72.9	78.0	78.0	71.2	74.3
ANN	74.6	69.5	78.0	72.9	74.6	78.0	74.6
ANN-D	17.0	17.0	17.0	17.0	17.0	37.3	20.3
Average	71.2	69.0	70.9	70.0	70.1	72.3	70.6

Table 4.8 draws the confusion matrix from the highest performing set including the texture features from the equivalent bands to the QuickBird image, ‘Main + QB texture’, with the B-J48 classifier. ‘LHE/CHE’ denotes combination of leafy (LHE) and caespitose (CHE) cryptophytes in the same object area. Apart from the undetected or misclassified urban herbaceous (GRA), LHE/CHE, and CHE objects, most of the other classes have been identified with perfect precision and recall accuracies, all of them being 60% and over, reaching at the same time a high final kappa coefficient value of 0.869.

It is notable that, although an inductive example-driven learning method with no a priori expert knowledge is applied, most misclassifications are between similar objects of the same GHC main category. Examples include an urban herbaceous (GRA) object misclassified as urban woody (TRE), and incorrect classifications among the aquatic herbaceous classes of SHY, EHY, and HEL. However, despite the advantages of time and labour efficiency achieved by the approach, a limitation compared with a deductive learning framework may be spotted on the fact that non-realistic classifications may arise. As an instance, a herbaceous mixed leafy and caespitose hemicryptophytes (LHE/CHE) object has been erroneously classified as tall phanerophyte tree (TPH) of height 2–5 m (Table 4.8), although its LCCS related features (L1, L6, L7) indicate herbaceous vegetation 0.3–0.8 m high. Prior knowledge embedded to the classifier could be beneficial to avoid such inconsistencies.

4.4.3. Transferability from Le Cesine to Lago Salso

In order to test the transferability of the proposed approach from one study area to the other, as an indication of its generalization performance, classifier models created in Le Cesine were evaluated in Lago Salso site. As noticeable from the previous experiments, 14 GHC classes were present in Le Cesine and 15 in Lago Salso, out of which 11 classes were present in both sites, namely ART, NON, CRO, WOC, SHY, EHY, HEL, CHE, THE, LPH, TPH (Table 4.3); this indicates that four classes in Lago Salso (i.e. TRE, GRA, SAN, LHE/CHE) could not be learned by the classifier model, whereas three classes only met in Le Cesine (i.e. SCH, MPH, FPH) could introduce misleading bias to the model, since they were not practically useful for the classification of the testing site. 250 and 59 objects were used from Le Cesine and Lago Salso, respectively. Each feature set discussed in the previous sections was used from Le Cesine to train the classifiers, whereas the respective from Lago Salso to test them.

The results from the classification are drawn in Table 4.9. As shown, accuracies of almost up to 73% were achieved by various feature sets. As expected, the performance of the classifiers dropped significantly compared with the case where they were trained using data from Lago Salso. How-

Table 4.8.: Confusion matrix from classification of the ‘Main + QB texture’ feature set with the Bagging classifier with J48 in Lago Salso. The rows represent the ground truth data, whereas the columns the classified objects.

[illegible]

Table 4.9.: Classification accuracies (%) applying classifiers trained with data from Le Cesine to Lago Salso, for combinations of datasets and feature sets. The total number of features of each set is written in parentheses. The best accuracies for each feature set are highlighted.

	Main (28)	Main + lidar (30)	Main + LH5 blue (29)	Main + LTBP4 NIR (29)	Main + LH5 + LTBP4 (30)	Main + QB texture (124)	Average
J48	67.8	71.2	67.8	67.8	67.8	69.5	68.6
RT	44.1	47.5	44.1	44.1	44.1	44.1	44.6
RF	62.7	66.1	66.4	66.1	64.4	30.5	59
A-RT	69.5	72.9	72.9	72.9	72.9	69.5	71.8
A-J48	67.8	69.5	67.8	67.8	69.5	62.7	67.5
B-RT	62.7	64.4	61.0	62.7	61.0	59.3	61.9
B-J48	66.1	69.5	66.1	66.1	66.1	62.7	66.1
SVM	47.5	49.2	47.5	47.5	45.8	35.6	45.5
SVM-M	59.3	64.4	61.0	61.0	61.0	39.0	57.6
ANN	30.5	37.3	30.5	27.1	35.6	40.7	33.6
ANN-D	15.3	15.3	15.3	15.3	15.3	13.6	15.0
Average	53.9	57.0	54.4	54.4	54.9	47.9	53.7

ever, the results were still superior than the 66.1% accuracy achieved by the respective rule-based classifier in [53], encouraging the applicability of the approach to different sites.

The AdaBoost.M1 classifier using REPTree as basis consistently outperformed the other classifiers in all feature sets. The inherent ability of boosting to improve weak classifiers was evidenced in this case, with AdaBoost.M1 with REPTree outperforming its counterpart with J48, whereas J48 showed significantly higher performance than REPTree as individual classifier. In fact, it is noteworthy that the simple J48 tree classifier was the second highest performing among the selected ones, outperforming more complicated classifiers. Up to a certain degree, that may be due to the scarce testing set, with only three of the classified classes having more than five objects, and the inconsistencies in classes present between the two sites, that limited the performance of ensemble and other complicated classifiers. As a note, feature sets using the GI (D1) and WI (D2) features extracted from the June image of Lago Salso are shown in Table 4.9, since they lead to significantly higher performance than the respective features from the February image.

Among the different feature sets, the ones with lidar information (‘Main + lidar’) and the ones with one or two added texture features (‘Main +

LH5 blue’, ‘Main + LTBP4 NIR’, ‘Main + LH5 + LTBP4’) resulted in the highest classification accuracies, under the AdaBoost.M1. Table 4.10 draws the confusion matrix resulting by the use of the main feature set with the addition of the local binary pattern based feature (‘Main + LTBP4 NIR’ dataset) with AdaBoost.M1 using REPTree, as the best performing set with the minimum number of features—same with the ‘Main + LH5 blue set’). In this case, the addition of a single feature from texture analysis resulted in equal performance with the addition of two lidar-derived features. Table 4.10 shows that the most populated classes, i.e. CRO, SHY, and LPH, with seven, seven, and ten objects, respectively, were perfectly identified (100% PA). This encourages the use of the classifier in case of a more populated testing site with multiple objects in each class. It is also encouraging that no object was erroneously classified to any of the classes present only at the training site (SCH, MPH, FPH). On the contrary, as expected, none of the objects belonging to a class that was not included to the training set (TRE, GRA, SAN, LHE/CHE) was correctly classified. However, it can be noticed that if the seven objects from these four classes are excluded from the classification, the resulting overall accuracy raises up to 82.7%, further supporting the promising nature of the developed classification framework.

4.5. Conclusions

A supervised learning scheme has been proposed in this chapter to convert land cover to habitat classes. A number of features proposed by expert ecologists in previous studies [52, 53] have been calculated from the available satellite imagery, lidar data, and object morphology. Furthermore, an approach to represent LCCS classes and attributes as numerical interval-scaled variables has been proposed, to allow their direct use as input in supervised classifiers. This representation proved capable in describing inter- and intra-class variabilities by providing features highly selected in the binary decisions of the tree classifiers. A number of supervised classifiers have been evaluated, including decision tree-based ones, support vector machines, and artificial neural networks; an implementation of Bagging trees with J48 as base classifier provided the best overall accuracies, with single J48 being proven a good trade-off between complexity and accuracy. Texture features

Table 4.10.: Confusion matrix from classification of the ‘Main + LTBP4 NIR’ feature set with the AdaBoost.M1 classifier with REPTree in Lago Salso, using the respective feature set from Le Cesine for training. The rows represent the ground truth data, whereas the columns the classified objects.

[illegible]

selected based on the outcomes of Chapter 3 have also been evaluated as surrogates of lidar features, and offered useful class discriminatory information in certain cases.

The proposed approach was tested in two individual sites with 10-fold cross-validation, and reached higher accuracies than the rule-based classification schemes in [52, 53]. Furthermore, the generalization performance of the approach was evaluated, using the extracted features from one study site to train the classifiers and testing the resulting model with the features from the other one. Accuracies outperforming the one from the baseline state-of-the-art classifier [53], despite inconsistencies in GHC classes between the training and testing sites, indicate the effectiveness of the approach as accurate alternative of labour and time demanding expert rule-based approaches.

5. Habitat classification with evidential reasoning and fuzzy logic

5.1. Dempster–Shafer theory for uncertainty handling

Whereas the previous chapter focused on developing a less labour and time consuming alternative to the GHC expert rule-based classification methodology discussed in [52, 53], the present chapter proposes an approach to handle uncertainty caused by missing or noise afflicted data, or vague classification rules provided by the experts. Uncertainty is an unavoidable factor in real world studies [347], including remote sensing applications [348, 349]. Various crisp rule-based habitat classification schemes proposed in the literature [46–48, 345], including the ones of particular interest in this study [52, 53], do not explicitly account for uncertainty; thus, they may prove inadequate in handling commonly met problems in remote sensing, such as data noise affliction from different stages of acquisition and pre-processing, unavailable data sources, or vague information. A classification framework based on evidential reasoning, in particular on Dempster–Shafer (DS) theory [54, 55], and fuzzy logic is proposed in this chapter to tackle such limitations.

DS theory, a mathematical theory of evidence, is broadly used for information fusion, and handling of uncertainty and missing data [350, 351]. It has been used in various fields as a means to combine results generated from multiple classifiers, even producing different classes, or data from multiple sources, and has been usually combined with fuzzy sets [352–355]. In remote sensing, DS theory has been successfully employed in a number of applications, including multiple image segmentation [356], road extrac-

tion [357], sea breeze front detection [358], building detection [359–361], and automatic target recognition [362].

In landscape monitoring, DS theory, mostly with fuzzy sets, has been used to combine sensor data or contextual information to improve mapping of LC classes, habitats, or plant functional types [363–367]. DS theory has been found to allow larger flexibility in the formulation of informative classes [368] than other schemes, whereas classifiers employing it have outperformed commonly used maximum likelihood [369], ISODATA [370], and k-nearest neighbour [338] classifiers in various applications and landscapes. In one of the few studies applying DS theory in habitat mapping, Franklin *et al.* [366] demonstrated the higher ability of the theory to incorporate multiple sources of information, compared with a conventional maximum likelihood classifier, resulting in significantly higher accuracy in discriminating habitat classes. The use of DS theory in conversion of LC maps to habitats with remote sensing data has not yet been evaluated.

The contribution of this chapter lies in the proposal of a robust methodology based on DS theory and incorporating fuzzy logic for habitat classification. The methodology builds on pre-existing LC maps, presented in the previous chapter, and converts them to GHC maps, incorporating domain expert rules. Different fuzzification methods are proposed and introduced to the DS theory framework to deal with inaccurate rules provided by experts or noise afflicted data. The flexibility of the framework in handling composite classes when adequate information for the discrimination of single classes is missing is studied. Thorough experimentation on final class selection is conducted and decision making trade-offs are discussed. Finally, the rule set designed for one site is applied to the other in order to test the transferability of the approach. Comparisons with the respective crisp classification implementations are made to evaluate the potential advantages of the proposed approach. Table 5.1 summarizes the statement of the problem being addressed in this chapter.

Table 5.1.: Problem statement of Chapter 5.

- **Objective:** Habitat classification of landscape objects through rule-based classifiers based on Dempster–Shafer theory and fuzzy sets, to handle uncertainty from missing information, inaccurate rules, and noise. Evaluation of method transferability to different sites. Comparison with state-of-the-art approach in [52, 53].
- **Input:** (i) Very high resolution multispectral satellite images from two study areas; (ii) land cover map of the area to delineate objects and provide LCCS class features assisting habitat classification; (iii) Canopy Height Model from lidar data.
- **Methodology:** (i) Extraction of spectral, morphological, topological, and lidar features, for classification; (ii) use of theoretical [51] and fine-tuned [52, 53] expert rules for classification, and adaptation to express uncertainty in their outcome; (iii) design of rule-based classifiers incorporating Dempster–Shafer theory principles and fuzzy sets; (iv) adaptation to return multiple classes in case little support in single ones is provided; (v) evaluation of different class selection criteria; (vi) fusion of classifiers.
- **Output:** Classification of study areas in GHC habitat classes, (i) for the area which the rules are developed for, (ii) for a second area to test the method transferability.
- **Evaluation measures:** Use of different interpretations of classification accuracy, as far as multiple classes are concerned; (i) interpretation tolerant to multiple classes; (ii) interpretation favouring single classes; (iii) averaging interpretation; (iv) interpretation of normalized difference.

5.2. Methods

5.2.1. Dempster–Shafer theory principles

A. Basic concepts

DS theory, introduced by Dempster [54] and Shafer [55], is a mathematical theory of evidence, considered as a generalised form of the Bayesian theory of subjective probability. It is popular in rule-based expert systems, mainly because of its ability to handle uncertainty, lack of information and vague rules leading to composite events [355].

To each individual event, or set of events, *belief* and *plausibility* values are assigned, defining a *belief interval*. Belief on an event expresses the degree of confidence that the event holds, based on supporting evidence. Its plausibility value reflects the highest confidence on an event if all missing information were to support its validity. The difference between the plau-

sibility and belief of a single or composite event expresses its uncertainty. When no uncertainty exists, plausibility and belief values coincide.

One of the principal concepts in DS theory is the basic probability assignment function, or mass function, m , describing the degree an event, A , from the set of all possible events, or *frame of discernment* Θ , is supported with evidence. A can be a single event or a set of two or more single events; m values assigned to the latter indicate lack of adequate evidence to discriminate the single events of the multiple event. Θ is defined as a finite and non-empty set that contains all possible values a certain variable (e.g. GHC class) can take, $\Theta = \{\theta_1, \dots, \theta_n\}$, where n is the total number of possible values of the variable. The set is collectively exhaustive and all its propositions are mutually exclusive, i.e. there is no more and no less than one true value at a time. Considering the power set 2^Θ , a set of all possible subsets of Θ , the basic probability assignment function is defined as $m : 2^\Theta \rightarrow [0, 1]$, where the following conditions hold:

1. $m(\emptyset) = 0$
2. $\sum_{A \subseteq \Theta} m(A) = 1$, for all $A \subseteq \Theta$.

$m(A)$ describes the degree the set A is supported with evidence. According to the terminology, the mass function assigned to the frame of discernment, $m(\Theta)$, represents the amount of belief not assigned to any other subset of Θ , i.e. the lack of information on specific propositions or sets of propositions of Θ . $m(\emptyset) = 0$ is a condition that arises naturally from the fact that there is always one proposition true. It is worth noticing that the mass function is defined on the power set 2^Θ . This allows mass function values to be assigned in sets of two or more propositions, when there is not enough information to distinguish among them, thus allowing multiple options in case of inadequate evidence.

The belief function, $bel : 2^\Theta \rightarrow [0, 1]$, of a set $A \subseteq \Theta$, is defined as the summation of the m values of all subsets of A , i.e.

$$bel(A) = \sum_{X \subseteq A} m(X), \quad \text{for all } A \subseteq \Theta. \quad (5.1)$$

$bel(A)$ is the total belief on set A and all its subsets X . The support on each subset of A is included in the belief value of A . Therefore, $bel(A)$ expresses

the confidence that at least one of the subsets of A is true.

Plausibility of event A is defined as

$$pls(A) \equiv 1 - bel(\overline{A}), \quad (5.2)$$

where \overline{A} stands for the complement set of A with regards to Θ . $pls(A)$ expresses how much the confidence that A is true would be if all missing evidence were in favour of A . In other words, plausibility expresses the maximum support that can potentially be assigned to the set A . Having in mind that $bel(A)$ expresses the belief in A based on the existing evidence, it can be inferred that the true probability of A lies in the interval $[bel(A), pls(A)]$, i.e. the belief interval. In the ideal case of no lack of information, i.e. no uncertainty, it is $bel(A) = pls(A)$.

Whereas in the Bayesian theory belief in one set A implies disbelief in its complement \overline{A} , thus no uncertainty is considered, in DS theory no such conjecture is necessarily true. Additionally, the DS approach provides the flexibility of assigning m values to composite events, in case not enough information is available for the discrimination of the constituting single events, and naturally update them, in case new information arises that supports single events. m values assigned to sets from different frames of discernment, e.g. values concerning different variables in a rule-based classifier, can be multiplied to assess the support in the combined event that all individual sets hold simultaneously.

B. Combination of evidence

One of the core elements of the DS evidential process is the combination of evidence, where information from different sources, e.g. data, expert opinions, or results from different classifiers, need to be fused. All evidence is expressed through the respective mass functions, which are appropriately combined. The events of these mass functions may refer to either the same or different frames of discernment, with different process being followed in each case.

Results from various classifiers deriving classes from a particular set, e.g. GHC classes in the case of the present study, is an example of events—i.e. the classes—belonging to the same frame of discernment—i.e. the GHC habitat set. When the evidence belongs to the same frame of discernment,

Θ , the *Dempster rule of combination* is applied to combine the mass functions of interest and lead to a new mass function whose events belong, as expected, to the same frame of discernment, Θ . If $m_i, i = 1, \dots, n$ are the n mass functions combined, the mass function value m of the event of interest A after the combination of evidence will be calculated as [55]

$$m(A) = \frac{\sum_{A_1 \cap A_2 \cap \dots \cap A_n = A} \prod_{i=1}^n m_i(A_i)}{1 - K}, \quad (5.3)$$

where $A_1 \cap A_2 \cap \dots \cap A_n = A$ represent all sets of events whose junction is the set A . $1 - K$ is a normalization factor used to reassure that the condition $\sum_{A \subseteq \Theta} m(A) = 1$, for all $A \subseteq \Theta$, holds and no mass function value is assigned to the empty set. K is equal to

$$K = \sum_{A_1 \cap A_2 \cap \dots \cap A_n = \emptyset} \prod_{i=1}^n m_i(A_i), \quad (5.4)$$

with $A_1 \cap A_2 \cap \dots \cap A_n = \emptyset$ standing for the sets whose junction is the empty set.

Values of various features, e.g. LCCS classes, greenness index, or object area in this study (Section 4.3), used as combined conditions of classification rules, are examples of evidence from different frames of discernment. In such cases, the resulting frame of discernment of the combination of evidence is the direct product of the initial frames of discernment. The mass function of the combination is the product of the combined mass functions. In case n mass functions, m_1, \dots, m_n , express the support in the events A_1, \dots, A_n belonging in the frames of discernment $\Theta_1, \dots, \Theta_n$, respectively, then the mass function m , expressing the support in the junction of these propositions, is calculated as

$$m(A_1 \cap A_2 \cap \dots \cap A_n) = \prod_{i=1}^n m_i(A_i), \quad (5.5)$$

whereas the new frame of discernment is $\Theta = \Theta_1 \times \Theta_2 \times \dots \times \Theta_n$.

C. Class selection

Concerning the final class selection, whereas in the Bayesian probability framework decisions are made according to the highest probability rule, in Dempster–Shafer theory decision making is customizable and not straightforward. At the end of the process, each potential single or composite event is accompanied with a belief and a plausibility value. The final classification decision may be made based on maximum belief, plausibility, or combination of the two. An additional consideration is related with the acceptable complexity of the selected event, i.e. whether a composite event with high belief consisting of a large number of non-distinguishable single classes is more preferable than a single class event with lower belief, and to what degree. The Dempster–Shafer theory permits flexibility in the final decision criteria after the extraction of belief intervals for all potential single or composite events, which is highly dependent on user preferences and the specific application.

5.2.2. Fuzzification methods

DS theory provides large flexibility in incorporating fuzzy logic in the classification process. Fuzzy sets have been extensively used to moderate the drawbacks of crisp classification approaches and counteract for inaccuracies in the process, caused mainly by noise afflicted data [371]. The rule-based classification task described in this study can be sensitive to inaccurate rules provided by the domain experts or noise introduced during data acquisition and processing. Furthermore, slight changes in rule thresholds, e.g. when applying the method in similar sites located in different areas, can, similarly, significantly decrease the accuracy achieved by a crisp classifier.

A number of linear fuzzification methods, some similar to ones used in previous studies [372,373], are proposed and evaluated, applied to the numerical features used for the classification. The numerical features for each object are the ones defined in Section 4.3.1, namely (i) greenness and (ii) water index; (iii) percentage of vegetated pixels in an object; (iv) object area and (v) ratio of object perimeter to the perimeter of the smallest rectangle enclosing the object; (vi) percentage of object pixels adjacent to artificial or non-vegetated urban areas and (vii) percentage of pixels adjacent to submerged hydrophytes (SHY); (viii) percentage of pixels higher than 0.6 m

within an object and (ix) mean vegetation height in an object. Within each fuzzification method, appropriate membership functions are defined to provide a confidence degree that a numerical feature value lies within the region set by the expert rule under consideration. Membership functions for a particular numerical feature are either defined by considering all thresholds included in the expert rules regarding the specific numerical feature and remain constant throughout the classification process, or defined individually for each rule checked.

For a specific numerical feature, the first proposed method, takes into consideration all n thresholds, t_i , $i = 1, \dots, n$, given by the experts in the rules involving the particular feature and splits the field of values of the feature in a respective number of regions. For instance, for mean height, the following thresholds are employed in the classification rules: $t_1 = 0.05$, $t_2 = 0.3$, $t_3 = 0.6$, $t_4 = 0.8$, $t_5 = 2$, $t_6 = 3$, $t_7 = 5$, and $t_8 = 40$ m. Thus, the following regions are formed for mean height feature: $(-\infty, 0.05)$, $[0.05, 0.3)$, $[0.3, 0.6)$, $[0.6, 0.8)$, $[0.8, 2)$, $[2, 3)$, $[3, 5)$, $[5, 40)$, and $[40, +\infty)$.

Then, membership functions are defined to represent the probability of a feature value to belong in the respective region. Membership functions $\mu_i(t)$, $\mu_{\bar{i}}(t)$, and $\mu_{i,j}(t)$ are defined to describe the membership of a value t to the regions $(-\infty, t_i]$, $[t_i, +\infty)$, and $[t_i, t_j]$, $t_i < t_j$. For instance, for the case of mean height feature, $\mu_1(t)$, $\mu_{\bar{1}}(t)$, and $\mu_{1,3}(t)$ represent the membership of a value t to regions $(-\infty, 0.05]$, $[0.05, +\infty)$, and $[0.05, 0.6]$, respectively. In general, $\mu_i(t)$ is defined as

$$\mu_i(t) = \begin{cases} 1 & \text{if } t \in (-\infty, t_i - s) \\ -\frac{1}{2s}(t - t_i) + \frac{1}{2} & \text{if } t \in [t_i - s, t_i + s) \\ 0 & \text{if } t \in [t_i + s, +\infty), \end{cases} \quad (5.6)$$

where $s \in \mathbb{R}$ represents a predefined value related to the slope of the membership functions. $\mu_{\bar{i}}(t)$ represents the membership to the complement region of $\mu_i(t)$, therefore is defined as $\mu_{\bar{i}}(t) = 1 - \mu_i(t)$. The membership to a closed region between two thresholds, t_i and t_j —not necessarily

consecutive—, is defined as

$$\mu_{i,j}(t) = \begin{cases} 0 & \text{if } t \in (-\infty, t_i - s) \\ \frac{1}{2s}(t - t_i) + \frac{1}{2} & \text{if } t \in [t_i - s, t_i + s) \\ 1 & \text{if } t \in [t_i + s, t_j - s) \\ -\frac{1}{2s}(t - t_j) + \frac{1}{2} & \text{if } t \in [t_j - s, t_j + s) \\ 0 & \text{if } t \in [t_j + s, +\infty). \end{cases} \quad (5.7)$$

The method is schematically depicted in Fig. 5.1a, where, functions (1), (2), (3), (4), and (5) represent the membership functions $\mu_1, \mu_{1,2}, \mu_{2,3}, \mu_{3,4}, \mu_4$, respectively. The functions are defined to satisfy two conditions:

1. A feature value t equal to a threshold value t_i has equal membership values to both regions $(-\infty, t_i]$ and $[t_i, +\infty)$, i.e. it is $\mu_i(t_i) = \mu_{\bar{i}}(t_i) = 0.5$; for instance, the membership values of an object with measured height value $t = 0.6$ m to regions $(-\infty, 0.6]$ and $[0.6, +\infty)$ are equal to 0.5, i.e. $\mu_3(0.6) = \mu_{\bar{3}}(0.6) = 0.5$.
2. A feature value t equal to the mean of two threshold values t_i and t_j has a membership value in the region $[t_i, t_j]$, $t_i < t_j$, equal to 1, i.e. $\mu_{i,j}((t_i + t_j)/2) = 1$. Following the previous example, the membership of an object with measured height value $t = 0.7$ m to the regions $[0.6, 0.8]$ is equal to 1, i.e. $\mu_{3,4}(0.7) = 1$.

Three versions of this method are considered: (i) The parameter s , defining the slope of the linear functions, is equal to half of the minimum distance between two consecutive thresholds, d_{min} ($d_{min} = \min(t_{i+1} - t_i), i = 1, \dots, n - 1$), for a specific feature, in order to avoid overlaps of the defined membership functions (F1); as an example, for the mean height feature, it is $d_{min} = t_4 - t_3 = 0.2$, thus, $s = 0.1$. (ii) s is set equal to half of the standard deviation, std , of the observed values of the specific feature considering all area elements, to link the membership functions with statistical characteristics of the feature (F2); for the mean height feature, the standard deviation of the measured values is $std = 2.2$, thus, $s = 1.1$, resulting in membership functions with less steep slope for this particular case. (iii) s equals the minimum value of the previous approaches, i.e. $s = \min(d_{min}, std)/2$ (F3); thus $s = 0.1$ for the height feature example. F1 and F3 methods are

defined to avoid overlapping memberships functions, in case where for two consecutive thresholds t_i and t_j it is $t_i + s > t_j - s$ (see (5.7)). In such cases, the parameter s in F2 method is decreased to $s = (t_j - t_i)/2$, for the specific membership function $\mu_{i,j}$, in order to continue satisfy conditions (1) and (2) (Fig. 5.1b, red line). As an example, for the region between the height thresholds $t_3 = 0.6$ and $t_4 = 0.8$, s reduces to $s = 0.1$, whereas for the region between $t_7 = 5$ and $t_8 = 40$, it remains as $s = std/2 = 1.1$.

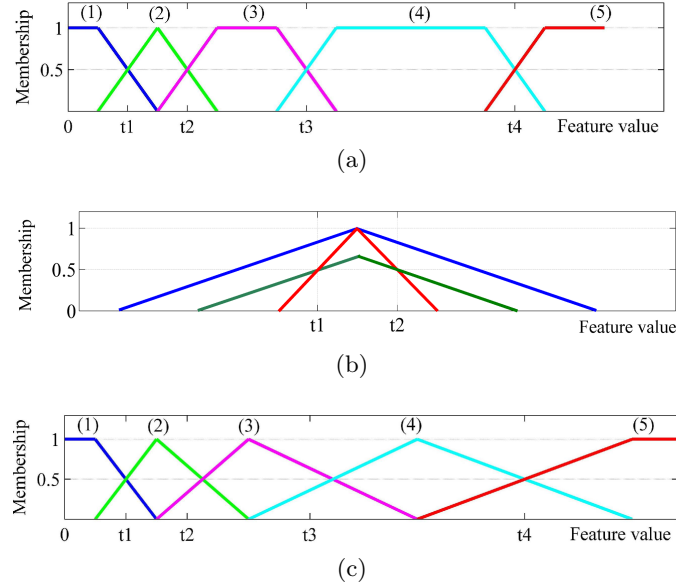


Figure 5.1.: The proposed fuzzification methods: (a) Membership functions with constant slopes (methods F1–F5); (b) F2 (red), F4 (green), and F5 (blue) methods in case of small distance thresholds; and (c) membership functions with variable slopes (method F6).

Two variations of the F2 method are also implemented. The first (F4) keeps the original s parameter constant, even in case where overlapping regions are caused and condition (2) is not satisfied (Fig. 5.1b, green line). The second (F5) keeps the s parameter steady as well, satisfying only condition (1) instead (Fig. 5.1b, blue line). Following some algebra, the membership function in the F4 method for the particular region $[t_i, t_j]$ is defined

as

$$\mu_{i,j}(t) = \begin{cases} 0 & \text{if } t \in (-\infty, t_i - s) \\ \frac{1}{2s}(t - t_i) + \frac{1}{2} & \text{if } t \in [t_i - s, \frac{t_i+t_j}{2}) \\ -\frac{1}{2s}(t - t_j) + \frac{1}{2} & \text{if } t \in [\frac{t_i+t_j}{2}, t_j + s) \\ 0 & \text{if } t \in [t_j + s, +\infty), \end{cases} \quad (5.8)$$

whereas in the F5 method as

$$\mu_{i,j}(t) = \begin{cases} 0 & \text{if } t \in (-\infty, \frac{t_i+t_j}{2} - 2s) \\ \frac{1}{2s}t + 1 - \frac{t_i+t_j}{4s} & \text{if } t \in [\frac{t_i+t_j}{2} - 2s, \frac{t_i+t_j}{2}) \\ -\frac{1}{2s}t + 1 + \frac{t_i+t_j}{4s} & \text{if } t \in [\frac{t_i+t_j}{2}, \frac{t_i+t_j}{2} + 2s) \\ 0 & \text{if } t \in [\frac{t_i+t_j}{2} + 2s, +\infty). \end{cases} \quad (5.9)$$

Additionally, another linear method (F6) is proposed, similar to the previous ones, with the difference that the slopes of the curves of the membership functions are not the same for all membership functions of a specific feature, but depend on the distance between two consecutive thresholds, as schematically represented in Fig. 5.1c. It is defined in such a way that the membership of a value t in a region between two consecutive thresholds t_i and t_{i+1} (i) equals 1 only if the feature value is equal to the mean of the two thresholds, $t = (t_i + t_{i+1})/2$, and it is smaller than 1 elsewhere; and (ii) equals 0 beyond the middle of the distance to the previous and the next thresholds, i.e. $\mu_{i,i+1}(t) = 0$, for $t \leq (t_{i-1} + t_i)/2$ and $t \geq (t_{i+1} + t_{i+2})/2$. After some algebra, the membership function of a value t in a region $[t_i, t_{i+1}]$ is calculated as

$$\mu_{i,i+1}(t) = \begin{cases} 0 & \text{if } t \in (-\infty, \frac{t_{i-1}+t_i}{2}) \\ \frac{2}{t_{i+1}-t_{i-1}}t - \frac{t_i+t_{i-1}}{t_{i+1}-t_{i-1}} & \text{if } t \in [\frac{t_{i-1}+t_i}{2}, \frac{t_i+t_{i+1}}{2}) \\ -\frac{2}{t_{i+2}-t_i}t + \frac{t_{i+2}+t_{i+1}}{t_{i+2}-t_i} & \text{if } t \in [\frac{t_i+t_{i+1}}{2}, \frac{t_{i+1}+t_{i+2}}{2}) \\ 0 & \text{if } t \in [\frac{t_{i+1}+t_{i+2}}{2}, +\infty). \end{cases} \quad (5.10)$$

In a similar way as previously, $\mu_i(t)$ is calculated as

$$\mu_i(t) = \begin{cases} 0 & \text{if } t \in (-\infty, \frac{t_{i-1}+t_i}{2}) \\ \frac{2}{t_{i+1}-t_{i-1}}t - \frac{t_i+t_{i-1}}{t_{i+1}-t_{i-1}} & \text{if } t \in [\frac{t_{i-1}+t_i}{2}, \frac{t_i+t_{i+1}}{2}) \\ 0 & \text{if } t \in [\frac{t_i+t_{i+1}}{2}, +\infty), \end{cases} \quad (5.11)$$

whereas for the complement function it is still $\mu_{\bar{i}}(t) = 1 - \mu_i(t)$. In the regions of the marginal thresholds, for both $\mu_{i,i+1}(t)$ and $\mu_i(t)$ calculations, a virtual threshold in equal distance to the closest threshold on the other direction is considered to calculate the function slope, e.g. a virtual threshold t_0 before the first threshold t_1 as $t_0 = t_1 - (t_2 - t_1)$ to allow the calculation of $\mu_1(t)$ or $\mu_{1,2}(t)$. For the mean height feature example, the virtual thresholds are calculated as $t_0 = 0.05 - (0.3 - 0.05) = -2$ and $t_9 = 40 + (40 - 5) = 75$. This fuzzification method tends to discourage large membership function value changes when small feature value changes occur, due to the smaller slopes in membership functions compared with the previous F1–F3 methods.

As an example demonstrating the differences among the fuzzification measures, the membership of an object with measured height value $t = 2.1$ to the region between $t_5 = 2$ and $t_6 = 3$, $\mu_{5,6}(2.1)$, is considered. As shown above, the slope parameter is $s = 0.1$ for fuzzification measure F1, thus, from (5.7) it is $\mu_{5,6}(2.1) = 1$. For F2, it is $s = 1.1$; however, since $t_6 - t_5 < 1.1$ the parameter reduces to $s = (3 - 2)/2 = 0.5$. From (5.7) it is $\mu_{5,6}(2.1) = 0.6$. For F3, the slope parameter is the same as in the F1 method, thus, $\mu_{5,6}(2.1) = 1$. For F4 and F5 methods, it is $s = std/2 = 1.1$. Thus, from (5.8) and (5.9), the membership values for the F4 and F5 methods are $\mu_{5,6}(2.1) = 0.5455$ and $\mu_{5,6}(2.1) = 0.5795$, respectively. For F6 method, following (5.10), it is $\mu_{5,6}(2.1) = 0.6364$. It is shown with a practical example that the different fuzzification methods can return a variety of membership values for a single feature, which, combined with the values for other features, may provide significantly different classification results.

5.3. Experimental setup

5.3.1. Classification process

The proposed methodology is applied on the two sites presented in the previous chapter. In particular, Le Cesine site is primarily tested, since the employed rule set by the expert ecologists was defined for this specific site. Lago Salso is used to test the transferability of the approach to a different site than the one the rule set has been defined.

As in Chapter 4, an object-oriented approach is followed during the process. A two-stage approach is followed for the habitat classification. During the first step, solely the LCCS classes are used to extract all potential GHC classes for each object, based on expert knowledge [51]. In general, more than one GHC classes correspond to each specific LCCS class, therefore, this process results in composite GHC classes. As an example, an object characterized by trees in semi-natural terrestrial vegetated area in LCCS, may correspond to either tall (TPH), forest (FPH), mega (GPH) phanerophytes, or urban woody vegetation (TRE) in GHC taxonomy. In such case, additional information of vegetation height and the degree of the object adjacency to urban areas is needed to dissolve the composite GHC class ('TPH or FPH or GPH or TRE') into its constituting single classes ('TPH', 'FPH', 'GPH', 'TRE'). Numerous rules were formed by expert knowledge to map LCCS classes, with different layers of attached attributes, to GHC classes. Overall, more than 140 different LCCS classes have been considered, from the most generic ones containing information only on the main LCCS class (e.g. A11: cultivated or managed terrestrial vegetation), to more detailed classes with several attributes (e.g. A11.A1-W8.A8.A9: needleleaved evergreen orchard or other type of plantation). The main classes can correspond to up to 18 possible GHC classes (e.g. A12: natural of semi-natural terrestrial vegetation), whereas LCCS classes including more attributes can be mapped to significantly less GHC classes, even only one. A detailed, almost complete, record of these rules is given in [51]. After the first-stage classification, the numerical features discussed in Section 4.3.1 are calculated, for each object, to be used in the main classification process.

The second stage of the classification is performed embedding in the framework knowledge provided by domain experts in the form of if-then rules [52, 53]. For each LCCS class present, domain experts provide the

conditions through which the composite GHC class of each object, acquired in the previous stage, can be refined in a single class or a composite one with less candidate single classes. The rules take into account the LCCS class of each object and a number of values of its aforementioned extracted numerical features.

The rules are examined sequentially for all objects. All features described in Section 4.3.1 are calculated for each object at the beginning of the process; the only exception is the adjacency degree to SHY objects (feature D7), which is updated before the execution of each rule involving it, since it is the only one related to GHC characteristics. The classification process is conducted both using the fuzzy methods discussed in Section 5.2.2 and crisp classification employing no fuzzy logic, as detailed in [52,53]. In the former case, a degree of support is assigned to each rule, based on the confidence in each individual condition, derived through the fuzzification methods and propagated using the DS principles. In the latter case of crisp classification, a binary selection is done on the validity of each examined rule, which may either hold or not. Following these approaches, multiple single or composite GHC classes may result for each object, after the consideration of all rules, with a belief interval assigned to each one of them. As a note, composite classes may result following the crisp classification too, when non-adequate information exists to discriminate among certain GHC classes, a typical example being herbaceous therophytes (THE) and geophytes (GEO).

5.3.2. Classifier implementations

Two further considerations in order to enhance the classifier flexibility and applicability in various landscapes are made, resulting in different classification implementations. In the original rule set, the rules provided by the experts are characterized by certainty on the final outcome in case the described conditions hold, e.g. valid rules may be in the form “If *condition 1* and *condition 2* hold, then the object is classified as *class A*”, where *A* may refer to either a single or composite class. However, uncertainty that may exist in the rules provided by the experts is not considered. As a countermeasure, rules of definite outcome are converted to rules leading in uncertain, soft, outcomes, providing higher support to the most possible classes, but still supporting to a smaller degree the less possible ones. For

instance, rules of the form “If *condition 1* and *condition 2* hold, then the object is classified as *class(es) A* with confidence $x\%$, or *class(es) B* with $(100 - x)\%$ ”, arise and are evaluated.

A second consideration is related with the restricted availability or acquisition difficulty of lidar data for various sites and landscapes. Aiming at developing a robust method with extensive applicability, such conditions of lack of information need to be taken into account. Therefore, implementation of rules without considering the lidar data, used for the disambiguation of several classes based on their canopy height, is also developed, to test the approach applicability in similar conditions. Thus, rules employing lidar data to discriminate among certain classes, e.g. of tree and shrub GHC classes, are replaced by rules resulting in more composite classes or entirely removed.

As a result of the aforementioned considerations, four different implementations are developed testing all four combinations of rules with definite or uncertain outcome, and availability or lack of lidar information. In particular, the main implementations are characterized by (A) absence of lidar data and rules expressing certainty (A1) or uncertainty in the outcome (A2); or (B) presence of lidar data and definite (B1) or uncertain (B2) outcome rules.

For each implementation, all fuzzification methods of Section 5.2.2 are tested, in addition to crisp classification (F0). F0 with implementations using definite rule outcomes (A1 and B1) assimilate the processes followed in [52, 53], and are used as reference. In total, 28 different classifier versions (Fig. 5.2) are tested for habitat mapping, based on the principles of DS theory, from the combination of the four implementations (A1, A2, B1, B2) and the F0–F6 fuzzification methods.

5.3.3. Final class selection

Each classification process may result in one or multiple single or composite classes for an object, each class being associated with a belief interval. Composite classes tend to have larger belief values than the single classes they include, since, based on (5.1), the belief in a composite event is calculated by aggregating the support to each of its subsets. Different selection criteria can be used for the assignment of the final class of each object, based on

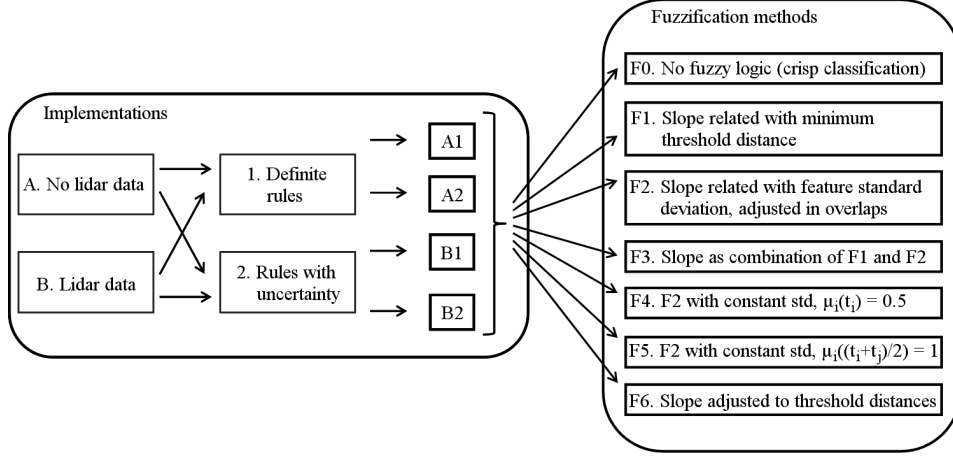


Figure 5.2.: The 28 classifier versions, resulting from the combination of the four implementations and the F0–F6 fuzzification methods.

the belief, plausibility, or a combination of the two values that the possible events have. In the present study, five selection criteria are evaluated: selection based on maximum (i) belief (*bel*), (ii) plausibility (*pls*), (iii) sum of belief and plausibility ($bel + pls$), and two weighted sums favouring larger (iv) belief ($2bel + pls$), or (v) plausibility ($bel + 2pls$) values. In addition, since events of multiple classes tend to have larger values of the different criteria than events with single classes, a further parameter is proposed to evaluate trade-offs between favouring single class events and events with high support in the selected criterion. Thus, a threshold, t , is applied as the minimum value in the selected criterion a single class event needs to have to be selected. The single class event with the largest value on the selected criterion is chosen if this value is larger than the threshold; otherwise, the event with the smallest number of classes with criterion value over 1.25 times the applied threshold t is chosen, to compensate the lack of single class events with high support. The 1.25 factor was selected after experimentation; in case of $t > 0.8$ and no single class event above this threshold exists, the simplest multiple class with criterion value equal to 1 is selected. It is worth noting that there will always be at least one event with criterion value equal to 1, since from the definition of the belief function in (5.1), the belief on the frame of discernment, i.e. a multiple event with all classes, is 1, $bel(\Theta) = 1$; and since $pls(A) \geq bel(A)$, for every event A , there will

always be an event with selection criterion equal to 1, either if the criterion is defined as belief, plausibility, or a linear combination of them. The process is summarized in Algorithm 1. All threshold values in the range $[0.1, 0.9]$, with step 0.1, are evaluated in the experiments for all selection criteria. These parameters demonstrate the flexibility of the algorithm in being adjusted to user defined criteria and selecting the most meaningful and informative final classes for each specific application and purpose.

Algorithm 1 Final class selection

Input: Define the class selection criterion, c ; define the selection threshold, t , for events with single classes

- 1: Calculate the value, v , for criterion c of each event
- 2: Find the single class event with the highest v
- 3: **if** $v \geq t$ **then**
- 4: Select this event and terminate the algorithm
- 5: **else**
- 6: **for** $n = 2$ **to** N , where n the number of classes and N the maximum number of classes of any event **do**
- 7: Find the event with the highest v
- 8: **if** $t \leq 0.8$ **then**
- 9: Set $T = 1.25t$
- 10: **else**
- 11: Set $T = 1$
- 12: **end if**
- 13: **if** $v \geq T$ **then**
- 14: Select this event and terminate the algorithm
- 15: **end if**
- 16: **end for**
- 17: **end if**

5.3.4. Fusion of classifiers

Besides the evaluation of the single classifiers with the different implementations and parameters discussed previously, combination of classification results is additionally performed and evaluated. Combination is applied based on the Dempster rule of combination, as described in (5.3), since the results belong to the same frame of discernment, i.e. in the GHC class taxonomy. Several combinations are evaluated, including: (i) for each implementation and fuzzification method, combination of the classifiers of all the class selection criteria and thresholds, i.e. 28 combinations of 45 clas-

sifiers (5 selection criteria \times 9 threshold values); and (ii) for each selection criterion, threshold value, and main implementation (A1, A2, B1, B2 in Fig. 5.2), combination of all fuzzification methods F0–F6 (including the crisp classification), i.e. 180 combinations (5 selection criteria \times 9 threshold values \times 4 implementations) of 7 classifiers (F0–F6 methods). For the latter combination, the same experiments were implemented excluding features F0, in order to evaluate the fusion of the fuzzy methods alone as well.

5.3.5. Transferability evaluation

The developed classifier for Le Cesine site is applied also to Lago Salso study area, in order to test its transferability to different areas, as an indication of its generalization performance. No separate rule set has been provided by the expert ecologists for Lago Salso site, thus the one implemented for Le Cesine is tested.

5.3.6. Classification accuracy evaluation

The overall classification accuracy of each classifier represents the percentage of correctly classified objects over the total number of objects, based on the available ground truth. In case single class events are selected, an object is considered as correctly classified if the selected class matches the validated one. In case of multiple class events, classification can be considered correct if the validated class is within the classes of the composite event. The aforementioned accuracy interpretation seems useful in case where ambiguity in classes is more preferable than omission of the correct class, for each object.

A second interpretation is also applied, that ‘penalizes’ commission errors in multiple classes. According to this interpretation, a single class event is considered correct as in the previous case. A composite event, though, is considered correct only by the ratio of the correct class(es) to the total number of classes in the event. For instance, if a selected event consists of four potential classes, among which one coincides with the ground truth class, it is considered 25% correct. The latter interpretation discourages the selection of events with multiple classes, with optimal classifiers minimizing the commission errors, although with the expense of increasing the omission errors, as shown below.

5.4. Results and discussion

5.4.1. Le Cesine study area

A total of 583 objects were formed in Le Cesine study site and each one was classified in a GHC single or composite class with all different classifiers. As in Chapter 4, 250 points were used for validation, from separate objects, identifying 14 different GHC classes, including 13 single and one composite class ('THE or GEO').

A. Accuracy interpretations

Fig. 5.3 draws an overview of the classification accuracies achieved by the different developed fuzzy Dempster–Shafer classifiers. Fig. 5.3a depicts the accuracies according to the consideration of multiple classes containing the correct single one as correct classifications. Fig. 5.3b shows the results from the second interpretation, where incorrect single classes within multiple class events are considered as commission errors and penalized. The columns of the figures represent the four main implementations (A1, A2, B1, B2), each including the crisp (F0) and the fuzzy methods (F1–F6), as described in Fig. 5.2. The rows represent the class selection parameters, organized in the five main approaches on the principal criterion (belief, plausibility, or combination), each including the nine different minimum criterion threshold values for a single class. Each pixel corresponds to a specific classifier, with its accuracy being represented by the pixel intensity; the grey-scale colours were stretched to the range between the minimum and maximum accuracy values, for each figure.

As noticed from Fig. 5.3a and 5.3b, the different interpretations of classification accuracy lead to different ranges of values. As expected, higher accuracies are observed in the cases where returned multiple classes are considered as correct when one of the single classes coincides with the ground truth class. In fact, accuracies over 70% are achieved—minimum accuracy 71.2%—, reaching even perfect classifications of 100%. The higher accuracies, however, often tend to refer to classifications with multiple classes, in general, returned instead of single ones. Thus, the commission errors in such cases are higher, as shown from the corresponding accuracies based on the second interpretation, where the resulting accuracies are notably lower.

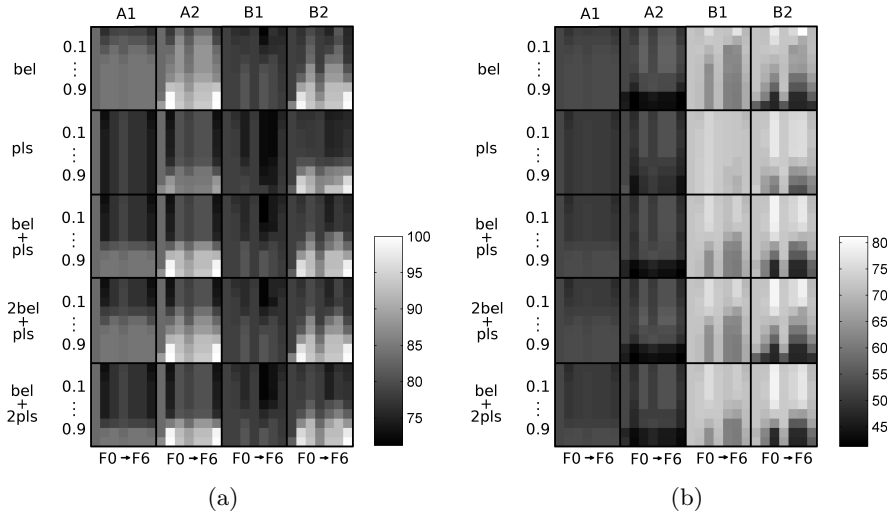


Figure 5.3.: Classification accuracies (%) for all DS fuzzy classifiers for Le Cesine study area, based on (a) tolerance to the existence of the correct class in the returned event, or (b) penalizing incorrect classes on a multiple class event. Columns represent the fuzzification measures (F0–F6) for each implementation (A1, A2, B1, B2) of the classifier (Figure 5.2), whereas rows the different minimum threshold values for single classes (0.1–0.9) for each selection criterion (*bel*, *pls*, or combination).

For instance, classifications of around 100% in Fig. 5.3a for the F1 and F6 fuzzification methods in implementation A2 and belief value as selection criterion with thresholds 0.8 or 0.9 (rows 8 and 9, columns 9 and 14), are among the lowest ones in Fig. 5.3b, due to the fact that definite decisions on single classes were not possible and many multiple classes were returned.

Each interpretation has its own advantages and limitations, and the decision on the optimal classifier depends on the specific application and user preferences. This flexibility is one of the main benefits of the proposed DS framework. More specifically, the interpretation favouring multiple classes is more appropriate for applications where low omission error is required. As an example, multiple classes like ‘TPH or FPH or TRE’ for a habitat classified as ‘FPH’ (forest phanerophytes, trees between 5–40 m) in a previous assessment, can be precious for forest management, since they might indicate change in structure and biomass, potentially by illegal logging, in case the actual class is ‘TPH’ (tall phanerophytes, between 2–5 m), or in-

dedicate urban expansion, even illegal construction, in case the actual class is ‘TRE’ (urban woody vegetation). A second example includes the appearance among the possible multiple classes of one that did not exist in previous classification that may indicate the existence of invasive species, e.g. the invasive silver wattle (*Acacia dealbata*) woody plant (TPH) over Portuguese laurel (*Prunus lusitanica*) formations (FPH) in certain sites. These cases can alert managing authorities of the area to inspect the specific habitat with a field visit. On the other hand, the interpretation penalising multiple classes and selecting the single one with maximum support, can be useful to identify abrupt changes that need to be taken into account. For instance, classification of a habitat with the same multiple potential classes in two time instances, e.g. ‘TPH or FPH’, as ‘TPH’ the first time and ‘FPH’ the second, may indicate either an actual class transition, or reveal intense spectral or structural changes resulting by pressures in the habitat or the appearance of understorey vegetation. In addition, the simplified classes resulting by the second interpretation favour the direct comparison of the classifier with other usually employed classifiers (resulting in a single class per habitat) and the use of the outcomes in comprehensive dissemination reports and maps.

A combination of the two interpretations is straightforward, as a trade-off between low omission (former interpretation) and low commission (latter interpretation) errors. Fig. 5.4 draws the average of the classification accuracies achieved by the two previous interpretations, identifying the classifiers performing overall well under both cases. As expected, the value boundaries of the previous interpretations are suppressed, resulting in accuracies between over 60% and slightly exceeding 80%. Besides other potential applications, this averaging approach seems suitable to the habitat classification problem of the present study, where site management and habitat monitoring are tolerant up to a degree to composite classes comprising of similar constituting ones—requiring same management practices or indicating same ecosystem services or trends—, being in parallel small enough to exclude irrelevant classes.

Various interpretations may be used to select the most appropriate classifier given the particular characteristics of each specific application. In case classifiers that perform similarly well under both interpretations of Fig. 5.3 are preferred, a selection process as depicted in Fig. 5.5 can be followed.

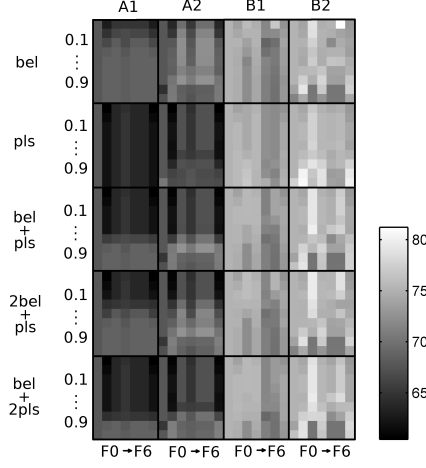


Figure 5.4.: Average accuracies (%) of the two classification interpretations of Fig. 5.3 for Le Cesine study area. Columns represent the fuzzification measures (F0–F6) for each implementation (A1, A2, B1, B2) of the classifier (Figure 5.2), whereas rows the different minimum threshold values for single classes (0.1–0.9) for each selection criterion (*bel*, *pls*, or combination).

First, the classifiers belonging to the upper quartile (i.e. the highest 25%) under both interpretations of Fig. 5.3 are selected, with the rest being masked out. Masking of classifiers is performed for each implementation using (B) or neglecting (A) lidar data separately, to provide guidelines for each individual case. The masked out classifiers are drawn in white colour. Then, the normalized difference of the accuracy under the interpretation tolerant to multiple classes, A_T , of Fig. 5.3a to the accuracy under the interpretation penalizing them, A_P , of Fig. 5.3b is calculated, for each of the remaining high performing classifiers, as

$$ND_A = \frac{A_T - A_P}{A_T + A_P}. \quad (5.12)$$

The lowest ND_A values represent highest similarity between the two interpretations, indicating high classification consistency. In addition, the normalization factor in the denominator of (5.12) allows the identification of the overall highest performing classifiers among ones with the same absolute difference. As a note, use of absolute difference is not necessary in the numerator of (5.12), since it is always $A_T \geq A_P$. The returned ND_A

values lie within the range $[0, 0.258]$.

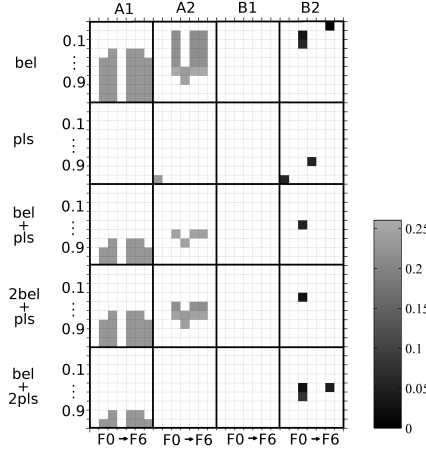


Figure 5.5.: Normalized difference of the two main classification interpretations for Le Cesine study area. Only the upper quartile classifiers under both interpretations, for each A and B implementations, are selected. Columns represent the fuzzification measures (F0–F6) for each implementation (A1, A2, B1, B2) of the classifier (Figure 5.2), whereas rows the different minimum threshold values (0.1–0.9) for each selection criterion (*bel*, *pls*, or combination).

As readily noticed from Fig. 5.5, the crisp classifiers representing the rule-based methodology in [52, 53] are not among the top 25% performing ones under both interpretations simultaneously. This is revealed by the white pixels in the first columns under the A1 and B1 implementations. In fact, the only crisp classifiers included in the top performing list are ones using rules adjusted to incorporate uncertainty in the outcome (row 19, first column under A2 and B2 implementations). On the contrary, DS classifiers with different fuzzy methods are among the selected ones, especially in the implementations where lidar information is not used. However, the ones using lidar data appear more consistent between the two interpretations of Fig. 5.3, with the lowest ND_A values. This was expected due to the further discrimination of single classes that tends to reduce the accuracies under the interpretation tolerant to multiple classes (Fig. 5.3a) and increase the opposite ones, thus reducing their difference and the ND_A value. As a final note, the number of common classifiers in the upper quartiles between the

main interpretations of Fig. 5.3 is larger for classifiers of implementations A than for implementations B where lidar data are used and further refinement of multiple classes occurs.

B. Performance of the fuzzy methods

The first column of A1 and B1 groups in Fig. 5.3a, 5.3b, and 5.4 represent the crisp classifiers, assimilating the results by Adamo *et al.* [52, 53]. In fact, accuracies of 68% and 75% are shown in Fig. 5.4 for the cases where lidar information is considered absent and available, respectively. These accuracies are close to the ones reported in [52, 53]. As noticed from the figures, the crisp classification results are outperformed by several classifiers with fuzzification methods, according to all interpretations, as revealed by the brighter colour pixels. Whereas in implementations A1 and B1 limited number of fuzzy classifiers outperform the respective crisp classification ones, significantly larger number exists when combined with the flexibility the framework offers for less strict outcome rules (implementations A2 and B2). Overall, there are also fuzzy classifiers that perform lower than the crisp ones; however, the existence of a significant number of fuzzy classifiers outperforming the crisp classifications shows the potential improvement the DS approach can bring along. It also indicates that the rule fine tuning by the experts is not optimal and better results are possible.

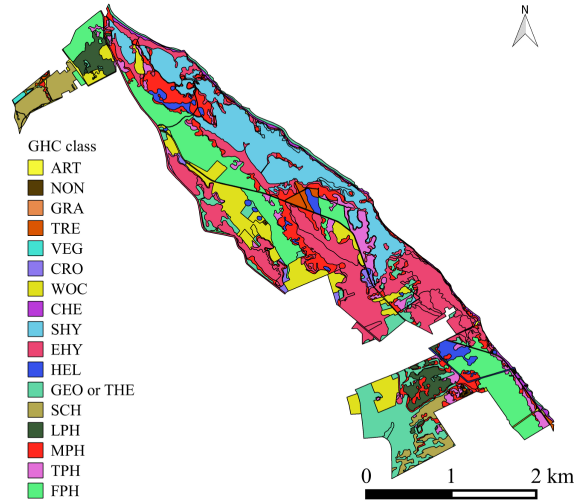
More specifically, a number of fuzzy classifiers perform better than the crisp ones under the interpretation favouring multiple classes (Fig. 5.3a), although often with the expense of higher commission errors and more vague classes. This is expected for soft classification, where membership values are shared to the possible single classes, none of them sometimes reaching the threshold to be selected individually; thus, multiple classes are returned. However, a significant number of fuzzy classifiers outperforming the crisp ones are found also under the interpretation penalizing multiple classes (Fig. 5.3b), as well as the averaging one (Fig. 5.4). More specifically, Table 5.2 reports the highest achieved accuracies by the fuzzy classifiers in comparison with the respective crisp ones; implementations considering lidar features either missing (A) or available (B) are shown, under the interpretations tolerant to (Fig. 5.3a) and penalizing (Fig. 5.3b) incorrect classes within multiple ones, as well as the averaging interpretation (Fig. 5.4). The crisp

classification assimilates the results from the state-of-the-art methodology described in [52, 53]. As seen, for every implementation and under any interpretation of accuracy, there were DS fuzzy classifiers, among the total implemented ones, that outperformed the reference crisp classifiers. This is further supported by the absence of these crisp classifiers from the selected highly consistent well performing ones, under the normalized difference interpretation (Fig. 5.5).

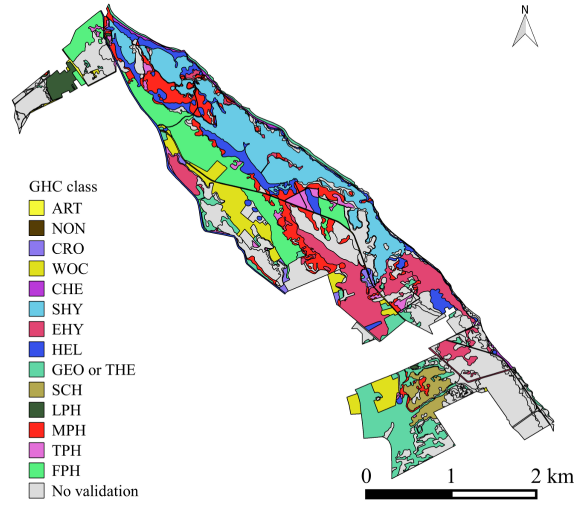
Table 5.2.: Maximum classification accuracies (%) achieved by the crisp and the fuzzy classifiers for implementations without and with lidar data for Le Cesine, under interpretations tolerant to and penalizing incorrect classes in multiple ones, as well as the averaging interpretation of the two.

		Crisp	Fuzzy
Multiple class tolerant interpr.	Without lidar (A)	83.2	100
	With lidar (B)	78.4	99.6
Multiple class penalizing interpr.	Without lidar (A)	52.3	56.6
	With lidar (B)	71.9	81.2
Averaging interpr.	Without lidar (A)	67.8	72.5
	With lidar (B)	75.1	81.2

As far as individual classifiers are regarded, the best performing one under the interpretations penalizing incorrect single classes in multiple ones (Fig. 5.3b) and the averaging interpretation (Fig. 5.4) is the one using the F5 fuzzification method under consideration of lidar data and less strict outcome rules, using belief value and threshold 0.1 as selection parameters (first row, second to last column in Fig. 5.3b and 5.4). Under both interpretations, the achieved accuracy is 81.2%, outperforming the respective crisp classification, in the former interpretation by around 10% (Table 5.2). Achieving the same accuracy under the interpretation tolerant to multiple classes (Fig. 5.3a), its normalized difference value, ND_A , is 0 according to (5.12), making it the highest performing classifier under the interpretation of Fig. 5.5 as well. The resulting GHC map, shown in Fig. 5.6a), demonstrates the wide selection of single classes over multiple ones. The map with the reference segments, based on the validated points, is provided in Fig. 5.6b. As a note, since 250 validation points were provided, each characterizing one segment, a number of segments is not validated and labelled as such in the map.



(a)



(b)

Figure 5.6.: GHC map resulting from the best performing fuzzy DS classifier under penalizing multiple class and averaging interpretations (a) and GHC validated classes (b) for Le Cesine.

Table 5.3 reports the correct classifications achieved by the crisp classification as provided by the experts [51–53] and the DS classifier with fuzzy F5 method and less definite rule outcomes. In both cases lidar data are used. The number of objects of each class is given. Then, the correct classifications under the interpretation of penalizing commission errors in multiple classes are provided for the crisp and the fuzzy classification. In

the final columns, the accuracy percent of each method is given, for each GHC class. As shown, the fuzzy method is able to identify with significantly higher accuracy the cultivated woody crops (WOC), herbaceous caespitose hemicryptophytes (CHE), and mid phanerophyte shrubs (MPH), whereas being outperformed only for the tall phanerophyte (TPH) objects. For the rest of the classes, both approaches perform similarly well.

Table 5.3.: Comparison of results applying crisp classification and fuzzy classification with less strict rule outcomes under the availability of lidar data, for each class. The number of ground truth samples, together with the absolute correct classifications of the two methods under penalizing commission errors are given, for each GHC class. The percentage of correct classifications is also shown in the last columns.

GHC	Ground truth no.	Correct Crisp	Correct Fuzzy	Acc. Crisp (%)	Acc. Fuzzy (%)
ART	3	3	3	100	100
NON	1	1	1	100	100
CRO	5	5	5	100	100
WOC	17	8	17	47.1	100
SHY	8	7	7	87.5	87.5
EHY	22	12	12	54.5	54.5
HEL	28	9	9	32.1	32.1
CHE	4	3	4	75	100
THE or GEO	40	40	40	100	100
SCH	3	2	2	66.7	66.7
LPH	6	3.25	4	54.2	66.7
MPH	72	48.5	66	67.4	91.7
TPH	32	29	24	90.6	75
FPH	9	9	9	100	100
Total	250	179.75	203	71.9	81.2

Among the fuzzification methods per se, high similarity in the results achieved by the F2, F4, and F5 methods can be observed. This is justified by the fact that the same slopes in the membership functions are used in all three methods, based on the standard deviation of the observed fuzzified features, as discussed in Section 5.2.2, being differentiated in case of rule thresholds in very close distance. Among these three methods, F2 seems to marginally outperform the other two in some cases, as in some classifiers of B2 implementations (Fig. 5.4, columns 3, 5, and 6 under B2 representing F2, F4, and F5 methods, respectively). Based on the results, fuzzification method F1 seems to be more related with the F6 one (as seen, for instance,

in Fig. 5.4 in columns 2 and 7 under each implementation), both deriving the membership function slopes from the threshold distances. On the other hand, F3 method is the closest one to the crisp classification; this can be justified by the selection of the minimum parameter s among the previous methods, resulting in the steepest slopes of the respective membership functions, thus closely related to the crisp classification—which can be thought of as using membership functions with perfectly vertical slopes. Each fuzzification method may under certain classifier parameters perform better than the others; however, as a general observation, method F2 seems to provide the best overall results, particularly combined with the use of lidar data and incorporation of uncertainty in rule outcomes (implementation B2). This is further supported by F2 classifiers being the most numerous among the selected ones under the normalized difference interpretation in Fig. 5.5 in B2 implementations, and among the most numerous in implementations A1 and A2.

C. Availability of lidar data

In implementations where lidar data are considered available (B1 and B2), different rules are provided by the experts, compared with the implementations without lidar (A1 and A2). In the former, features D8 and D9, as described in Section 4.3.1, are used to discriminate a number of classes that without the presence of height information remain ambiguous, e.g. trees and shrubs whose main discrimination criterion is vegetation height, as discussed in Chapter 3. Thus, as expected, implementations including lidar data tend to outperform, in general, their counterparts where such data are not used, as clearly depicted in Fig. 5.3b where single classes are favoured, and less intensely under the averaging interpretation of Fig. 5.4. On the contrary, A1 and A2 implementations seem to slightly outperform the ones using lidar data under accuracy interpretation of Fig. 5.3a. This is justified by the tendency to select multiple classes instead of single ones, when there is no or little support in further discrimination.

Table 5.4 shows the classes returned by the classifications using the F1 method with the sum of belief and plausibility and threshold 0.9 as class selection parameters, for the cases where lidar are considered missing (A1) or available (B1), for the validated objects, as an indicative example from

a high performing classifier in both cases. As shown, the former classifier identifies 10 single classes and five multiple ones. On the contrary, using the lidar derived features, the latter classifier manages to distinguish 16 single classes, reducing in parallel the number of multiple ones to three. Thus, lidar information is able to refine certain multiple classes and discriminate among their constituting single ones. However, this further class separation entails the risk of misclassifications, as seen from the comparison of the accuracies of the two classifiers based on the interpretation more tolerant to multiple classes (Fig. 5.3a). Therein, the classifier ignoring lidar data achieves an accuracy of 84.4%, in comparison with 78.4% of the second classifier. Their difference indicates the incorrect multiple class separations by the lidar data. However, according to the interpretation penalizing incorrect classes within multiple ones (Fig 5.3b), the advantage by the use of lidar in class separability is more obvious, significantly outperforming the A1 classifier by 70.9% over 52.97%, discriminating single classes that were not distinguishable previously. As a note, despite its decrement in accuracy, the A1 classifier outperformed its crisp classification counterpart under both interpretations described in Fig. 5.3a and 5.3b.

D. Uncertainty in rule outcome

As far as the type of outcome rules are regarded, it is observed from Fig. 5.3 and 5.4 that the use of membership rules, expressing uncertainty in the outcome (implementations A2 and B2) seems to provide higher classification accuracies than the classifiers using rules with strictly defined outcomes (implementations A1 and B1, respectively). This flexibility in incorporating uncertainty in expert rules demonstrated in this study, is another advantage of the DS theory over crisp rule-based classifications. A2 and B2 outperformed the respective A1 and B1 implementations in most cases, under all interpretations in Fig. 5.3a, 5.3b, and 5.4.

E. Class selection criteria

The choice of the class selection criterion can influence the classification results, and thus, the performance of the classifier. Table 5.5 reports the average classification accuracies under the averaging interpretation (Fig. 5.4) for the two implementations using (B) or not (A) lidar data, for the

Table 5.4.: Classes returned by DS fuzzy F1 classifiers with the sum of belief and plausibility and 0.9 threshold value as selection parameters, in case lidar are considered either missing (A1) or available (B1).

Classes without lidar (A1)	Classes using lidar (B1)
ART	ART
NON	NON
GRA	GRA
TRE	TRE
CRO	CRO
WOC	WOC
CHE	CHE
SHY	SHY
EHY	EHY
HEL	HEL
THE or GEO	THE or GEO
DCH or LPH or SCH	DCH
DCH or LPH or SCH or VEG	DCH or LPH or SCH or VEG
MPH or TPH or TRE	MPH or TRE
FPH or TPH	FPH
	LPH
	MPH
	SCH
	TPH

cases where the selection is based on: (i) the maximum event belief ('bel'), (ii) the maximum plausibility ('pls'), (iii) the maximum sum of the two ('bel + pls'), and combinations where (iv) belief or (v) plausibility counts twice as much as the other ('2bel + pls' and 'bel + 2pls', respectively). Interestingly, the criterion on maximum belief leads to best classification results in A implementations, whereas the plausibility criterion provides the highest performance in B implementations.

Table 5.5.: Average classification accuracies (%) following different selection criteria, for implementations ignoring (A) or using (B) lidar data.

Criterion	Without lidar (A)	With lidar (B)
bel	68.4	74.0
pls	64.8	75.1
bel + pls	66.3	74.5
2bel + pls	67.1	74.3
bel + 2pls	65.7	74.7

This may be attributed to the existence of more multiple classes in A

implementations, due to the lack of sufficient data for discrimination. In such a case, different multiple class events may be characterized by the same plausibility values, when little information in excluding some single classes is provided, thus making plausibility a non-informative selection criterion. At the same time, the minimum support on some classes, expressed by the belief value, can be more discriminatory. On the other hand, in B implementations, as data are provided in the classifier, multiple classes are decreased by the elimination of improbable single ones and plausibility values appear more important for selection. This is supported by the observation that significantly higher results are achieved using the maximum plausibility criterion over the belief one, under the interpretation penalizing commission errors (Fig. 5.3b, B implementations). On the contrary, maximum belief classifiers seem to clearly outperform the plausibility ones in implementations A under the interpretation favouring multiple classes (Fig. 5.3a, A implementations). Thus, maximum belief criterion seems more suitable in cases where incomplete data hinder the discrimination of single classes and highest priority in including the correct class in the returned multiple one is given; on the contrary, the maximum plausibility criterion appears preferable in cases where the available data favour class separability and commission errors in multiple events are considered. Finally, as noted from Table 5.5, the linear combinations of the two previous criteria perform between the two extremes, in analogy with the contribution of each belief or plausibility value.

As far as the selected threshold value for the minimum support of the chosen criterion to a single class is concerned, variations in performance occur, as seen in Fig. 5.3 and 5.4. As a general rule, lowest values favour the selection of single classes, since less minimum support is required for the selection of the best one. This leads to classifications with less multiple classes and, in many cases, in highest accuracies under the interpretation penalizing commission errors in multiple classes (Fig. 5.3b). On the contrary, highest values hinder the separability of multiple classes in single ones when high support is not provided, and thus perform higher under the interpretation more tolerant to multiple classes (Fig. 5.3a).

Table 5.6 gives an indicative example of the simpler classes returned by classifiers with lower threshold values compared with the higher threshold ones for the validated objects; the best performing classifier under inter-

pretations in Fig. 5.3b and 5.4, from implementation B2 and maximum belief as selection criterion using threshold value 0.1 (row 1, second to last column), is compared with the respective classifier using threshold 0.9 (row 9, second to last column). The former classifier returns 14 single classes and the double class of the undistinguishable, based on the data, ‘THE or GEO’ classes (OA 81.2%). On the contrary, the latter classifier separates only nine single classes, while returning eight multiple ones, among which one with seven single classes (OA 47.18%). However, it performs better than the former one under interpretation of Fig. 5.3a (OA 93.6%), keeping within its multiple classes correct ones which are erroneously excluded by the former classifier (OA 81.2%).

Table 5.6.: Classes returned by DS fuzzy F5 classifier with implementation B2 and belief as selection criterion, for threshold values 0.1 and 0.9.

Threshold 0.1	Threshold 0.9
ART	ART
NON	NON
TRE	TRE or WOC
CRO	CRO
WOC	WOC
SHY	SHY
HEL	EHY or HEL or SHY or GRA
EHY	EHY
THE or GEO	THE or GEO or GRA
CHE	CHE
SCH	CHE or GRA
MPH	CRO or GEO or HCH or LHE or THE or GRA or VEG
LPH	DCH or LPH or SCH or VEG
TPH	MPH or TPH or TRE
FPH	TPH
	TPH or FPH
	FPH

Close look on Fig. 5.3a and 5.3b reveals that higher threshold values lead to better classifications under the approach considering multiple classes containing the correct single one as correct, and vice versa. Thus, the selection of the appropriate threshold value depends on the interpretation of the accuracy followed by each specific application. In studies where a combination of the two extreme interpretations seems applicable, as this study, Fig. 5.4 or 5.5 can be used as a guide to indicate the most suitable threshold values.

Besides some high performing methods with extreme threshold values, as the one in Table 5.6, classifiers with average values of around 0.5 seem to provide a safe option.

F. Fusion of classifiers

As discussed in Section 5.3.4, fusion of the individual classifiers was also attempted, applying the Dempster rule of combination to different groups of classifiers. Fusion was performed following (5.3), where m_i represents the basic probability assignment function value by the i -th classifier fused. In the first fusion attempt, all classifiers of each specific implementation and fuzzification method were combined, resulting in 28 new classifiers, each being the combination of 45 individual classifiers (5 selection criteria \times 9 threshold values). The achieved accuracies were between the minimum and maximum accuracies from the individual classifiers, under both interpretations shown in Fig 5.3. Table 5.7 reports the classification accuracies together with the ones achieved by the best individual classifiers, for each implementation and fuzzification method (including the crisp classification), under the most conservative interpretation penalizing multiple classes including inaccurate single ones besides the validated class (Fig. 5.3b). As observed from the table, the fused classifiers do not outperform the best individual ones in any case; in fact, in all cases, the achieved accuracies are inferior than the individual ones. The only exception are the crisp classifications (F0) of implementations A1 and B1, where results are the same, since all individual classifiers provide the exact same classification outcome.

The second fusion attempt combined classifiers of each particular selection criterion and respective threshold for each implementation; thus, 180 classifiers were created (5 selection criteria \times 9 threshold values \times 4 implementations), each being the result of the individual classifiers with different fuzzification methods (F0–F6). As previously, classification accuracies achieved were between the minimum and maximum accuracies of the individual classifiers involved in each combination. The same experiments were performed excluding the crisp classification method (F0) for each combination. Increase in accuracy by around 0.4% was observed; however, the values were still inferior to the best performing individuals. Interestingly, accuracy increase was observed also for combinations in which the excluded individ-

Table 5.7.: Classification accuracies (%) achieved by the fusion of classifiers for each implementation (A1, A2, B1, B2) and fuzzification method (F0–F6), under the interpretation penalizing multiple classes. In parenthesis, the accuracy of the maximum individual classifier of each case is reported.

	A1	A2	B1	B2
F0	52.3 (52.3)	52.3 (54.1)	71.9 (71.9)	71.9 (74.4)
F1	50.3 (53.0)	50.0 (52.6)	72.7 (73.1)	72.1 (72.9)
F2	50.8 (53.0)	54.4 (56.6)	73.8 (76.0)	76.7 (79.6)
F3	51.0 (52.6)	51.0 (56.6)	72.7 (72.9)	72.5 (73.5)
F4	50.8 (53.0)	54.4 (56.6)	64.2 (72.4)	66.3 (75.4)
F5	50.8 (53.0)	54.4 (56.6)	57.7 (76.8)	59.0 (81.2)
F6	50.3 (53.0)	50.0 (52.6)	71.7 (72.1)	71.3 (71.7)

ual crisp classifier had performed better than both combinations alone, i.e. exclusion of a strong classifier from the first combination lead to a better performing final combination. This may be attributed to limitations of the Dempster rule of combination when highly conflicting evidence is provided [351, 374]. This practically means that the presence of a single classifier assigning no support in the correct class will assign m value equal to 0 to this class in the final classifier as well, as may be deduced from (5.3). Thus, the existence of a single very weak classifier in certain classes may deteriorate the performance of the combined one. This explains the decrease in performance when including the crisp classifiers, which assign only binary support values to selected classes (i.e. 1 for full support, 0 for no support) and thus transfer their erroneously excluded classes to the combined classifiers.

5.4.2. Transferability to Lago Salso study area

To evaluate the applicability of the proposed approach to different sites, the developed classifiers were directly applied to Lago Salso study areas. A total number of 259 objects were classified, out of which 59 were available as validation points, belonging in 15 GHC classes.

A. Accuracy interpretations

The achieved accuracies, according to the two different interpretations discussed in the previous section, are given in Fig. 5.7. In particular, Fig. 5.7a

draws the accuracies when incorrect single classes among the correct one in multiple class events are not penalized, whereas Fig. 5.7b the respective accuracies when the opposite happens. The average accuracies of the two extreme cases are drawn in Fig. 5.8.

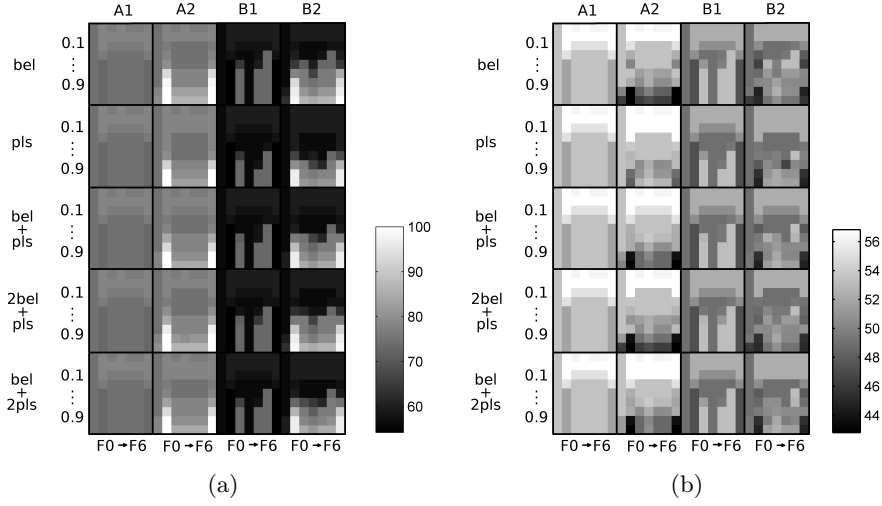


Figure 5.7.: Classification accuracies (%) for all DS fuzzy classifiers for Lago Salso study area, based on (a) tolerance to the existence of the correct class in the returned event, or (b) penalizing incorrect classes on a multiple class event. Columns represent the fuzzification measures (F0–F6) for each implementation (A1, A2, B1, B2) of the classifier (Figure 5.2), whereas rows the different minimum threshold values for single classes (0.1–0.9) for each selection criterion (*bel*, *pls*, or combination).

Accuracies ranging from 54.2% to 100% were achieved according to the first interpretation (Fig. 5.7a), whereas they were restricted to the range between 42.8% and 56.8% for the second one (Fig. 5.7b). In the averaging interpretation, 50.7% and 75.2% were the lowest and highest accuracy values, respectively. In general, the achieved accuracies were significantly lower than the ones achieved by the same classifiers applied in Le Cesine site, which was expected, up to a degree, since the rule set was not fine tuned for Lago Salso but for Le Cesine.

Similarly to Le Cesine, as an additional interpretation and classifier selection process, the classifiers simultaneously belonging to the upper quartiles under both interpretations of Fig. 5.7 are identified. For those classifiers,

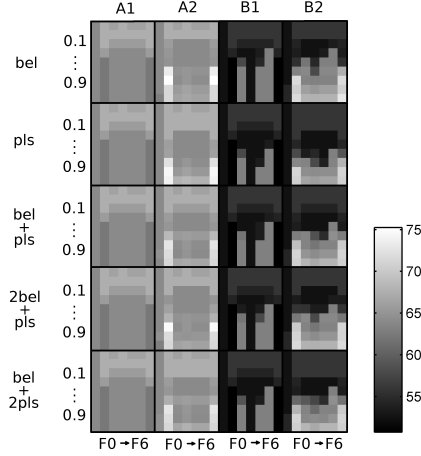


Figure 5.8.: Average accuracies (%) of the two classification interpretations of Fig. 5.7 for Lago Salso study area. Columns represent the fuzzification measures (F0–F6) for each implementation (A1, A2, B1, B2) of the classifier (Figure 5.2), whereas rows the different minimum threshold values for single classes (0.1–0.9) for each selection criterion (*bel*, *pls*, or combination).

the normalized difference in accuracy, ND_A , is calculated from the accuracies under the two interpretations. The resulting ND_A values of the selected classifiers are shown in Fig. 5.9. No classifiers achieved the exact same performance under both interpretations, thus ND_A values larger than 0 are returned, in particular $ND_A \in [0.156, 0.216]$. Furthermore, as in Le Cesine, it is noticed that a higher number of classifiers are selected for implementations A where lidar data were ignored than for implementations B where lidar data were used, i.e. more classifiers were common in the upper quartile under both interpretations for the former case. Among the selected classifiers, there are some common ones with the classifiers selected for Le Cesine (Fig. 5.5), for both implementations of using or neglecting lidar information, further supporting the direct transferability of the approach to different sites. They include the classifier with F5 method, ‘bel + 2pls’ as selection criterion with threshold 0.5, under B2 implementation (row 41, column 6 under B2 in Fig. 5.5 and 5.9), as well as classifiers with methods F2, F4, and F5, ‘bel’ as selection criterion with threshold 0.2, under A2 implementation (row 2, columns 3, 5, and 6 under A2 in Fig. 5.5 and 5.9).

Fig. 5.10 depicts the correlation between the classification results in Le

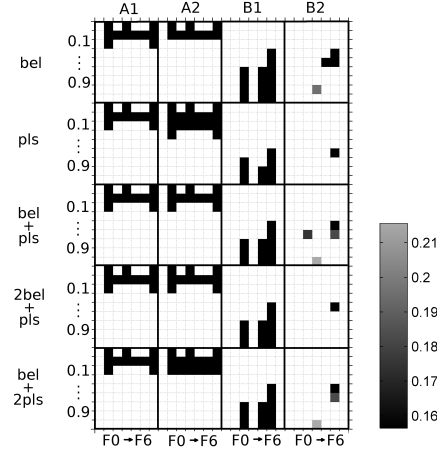
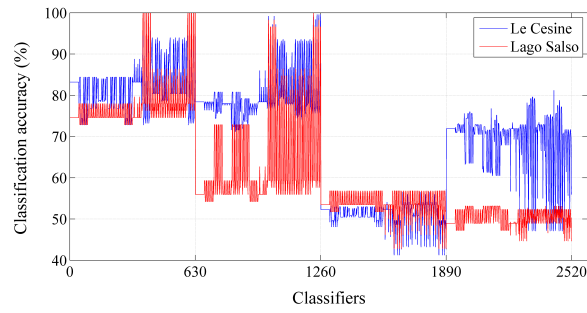
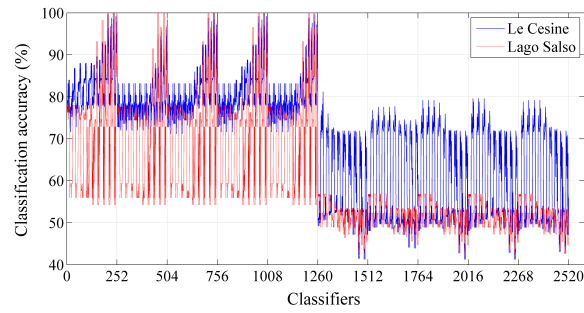


Figure 5.9.: Normalized difference of the two main classification interpretations for Lago Salso study area. Only the upper quartile classifiers under both interpretations are selected. Columns represent the fuzzification measures (F0–F6) for each implementation (A1, A2, B1, B2) of the classifier (Figure 5.2), whereas rows the different minimum threshold values for single classes (0.1–0.9) for each selection criterion (*bel*, *pls*, or combination).

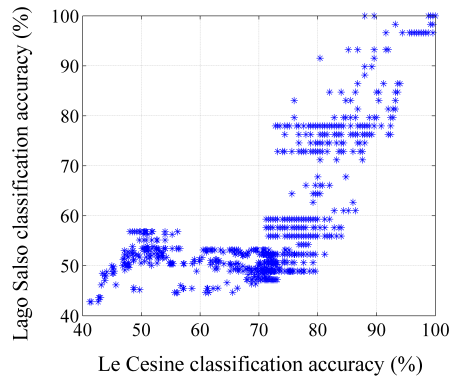
Cesine and Lago Salso, drawing the accuracies of all classifiers under the interpretations tolerant to (Fig. 5.3a and 5.7a) and penalizing (Fig. 5.3b and 5.7b) multiple classes. Fig. 5.10a draws the classifier results scanning Fig. 5.3 and 5.7 column per column, i.e. drawing all selection criteria and thresholds, for each fuzzification method. The first 630 classifiers represent implementations A1 and A2 (without lidar) from the interpretation tolerant to multiple classes, the next 630 implementations B1 and B2 from the same interpretation, whereas the next 1260 the respective classifiers from the interpretation penalizing multiple classes. As seen, the classification results for the two sites follow, in general, similar patterns for the first interpretation, where implementations A2 and B2, with uncertainty in the rule outcome, outperform the respective crisp outcome ones for both sites. Under the penalizing interpretation (classifiers 1261–2520), higher classification accuracies are achieved in Le Cesine for implementations using the lidar data than Lago Salso, as previously; however, this pattern is reversed for implementations ignoring the lidar data, where the classification accuracies achieved for Lago Salso are higher than for Le Cesine site.



(a)



(b)



(c)

Figure 5.10.: Correlation between the classifier results for Le Cesine and Lago Salso, based on results shown in Fig. 5.3 and 5.7. Fig. 5.3a and 5.7a are crossed (a) column per column or (b) row per row; the same is repeated for Fig. 5.3b and 5.7b. (c) The accuracies of the classifiers applied in the two sites are also provided in a scatter diagram.

Fig. 5.10b presents the same data, drawing the classifier accuracies row per row, for the interpretations tolerant to (classifiers 1–1260) and penaliz-

ing (classifiers 1261–2520) multiple classes. It is clear that the results for the two sites follow similar patterns as far as the threshold selection criteria are regarded. As an example, classifiers 1–252, adopting maximum belief as the selection criterion, show trends of increasing value as the selection threshold increases from 0.1 to 0.9, for the different fuzzification methods and implementations. The opposite trend is followed under the interpretation penalizing multiple classes; however, the pattern is still similar for the two sites. Fig. 5.10c draws a scatter diagram of the classifier accuracies for the two sites. The Pearson product-moment correlation coefficient [375] has been calculated as a means to quantify the degree of correlation of the results between the two sites, as

$$\rho(X, Y) = \frac{\text{cov}(X, Y)}{\sigma(X)\sigma(Y)} = \frac{\sum_{i=1}^N (x_i - \mu_x)(y_i - \mu_y)}{\sqrt{\sum_{i=1}^N (x_i - \mu_x)^2} \sqrt{\sum_{i=1}^N (y_i - \mu_y)^2}}, \quad (5.13)$$

where N stands for the total number of classifiers ($N = 2520$); x_i, y_i for the classifier accuracies for Le Cesine and Lago Salso sites, respectively, i, \dots, N ; $\text{cov}(X, Y)$ for the covariance of the classifiers of the two sites; $\sigma(X)$ and $\sigma(Y)$ for the standard deviations of the classifier accuracy values for Le Cesine and Lago Salso, respectively, whereas μ_x and μ_y for their respective average values. It was found that $\rho(X, Y) = 0.6791$, demonstrating a moderate to good correlation between the classification accuracies of the two sites. In fact, good accordance of Le Cesine accuracies to Lago Salso is observed in Fig. 5.10c for classifiers with performance lower than 55% or higher than 75%, whereas Lago Salso accuracies are inferior to Le Cesine for the rest of the value range, between 55% and 75%.

B. Performance of the fuzzy methods

Many fuzzy classifiers have outperformed the respective crisp ones under all interpretations and implementations, as shown in Fig. 5.7, 5.8, and 5.9. More specifically, most classifiers with F2, F4, and F5 methods seem to outperform the crisp classifiers (F0) for implementations with lidar data (B1 and B2) under all interpretations, especially for high selection criterion threshold values, as shown from their brighter colours in Fig. 5.7 and 5.8 than the crisp classifiers. In particular, for the B1 and B2 implementations, fuzzy F2, F4, and F5 classifiers with threshold values > 0.5 perform bet-

ter than the respective crisp ones by around 20% under interpretations of Fig. 5.7a and 5.8, and around 10% in Fig. 5.7b; in addition, they achieve a low normalized difference value of around 0.16, in comparison with the respective crisp classifiers that are not even included in the upper performance quartile (Fig. 5.9). Specifically under the normalized difference interpretation (Fig. 5.9), F5 seems to outperform the other methods in B1 and B2 implementations, with a higher number of classifiers and lower ND_A values. On the other hand, classifiers with F1 and F6 methods perform better than the respective crisp classifiers in A1 and A2 implementations, whereas classifiers with all fuzzification methods outperform the crisp classifiers in implementations A1 and A2, for low selection criterion threshold values. In particular, for both A and B implementations, under the normalized difference interpretation of Fig. 5.9, no crisp classifier has even been selected among the ones in the upper quartiles under the two main interpretations of Fig. 5.7.

Table 5.8 reports the highest achieved accuracies by the fuzzy classifiers in comparison with the respective crisp ones, for implementations without (A) and with lidar (B), under the interpretations tolerant to and penalizing incorrect classes within multiple ones, as well as the averaging interpretation. The crisp classification assimilates the results from the state-of-the-art methodology described in [52, 53]. As seen, for every implementation and under any interpretation of accuracy, DS fuzzy classifiers were implemented that outperform the reference crisp ones.

Table 5.8.: Maximum classification accuracies (%) achieved by the crisp and the fuzzy classifiers for implementations without and with lidar data, under interpretations tolerant to and penalizing incorrect classes in multiple ones, as well as the averaging interpretation of the two.

		Crisp	Fuzzy
Multiple class tolerant interpr.	Without lidar (A)	74.6	100
	With lidar (B)	55.9	100
Multiple class penalizing interpr.	Without lidar (A)	53.5	56.8
	With lidar (B)	49.9	53.2
Averaging interpr.	Without lidar (A)	64.0	75.2
	With lidar (B)	52.4	72.8

The highest performance under the interpretation tolerant to multiple

classes (Fig. 5.7a) and the averaging one (Fig. 5.8) was achieved by classifiers using F1 and F6 methods in implementations A2, equal to 100% and 75.2%, respectively. The same classifiers are identified as the highest performing under the normalized difference interpretation as well, with $ND_A = 0.157$. Under the interpretation penalizing commission errors in multiple classes (Fig. 5.7b), the maximum accuracies were found in implementations A1 and A2, including all fuzzification methods. The outcomes support the advantages that the DS fuzzification scheme has over a crisp rule-based classification. This notion is further substantiated by the parallel higher performance of the implementations with rules with soft outcomes (A2 and B2), over the ones with definite outcomes, that demonstrates successful uncertainty handling.

The GHC map extracted by the best performing classifier under the averaging interpretation (Fig. 5.8) is shown in Fig. 5.11a, together with the validated map used as reference (Fig. 5.11b). The classifier followed A2 implementation with F1 fuzzification method and selection of maximum belief as criterion and 0.7 as threshold. The classifier was among the highest performing ones under the interpretations tolerant to multiple classes (OA 98.3%) and penalizing them (OA 52.2%). Eight single classes were identified, together with 13 multiple ones. However, the maximum class discrimination level was achieved, since the same number of single classes were returned by the best classifier under the interpretation penalizing commission errors in multiple classes. Their difference was the larger number of multiple classes in the former classifier, resulting in its lower OA under the penalizing interpretation.

C. Availability of lidar data

A notable difference with the results in Le Cesine site was the fact that implementations not involving lidar information (A1 and A2) outperformed consistently the respective implementations using lidar (B1 and B2). This contradicts the expectation that additional information leads to further discrimination and higher accuracies under the interpretation penalizing commission errors in multiple classes (Fig. 5.7b). The use of lidar information deteriorated the performance of the classifiers. In particular, lidar provided lower object heights than the actual ones; characteristic implication of that

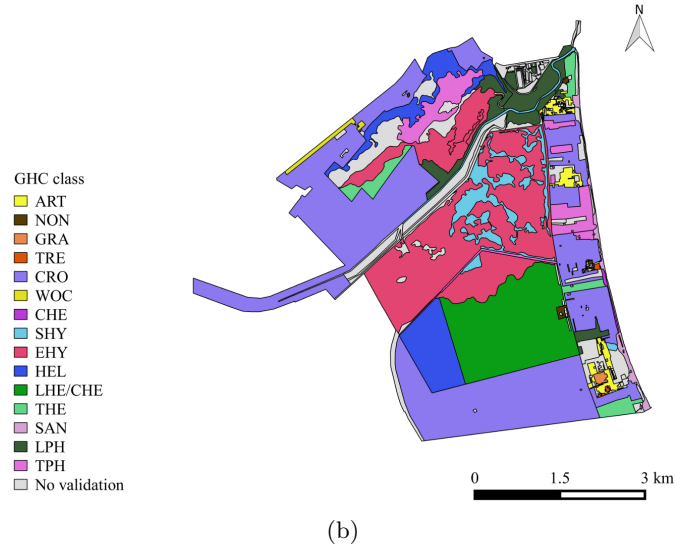
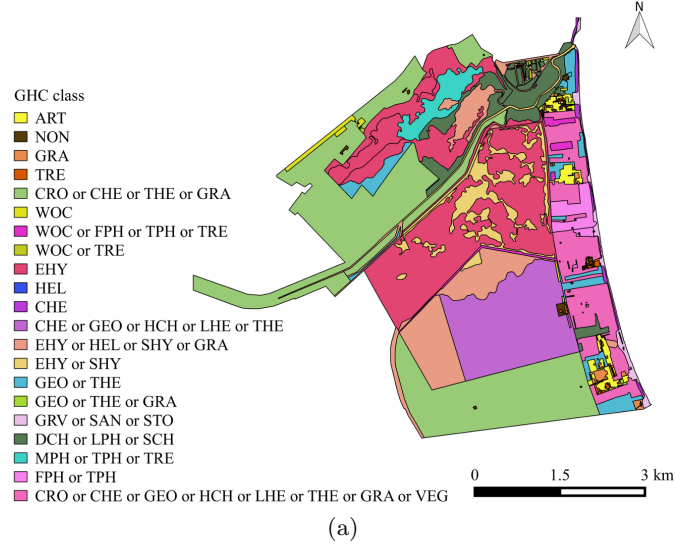


Figure 5.11.: GHC map resulting from the best performing fuzzy DS classifier under the averaging interpretation (a) and GHC validated classes (b) for Lago Salso.

was the erroneous classification of several LPH (0.3–0.6 m) objects as SCH (0.05–0.3 m) or DCH (<0.05 m) and of TPH (2–5 m) objects as MPH (0.6–2 m). This is an indication that the object height models derived by the lidar data do not coincide well with information on the ground. This might be due to technical and noise issues during the extraction of the models, or due to lidar data being captured in different dates to the validation ones (2009

and 2011–2012, respectively, Section 4.2.3). Lower height values derived by lidar compared with the field data may indicate changes in vegetated structure, in particular vegetation growing, during the two-year period from the capturing of lidar information to the validation field campaigns in Lago Salso (in Le Cesine lidar and validation data were from the same year, as discussed in Section 4.2.2), creating the aforementioned misclassifications. Therefore, an up-to-date lidar data set or a more focused rule fine tuning for Lago Salso area seems to be required to improve the performance of implementations B1 and B2. These ideas are further supported by the fact that lidar features did not improve, but even decreased, the performance of the supervised classifiers of the previous chapter trained and tested in Lago Salso, compared with the feature sets where lidar data were not included (Section 4.4.2).

D. Uncertainty in rule outcome

In a similar manner to Le Cesine site, implementations using rules expressing uncertainty in the outcome (A2 and B2 implementations) outperformed in most cases the ones using definite rules (A1 and B1, respectively), under the interpretations tolerant to multiple classes (Fig. 5.7a) and the averaging one (Fig. 5.8). However, contrary to Le Cesine, A1 and B1 implementations provided, in general, higher accuracies under the interpretation penalizing multiple classes including incorrect single ones (Fig. 5.7b), than the respective A2 and B2 ones. In addition, B2 implementation provided a smaller number of classifiers after the masking under the normalized difference interpretation of Fig. 5.9 than B1, indicating lower consistency in the former case. Thus, membership rules more adjusted to Lago Salso particular characteristics were probably needed to lead to higher accuracies of A2 and B2 implementations than A1 and B1 under all three interpretations.

E. Class selection criteria

In this study area, little differences in accuracy were observed as far as the class selection criterion was concerned, with all criteria resulting in classifiers with similar performances. However, differentiations were observed among the selected minimum threshold values, in a similar manner to the case of Le Cesine site. In particular, the highest accuracies were achieved

by classifiers with lower values under the interpretation penalizing commission errors in multiple classes (Fig. 5.7b), and higher threshold values under the alternative interpretation (Fig. 5.7a). Average threshold values seem to be preferable in applications where an intermediate interpretation is followed, as seen from the brighter pixels in Fig. 5.8. Lower threshold values seem preferable for A1 and A2 implementations according to the normalized difference interpretation (Fig. 5.9), whereas the opposite holds for implementations B1 and B2.

F. Fusion of classifiers

Fusion of classifiers was also performed for Lago Salso, in the same manner as for Le Cesine in the previous section. Similar to Le Cesine, no increase in accuracy over the maximum values from individual classifiers was achieved from different combinations. In fact, accuracy values between the minimum and maximum accuracies of the involved single classifiers were reached, both by fusing over the different fuzzification methods or the different class selection criteria and thresholds, as described in Section 5.3.4.

5.4.3. Comparison with the supervised learning approach

Overall, two different approaches have been proposed in Chapters 4 and 5 to improve the results and efficiency of the rule-based habitat classifier described in [52, 53]. The supervised learning approach presented in the previous chapter was found effective in providing a more automatic and less labour and time consuming process, where the rules are extracted from the data without requiring user input. The Dempster–Shafer approach was proposed to counteract missing information, noise afflicted data, and vague or inaccurate rules by the experts, thus handle uncertainty caused by different real-life factors. Both approaches proved successful in providing comparative advantages in those aspects over the state-of-the-art land cover to habitat classification method by Adamo *et al.* [52, 53].

As far as the achieved accuracies are regarded, both approaches provided classifiers outperforming the crisp rule-based classifier of reference. Accuracies up to 82.4% and 86% were provided for Le Cesine site by supervised classifiers, without or with the use of lidar data, respectively. The respective accuracies with the model derived in Le Cesine and applied in Lago Salso

reached 72.9% for both with and without the use of lidar. An additional result was derived by training the classifiers with Lago Salso data and testing them at the same site, with accuracies of up to 88.1% without and 86.4% with the use of lidar data. All these accuracies were higher than the ones reported in [52,53].

On the other hand, the accuracies from the DS fuzzy classifiers varied significantly according to the classification interpretation, arising from the provided flexibility to extract multiple classes in case not sufficient support to their separation into single ones existed. When multiple classes including the correct single one were considered as correct, higher classification accuracies than the supervised classifiers, reaching even perfect classifications, were achieved, both from Le Cesine site and the application of the rule set in Lago Salso. Although several multiple classes appeared, especially in perfect classification cases, this does not mean that all possible classes were considered. In fact, the outcomes were refined compared with the theoretical mapping performed in the first stage of the classification, where all possible classes were included (Section 5.3.1). As an example, the classifier of implementation A2 and fuzzification measure F1 with belief as the selection criterion and 0.9 as threshold achieved perfect accuracy of 100% according to the interpretation favouring multiple classes (Fig. 5.3a); whereas after the first stage of the classification, there was only one single class among the classified objects, after the second stage there were four single ones, resulting from the refinement of multiple classes. Under a different interpretation, when the single classes within multiple ones not matching the correct single one were considered as commission errors and penalized, lower accuracies than the supervised classifiers were reached. The two interpretations provide the higher and lower boundaries of accuracy estimation and may be chosen alternately depending on the application. Furthermore, in certain applications, a rational choice may lie on the average of these two extremes or a normalized difference. In the averaging case, the achieved accuracies for Le Cesine reached 72.5% and 81.2% when lidar data were considered missing and available, respectively. For Lago Salso, the respective accuracies were 75.2% and 72.8%. In the latter cases, the DS classifiers performed similarly or higher than the supervised learning ones (Section 4.4.3). Under all interpretations, DS classifiers outperforming the respective rule-based crisp ones were derived.

A notable difference between the rule-based (deductive learning) and the supervised classifiers (inductive learning) lies in the way the potential classes are taught to the system, the former being provided a priori theoretical knowledge, while the latter being taught solely from the available data. This may influence the classification results and severely affect the classifier performance. In this particular study, the rule-based classifier had the advantage of incorporating a large number of rules leading to GHC classes beyond the ones found in Le Cesine validation set. An example may be seen in Table 5.4, where the GRA, TRE, and DCH classes, not included in the validation set, were returned by the DS classifier. This fact gave the classifier the flexibility to identify classes in Lago Salso that had not been met among Le Cesine validation points. This may be seen in Table 5.9, where the classification results are shown for one of the best performing classifiers under the interpretation penalizing multiple classes. TRE, GRA, SAN, and LHE/CHE classes were able to be identified in Lago Salso up to a degree (perfectly for TRE and GRA), although not included in Le Cesine objects used to train the rule-based system. On the contrary, testing of the supervised learning model extracted for Le Cesine in Lago Salso resulted in wrong class assignments to all objects of Lago Salso of classes not present in Le Cesine.

From a different perspective of the previous notion, a supervised classifier may return a class that belongs in the training set but may be physically irrelevant to the correct one, as shown in Section 4.4.2. This is attributed to the fact that features in the supervised classifiers are handled as numerical variables with no physical meaning, thus classification occurs based on their observed value similarities. On the contrary, the DS fuzzy approach relies on the expert knowledge provided, and if consistent, no physically irrelevant classes to the validated ones are possible to occur. It is noteworthy to mention, though, that the vast majority of the incorrect classes returned by the best performing supervised classifiers in Chapter 4 were highly relevant to the respective validation classes.

A further difference of the approaches lies on the classification model inspection. Whereas in the DS fuzzy rule-based approach, a conceptual understanding of the process is straightforward, the derived models from supervised classifiers are often difficult to interpret. This is a further reason for the choice of decision tree classifiers selected among the supervised ones,

Table 5.9.: Results of one of the best performing classifier under the interpretation penalizing commission errors, for each class. The classifier applies fuzzification method F1 with less strict rule outcomes ignoring lidar data, maximum belief as selection criterion and threshold value 0.1. The number of ground truth samples, together with the absolute correct classifications of the method under this interpretation are given, for each GHC class. The percentage of correct classifications is also shown in the last column.

GHC	Ground truth no.	Correct Fuzzy	Acc. Fuzzy (%)
ART	3	3	100
NON	4	4	100
TRE	3	3	100
GRA	1	1	100
CRO	7	6	85.71
WOC	2	2	100
SAN	2	0.67	33.33
SHY	7	1	14.29
EHY	5	5	100
HEL	2	0	0
LHE/CHE	1	0.2	20
CHE	1	1	100
THE	4	2	50
LPH	10	3.33	33.33
TPH	7	1.33	19.05
Total	59	33.53	56.84

since their produced model can be visually inspected in a more straightforward manner than the one from SVM or ANN classifiers. The flexibility of changing a parameter in the model is also higher in the rule-based approach, including the rules themselves and also the classification parameters, such as the selection class criterion and the respective minimum threshold values. However, this is also related to higher labour and time consuming effort in comparison with the more automated supervised learning.

Overall, both classification approaches performed significantly better than the state-of-the-art crisp rule-based classifier used as reference [52,53]. They have particular advantages and limitations compared to each other, both in the extracted classification results and their characteristics. Both approaches provide an enhanced solution for habitat classification using remote sensing data and land cover reference maps that seems to be useful for wide use and application in different study areas. The choice of the most suitable approach depends on the requirements and expectations dictated

by the specific application under study. These include the interpretation of accurate classification and class preferences, limitations in time and labour resources, and/or the desirable degree of possible parameterization.

5.5. Conclusions

In this chapter, a rule-based classification methodology, built on DS theory principles and employing fuzzy sets, has been proposed for habitat mapping, using remote sensing data. A pre-existing LC map was considered and its conversion into a habitat map was attempted, incorporating domain expert rules. No previous attempt has been made so far to involve evidential reasoning in a LC to habitat classification task, providing an efficient framework for handling uncertainty and missing information.

Comparison with the reference state-of-the-art methodology by Adamo *et al.* [52, 53] proved the advantageous characteristics of the introduction of DS theory and fuzzy logic in a crisp rule-based classification framework. Linear fuzzification methods embodied in the framework notably improved the results of crisp classification. The DS framework allowed the expression of rules with soft outcomes and efficiently handled the uncertainty from such rules, outperforming the respective classifiers using rules with crisp outcomes. In addition, the use of multiple classes, when sufficient support for single class discrimination was not provided, increased the efficiency of the approach and demonstrated its ability in handling missing information.

The use of multiple classes initiated the consideration of different interpretations of classification accuracy, addressing the particular preferences and requirements of different application areas of the approach. Under all interpretations, appropriate DS fuzzy classifiers were developed outperforming the respective crisp ones. Class selection criteria based on maximum belief, plausibility, or combinations of the two were proposed, together with a variety of criterion threshold values. Large threshold values proved more effective under the interpretation considering as correct multiple classes that contained incorrect single ones together with the correct one, whereas small values more suitable under interpretations penalizing such multiple classes. Fusion of classifiers was performed in different ways, without though demonstrating better accuracies than the top performing individual ones. Finally, the approach was tested to a second site, without further fine tuning, demon-

strating its advantages over the respective crisp classification.

Potential future research directions may involve the development and evaluation of non-linear fuzzification methods besides the linear ones. A second focus point might include design and development of alternative approaches for classifier fusion, in an effort to counteract the limitations found in Dempster rule of combination [351, 374].

Overall, the proposed approach seems to provide an efficient framework for the conversion of land cover into habitat classes using remote sensing data and prior knowledge, largely beneficial for sustainability management, conservation planning, and biodiversity monitoring. It is able to successfully handle uncertainty and missing information, and flexible to be parameterized and adapted to user preferences and application requirements. The permission of multiple classes in the classification results, when enough confidence on their refinement into single ones does not exist, may offer the potential to field ecologists and site managers to identify landscape objects that require further investigation and focus.

6. Thesis summary, conclusions, and future research

6.1. Summary

Biodiversity constitutes a crucial factor in ecosystem stability and human well-being. The thesis demonstrated the potential of remote sensing data, derived mainly from satellite sensors, in monitoring different aspects of biodiversity. Emphasis was given on estimation of vegetation height and classification of habitat categories, as core elements linked to biodiversity, using very high resolution (VHR) multispectral data. In particular, the following main issues have been studied:

- A wide number of recent state-of-the-art remote sensing methods related to biodiversity monitoring were identified in the literature, reviewed, and linked (i) to a number of headline indicators proposed by the United Nations Convention on Biological Diversity (CBD), to describe biodiversity status and trends, and consequently, (ii) to the Aichi targets defined by CBD for global biodiversity preservation (Chapter 2). Such link has rarely been explicitly attempted before. The methods were sorted based on their accuracy, when feasible, and connected to all six CBD headline indicators identified as able to be calculated through remote sensing. Capacity and limitations of the methods were discussed, and future directions were proposed, to decrease the knowledge gap between the remote sensing and the ecology, conservation biology, site manager, and policy making communities.
- A cost and resource effective approach for vegetation height estimation was proposed, based on texture analysis of satellite VHR multispectral imagery (Chapter 3). The method extended the study limits of previous approaches by evaluating synergies of data from two dates,

besides single-date images, objects of various vegetation types, and height categories ranging from less than 5 cm to several tens of metres. A number of texture features were proposed, based on local variance, entropy, and local binary patterns. A wide range of processing algorithms, including handling of missing values, outlier removal, data normalization, and dimensionality reduction with data transformation and feature selection, and several supervised classifiers were employed and evaluated.

- A supervised learning approach for the conversion of land cover to habitat classes using remote sensing data was proposed (Chapter 4), to provide a labour and time effective alternative to previous reference rule-based classification studies [52,53]. A number of features describing spectral, morphological, topological, and structural properties of the objects were extracted. In addition, a methodology to convert land cover classes from characters (string variables) to interval-scaled numerical values, in order to be directly fed as input to the supervised classifiers, expressing inter- and intra-class variabilities, was proposed. Various classifiers were employed, ranging from decision tree single and ensemble ones to support vector machines and artificial neural networks. The approach was evaluated at two study areas individually, whereas, in addition, the transferability of the model extracted in one area was tested in the other.
- A rule-based approach for the conversion of land cover to habitat classes was additionally proposed, where evidential reasoning and fuzzy logic were employed to handle uncertainty from missing information, vague expert rules, and data noise affliction, and enhance information fusion (Chapter 5). Classifiers built around the principles of Dempster–Shafer theory were introduced, and a number of linear fuzzification methods were proposed and evaluated, in comparison with the respective crisp classifier. The approach allowed the extraction of multiple classes, in case strong support for the discrimination of constituent single ones was not provided, and offered the flexibility of the classifier adaptation and parameterization to the particular user preferences and application requirements, as far as the class selection criteria were regarded. The approach was evaluated at two study ar-

eas, the former being the one where the rule set was defined and the latter used to test its transferability to different areas.

6.2. Conclusions

The most important conclusions extracted by the outcomes of this research can be summarized as follows:

- Remote sensing data offer wide potential in monitoring several characteristics related to biodiversity, including habitat extent, species distribution, and ecosystem services. Numerous effective methods have been presented. The operational use of remote sensing data, though, remains restricted and wide knowledge gap exists between remote sensing and user community.
- No single sensor data and processing methods have been proven universally high performing. Each application requires careful selection of both data (e.g. lidar favour 3D structure studies, whereas hyperspectral species discrimination) and methods (e.g. object-based methods for habitat characterization over pixel-based ones), or effective synergies.
- Texture features based on local variance, entropy, and local binary patterns, derived from passive sensor satellite imagery, can be used as effective surrogates of active sensor (e.g. lidar) information in vegetation height estimation studies. Coupled with dimensionality reduction through either feature selection or transformation, a small feature set can be formed providing significant accuracies in height discrimination among diverse types of vegetation at different seasons.
- Decision tree ensemble classifiers, in particular bagging trees, have been consistently among the top performing supervised classifiers in both vegetation height estimation and habitat classification applications.
- The proposed methodology for land cover class name conversion to interval-scaled variables was able to successfully express inter- and

intra-class variabilities under the supervised learning habitat classification approach. As a result, besides the high achieved accuracies, the majority of misclassifications mostly occurred among highly relevant classes.

- The proposed supervised learning approach was able to provide a more accurate and automated, and less time and labour demanding classification approach, compared with the rule-based classifier by Adamo *et al.* [52, 53] used as reference. Classification accuracies were higher in both evaluated study areas than the reference study. This included the application of the model extracted in one area to the other, supporting the potential for wider applicability of the approach.
- The rule-based classification approach based on Dempster–Shafer theory and linear fuzzification methods provided higher accuracies than the respective crisp classifier, using the same rule set. The proposed framework was flexible in providing multiple classes when enough support for the discrimination of single ones was not available, offering the possibility of different accuracy interpretations depending on user and application particular requirements. Thorough experimentation on class selection criteria indicated the most appropriate selection criteria for each interpretation. It also allowed the expression of uncertainty and degree of confidence in rule outcomes defined by the experts.
- Both the proposed Dempster–Shafer fuzzy and the supervised learning approaches outperformed the reference rule-based classifiers in [52, 53]. Between the two, the DS fuzzy approach offered higher parameterization ability to user defined criteria than the supervised learning one, e.g. by offering high performing classifiers for various levels of desirable class separability into single classes, allowing the formation of accurate classifications for different applications. In addition, the DS fuzzy approach allowed the extraction of classes outside the validation data set, whereas the supervised approach was restricted to the ones used for training. On the contrary, the supervised approach offered a more automated process, requiring no a priori expert knowledge and trial-and-error fine tuning used in rule-based classifiers, thus resulting

in a faster implementation.

- Trained to Le Cesine and applied to Lago Salso site, the two approaches brought similar results for certain classes. For instance, as can be seen from Tables 4.10 and 5.9, both the supervised classifier and the rule-based one under the interpretation penalizing multiple classes had perfect user's accuracies (no commission error) for classes NON, EHY, and CHE. For most of the other classes, the former classifier outperformed the latter one, both not using lidar data. The rule-based classifier, though, was able to perfectly (TRE, GRA) or partially (SAN, LHE/CHE) identify classes completely missed by the supervised classifier, since not included in the training set of the latter.
- Overall, it has been shown that remote sensing data offer wide potential in biodiversity monitoring studies, with very high resolution optical imagery, in particular, proving effective in vegetation height estimation and habitat classification. However, these passive sensor data have limitations in characterizing the vertical structure with a high level of accuracy required for some applications, such as forest carbon stock assessment, and cannot fully replace active sensor data, such as lidar. In addition, spectral features from VHR imagery alone may prove inadequate for applications such as habitat classification and need to be coupled with morphological, topological, or structural features. In most tasks, precise pre-processing is necessary to minimize geometric and radiometric distortions of the remote sensing data and allow the synergistic use of multiple images. Cloud free conditions are a further requirement for the use of optical data.

6.3. Future research

Although satisfactory results have been achieved by the methodologies proposed in this thesis, interesting future research directions and opportunities can be identified to further investigate and expand its outcomes. Some future work suggestions include the following:

- In a generic sense, new research opportunities and higher capacity for biodiversity monitoring are constantly created from upcoming satellite missions, providing enhanced combinations of spatial resolution,

spectral properties, and revisit time. Studies on new passive and active sensor data fusion and processing methodologies are expected to exploit such unprecedented potential for operational monitoring on a wide scale.

- Data with different spatial resolutions and angles of sun during image capturing can be employed to study the effects of scale and different illumination conditions on the accuracy of the height estimation approach of Chapter 3.
- Further improvement to the supervised learning approach might be brought through the introduction of constraints on the possible outcome based on the land cover features, to eliminate irrelevant habitat classes, e.g. by incorporating post-classification processes.
- Development and incorporation of non-linear fuzzification methods in addition to the linear ones proposed in Section 5.2.2, may further improve the performance of the Dempster–Shafer fuzzy approach.
- Development of new classifier fusion techniques, as alternatives to the Dempster rule of combination described in Section 5.2.1, might lead to classifiers with higher performance than the best individual ones.

Bibliography

- [1] J. Pearsall, Ed., *Concise Oxford English Dictionary*, 10th ed. Oxford: Oxford University Press, 2001.
- [2] B. J. Cardinale, J. E. Duffy *et al.*, “Biodiversity loss and its impact on humanity,” *Nature*, vol. 486, pp. 59–67, Jun. 2012.
- [3] P. Balvanera, A. B. Pfisterer *et al.*, “Quantifying the evidence for biodiversity effects on ecosystem functioning and services,” *Ecol. Lett.*, vol. 9, no. 10, pp. 1146–1156, Oct. 2006.
- [4] T. W. Gillespie, G. M. Foody, D. Rocchini, A. P. Giorgi, and S. Saatchi, “Measuring and modelling biodiversity from space,” *Prog. Phys. Geog.*, vol. 32, no. 2, pp. 203–221, Apr. 2008.
- [5] D. C. Duro, N. C. Coops, M. A. Wulder, and T. Han, “Development of a large area biodiversity monitoring system driven by remote sensing,” *Prog. Phys. Geog.*, vol. 31, no. 3, pp. 235–260, Jun. 2007.
- [6] S. H. M. Butchart, M. Walpole *et al.*, “Global biodiversity: indicators of recent declines,” *Science*, vol. 328, no. 5982, pp. 1164–1168, May 2010.
- [7] EEA, “Halting the loss of biodiversity by 2010: proposal for a first set of indicators to monitor progress in europe,” European Environment Agency, Copenhagen, Tech. Rep. 11, 2007.
- [8] P. Duelli and M. K. Obrist, “Biodiversity indicators: the choice of values and measures,” *Agr. Ecosyst. Environ.*, vol. 98, no. 1–3, pp. 87–98, Sep. 2003.
- [9] C. K. Feld, P. M. da Silva *et al.*, “Indicators of biodiversity and ecosystem services: a synthesis across ecosystems and spatial scales,” *Oikos*, vol. 118, no. 12, pp. 1862–1871, Dec. 2009.

- [10] H. Strand, R. Höft *et al.*, “Sourcebook on Remote Sensing and Biodiversity Indicators,” Secretariat of the Convention on Biological Diversity, Montreal, Tech. Rep. 32, 2007.
- [11] V. Kati, P. Devillers *et al.*, “Testing the value of six taxonomic groups as biodiversity indicators at a local scale,” *Conserv. Biol.*, vol. 18, no. 3, pp. 667–675, Jun. 2004.
- [12] D. B. Lindenmayer, C. R. Margules, and D. B. Botkin, “Indicators of biodiversity for ecologically sustainable forest management,” *Conserv. Biol.*, vol. 14, no. 4, pp. 941–950, Aug. 2000.
- [13] B. G. Jonsson and M. Jonsell, “Exploring potential biodiversity indicators in boreal forests,” *Biodivers. Conserv.*, vol. 8, no. 10, pp. 1417–1433, Oct. 1999.
- [14] 2010BIP, “Biodiversity indicators and the 2010 Target: Experiences and lessons learnt from the 2010 Biodiversity Indicators Partnership,” Secretariat of the Convention on Biological Diversity, Montreal, Tech. Rep. 53, 2010.
- [15] AHTEG, “Report of the Ad Hoc Technical Expert Group on Indicators for the Strategic Plan for Biodiversity 2011-2020,” Ad Hoc Technical Expert Group on Indicators for the Strategic Plan for Biodiversity 2011-2020, High Wycombe, United Kingdom, Tech. Rep., 2011.
- [16] H. M. Pereira, S. Ferrier *et al.*, “Essential biodiversity variables,” *Science*, vol. 339, pp. 277–278, Jan. 2013.
- [17] T. M. Brooks, R. A. Mittermeier, G. A. B. da Fonseca, J. Gerlach, and M. Hoffmann, “Global biodiversity conservation priorities,” *Science*, vol. 313, pp. 58–61, Jul. 2006.
- [18] CBD, “Report of the tenth meeting of the conference of the parties to the convention on biological diversity,” Convention on Biological Diversity, Nagoya, Japan, Tech. Rep., October 2010.
- [19] —, “Report of the eleventh meeting of the conference of the parties to the convention on biological diversity,” Convention on Biological Diversity, Hyderabad, India, Tech. Rep., October 2012.

- [20] EEA, “Streamlining european biodiversity indicators 2020: Building a future on lessons learnt from the sebi 2010 process,” European Environment Agency, Copenhagen, Tech. Rep. 11, 2012.
- [21] G. M. Buchanan, A. Nelson, P. Mayaux, A. Hartley, and P. F. Donald, “Delivering a global, terrestrial, biodiversity observation system through remote sensing,” *Conserv. Biol.*, vol. 23, no. 2, pp. 499–502, Apr. 2009.
- [22] Z. Gong, H. Gong, W. Zhao, X. Li, and Z. Hu, “Using RS and GIS to monitoring Beijing wetland resources evolution,” in *Int. Geoscience and Remote Sensing Symp.* Barcelona: IEEE, 2007, pp. 4596–4599.
- [23] H. Nagendra, R. Lucas *et al.*, “Remote sensing for conservation monitoring: Assessing protected areas, habitat extent, habitat condition, species diversity, and threats,” *Ecol. Indic.*, vol. 33, pp. 45–59, Oct. 2013.
- [24] K. M. Bergen, S. J. Goetz *et al.*, “Remote sensing of vegetation 3-D structure for biodiversity and habitat: Review and implications for lidar and radar spaceborne missions,” *J. Geophys. Res.-Bioge.*, vol. 114, no. G2, p. G00E06, Jun. 2009.
- [25] W. Turner, S. Spector *et al.*, “Remote sensing for biodiversity science and conservation,” *Trends Ecol. Evol.*, vol. 18, no. 6, pp. 306–314, Jun. 2003.
- [26] H. Nagendra, “Using remote sensing to assess biodiversity,” *Int. J. Remote Sens.*, vol. 22, no. 12, pp. 2377–2400, 2001.
- [27] C. Secades, B. O’Connor, C. Brown, and M. Walpole, “Earth Observation for biodiversity Monitoring: A review of current approaches and future opportunities for tracking progress towards the Aichi Biodiversity Targets,” Secretariat of the Convention on Biological Diversity, Montreal, Tech. Rep. 72, 2014.
- [28] W. Xiangping, O. Shuai, J. S. Osbert, and F. Jingyun, “Forest biomass patterns across northeast China are strongly shaped by forest height,” *Forest Ecol. Manag.*, vol. 293, pp. 149–160, Apr. 2013.

- [29] M. Dees, C. Straub, and B. Koch, “Can biodiversity study benefit from information on the vertical structure of forests? Utility of LiDAR remote sensing,” *Curr. Sci.*, vol. 102, no. 8, pp. 1181–1187, Apr. 2012.
- [30] E. Næsset, “Determination of mean tree height of forest stands by digital photogrammetry,” *Scand. J. Forest Res.*, vol. 17, no. 5, pp. 446–459, Jan. 2002.
- [31] B. St-Onge, Y. Hu, and C. Vega, “Mapping the height and above-ground biomass of a mixed forest using lidar and stereo Ikonos images,” *Int. J. Remote Sens.*, vol. 29, no. 5, pp. 1277–1294, Mar. 2008.
- [32] W. S. Walker, J. M. Kellndorfer, E. LaPoint, M. Hoppus, and J. Westfall, “An empirical InSAR-optical fusion approach to mapping vegetation canopy height,” *Remote Sens. Environ.*, vol. 109, no. 4, pp. 482–499, Aug. 2007.
- [33] A. Di Gregorio and L. J. M. Jansen, “Land Cover Classification System (LCCS): classification concepts and user manual for software version 2,” FAO Environment and Natural Resources Service Series, Rome, Tech. Rep. 8, 2005.
- [34] R. G. H. Bunce, M. J. Metzger *et al.*, “A standardized procedure for surveillance and monitoring European habitats and provision of spatial data,” *Landscape Ecol.*, vol. 23, no. 1, pp. 11–25, Jan. 2008.
- [35] X. Wang, H. Huang *et al.*, “Forest canopy height extraction in rugged areas with ICESat/GLAS data,” *IEEE T. Geosci. Remote*, vol. 52, no. 8, pp. 4650–4657, Aug. 2014.
- [36] A. Arnaubec, A. Roueff, P. C. Dubois-Fernandez, and P. Réfrégier, “Vegetation height estimation precision with compact PolInSAR and homogeneous random volume over ground model,” *IEEE Trans. Geosci. Remote Sens.*, vol. 52, no. 3, pp. 1879–1891, Mar. 2014.
- [37] R. J. M. Hans-Erik Andersen, Stephen E. Reutebuch, “Estimation of tree heights and stand volume using an airborne lidar system,” *Can. J. Remote Sens.*, vol. 32, no. 5, pp. 355–366, Oct. 2006.

- [38] D. N. M. Donoghue and P. J. Watt, “Using LiDAR to compare forest height estimates from IKONOS and Landsat ETM+ data in Sitka spruce plantation forests,” *Int. J. Remote Sens.*, vol. 27, no. 11, pp. 2161–2175, Jun. 2006.
- [39] M. C. Anderson, C. M. U. Neale *et al.*, “Upscaling ground observations of vegetation water content, canopy height, and leaf area index during SMEX02 using aircraft and Landsat imagery,” *Remote Sens. Environ.*, vol. 92, no. 4, pp. 447–464, Sep. 2004.
- [40] P. T. Wolter, P. A. Townsend, and B. R. Sturtevant, “Estimation of forest structural parameters using 5 and 10 meter SPOT-5 satellite data,” *Remote Sens. Environ.*, vol. 113, no. 9, pp. 2019–2036, Sep. 2009.
- [41] F. Kayitakire, C. Hamel, and P. Defourny, “Retrieving forest structure variables based on image texture analysis and IKONOS-2 imagery,” *Remote Sens. Environ.*, vol. 102, no. 3–4, pp. 390–401, Jun. 2006.
- [42] G. J. McDermid, S. E. Franklin, and E. F. LeDrew, “Remote sensing for large-area habitat mapping,” *Prog. Phys. Geog.*, vol. 29, no. 4, pp. 449–474, Dec. 2005.
- [43] R. G. H. Bunce, M. M. B. Bogers *et al.*, “The significance of habitats as indicators of biodiversity and their link to species,” *Ecol. Indic.*, vol. 33, pp. 19–25, Oct. 2013.
- [44] D. S. Schmeller, “European species and habitat monitoring: where are we now?” *Biodivers. Conserv.*, vol. 17, no. 14, pp. 3321–3326, Dec. 2008.
- [45] S. Lengyel, E. Déri *et al.*, “Habitat monitoring in Europe: a description of current practices,” *Biodivers. Conserv.*, vol. 17, no. 14, pp. 3327–3339, Dec. 2008.
- [46] R. M. Lucas, K. Medcalf *et al.*, “Updating the Phase 1 habitat map of Wales, UK, using satellite sensor data,” *ISPRS J. Photogramm.*, vol. 66, no. 1, pp. 81–102, Nov. 2011.

- [47] M. Bock, P. Xofis, J. Mitchley, G. Rossner, and M. Wissen, "Object-oriented methods for habitat mapping at multiple scales – Case studies from Northern Germany and Wye Downs, UK," *J. Nat. Conserv.*, vol. 13, no. 2–3, pp. 75–89, Jul. 2005.
- [48] D. R. Mishra, S. Narumalani, D. Rundquist, and M. Lawson, "High-resolution ocean color remote sensing of benthic habitats: a case study at the Roatan island, Honduras," *IEEE T. Geosci. Remote*, vol. 43, no. 7, pp. 1592–1604, Jul. 2005.
- [49] V. Tomaselli, P. Dimopoulos *et al.*, "Translating land cover/land use classifications to habitat taxonomies for landscape monitoring: a Mediterranean assessment," *Landscape Ecol.*, vol. 28, no. 5, pp. 905–930, May 2013.
- [50] D. Moss and C. E. Davies, "Cross-references between the EUNIS habitat classification and the nomenclature of CORINE land cover," NERC/CEH, Huntingdon, UK, Tech. Rep., 2002.
- [51] V. Kosmidou, Z. I. Petrou *et al.*, "Harmonization of the Land Cover Classification System (LCCS) with the General Habitat Categories (GHC) classification system," *Ecol. Indic.*, vol. 36, pp. 290–300, Jan. 2014.
- [52] M. Adamo, C. Tarantino *et al.*, "Land cover to habitat map translation: Disambiguation rules based on Earth Observation data," in *Int. Geoscience and Remote Sensing Symp.* Melbourne: IEEE, 2013, pp. 3817–3820.
- [53] —, "Expert knowledge for translating land cover/use maps to General Habitat Categories (GHC)," *Landscape Ecol.*, vol. 29, no. 6, pp. 1045–1067, Jul. 2014.
- [54] A. P. Dempster, "Upper and lower probabilities induced by a multivalued mapping," *Annals Math. Stat.*, vol. 38, no. 2, pp. 325–339, 1967.
- [55] G. Shafer, *A Mathematical Theory of Evidence*. Princeton, NJ: Princeton University Press, 1976.

- [56] GEO BON, “Adequacy of biodiversity observation systems to support the cbd 2020 targets,” Group on Earth Observations Biodiversity Observation Network, Pretoria, South Africa, Tech. Rep., 2011.
- [57] H. M. Pereira, L. M. Navarro, and I. S. Martins, “Global biodiversity change: The bad, the good, and the unknown,” *Annu. Rev. Env. Resour.*, vol. 37, pp. 25–50, Nov. 2012.
- [58] R. J. Scholes, M. Walters *et al.*, “Building a global observing system for biodiversity,” *Curr. Opin. Env. Sustain.*, vol. 4, no. 1, pp. 139–146, Feb. 2012.
- [59] J. B. Campbell and R. H. Wynne, *Introduction to Remote Sensing*, 5th ed. New York, NY: The Guilford Press, 2011.
- [60] T. Lillesand, R. W. Kiefer, and J. Chipman, *Remote Sensing and Image Interpretation*, 6th ed. Hoboken, NJ: John Wiley & Sons, Inc., 2008.
- [61] P. M. Mather and M. Koch, *Computer Processing of Remotely-Sensed Images: An Introduction*, 4th ed. Chichester, United Kingdom: John Wiley & Sons, 2011.
- [62] M. C. Hansen and T. R. Loveland, “A review of large area monitoring of land cover change using Landsat data,” *Remote Sens. Environ.*, vol. 122, pp. 66–74, Jul. 2012.
- [63] Y. Xie, Z. Sha, and M. Yu, “Remote sensing imagery in vegetation mapping: a review,” *J. Plant Ecol.*, vol. 1, no. 1, pp. 9–23, Apr. 2008.
- [64] M. A. Wulder, J. C. White *et al.*, “Lidar sampling for large-area forest characterization: A review,” *Remote Sens. Environ.*, vol. 121, pp. 196–209, Jun. 2012.
- [65] E. Adam, O. Mutanga, and D. Rugege, “Multispectral and hyperspectral remote sensing for identification and mapping of wetland vegetation: a review,” *Wetl. Ecol. Manag.*, vol. 18, no. 3, pp. 281–296, Dec. 2009.

- [66] D. S. Boyd, C. SanchezHernandez, and G. M. Foody, "Mapping a specific class for priority habitats monitoring from satellite sensor data," *Int. J. Remote Sens.*, vol. 27, no. 13, pp. 2631–2644, Jul. 2006.
- [67] J. Paneque-Gálvez, J.-F. Mas *et al.*, "Enhanced land use/cover classification of heterogeneous tropical landscapes using support vector machines and textural homogeneity," *Int. J. Appl. Earth Obs.*, vol. 23, pp. 372–383, Aug. 2013.
- [68] E. E. Sano, R. Rosa, J. L. S. Brito, and L. G. Ferreira, "Land cover mapping of the tropical savanna region in Brazil," *Environ. Monit. Assess.*, vol. 166, no. 1–4, pp. 113–124, Jul. 2010.
- [69] K. P. Price, X. Guo, and J. M. Stiles, "Optimal Landsat TM band combinations and vegetation indices for discrimination of six grassland types in eastern Kansas," *Int. J. Remote Sens.*, vol. 23, no. 23, pp. 5031–5042, Dec. 2002.
- [70] H. Jiang, S. James R., P. A. Frost, and N. C. Slosser, "The classification of late seral forests in the Pacific Northwest, USA using Landsat ETM+ imagery," *Remote Sens. Environ.*, vol. 91, no. 3-4, pp. 320–331, Jun. 2004.
- [71] L. S. Wijedasa, S. Sloan, D. G. Michelakis, and G. R. Clements, "Overcoming limitations with Landsat imagery for mapping of peat swamp forests in Sundaland," *Remote Sens.*, vol. 4, no. 12, pp. 2595–2618, Sep. 2012.
- [72] B. Demir, F. Bovolo, and L. Bruzzone, "Updating land-cover maps by classification of image time series: A novel change-detection-driven transfer learning approach," *IEEE T. Geosci. Remote*, vol. 51, no. 1, pp. 300–312, 2013.
- [73] S. Berberoglu and A. Akin, "Assessing different remote sensing techniques to detect land use/cover changes in the eastern Mediterranean," *Int. J. Appl. Earth Obs.*, vol. 11, no. 1, pp. 46–53, Feb. 2009.
- [74] M. Reiche, R. Funk *et al.*, "Application of satellite remote sensing for mapping wind erosion risk and dust emission-deposition in Inner

- Mongolia grassland, China,” *Grassland Sci.*, vol. 58, no. 1, pp. 8–19, Mar. 2012.
- [75] G. Vaglio Laurin, V. Liesenberg *et al.*, “Optical and SAR sensor synergies for forest and land cover mapping in a tropical site in West Africa,” *Int. J. Appl. Earth Obs.*, vol. 21, pp. 7–16, Apr. 2013.
 - [76] C. Hüttich, U. Gessner *et al.*, “On the suitability of MODIS time series metrics to map vegetation types in dry savanna ecosystems: a case study in the Kalahari of NE Namibia,” *Remote Sens.*, vol. 1, no. 4, pp. 620–643, Sep. 2009.
 - [77] G. Forzieri, L. Tanteri, G. Moser, and F. Catani, “Mapping natural and urban environments using airborne multi-sensor ADS40-MIVIS-LiDAR synergies,” *Int. J. Appl. Earth Obs.*, vol. 23, pp. 313–323, Aug. 2013.
 - [78] D. Vyas, N. S. R. Krishnayya, K. R. Manjunath, S. S. Ray, and S. Panigrahy, “Evaluation of classifiers for processing Hyperion (EO-1) data of tropical vegetation,” *Int. J. Appl. Earth Obs.*, vol. 13, no. 2, pp. 228–235, Apr. 2011.
 - [79] J. C.-W. Chan, P. Beckers, T. Spanhove, and J. Vanden Borre, “An evaluation of ensemble classifiers for mapping Natura 2000 heathland in Belgium using spaceborne angular hyperspectral (CHRIS/Proba) imagery,” *Int. J. Appl. Earth Obs.*, vol. 18, pp. 13–22, Aug. 2012.
 - [80] W. S. Walker, C. M. Stickler, J. M. Kellndorfer, K. M. Kirsch, and D. C. Nepstad, “Large-area classification and mapping of forest and land cover in the Brazilian Amazon: A comparative analysis of ALOS/PALSAR and Landsat data sources,” *IEEE J. Sel. Top. Appl.*, vol. 3, no. 4, pp. 594–604, 2010.
 - [81] Y. Maghsoudi, M. Collins, and D. G. Leckie, “Polarimetric classification of Boreal forest using nonparametric feature selection and multiple classifiers,” *Int. J. Appl. Earth Obs.*, vol. 19, pp. 139–150, Oct. 2012.
 - [82] N. Longép  , P. Rakwatin, O. Isoguchi, and M. Shimada, “Assessment of ALOS PALSAR 50 m orthorectified FBD data for

- regional land cover classification by Support Vector Machines,” *IEEE T. Geosci. Remote*, vol. 49, no. 6, pp. 2135–2150, 2011.
- [83] V. Liesenberg and R. Gloaguen, “Evaluating SAR polarization modes at L-band for forest classification purposes in Eastern Amazon, Brazil,” *Int. J. Appl. Earth Obs.*, vol. 21, pp. 122–135, Apr. 2013.
- [84] L. Eysn, M. Hollaus, K. Schadauer, and N. Pfeifer, “Forest delineation based on airborne LIDAR data,” *Remote Sens.*, vol. 4, no. 12, pp. 762–783, Mar. 2012.
- [85] M. Chi, R. Feng, and L. Bruzzone, “Classification of hyperspectral remote-sensing data with primal SVM for small-sized training dataset problem,” *Adv. Space Res.*, vol. 41, no. 11, pp. 1793–1799, 2008.
- [86] T. Blaschke, “Object based image analysis for remote sensing,” *ISPRS J. Photogramm.*, vol. 65, no. 1, pp. 2–16, Jan. 2010.
- [87] T. Blaschke, S. Lang, and G. J. Hay, Eds., *Object-based Image Analysis: Spatial Concepts for Knowledge-Driven Remote Sensing Applications*. Berlin Heidelberg: Springer, 2008.
- [88] I. Manakos, T. Schneider, and U. Ammer, “A comparison between the ISODATA and the eCognition classification methods on basis of field data,” in *International Archives of Photogrammetry and Remote Sensing*, vol. XXXIII (Supplement B7). Amsterdam: ISPRS, 2000, pp. 133–139.
- [89] D. Flanders, M. Hall-Beyer, and J. Pereverzoff, “Preliminary evaluation of eCognition object-based software for cut block delineation and feature extraction,” *Can. J. Remote Sens.*, vol. 29, no. 4, pp. 441–452, 2003.
- [90] M. Zohmann, J. Pennerstorfer, and U. Nopp-Mayr, “Modelling habitat suitability for alpine rock ptarmigan (*Lagopus muta helvetica*) combining object-based classification of IKONOS imagery and Habitat Suitability Index modelling,” *Ecol. Model.*, vol. 254, pp. 22–32, 2013.

- [91] A. Kobler, S. Džeroski, and I. Keramitsoglou, “Habitat mapping using machine learning-extended kernel-based reclassification of an Ikonos satellite image,” *Ecol. Model.*, vol. 191, no. 1, pp. 83–95, Jan. 2006.
- [92] J. Lynch, M. Maslin, H. Balzter, and M. Sweeting, “Choose satellites to monitor deforestation,” *Nature*, vol. 496, no. 7445, pp. 293–294, Apr. 2013.
- [93] P. Griffiths, T. Kuemmerle *et al.*, “Using annual time-series of Landsat images to assess the effects of forest restitution in post-socialist Romania,” *Remote Sens. Environ.*, vol. 118, pp. 199–214, Mar. 2012.
- [94] T. A. Schroeder, M. A. Wulder, S. P. Healey, and G. G. Moisen, “Mapping wildfire and clearcut harvest disturbances in boreal forests with Landsat time series data,” *Remote Sens. Environ.*, vol. 115, no. 6, pp. 1421–1433, Jun. 2011.
- [95] Z. Zhu, C. E. Woodcock, and P. Olofsson, “Continuous monitoring of forest disturbance using all available Landsat imagery,” *Remote Sens. Environ.*, vol. 122, pp. 75–91, Jul. 2012.
- [96] C. Grinand, F. Rakotomalala *et al.*, “Estimating deforestation in tropical humid and dry forests in Madagascar from 2000 to 2010 using multi-date Landsat satellite images and the random forests classifier,” *Remote Sens. Environ.*, vol. 139, pp. 68–80, Dec. 2013.
- [97] C. Huang, S. N. Goward *et al.*, “An automated approach for reconstructing recent forest disturbance history using dense Landsat time series stacks,” *Remote Sens. Environ.*, vol. 114, no. 1, pp. 183–198, Jan. 2010.
- [98] V. Gorsevski, E. Kasischke, J. Dempewolf, T. Loboda, and F. Grossmann, “Analysis of the impacts of armed conflict on the Eastern Afrotropical forest region on the South Sudan–Uganda border using multitemporal Landsat imagery,” *Remote Sens. Environ.*, vol. 118, pp. 10–20, Mar. 2012.

- [99] V. F. Renó, E. M. Novo, C. Suemitsu, C. D. Rennó, and T. S. Silva, "Assessment of deforestation in the Lower Amazon floodplain using historical Landsat MSS/TM imagery," *Remote Sens. Environ.*, vol. 115, no. 12, pp. 3446–3456, Dec. 2011.
- [100] N. R. Goodwin and L. J. Collett, "Development of an automated method for mapping fire history captured in Landsat TM and ETM+ time series across Queensland, Australia," *Remote Sens. Environ.*, vol. 148, pp. 206–221, May 2014.
- [101] M. Lück-Vogel, P. J. O'Farrell, and W. Roberts, "Remote sensing based ecosystem state assessment in the Sandveld Region, South Africa," *Ecol. Indic.*, vol. 33, pp. 60–70, Oct. 2013.
- [102] W. Turner, "Satellites: make data freely accessible," *Nature*, vol. 498, no. 7452, p. 37, Jun. 2013.
- [103] M. Dubinin, P. Potapov, A. Lushchekina, and V. C. Radeloff, "Reconstructing long time series of burned areas in arid grasslands of southern Russia by satellite remote sensing," *Remote Sens. Environ.*, vol. 114, no. 8, pp. 1638–1648, Aug. 2010.
- [104] F. Sedano, P. Kempeneers, J. S. Miguel, P. Strobl, and P. Vogt, "Towards a pan-European burnt scar mapping methodology based on single date medium resolution optical remote sensing data," *Int. J. Appl. Earth Obs.*, vol. 20, pp. 52–59, Feb 2013.
- [105] T. Motohka, M. Shimada, Y. Uryu, and B. Setiabudi, "Using time series PALSAR gamma nought mosaics for automatic detection of tropical deforestation: A test study in Riau, Indonesia," *Remote Sens. Environ.*, May 2014, in press.
- [106] M. Whittle, S. Quegan, Y. Uryu, M. Stüewe, and K. Yulianto, "Detection of tropical deforestation using ALOS-PALSAR: A Sumatran case study," *Remote Sens. Environ.*, vol. 124, pp. 83–98, Sep. 2012.
- [107] L. Fahrig, "Effects of habitat fragmentation on biodiversity," *Annu. Rev. Ecol. Evol. S.*, vol. 34, no. 1, pp. 487–515, Nov. 2003.

- [108] P. Kindlmann and F. Burel, “Connectivity measures: a review,” *Landscape Ecol.*, vol. 23, no. 8, pp. 879–890, Jul. 2008.
- [109] K. McGarigal, S. A. Cushman, and E. Ene, “FRAGSTATS v4: Spatial pattern analysis program for categorical and continuous maps,” 2012, computer software program. University of Massachusetts, Amherst. Available at <http://www.umass.edu/landeco/research/fragstats/fragstats.html>.
- [110] J. Tang, K. Bu, J. Yang, S. Zhang, and L. Chang, “Multitemporal analysis of forest fragmentation in the upstream region of the Nenjiang River Basin, Northeast China,” *Ecol. Indic.*, vol. 23, pp. 597–607, Dec. 2012.
- [111] Z. Wang, N. Huang *et al.*, “Shrinkage and fragmentation of marshes in the West Songnen Plain, China, from 1954 to 2008 and its possible causes,” *Int. J. Appl. Earth Obs.*, vol. 13, no. 3, pp. 477–486, Jun. 2011.
- [112] S. Liu, Y. Dong *et al.*, “Forest fragmentation and landscape connectivity change associated with road network extension and city expansion: A case study in the Lancang River Valley,” *Ecol. Indic.*, vol. 36, pp. 160–168, Jan. 2014.
- [113] T. Virtanen and M. Ek, “The fragmented nature of tundra landscape,” *Int. J. Appl. Earth Obs.*, vol. 27, pp. 4–12, Apr. 2014.
- [114] S. García-Gigorro and S. Saura, “Forest fragmentation estimated from remotely sensed data: Is comparison across scales possible?” *Forest Sci.*, vol. 51, no. 1, pp. 51–63, 2005.
- [115] M. E. Newman, K. P. McLaren, and B. S. Wilson, “Assessing deforestation and fragmentation in a tropical moist forest over 68 years; the impact of roads and legal protection in the Cockpit Country, Jamaica,” *Forest Ecol. Manag.*, vol. 315, pp. 138–152, Mar. 2014.
- [116] M. A. Cho, P. Debba *et al.*, “Potential utility of the spectral red-edge region of SumbandilaSat imagery for assessing indigenous

- forest structure and health,” *Int. J. Appl. Earth Obs.*, vol. 16, pp. 85–93, Jun 2012.
- [117] C. Martín-Martín, R. G. Bunce, S. Saura, and R. Elena-Rosselló, “Changes and interactions between forest landscape connectivity and burnt area in Spain,” *Ecol. Indic.*, vol. 33, pp. 129–138, Oct. 2013.
 - [118] B. J. Goodwin, “Is landscape connectivity a dependent or independent variable?” *Landscape Ecol.*, vol. 18, no. 7, pp. 687–699, Oct. 2003.
 - [119] S. Saura and L. Pascual-Hortal, “A new habitat availability index to integrate connectivity in landscape conservation planning: Comparison with existing indices and application to a case study,” *Landscape Urban Plan.*, vol. 83, no. 2-3, pp. 91–103, Nov. 2007.
 - [120] S. G. Plexida, A. I. Sfougaris, I. P. Ispikoudis, and V. P. Papanastasis, “Selecting landscape metrics as indicators of spatial heterogeneityA comparison among Greek landscapes,” *Int. J. Appl. Earth Obs.*, vol. 26, pp. 26–35, Feb. 2014.
 - [121] M. W. Lang and G. W. McCarty, “Lidar intensity for improved detection of inundation below the forest canopy,” *Wetlands*, vol. 29, no. 4, pp. 1166–1178, Dec. 2009.
 - [122] R. B. Jenkins and P. S. Frazier, “High-resolution remote sensing of upland swamp boundaries and vegetation for baseline mapping and monitoring,” *Wetlands*, vol. 30, no. 3, pp. 531–540, May 2010.
 - [123] B. Höfle and M. Vetter, “Water surface mapping from airborne laser scanning using signal intensity and elevation data,” *Earth Surf. Proc. Land.*, vol. 34, no. 12, pp. 1635–1649, Sep. 2009.
 - [124] A. Brzank, C. Heipke, J. Goepfert, and U. Soergel, “Aspects of generating precise digital terrain models in the Wadden Sea from lidarwater classification and structure line extraction,” *ISPRS J. Photogramm. Remote Sens.*, vol. 63, no. 5, pp. 510–528, Sep. 2008.
 - [125] A. Brzank, C. Heipke, and J. Goepfert, “Morphologic change detection in the Wadden Sea from lidar data,” in *International*

Archives of the Photogrammetry, Remote Sensing and Spatial Information Sciences. Beijing: ISPRS, 2008, pp. 647–652.

- [126] A. Schmidt and U. Soergel, “Monitoring and change detection of Wadden Sea areas using Lidar data,” in *International Archives of the Photogrammetry, Remote Sensing and Spatial Information Sciences*, vol. XL-7/W2. Antalya: ISPRS, Oct. 2013, pp. 219–224.
- [127] J.-R. B. Bwangoy, M. C. Hansen, D. P. Roy, G. D. Grandi, and C. O. Justice, “Wetland mapping in the Congo Basin using optical and radar remotely sensed data and derived topographical indices,” *Remote Sens. Environ.*, vol. 114, no. 1, pp. 73–86, Jan. 2010.
- [128] T. L. Evans, M. Costa, K. Telmer, and T. S. F. Silva, “Using ALOS/PALSAR and RADARSAT-2 to map land cover and seasonal inundation in the Brazilian Pantanal,” *IEEE J. Sel. Top. Appl.*, vol. 3, no. 4, pp. 560–575, 2010.
- [129] M. W. Lang, E. S. Kasischke, S. D. Prince, and K. W. Pittman, “Assessment of C-band synthetic aperture radar data for mapping and monitoring Coastal Plain forested wetlands in the Mid-Atlantic Region, U.S.A.” *Remote Sens. Environ.*, vol. 112, no. 11, pp. 4120–4130, Nov. 2008.
- [130] T. Kumar and C. Patnaik, “Discrimination of mangrove forests and characterization of adjoining land cover classes using temporal C-band Synthetic Aperture Radar data: A case study of Sundarbans,” *Int. J. Appl. Earth Obs.*, vol. 23, pp. 119–131, Aug. 2013.
- [131] E. Belluco, M. Camuffo *et al.*, “Mapping salt-marsh vegetation by multispectral and hyperspectral remote sensing,” *Remote Sens. Environ.*, vol. 105, no. 1, pp. 54–67, Nov. 2006.
- [132] R. Pu, S. Bell, K. H. Levy, and C. Meyer, “Mapping detailed seagrass habitats using satellite imagery,” in *Int. Geoscience and Remote Sensing Symp.* Honolulu, Hi: IEEE, 2010, pp. 1–4.
- [133] A. Lechner, A. Fletcher, K. Johansen, and P. Erskine, “Characterising upland swamps using object-based classification

- methods and hyper-spatial resolution imagery derived from an unmanned aerial vehicle,” in *ISPRS Annals of Photogrammetry, Remote Sensing and Spatial Information Sciences*, vol. I-4, no. September. Melbourne: ISPRS, 2012, pp. 101–106.
- [134] E. Mwita, G. Menz *et al.*, “Mapping small wetlands of Kenya and Tanzania using remote sensing techniques,” *Int. J. Appl. Earth Obs.*, vol. 21, pp. 173–183, Apr. 2013.
 - [135] A. M. Muad and G. M. Foody, “Super-resolution mapping of lakes from imagery with a coarse spatial and fine temporal resolution,” *Int J. Appl. Earth Obs.*, vol. 15, pp. 79–91, Apr. 2012.
 - [136] C. Joshi, J. de Leeuw, and I. C. van Duren, “Remote sensing and GIS applications for mapping and spatial modelling of invasive species,” in *International Archives of the Photogrammetry, Remote Sensing and Spatial Information Sciences*, vol. XXXV-B7. Istanbul: ISPRS, 2004, pp. 669–677.
 - [137] W. Dorigo, A. Lucieer, T. Podobnikar, and A. Čarni, “Mapping invasive *Fallopia japonica* by combined spectral, spatial, and temporal analysis of digital orthophotos,” *Int. J. Appl. Earth Obs.*, vol. 19, pp. 185–195, Oct. 2012.
 - [138] M. Shouse, L. Liang, and S. Fei, “Identification of understory invasive exotic plants with remote sensing in urban forests,” *Int. J. Appl. Earth Obs.*, vol. 21, pp. 525–534, Apr. 2013.
 - [139] F. Artigas and I. C. Pechmann, “Balloon imagery verification of remotely sensed *Phragmites australis* expansion in an urban estuary of New Jersey, USA,” *Landscape Urban Plan.*, vol. 95, no. 3, pp. 105–112, Apr. 2010.
 - [140] W. Hantson, L. Kooistra, and P. A. Slim, “Mapping invasive woody species in coastal dunes in the Netherlands: a remote sensing approach using LIDAR and high-resolution aerial photographs,” *Appl. Veg. Sci.*, vol. 15, no. 4, pp. 536–547, Oct. 2012.
 - [141] M. L. Clark and D. A. Roberts, “Species-level differences in hyperspectral metrics among tropical rainforest trees as determined

- by a tree-based classifier,” *Remote Sens.*, vol. 4, no. 12, pp. 1820–1855, Jun. 2012.
- [142] M. Colgan, C. Baldeck, J.-B. Féret, and G. Asner, “Mapping savanna tree species at ecosystem scales using support vector machine classification and BRDF correction on airborne hyperspectral and LiDAR data,” *Remote Sens.*, vol. 4, no. 12, pp. 3462–3480, Nov. 2012.
 - [143] M. Laba, R. Downs *et al.*, “Mapping invasive wetland plants in the Hudson River National Estuarine Research Reserve using Quickbird satellite imagery,” *Remote Sens. Environ.*, vol. 112, no. 1, pp. 286–300, Jan. 2008.
 - [144] S. J. Walsh, A. L. McCleary *et al.*, “QuickBird and Hyperion data analysis of an invasive plant species in the Galapagos Islands of Ecuador: Implications for control and land use management,” *Remote Sens. Environ.*, vol. 112, no. 5, pp. 1927–1941, May 2008.
 - [145] M. Immitzer, C. Atzberger, and T. Koukal, “Tree species classification with random forest using very high spatial resolution 8-band WorldView-2 satellite data,” *Remote Sens.*, vol. 4, no. 12, pp. 2661–2693, Sep. 2012.
 - [146] K. S. He, D. Rocchini, M. Neteler, and H. Nagendra, “Benefits of hyperspectral remote sensing for tracking plant invasions,” *Divers. Distrib.*, vol. 17, no. 3, pp. 381–392, May 2011.
 - [147] J. B. Féret and G. P. Asner, “Tree species discrimination in tropical forests using airborne imaging spectroscopy,” *IEEE T. Geosci. Remote*, vol. 51, no. 1, pp. 73–84, Jan. 2013.
 - [148] E. L. Hestir, S. Khanna *et al.*, “Identification of invasive vegetation using hyperspectral remote sensing in the California Delta ecosystem,” *Remote Sens. Environ.*, vol. 112, no. 11, pp. 4034–4047, Nov. 2008.
 - [149] C. A. Baldeck, M. S. Colgan *et al.*, “Landscape-scale variation in plant community composition of an African savanna from airborne species mapping,” *Ecol. Appl.*, vol. 24, no. 1, pp. 84–93, Jan. 2014.

- [150] A. Ghiyamat, H. Z. M. Shafri, G. Amouzad Mahdiraji, A. R. M. Shariff, and S. Mansor, “Hyperspectral discrimination of tree species with different classifications using single- and multiple-endmember,” *Int. J. Appl. Earth Obs.*, vol. 23, pp. 177–191, Aug. 2013.
- [151] B. W. Pengra, C. a. Johnston, and T. R. Loveland, “Mapping an invasive plant, *Phragmites australis*, in coastal wetlands using the EO-1 Hyperion hyperspectral sensor,” *Remote Sens. Environ.*, vol. 108, no. 1, pp. 74–81, May 2007.
- [152] X. Miao, P. Gong *et al.*, “Estimation of yellow starthistle abundance through CASI-2 hyperspectral imagery using linear spectral mixture models,” *Remote Sens. Environ.*, vol. 101, no. 3, pp. 329–341, Apr. 2006.
- [153] B. Somers and G. P. Asner, “Hyperspectral time series analysis of native and invasive species in Hawaiian rainforests,” *Remote Sens.*, vol. 4, no. 12, pp. 2510–2529, Aug. 2012.
- [154] P. S. Thenkabail, E. A. Enclona, M. S. Ashton, and B. Van Der Meer, “Accuracy assessments of hyperspectral waveband performance for vegetation analysis applications,” *Remote Sens. Environ.*, vol. 91, no. 3–4, pp. 354–376, Jun. 2004.
- [155] A. Zlinszky, W. Mücke, H. Lehner, C. Brieze, and N. Pfeifer, “Categorizing wetland vegetation by airborne laser scanning on Lake Balaton and Kis-Balaton, Hungary,” *Remote Sens.*, vol. 4, no. 12, pp. 1617–1650, Jun. 2012. [Online]. Available: <http://www.mdpi.com/2072-4292/4/6/1617/>
- [156] EEA, “The impacts of invasive alien species in europe,” European Environment Agency, Copenhagen, Tech. Rep. 16, 2012.
- [157] P. T. Fretwell, I. J. Staniland, and J. Forcada, “Whales from space: counting southern right whales by satellite.” *PloS One*, vol. 9, no. 2, p. e88655, Jan. 2014.
- [158] S. Suarez-Seoane, P. E. Osborne, and J. C. Alonso, “Large-scale habitat selection by agricultural steppe birds in Spain: identifying

- species-habitat responses using generalized additive models,” *J. Appl. Ecol.*, vol. 39, no. 5, pp. 755–771, Oct. 2002.
- [159] G. Buchanan, J. Pearce-Higgins, M. Grant, D. Robertson, and T. Waterhouse, “Characterization of moorland vegetation and the prediction of bird abundance using remote sensing,” *J. Biogeogr.*, vol. 32, no. 4, pp. 697–707, Feb. 2005.
- [160] J. C. Vogeler, A. T. Hudak *et al.*, “Terrain and vegetation structural influences on local avian species richness in two mixed-conifer forests,” *Remote Sens. Environ.*, vol. 147, pp. 13–22, May 2014.
- [161] S. Bejarano, P. J. Mumby, and I. Sotheran, “Predicting structural complexity of reefs and fish abundance using acoustic remote sensing (RoxAnn),” *Mar. Biol.*, vol. 158, no. 3, pp. 489–504, Nov. 2010.
- [162] D. C. Duro, J. Girard *et al.*, “Predicting species diversity in agricultural environments using Landsat TM imagery,” *Remote Sens. Environ.*, vol. 144, pp. 214–225, Mar. 2014.
- [163] K.-W. Yen, H.-J. Lu, Y. Chang, and M.-A. Lee, “Using remote-sensing data to detect habitat suitability for yellowfin tuna in the Western and Central Pacific Ocean,” *Int. J. Remote Sens.*, vol. 33, no. 23, pp. 7507–7522, Dec. 2012.
- [164] M. Melin, P. Packalén, J. Matala, L. Mehtätalo, and J. Pusenius, “Assessing and modeling moose (*Alces alces*) habitats with airborne laser scanning data,” *Int. J. Appl. Earth Obs.*, vol. 23, pp. 389–396, Aug. 2013.
- [165] P. T. Fretwell and P. N. Trathan, “Penguins from space: faecal stains reveal the location of emperor penguin colonies,” *Global Ecol. Biogeogr.*, vol. 18, no. 5, pp. 543–552, Sep. 2009.
- [166] P. T. Fretwell, M. A. Larue *et al.*, “An emperor penguin population estimate: the first global, synoptic survey of a species from space.” *PloS One*, vol. 7, no. 4, p. e33751, Jan. 2012.
- [167] K. M. Bergen, A. M. Gilboy, and D. G. Brown, “Multi-dimensional vegetation structure in modeling avian habitat,” *Ecol. Inform.*, vol. 2, no. 1, pp. 9–22, Jan. 2007.

- [168] R. Clawges, K. Vierling, L. Vierling, and E. Rowell, "The use of airborne lidar to assess avian species diversity, density, and occurrence in a pine/aspen forest," *Remote Sens. Environ.*, vol. 112, no. 5, pp. 2064–2073, May 2008.
- [169] S. J. Purkis, N. a. J. Graham, and B. M. Riegl, "Predictability of reef fish diversity and abundance using remote sensing data in Diego Garcia (Chagos Archipelago)," *Coral Reefs*, vol. 27, no. 1, pp. 167–178, Sep. 2008.
- [170] K. T. Vierling, C. Bässler *et al.*, "Spinning a laser web: predicting spider distributions using LiDAR," *Ecol. Appl.*, vol. 21, no. 2, pp. 577–588, Mar. 2011.
- [171] J. Müller and R. Brandl, "Assessing biodiversity by remote sensing in mountainous terrain: the potential of LiDAR to predict forest beetle assemblages," *J. Appl. Ecol.*, vol. 46, no. 4, pp. 897–905, Aug. 2009.
- [172] S. Kumar, S. E. Simonson, and T. J. Stohlgren, "Effects of spatial heterogeneity on butterfly species richness in Rocky Mountain National Park, CO, USA," *Biodiv. Conserv.*, vol. 18, no. 3, pp. 739–763, Dec. 2009.
- [173] C. Pittiglio, A. K. Skidmore, H. A. M. J. van Gils, and H. H. Prins, "Identifying transit corridors for elephant using a long time-series," *Int. J. Appl. Earth Obs.*, vol. 14, no. 1, pp. 61–72, Feb 2012.
- [174] J. E. Arias-González, G. Acosta-González, N. Membrillo, J. R. Garza-Pérez, and J. M. Castro-Pérez, "Predicting spatially explicit coral reef fish abundance, richness and ShannonWeaver index from habitat characteristics," *Biodivers. Conserv.*, vol. 21, no. 1, pp. 115–130, Oct. 2011.
- [175] K. Koy, W. J. McShea, P. Leimgruber, B. N. Haack, and M. Aung, "Percentage canopy cover – using Landsat imagery to delineate habitat for Myanmar's endangered Eld's deer (*Cervus eldi*)," *Anim. Conserv.*, vol. 8, no. 3, pp. 289–296, Aug. 2005.

- [176] M. Zainuddin, H. Kiyofuji, K. Saitoh, and S.-I. Saitoh, “Using multi-sensor satellite remote sensing and catch data to detect ocean hot spots for albacore (*Thunnus alalunga*) in the northwestern North Pacific,” *Deep-Sea Res. Pt. II*, vol. 53, no. 3-4, pp. 419–431, Feb. 2006.
- [177] A. Langner, H. Samejima, R. C. Ong, J. Titin, and K. Kitayama, “Integration of carbon conservation into sustainable forest management using high resolution satellite imagery: A case study in Sabah, Malaysian Borneo,” *Int. J. Appl. Earth Obs.*, vol. 18, pp. 305–312, Aug 2012.
- [178] A. Abbas, S. Khan, N. Hussain, M. A. Hanjra, and S. Akbar, “Characterizing soil salinity in irrigated agriculture using a remote sensing approach,” *Phys. Chem. Earth Pt A/B/C*, vol. 55-57, pp. 43–52, Jan. 2013.
- [179] J. Martínez-López, M. Carreño, J. Palazón-Ferrando, J. Martínez-Fernández, and M. Esteve, “Remote sensing of plant communities as a tool for assessing the condition of semiarid Mediterranean saline wetlands in agricultural catchments,” *Int. J. Appl. Earth Obs.*, vol. 26, pp. 193–204, Feb. 2014.
- [180] M. Shahriar Pervez, M. Budde, and J. Rowland, “Mapping irrigated areas in Afghanistan over the past decade using MODIS NDVI,” *Remote Sens. Environ.*, vol. 149, pp. 155–165, Jun. 2014.
- [181] A. K. Tilling, G. J. O’Leary *et al.*, “Remote sensing of nitrogen and water stress in wheat,” *Field Crop. Res.*, vol. 104, no. 1-3, pp. 77–85, Oct. 2007.
- [182] P. Chen, D. Haboudane *et al.*, “New spectral indicator assessing the efficiency of crop nitrogen treatment in corn and wheat,” *Remote Sens. Environ.*, vol. 114, no. 9, pp. 1987–1997, Sep. 2010.
- [183] E. M. Perry, G. J. Fitzgerald *et al.*, “Rapid estimation of canopy nitrogen of cereal crops at paddock scale using a Canopy Chlorophyll Content Index,” *Field Crop. Res.*, vol. 134, pp. 158–164, Aug. 2012.

- [184] L. Zhong, P. Gong, and G. S. Biging, “Efficient corn and soybean mapping with temporal extendability: A multi-year experiment using Landsat imagery,” *Remote Sens. Environ.*, vol. 140, pp. 1–13, Jan. 2014.
- [185] C. Alcantara, T. Kuemmerle, A. V. Prishchepov, and V. C. Radeloff, “Mapping abandoned agriculture with multi-temporal MODIS satellite data,” *Remote Sens. Environ.*, vol. 124, pp. 334–347, Sep. 2012.
- [186] M. Jain, P. Mondal, R. S. DeFries, C. Small, and G. L. Galford, “Mapping cropping intensity of smallholder farms: A comparison of methods using multiple sensors,” *Remote Sens. Environ.*, vol. 134, pp. 210–223, Jul. 2013.
- [187] I. Herrmann, A. Pimstein *et al.*, “LAI assessment of wheat and potato crops by VEN μ S and Sentinel-2 bands,” *Remote Sens. Environ.*, vol. 115, no. 8, pp. 2141–2151, Aug. 2011.
- [188] E. Lindberg and M. Hollaus, “Comparison of methods for estimation of stem volume, stem number and basal area from airborne laser scanning data in a hemi-boreal forest,” *Remote Sens.*, vol. 4, no. 12, pp. 1004–1023, Apr. 2012. [Online]. Available: <http://www.mdpi.com/2072-4292/4/4/1004/>
- [189] J. Hyypä, X. Yu *et al.*, “Advances in forest inventory using airborne laser scanning,” *Remote Sens.*, vol. 4, no. 12, pp. 1190–1207, May 2012.
- [190] B. Koch, “Status and future of laser scanning, synthetic aperture radar and hyperspectral remote sensing data for forest biomass assessment,” *ISPRS J Photogramm.*, vol. 65, no. 6, pp. 581–590, Nov. 2010.
- [191] L. Duncanson, K. Niemann, and M. Wulder, “Estimating forest canopy height and terrain relief from GLAS waveform metrics,” *Remote Sens. Environ.*, vol. 114, no. 1, pp. 138–154, Jan. 2010.
- [192] F. Kugler, D. Schulze, I. Hajnsek, H. Pretzsch, and K. P. Papathanassiou, “TanDEM-X Pol-InSAR performance for forest

- height estimation,” *IEEE T. Geosci. Remote*, vol. 52, no. 10, pp. 6404–6422, Oct. 2014.
- [193] M. A. Cho, A. K. Skidmore, and I. Sobhan, “Mapping beech (*Fagus sylvatica* L.) forest structure with airborne hyperspectral imagery,” *Int. J. Appl. Earth Obs.*, vol. 11, no. 3, pp. 201–211, Jun. 2009.
- [194] J. C. White, C. Gómez, M. A. Wulder, and N. C. Coops, “Characterizing temperate forest structural and spectral diversity with Hyperion EO-1 data,” *Remote Sens. Environ.*, vol. 114, no. 7, pp. 1576–1589, Jul 2010.
- [195] J. E. Nichol and M. L. R. Sarker, “Improved biomass estimation using the texture parameters of two high-resolution optical sensors,” *IEEE T. Geosci. Remote*, vol. 49, no. 3, pp. 930–948, Mar. 2011.
- [196] K. Kronseder, U. Ballhorn, V. Böhm, and F. Siegert, “Above ground biomass estimation across forest types at different degradation levels in Central Kalimantan using LiDAR data,” *Int. J. Appl. Earth Obs.*, vol. 18, pp. 37–48, Aug 2012.
- [197] A. Banskota, R. H. Wynne, P. Johnson, and B. Emessiene, “Synergistic use of very high-frequency radar and discrete-return lidar for estimating biomass in temperate hardwood and mixed forests,” *Ann. For. Sci.*, vol. 68, no. 2, pp. 347–356, Mar. 2011.
- [198] M. Vastaranta, M. Holopainen *et al.*, “TerraSAR-X stereo radargrammetry and airborne scanning LiDAR height metrics in imputation of forest aboveground biomass and stem volume,” *IEEE T. Geosci. Remote*, vol. 52, no. 2, pp. 1197–1204, Feb. 2014.
- [199] G. Sandberg, L. Ulander, J. Fransson, J. Holmgren, and T. Le Toan, “L- and P-band backscatter intensity for biomass retrieval in hemiboreal forest,” *Remote Sens. Environ.*, vol. 115, no. 11, pp. 2874–2886, Nov. 2011.
- [200] Z. Hou, Q. Xu, and T. Tokola, “Use of ALS, Airborne CIR and ALOS AVNIR-2 data for estimating tropical forest attributes in Lao PDR,” *ISPRS J. Photogramm.*, vol. 66, no. 6, pp. 776–786, Nov. 2011.

- [201] I. Ozdemir and A. Karnieli, “Predicting forest structural parameters using the image texture derived from WorldView-2 multispectral imagery in a dryland forest, Israel,” *Int. J. Appl. Earth Obs.*, vol. 13, no. 5, pp. 701–710, Oct 2011.
- [202] K. Soudani, C. François, G. le Maire, V. Le Dantec, and E. Dufrêne, “Comparative analysis of IKONOS, SPOT, and ETM+ data for leaf area index estimation in temperate coniferous and deciduous forest stands,” *Remote Sens. Environ.*, vol. 102, no. 1-2, pp. 161–175, May 2006.
- [203] K. Zhao and S. Popescu, “Lidar-based mapping of leaf area index and its use for validating GLOBCARBON satellite LAI product in a temperate forest of the southern USA,” *Remote Sens. Environ.*, vol. 113, no. 8, pp. 1628–1645, Aug. 2009.
- [204] T. Kuemmerle, O. Chaskovskyy *et al.*, “Forest cover change and illegal logging in the Ukrainian Carpathians in the transition period from 1988 to 2007,” *Remote Sens. Environ.*, vol. 113, no. 6, pp. 1194–1207, Jun. 2009.
- [205] J. Franke, P. Navratil, V. Keuck, K. Peterson, and F. Siegert, “Monitoring fire and selective logging activities in tropical peat swamp forests,” *IEEE J. Sel. Top. Appl.*, vol. 5, no. 6, pp. 1811–1820, 2012.
- [206] C. Bellard, C. Bertelsmeier, P. Leadley, W. Thuiller, and F. Courchamp, “Impacts of climate change on the future of biodiversity,” *Ecol. Lett.*, vol. 15, pp. 365–377, Jan. 2012.
- [207] D. Guyon, M. Guillot *et al.*, “Monitoring elevation variations in leaf phenology of deciduous broadleaf forests from SPOT/VEGETATION time-series,” *Remote Sens. Environ.*, vol. 115, no. 2, pp. 615–627, Feb. 2011.
- [208] G. Hmimina, E. Dufrêne *et al.*, “Evaluation of the potential of MODIS satellite data to predict vegetation phenology in different biomes: An investigation using ground-based NDVI measurements,” *Remote Sens. Environ.*, vol. 132, pp. 145–158, May 2013.

- [209] K. Hufkens, M. Friedl *et al.*, “Linking near-surface and satellite remote sensing measurements of deciduous broadleaf forest phenology,” *Remote Sens. Environ.*, vol. 117, pp. 307–321, Feb. 2012.
- [210] K. White, J. Pontius, and P. Schaberg, “Remote sensing of spring phenology in northeastern forests: A comparison of methods, field metrics and sources of uncertainty,” *Remote Sens. Environ.*, vol. 148, pp. 97–107, May 2014.
- [211] C. Wu, A. Gonsamo, C. M. Gough, J. M. Chen, and S. Xu, “Modeling growing season phenology in North American forests using seasonal mean vegetation indices from MODIS,” *Remote Sens. Environ.*, vol. 147, pp. 79–88, May 2014.
- [212] Y. Ryu, G. Lee, S. Jeon, Y. Song, and H. Kimm, “Monitoring multi-layer canopy spring phenology of temperate deciduous and evergreen forests using low-cost spectral sensors,” *Remote Sens. Environ.*, vol. 149, pp. 227–238, Jun. 2014.
- [213] I. Leifer, W. J. Lehr *et al.*, “State of the art satellite and airborne marine oil spill remote sensing: Application to the BP Deepwater Horizon oil spill,” *Remote Sens. Environ.*, vol. 124, pp. 185–209, Sep. 2012.
- [214] M. Fingas and C. Brown, “Review of oil spill remote sensing.” *Mar. Pollut. Bull.*, vol. 83, no. 1, pp. 9–23, Apr. 2014. [Online]. Available: <http://www.ncbi.nlm.nih.gov/pubmed/24759508>
- [215] D. Mera, J. M. Cotos, J. Varela-Pet, and O. Garcia-Pineda, “Adaptive thresholding algorithm based on SAR images and wind data to segment oil spills along the northwest coast of the Iberian Peninsula.” *Mar. Pollut. Bull.*, vol. 64, no. 10, pp. 2090–2096, Oct. 2012.
- [216] O. Garcia-Pineda, B. Zimmer *et al.*, “Using SAR images to delineate ocean oil slicks with a texture-classifying neural network algorithm (TCNNA),” *Can. J. Remote Sens.*, vol. 35, no. 5, pp. 411–421, Jun. 2009.

- [217] K. Topouzelis and A. Psyllos, “Oil spill feature selection and classification using decision tree forest on SAR image data,” *ISPRS J. Photogramm.*, vol. 68, pp. 135–143, Mar. 2012.
- [218] R. F. Kokaly, B. R. Couvillion *et al.*, “Spectroscopic remote sensing of the distribution and persistence of oil from the Deepwater Horizon spill in Barataria Bay marshes,” *Remote Sens. Environ.*, vol. 129, pp. 210–230, Feb. 2013.
- [219] Z. Shen, Q. Liao, Q. Hong, and Y. Gong, “An overview of research on agricultural non-point source pollution modelling in China,” *Sep. Purif. Technol.*, vol. 84, pp. 104–111, Jan. 2012.
- [220] X. Wang, Q. Wang *et al.*, “A method coupled with remote sensing data to evaluate non-point source pollution in the Xin’anjiang catchment of China,” *Sci. Total Environ.*, vol. 430, pp. 132–143, Jul. 2012.
- [221] S. C. Kefauver, J. Peñuelas, and S. Ustin, “Using topographic and remotely sensed variables to assess ozone injury to conifers in the Sierra Nevada (USA) and Catalonia (Spain),” *Remote Sens. Environ.*, vol. 139, pp. 138–148, Dec. 2013.
- [222] M. J. Bechle, D. B. Millet, and J. D. Marshall, “Remote sensing of exposure to NO₂: Satellite versus ground-based measurement in a large urban area,” *Atmos. Environ.*, vol. 69, no. 2, pp. 345–353, Apr. 2013.
- [223] R. Costanza, R. de Groot *et al.*, “Changes in the global value of ecosystem services,” *Global Environ. Change*, vol. 26, pp. 152–158, May 2014.
- [224] J. Maes, M. L. Paracchini, and G. Zulian, “A European assessment of the provision of ecosystem services: Towards an atlas of ecosystem services,” European Commission Joint Research Centre, Luxembourg, Tech. Rep., 2011.
- [225] Y. Z. Ayanu, C. Conrad, T. Nauss, M. Wegmann, and T. Koellner, “Quantifying and mapping ecosystem services supplies and demands:

- a review of remote sensing applications.” *Environ. Sci. Technol.*, vol. 46, no. 16, pp. 8529–8541, Aug. 2012.
- [226] H. Fang, S. Liang, and G. Hoogenboom, “Integration of MODIS LAI and vegetation index products with the CSM-CERES-Maize model for corn yield estimation,” *Int. J. Remote Sens.*, vol. 32, no. 4, pp. 1039–1065, Feb. 2011.
- [227] M. Moriondo, F. Maselli, and M. Bindi, “A simple model of regional wheat yield based on NDVI data,” *Eur. J. Agron.*, vol. 26, no. 3, pp. 266–274, Apr. 2007.
- [228] J. Ren, Z. Chen, Q. Zhou, and H. Tang, “Regional yield estimation for winter wheat with MODIS-NDVI data in Shandong, China,” *Int. J. Appl. Earth Obs.*, vol. 10, no. 4, pp. 403–413, Dec. 2008.
- [229] H. Yan, Y. Fu *et al.*, “Modeling gross primary productivity for winter wheatmaize double cropping system using MODIS time series and CO₂ eddy flux tower data,” *Agr. Ecosyst. Environ.*, vol. 129, no. 4, pp. 391–400, Feb. 2009.
- [230] L. Dente, G. Satalino, F. Mattia, and M. Rinaldi, “Assimilation of leaf area index derived from ASAR and MERIS data into CERES-Wheat model to map wheat yield,” *Remote Sens. Environ.*, vol. 112, no. 4, pp. 1395–1407, Apr. 2008.
- [231] D. Jaskierniak, P. N. Lane, A. Robinson, and A. Lucieer, “Extracting LiDAR indices to characterise multilayered forest structure using mixture distribution functions,” *Remote Sens. Environ.*, vol. 115, no. 2, pp. 573–585, Feb. 2011.
- [232] S. Tonolli, M. Dalponte *et al.*, “Fusion of airborne LiDAR and satellite multispectral data for the estimation of timber volume in the Southern Alps,” *Remote Sens. Environ.*, vol. 115, no. 10, pp. 2486–2498, Oct. 2011.
- [233] H. Latifi, A. Nothdurft, and B. Koch, “Non-parametric prediction and mapping of standing timber volume and biomass in a temperate forest: application of multiple optical/LiDAR-derived predictors,” *Forestry*, vol. 83, no. 4, pp. 395–407, Jul. 2010.

- [234] R. Nelson, K. Ranson *et al.*, “Estimating Siberian timber volume using MODIS and ICESat/GLAS,” *Remote Sens. Environ.*, vol. 113, no. 3, pp. 691–701, Mar. 2009.
- [235] L. G. Olmanson, M. E. Bauer, and P. L. Brezonik, “A 20-year Landsat water clarity census of Minnesota’s 10,000 lakes,” *Remote Sens. Environ.*, vol. 112, no. 11, pp. 4086–4097, Nov. 2008.
- [236] D. Zhao, Y. Cai *et al.*, “Estimation of water clarity in Taihu Lake and surrounding rivers using Landsat imagery,” *Adv. Water Resour.*, vol. 34, no. 2, pp. 165–173, Feb. 2011.
- [237] N. Kabbara, J. Benkhelil, M. Awad, and V. Barale, “Monitoring water quality in the coastal area of Tripoli (Lebanon) using high-resolution satellite data,” *ISPRS J. Photogramm.*, vol. 63, no. 5, pp. 488–495, Sep. 2008.
- [238] S. Chen, L. Fang, L. Zhang, and W. Huang, “Remote sensing of turbidity in seawater intrusion reaches of Pearl River Estuary A case study in Modaomen water way, China,” *Estuar. Coast. Shelf S.*, vol. 82, no. 1, pp. 119–127, Mar. 2009.
- [239] Z. Chen, F. E. Muller-Karger, and C. Hu, “Remote sensing of water clarity in Tampa Bay,” *Remote Sens. Environ.*, vol. 109, no. 2, pp. 249–259, Jul. 2007.
- [240] D. Fuentes, J. Gamon *et al.*, “Mapping carbon and water vapor fluxes in a chaparral ecosystem using vegetation indices derived from AVIRIS,” *Remote Sens. Environ.*, vol. 103, no. 3, pp. 312–323, Aug. 2006.
- [241] M. García, D. Riaño, E. Chuvieco, and F. M. Danson, “Estimating biomass carbon stocks for a Mediterranean forest in central Spain using LiDAR height and intensity data,” *Remote Sens. Environ.*, vol. 114, no. 4, pp. 816–830, Apr. 2010.
- [242] H. Fuchs, P. Magdon, C. Kleinn, and H. Flessa, “Estimating aboveground carbon in a catchment of the Siberian forest tundra: Combining satellite imagery and field inventory,” *Remote Sens. Environ.*, vol. 113, no. 3, pp. 518–531, Mar. 2009.

- [243] M. A. Wulder, J. C. White, N. C. Coops, and C. R. Butson, "Multi-temporal analysis of high spatial resolution imagery for disturbance monitoring," *Remote Sens. Environ.*, vol. 112, no. 6, pp. 2729–2740, Jun. 2008.
- [244] K. Debeurs and P. Townsend, "Estimating the effect of gypsy moth defoliation using MODIS," *Remote Sens. Environ.*, vol. 112, no. 10, pp. 3983–3990, Oct. 2008.
- [245] J. Pontius, M. Martin, L. Plourde, and R. Hallett, "Ash decline assessment in emerald ash borer-infested regions: A test of tree-level, hyperspectral technologies," *Remote Sens. Environ.*, vol. 112, no. 5, pp. 2665–2676, May 2008.
- [246] N. C. Coops, R. H. Waring, M. A. Wulder, and J. C. White, "Prediction and assessment of bark beetle-induced mortality of lodgepole pine using estimates of stand vigor derived from remotely sensed data," *Remote Sens. Environ.*, vol. 113, no. 5, pp. 1058–1066, May 2009.
- [247] D. Kachelriess, M. Wegmann, M. Gollock, and N. Pettorelli, "The application of remote sensing for marine protected area management," *Ecol. Indic.*, vol. 36, pp. 169–177, Jan. 2014.
- [248] W. F. Laurance, D. C. Useche *et al.*, "Averting biodiversity collapse in tropical forest protected areas." *Nature*, vol. 489, no. 7415, pp. 290–294, Sep. 2012.
- [249] A. Altamirano, R. Field *et al.*, "Woody species diversity in temperate Andean forests: The need for new conservation strategies," *Biol. Conserv.*, vol. 143, no. 9, pp. 2080–2091, Sep. 2010.
- [250] S. Delalieux, B. Somers *et al.*, "Heathland conservation status mapping through integration of hyperspectral mixture analysis and decision tree classifiers," *Remote Sens. Environ.*, vol. 126, pp. 222–231, Nov. 2012.
- [251] W. D. Simonson, H. D. Allen, and D. a. Coomes, "Remotely sensed indicators of forest conservation status: Case study from a Natura

- 2000 site in southern Portugal,” *Ecol. Indic.*, vol. 24, pp. 636–647, Jan. 2013.
- [252] C. Schuster, I. Ali *et al.*, “Towards detecting swath events in TerraSAR-X time series to establish Natura 2000 grassland habitat swath management as monitoring parameter,” *Remote Sens.*, vol. 3, no. 12, pp. 1308–1322, Jun. 2011.
- [253] W. Cornforth, T. Fatoyinbo, T. Freemantle, and N. Pettorelli, “Advanced Land Observing Satellite Phased Array type L-band SAR (ALOS PALSAR) to inform the conservation of mangroves: Sundarbans as a case study,” *Remote Sens.*, vol. 5, no. 1, pp. 224–237, Jan. 2013.
- [254] J. Vanden Borre, D. Paelinckx *et al.*, “Integrating remote sensing in Natura 2000 habitat monitoring: Prospects on the way forward,” *J. Nat. Conserv.*, vol. 19, no. 2, pp. 116–125, May 2011.
- [255] N. Pettorelli, W. F. Laurance *et al.*, “Satellite remote sensing for applied ecologists: opportunities and challenges,” *J. Appl. Ecol.*, vol. 51, pp. 839–848, May 2014.
- [256] J. Gallego and C. Bamps, “Using CORINE land cover and the point survey LUCAS for area estimation,” *Int. J. Appl. Earth Obs.*, vol. 10, no. 4, pp. 467–475, Dec. 2008.
- [257] S. C. Popescu, K. Zhao, A. Neuenschwander, and C. Lin, “Satellite lidar vs. small footprint airborne lidar: Comparing the accuracy of aboveground biomass estimates and forest structure metrics at footprint level,” *Remote Sens. Environ.*, vol. 115, no. 11, pp. 2786–2797, Nov. 2011.
- [258] A. Achim, E. E. Kuruoğlu, and J. Zerubia, “SAR image filtering based on the heavy-tailed Rayleigh model,” *IEEE T. Image Process.*, vol. 15, no. 9, pp. 2686–2693, Sep. 2006.
- [259] F. Lang, J. Yang, D. Li, L. Shi, and J. Wei, “Mean-shift-based speckle filtering of polarimetric SAR data,” *IEEE T. Geosci. Remote*, vol. 52, no. 7, pp. 4440–4454, Jul. 2014.

- [260] L. Gomez, C. G. Munteanu, M. E. Buemi, J. C. Jacobo-Berlles, and M. E. Mejail, “Supervised constrained optimization of Bayesian nonlocal means filter with sigma preselection for despeckling SAR images,” *IEEE T. Geosci. Remote*, vol. 51, no. 8, pp. 4563–4575, Aug. 2013.
- [261] O. Duran and M. Petrou, “Robust endmember extraction in the presence of anomalies,” *IEEE T. Geosci. Remote*, vol. 49, no. 6, pp. 1986–1996, Jun. 2011.
- [262] —, “A time-efficient method for anomaly detection in hyperspectral images,” *IEEE T. Geosci. Remote*, vol. 45, no. 12, pp. 3894–3904, Dec. 2007.
- [263] Q. Du, N. Raksuntorn, N. H. Younan, and R. L. King, “End-member extraction for hyperspectral image analysis,” *Appl. Optics*, vol. 47, no. 28, pp. F77–F84, Oct. 2008.
- [264] A. Plaza, P. Martínez, R. Pérez, and J. Plaza, “A quantitative and comparative analysis of endmember extraction algorithms from hyperspectral data,” *IEEE T. Geosci. Remote*, vol. 42, no. 3, pp. 650–663, Mar. 2004.
- [265] E. T. Gormus, N. Canagarajah, and A. Achim, “Dimensionality reduction of hyperspectral images using empirical mode decompositions and wavelets,” *IEEE J. Sel. Top. Appl.*, vol. 5, no. 6, pp. 1821–1830, Dec. 2012.
- [266] T. Stathaki, Ed., *Image Fusion: Algorithms and Applications*. Oxford: Academic Press, 2008.
- [267] M. A. Lefsky, D. J. Harding *et al.*, “Estimates of forest canopy height and aboveground biomass using ICESat,” *Geophys. Res. Lett.*, vol. 32, no. 22, Nov. 2005.
- [268] K. C. Slatton, “Fusing interferometric radar and laser altimeter data to estimate surface topography and vegetation heights,” *IEEE Trans. Geosci. Remote Sens.*, vol. 39, no. 11, pp. 2470–2482, Nov. 2001.
- [269] P. Hyde, R. Dubayah *et al.*, “Mapping forest structure for wildlife habitat analysis using multi-sensor (LiDAR, SAR/InSAR, ETM+,

- Quickbird) synergy,” *Remote Sens. Environ.*, vol. 102, no. 1–2, pp. 63–73, May 2006.
- [270] K. P. Papathanassiou and S. R. Cloude, “Single-baseline polarimetric SAR interferometry,” *IEEE Trans. Geosci. Remote Sens.*, vol. 39, no. 11, pp. 2352–2363, Nov. 2001.
- [271] C. G. Brown, K. Sarabandi, and L. E. Pierce, “Model-based estimation of forest canopy height in red and Austrian pine stands using shuttle radar topography mission and ancillary data: A proof-of-concept study,” *IEEE Trans. Geosci. Remote Sens.*, vol. 48, no. 3, pp. 1105–1118, Mar. 2010.
- [272] M. Vastaranta, M. Niemi *et al.*, “Prediction of forest stand attributes using TerraSAR-X stereo imagery,” *Remote Sens.*, vol. 6, no. 4, pp. 3227–3246, Apr. 2014.
- [273] R. Perko, H. Raggam, K. Gutjahr, and M. Schardt, “The capabilities of TerraSAR-X imagery for retrieval of forest parameters,” in *Int. Archives Photogrammetry, Remote Sensing and Spatial Information Sciences*, vol. XXXVIII-7B. Vienna, Austria: ISPRS, 2010, pp. 452–456.
- [274] P. R. Chowdhury, B. Deshmukh, A. K. Goswami, and S. S. Prasad, “Neural network based dunal landform mapping from multispectral images using texture features,” *J. Sel. Top. Appl.*, vol. 4, no. 1, pp. 171–184, Mar. 2011.
- [275] A. Sarkar, M. K. Biswas *et al.*, “A MRF model-based segmentation approach to classification for multispectral imagery,” *IEEE T. Geosci. Remote*, vol. 40, no. 5, pp. 1102–1113, May 2002.
- [276] P. Planinšič, J. Singh, and D. Gleich, “SAR image categorization using parametric and nonparametric approaches within a dual tree CWT,” *IEEE Geosci. Remote S.*, vol. 11, no. 10, pp. 1757–1761, Oct. 2014.
- [277] C. B. Pühr and D. N. M. Donoghue, “Remote sensing of upland conifer plantations using Landsat TM data: A case study from

- Galloway, south-west Scotland,” *Int. J. Remote Sens.*, vol. 21, no. 4, pp. 633–646, Jan. 2000.
- [278] J. Franklin, T. L. Logan, C. E. Woodcock, and A. H. Strahler, “Coniferous forest classification and inventory using Landsat and digital terrain data,” *IEEE Trans. Geosci. Remote Sens.*, vol. GE-24, no. 1, pp. 139–149, Jan. 1986.
- [279] P. Holmgren and T. Thuresson, “Satellite remote sensing for forestry planning—A review,” *Scand. J. Forest Res.*, vol. 13, no. 1–4, pp. 90–110, 1998.
- [280] G. Chen, G. J. Hay, G. Castilla, B. St-Onge, and R. Powers, “A multiscale geographic object-based image analysis to estimate lidar-measured forest canopy height using Quickbird imagery,” *Int. J. Geogr. Inf. Sci.*, vol. 25, no. 6, pp. 877–893, Jun. 2011.
- [281] C. A. Múcher, L. Kooistra *et al.*, “Quantifying structure of Natura 2000 heathland habitats using spectral mixture analysis and segmentation techniques on hyperspectral imagery,” *Ecol. Indic.*, vol. 33, pp. 71–81, Oct. 2013.
- [282] G. W. Hazeu, A. K. Bregt, A. J. W. de Wit, and J. G. P. W. Clevers, “A Dutch multi-date land use database: Identification of real and methodological changes,” *Int. J. Appl. Earth Obs.*, vol. 13, no. 4, pp. 682–689, Aug. 2011.
- [283] G. F. Ficetola, A. Bonardi, C. A. Múcher, N. L. M. Gilissen, and E. Padoa-Schioppa, “How many predictors in species distribution models at the landscape scale? Land use versus LiDAR-derived canopy height,” *Int. J. Geogr. Inf. Sci.*, 2014, doi: 10.1080/13658816.2014.891222.
- [284] C. A. Múcher, L. Roupioz *et al.*, “Synergy of airborne LiDAR and Worldview-2 satellite imagery for land cover and habitat mapping: A BIO_SOS-EODHaM case study for the Netherlands,” *Int. J. Appl. Earth Obs.*, vol. 37, pp. 48–55, May 2015.
- [285] Q. Meng, B. E. Borders, C. J. Cieszewski, and M. Madden, “Closest

- spectral fit for removing clouds and cloud shadows,” *Photogramm. Eng. Rem. S.*, vol. 75, no. 5, pp. 569–576, May 2009.
- [286] C. E. Shannon, “A mathematical theory of communication,” *Bell Syst. Tech. J.*, vol. 27, no. 3, pp. 379–423, Jul. 1948.
- [287] ———, “A mathematical theory of communication,” *Bell Syst. Tech. J.*, vol. 27, no. 4, pp. 623–656, Oct. 1948.
- [288] M. Petrou and P. García-Sevilla, *Image Processing: Dealing with Texture*. Chichester, United Kingdom: John Wiley & Sons, 2006, ch. 4, pp. 297–606.
- [289] X. Tan and B. Triggs, “Enhanced local texture feature sets for face recognition under difficult lighting conditions,” *IEEE T. Image Process.*, vol. 19, no. 6, pp. 1635–1650, Jun. 2010.
- [290] J. L. Schafer and J. W. Graham, “Missing data: our view of the state of the art,” *Psychol. Methods*, vol. 7, no. 2, pp. 147–177, Jun. 2002.
- [291] R. J. A. Little and D. B. Rubin, *Statistical Analysis with Missing Data*. New York, NY: John Wiley & Sons, 1987, ch. 3, pp. 39–49.
- [292] R. R. Andridge and R. J. A. Little, “A review of hot deck imputation for survey non-response,” *Int. Stat. Rev.*, vol. 78, no. 1, pp. 40–64, Apr. 2010.
- [293] J. Honaker, G. King, and M. Blackwell, “Amelia II: A program for missing data,” *J. Stat. Softw.*, vol. 45, no. 7, pp. 1–47, Dec. 2011.
- [294] M. Templ, A. Kowarik, and P. Filzmoser, “Iterative stepwise regression imputation using standard and robust methods,” *Comput. Stat. Data An.*, vol. 55, no. 10, pp. 2793–2806, Oct. 2011.
- [295] D. B. Rubin, “Inference and missing data,” *Biometrika*, vol. 63, no. 3, pp. 581–592, Dec. 1976.
- [296] V. Barnett and T. Lewis, *Outliers in Statistical Data*, 3rd ed. Chichester, United Kingdom: John Wiley & Sons, 1994, ch. 1, pp. 3–26.

- [297] F. E. Grubbs, "Procedures for detecting outlying observations in samples," *Technometrics*, vol. 11, no. 1, pp. 1–21, Feb. 1969.
- [298] Y. Zhang, N. Meratnia, and P. Havinga, "Outlier detection techniques for wireless sensor networks: A survey," *IEEE Communications Surveys & Tutorials*, vol. 12, no. 2, pp. 159–170, Apr. 2010.
- [299] F. Angiulli, S. Basta, and C. Pizzuti, "Distance-based detection and prediction of outliers," *IEEE T. Knowl. Data En.*, vol. 18, no. 2, pp. 145–160, Feb. 2006.
- [300] A. Albanese, S. K. Pal, and A. Petrosino, "Rough sets, kernel set, and spatiotemporal outlier detection," *IEEE T. Knowl. Data En.*, vol. 26, no. 1, pp. 194–207, Jan. 2014.
- [301] J. W. Tukey, *Exploratory Data Analysis*. London, United Kingdom: Addison-Wesley, 1977, ch. 2, pp. 27–56.
- [302] J. Laurikkala, M. Juhola, and E. Kentala, "Informal identification of outliers in medical data," in *5th Int. Workshop Intelligent Data Analysis in Medicine and Pharmacology*, Berlin, Germany, 2000.
- [303] M. Hubert and E. Vandervieren, "An adjusted boxplot for skewed distributions," *Comput. Stat. Data An.*, vol. 52, no. 12, pp. 5186–5201, Aug. 2008.
- [304] G. Brys, M. Hubert, and P. J. Rousseeuw, "A robustification of independent component analysis," *J. Chemometr.*, vol. 19, no. 5–7, pp. 364–375, Sep. 2005.
- [305] B. Iglewicz and D. C. Hoaglin, *How to Detect and Handle Outliers*. Milwaukee, WI: ASQC Quality Press, 1993.
- [306] S. Theodoridis and K. Koutroumbas, *Pattern Recognition*, 4th ed. Burlington, MA: Academic Press, 2009, ch. 5, pp. 261–322.
- [307] G. Chen and S. E. Qian, "Denoising of hyperspectral imagery using principal component analysis and wavelet shrinkage," *IEEE T. Geosci. Remote*, vol. 49, no. 3, pp. 973–980, Mar. 2011.

- [308] V. Zubko, Y. J. Kaufman, R. Burg, and J. V. Martins, “Principal component analysis of remote sensing of aerosols over oceans,” *IEEE T. Geosci. Remote*, vol. 45, no. 3, pp. 730–745, Mar. 2007.
- [309] Q. Weng, “Remote sensing of impervious surfaces in the urban areas: Requirements, methods, and trends,” *Remote Sens. Environ.*, vol. 117, no. 15, pp. 34–49, Feb. 2012.
- [310] A. Garzelli and L. Capobianco, “Effects of the spatial enhancement of hyperspectral images on the distribution of spectral classes,” in *Optical Remote Sensing: Advances in Signal Processing and Exploitation Techniques*, ser. Augmented Vision and Reality 3, S. Prasad, L. M. Bruce, and J. Chanussot, Eds. Berlin Heidelberg, Germany: Springer-Verlag, 2011, ch. 14, pp. 301–327.
- [311] X. He, D. Cai, S. Yan, and H.-J. Zhang, “Neighborhood preserving embedding,” in *Proc. Tenth IEEE Int. Conf. Computer Vision (ICCV’05)*, vol. 2. Beijing: IEEE, 2005, pp. 1208–1213.
- [312] L. Wenzhi, A. Pizurica, W. Philips, and P. Youguo, “Feature extraction for hyperspectral images based on semi-supervised local discriminant analysis,” in *2011 Joint Urban Remote Sensing Event*, Munich, Germany, 2011, pp. 401–404.
- [313] J. B. Tenenbaum, V. de Silva, and J. C. Langford, “A global geometric framework for nonlinear dimensionality reduction.” *Science (New York, N.Y.)*, vol. 290, no. 5500, pp. 2319–2323, Dec. 2000.
- [314] C. I. Chang and H. Ren, “An experiment-based quantitative and comparative analysis of target detection and image classification algorithms for hyperspectral imagery,” *IEEE T. Geosci. Remote*, vol. 38, no. 2, pp. 1044–1063, Mar. 2000.
- [315] P. Langley, “Selection of relevant features in machine learning,” in *Proc. AAAI Fall Symp. Relevance*, 1994, pp. 127–131.
- [316] I. H. Witten, E. Frank, and M. A. Hall, *Data Mining: Practical Machine Learning Tools and Techniques*, 3rd ed. Burlington, MA: Morgan Kaufmann Publishers, 2011.

- [317] M. A. Hall, “Correlation-based feature selection for machine learning,” Ph.D. dissertation, Univ. of Waikato, Hamilton, New Zealand, 1999.
- [318] H. Liu and R. Setiono, “A probabilistic approach to feature selection - a filter solution,” in *13th Int. Conf. Machine Learning*, 1996, pp. 319–327.
- [319] R. Kohavi and G. H. John, “Wrappers for feature subset selection,” *Artif. Intell.*, vol. 97, no. 1–2, pp. 273–324, Dec. 1997.
- [320] M. Gütlein, E. Frank, M. Hall, and A. Karwath, “Large-scale attribute selection using wrappers,” in *IEEE Symp. Computational Intelligence and Data Mining*, 2009, pp. 332–339.
- [321] P. Pudil, J. Novovičová, and J. Kittler, “Floating search methods in feature selection,” *Pattern Recogn. Lett.*, vol. 15, no. 11, pp. 1119–1125, Nov. 1994.
- [322] A. M. Prasad, L. R. Iverson, and A. Liaw, “Newer classification and regression tree techniques: Bagging and random forests for ecological prediction,” *Ecosystems*, vol. 9, no. 2, pp. 181–199, Mar. 2006.
- [323] P. Gislason, J. Benediktsson, and J. Sveinsson, “Random forests for land cover classification,” *Pattern Recogn. Lett.*, vol. 27, no. 4, pp. 294–300, Mar. 2006.
- [324] J. Leitloff, S. Hinz, and U. Stilla, “Vehicle detection in very high resolution satellite images of city areas,” *IEEE T. Geosci. Remote*, vol. 48, no. 7, pp. 2795–2806, Jul. 2010.
- [325] M. Dalponte, L. Bruzzone, and D. Gianelle, “Fusion of hyperspectral and LIDAR remote sensing data for classification of complex forest areas,” *IEEE Trans. Geosci. Remote Sens.*, vol. 46, no. 5, pp. 1416–1427, May 2008.
- [326] G. M. Foody and A. Mathur, “A relative evaluation of multiclass image classification by support vector machines,” *IEEE Trans. Geosci. Remote Sens.*, vol. 42, no. 6, pp. 1335–1343, Jun. 2004.

- [327] R. Quinlan, *C4.5: Programs for Machine Learning*. San Mateo, CA: Morgan Kaufmann Publishers, 1993.
- [328] L. Breiman, “Random forests,” *Mach. Learn.*, vol. 45, no. 1, pp. 5–32, Oct. 2001.
- [329] ———, “Bagging predictors,” *Mach. Learn.*, vol. 24, no. 2, pp. 123–140, Aug. 1996.
- [330] Y. Freund and R. E. Schapire, “Experiments with a new boosting algorithm,” in *Proc. 13th Int. Conf. Machine Learning*. San Mateo, CA: Morgan Kaufmann Publishers, 1996, pp. 148–156.
- [331] J. C. Platt, “Fast training of support vector machines using sequential minimal optimization,” in *Advances in Kernel Methods: Support Vector Learning*, B. Schölkopf, C. J. C. Burges, and A. J. Smola, Eds. Cambridge, MA: The MIT Press, 1998, ch. 12.
- [332] T. Hastie and R. Tibshirani, “Classification by pairwise coupling,” *Ann. Statist.*, vol. 26, no. 2, pp. 451–471, Apr. 1998.
- [333] S. Koelstra, M. Pantic, and I. Patras, “A dynamic texture-based approach to recognition of facial actions and their temporal models,” *IEEE T. Pattern Anal.*, vol. 32, no. 11, pp. 1940–1954, Nov. 2010.
- [334] C. M. Roelfsema, M. Lyons *et al.*, “Multi-temporal mapping of seagrass cover, species and biomass: A semi-automated object based image analysis approach,” *Remote Sens. Environ.*, vol. 150, pp. 172–187, Jul. 2014.
- [335] L. Xu, J. Li, and A. Brenning, “A comparative study of different classification techniques for marine oil spill identification using RADARSAT-1 imagery,” *Remote Sens. Environ.*, vol. 141, pp. 14–23, Feb. 2014.
- [336] R. Kohavi, “A study of cross-validation and bootstrap for accuracy estimation and model selection,” in *Proc. 14th Int. Joint Conf. Artificial Intelligence (IJCAI)*, vol. 2, 1995, pp. 1137–1143.

- [337] C. Chatfield, *Statistics for Technology: A Course in Applied Statistics*, 3rd ed. Boca Raton, FL: Chapman and Hall/CRC, 1983, ch. 7, pp. 134–165.
- [338] H. Zhu and O. Basir, “An adaptive fuzzy evidential nearest neighbor formulation for classifying remote sensing images,” *IEEE T. Geosci. Remote*, vol. 43, no. 8, pp. 1874–1889, Aug. 2005.
- [339] J. Cohen, “A coefficient of agreement for nominal scales,” *Educ. Psychol. Meas.*, vol. 20, no. 1, pp. 37–46, Apr. 1960.
- [340] J. R. Landis and G. G. Koch, “The measurement of observer agreement for categorical data,” *Biometrics*, vol. 33, no. 1, pp. 159–174, Mar. 1977.
- [341] L. Bottou and C.-J. Lin, “Support vector machine solvers,” in *Large-Scale Kernel Machines*, L. Bottou, O. Chapelle, D. DeCoste, and J. Weston, Eds. Cambridge, MA: The MIT Press, 2007, ch. 1, pp. 1–27.
- [342] I. W. Tsang, J. T. Kwok, and P.-M. Cheung, “Core vector machines: Fast SVM training on very large data sets,” *J. Mach. Learn. Res.*, vol. 6, pp. 363–392, Apr. 2005.
- [343] T. Joachims, “Training linear SVMs in linear time,” in *Proc. 12th ACM SIGKDD int. conf. on Knowledge discovery and data mining*. Philadelphia, PA: ACM, 2006, pp. 217–226.
- [344] Z. I. Petrou, C. Tarantino, M. Adamo, P. Blonda, and M. Petrou, “Estimation of vegetation height through satellite image texture analysis,” in *International Archives of the Photogrammetry, Remote Sensing and Spatial Information Sciences*, vol. XXXIX-B8. Melbourne: ISPRS, 2012, pp. 321–326.
- [345] M. Förster and B. Kleinschmit, “Recent advances in remote sensing: Change detection – a review,” in *Object-based Image Analysis: Spatial Concepts for Knowledge-Driven Remote Sensing Applications*, T. Blaschke, S. Lang, and G. J. Hay, Eds. Berlin Heidelberg: Springer, 2008, ch. 3.1, pp. 275–290.

- [346] R. Bunce, M. Bogers *et al.*, “Manual for habitat and vegetation surveillance and monitoring: Temperate, mediterranean and desert biomes,” Alterra, Tech. Rep. 2154, 2011.
- [347] J. A. Malpica, M. C. Alonso, and M. A. Sanz, “Dempster-Shafer theory in geographic information systems: A survey,” *Expert Syst. Appl.*, vol. 32, no. 1, pp. 47–55, Jan. 2007.
- [348] E. Binaghi and P. Madella, “Fuzzy Dempster–Shafer reasoning for rule-based classifiers,” *Int. J. Intell. Syst.*, vol. 14, no. 6, pp. 559–583, Jun. 1999.
- [349] A. Pinz, M. Prantl, H. Ganster, and H. Kopp-Borotschnig, “Active fusion - A new method applied to remote sensing image interpretation,” *Pattern Recogn. Lett.*, vol. 17, no. 13, pp. 1349–1359, Nov. 1996.
- [350] A. Saffiotti, “Issues of knowledge representation in Dempster–Shafer’s Theory,” in *Advances in the Dempster-Shafer theory of evidence*, J. K. R. R. Yager, M. Fedrizi, Ed. New York, NY: John Wiley & Sons, Inc., 1994, ch. 19, pp. 415–440.
- [351] R. R. Yager, “On the Dempster–Shafer framework and new combination rules,” *Inform. Sciences*, vol. 41, no. 2, pp. 93–137, Mar. 1987.
- [352] A. Osman, V. Kaftandjian, and U. Hassler, “Improvement of X-ray castings inspection reliability by using Dempster-Shafer data fusion theory,” *Pattern Recogn. Lett.*, vol. 32, no. 2, pp. 168–180, Jan. 2011.
- [353] O. Basir and X. Yuan, “Engine fault diagnosis based on multi-sensor information fusion using Dempster–Shafer evidence theory,” *Inform. Fusion*, vol. 8, no. 4, pp. 379–386, Oct. 2007.
- [354] Y. Deng, X. Su, D. Wang, and Q. Li, “Target recognition based on fuzzy Dempster data fusion method,” *Defence Sci. J.*, vol. 60, no. 5, pp. 525–530, 2010.
- [355] M. R. Ahmadzadeh and M. Petrou, “Use of Dempster–Shafer theory to combine classifiers which use different class boundaries,” *Pattern Anal. Appl.*, vol. 6, no. 1, pp. 41–46, Apr. 2003.

- [356] A. Bendjebbour, Y. Delignon, L. Fouque, V. Samson, and W. Pieczynski, "Multisensor image segmentation using Dempster–Shafer fusion in Markov fields context," *IEEE T. Geosci. Remote*, vol. 39, no. 8, pp. 1789–1798, 2001.
- [357] J. Van Cleynenbreugel, S. A. Osinga, F. Fierens, P. Suetens, and A. Oosterlinck, "Road extraction from multi-temporal satellite images by an evidential reasoning approach," *Pattern Recogn. Lett.*, vol. 12, no. 6, pp. 371–380, Jun. 1991.
- [358] T. Corpetti and O. Planchon, "Front detection on satellite images based on wavelet and evidence theory: Application to the sea breeze fronts," *Remote Sens. Environ.*, vol. 115, no. 2, pp. 306–324, Feb. 2011.
- [359] J. Tian, S. Cui, and P. Reinartz, "Building change detection based on satellite stereo imagery and digital surface models," *IEEE T. Geosci. Remote*, vol. 52, no. 1, pp. 406–417, Jan. 2014.
- [360] V. Poulain, J. Inglada, M. Spigai, J. Tourneret, and P. Marthon, "High-resolution optical and SAR image fusion for building database updating," *IEEE T. Geosci. Remote*, vol. 49, no. 8, pp. 2900–2910, Aug. 2011.
- [361] F. Rottensteiner, J. Trinder, S. Clode, and K. Kubik, "Using the Dempster–Shafer method for the fusion of LIDAR data and multi-spectral images for building detection," *Inform. Fusion*, vol. 6, no. 4, pp. 283–300, Dec. 2005.
- [362] T. Fei, D. Kraus, and A. M. Zoubir, "Contributions to automatic target recognition systems for underwater mine classification," *IEEE T. Geosci. Remote*, vol. 53, no. 1, pp. 505–518, Jan. 2015.
- [363] A. Sarkar, A. Banerjee *et al.*, "Landcover classification in MRF context using Dempster–Shafer fusion for multisensor imagery," *IEEE T. Image Process.*, vol. 14, no. 5, pp. 634–645, May 2005.
- [364] V. Saeidi, B. Pradhan, M. O. Idrees, and Z. Abd Latif, "Fusion of airborne LiDAR with multispectral SPOT 5 image for enhancement

- of feature extraction using Dempster–Shafer theory,” *IEEE T. Geosci. Remote*, vol. 52, no. 10, pp. 6017–6025, Oct. 2014.
- [365] W. Sun, S. Liang, G. Xu, H. Fang, and R. Dickinson, “Mapping plant functional types from MODIS data using multisource evidential reasoning,” *Remote Sens. Environ.*, vol. 112, no. 3, pp. 1010–1024, Mar. 2008.
- [366] S. E. Franklin, D. R. Peddle, J. A. Dechka, and G. B. Stenhouse, “Evidential reasoning with Landsat TM, DEM and GIS data for landcover classification in support of grizzly bear habitat mapping,” *Int. J. Remote Sens.*, vol. 23, no. 21, pp. 4633–4652, 2002.
- [367] A. Laha, N. R. Pal, and J. Das, “Land cover classification using fuzzy rules and aggregation of contextual information through evidence theory,” *IEEE T. Geosci. Remote S.*, vol. 44, no. 6, pp. 1633–1641, Jun. 2006.
- [368] J. K. Lein, “Applying evidential reasoning methods to agricultural land cover classification,” *Int. J. Remote Sens.*, vol. 24, no. 21, pp. 4161–4180, 2003.
- [369] L. Cayuela, J. D. Golicher, J. S. Rey, and J. M. R. Benayas, “Classification of a complex landscape using Dempster–Shafer theory of evidence,” *Int. J. Remote Sens.*, vol. 27, no. 10, pp. 1951–1971, May 2006.
- [370] Y. Cohen and M. Shoshany, “Analysis of convergent evidence in an evidential reasoning knowledge-based classification,” *Remote Sens. Environ.*, vol. 96, no. 3-4, pp. 518–528, Jun. 2005.
- [371] G. J. Klir, “Foundations of fuzzy set theory and fuzzy logic: A historical overview,” *Int. J. Gen. Syst.*, vol. 2, no. 30, pp. 91–132, 2001.
- [372] F. Aminravan, R. Sadiq *et al.*, “Evidential reasoning using extended fuzzy Dempster–Shafer theory for handling various facets of information deficiency,” *Int. J. Intell. Syst.*, vol. 26, no. 8, pp. 731–758, 2011.

- [373] Y. Deng, R. Sadiq, W. Jiang, and S. Tesfamariam, “Risk analysis in a linguistic environment: A fuzzy evidential reasoning-based approach,” *Expert Syst. Appl.*, vol. 38, no. 12, pp. 15 438–15 446, Nov.–Dec. 2011.
- [374] L. A. Zadeh, “A simple view of the Dempster–Shafer theory of evidence and its implication for the rule of combination,” *AI Mag.*, vol. 7, no. 2, pp. 85–90, 1986.
- [375] J. D. Gibbons and S. Chakraborti, *Nonparametric Statistical Inference*, 4th ed., ser. Statistics: Textbooks and Monographs. New York, NY: Marcel Dekker, 2003, ch. 11, pp. 399–449.
- [376] D. Pflugmacher, W. B. Cohen, and R. E. Kennedy, “Using Landsat-derived disturbance history (1972–2010) to predict current forest structure,” *Remote Sens. Environ.*, vol. 122, pp. 146–165, Jul. 2012.
- [377] A. Collin, B. Long, and P. Archambault, “Salt-marsh characterization, zonation assessment and mapping through a dual-wavelength LiDAR,” *Remote Sens. Environ.*, vol. 114, no. 3, pp. 520–530, Mar. 2010.
- [378] M. Masocha and A. K. Skidmore, “Integrating conventional classifiers with a GIS expert system to increase the accuracy of invasive species mapping,” *Int. J. Appl. Earth Obs.*, vol. 13, no. 3, pp. 487–494, Jun. 2011.
- [379] C. Joshi, J. De Leeuw *et al.*, “Indirect remote sensing of a cryptic forest understorey invasive species,” *Forest Ecol. Manag.*, vol. 225, no. 1–3, pp. 245–256, Apr. 2006.

A. Methods for CBD indicator extraction

A.1. Abbreviations in Tables A.1–A.6

A

AGB: Above Ground Biomass; AgI: Aggregation Index; ALS: Airborne Laser Scanning (LiDAR); ANN: Artificial Neural Networks; APAR: Absorbed Photosynthetically Active Radiation (APAR); ARI: Anthocyanin Reflectance Index; AWMFPD: Area-Weighted Mean Patch Fractal Dimension

B

BA: basal area; BRDF: Bidirectional Reflectance Distribution Function

C

CAI: Cellulose Absorption Index; CAMx: Comprehensive Air-Quality Model with extensions; CART: Classification And Regression Tree; CCA: Canonical Correlation Analysis; CCCI: Canopy Chlorophyll Content Index; CCFS: Crown Cover and Forest Status index; CD-AL: change-detection-based Active Learning; CDIA: tree canopy diameter; ChD: Change Detection; chl-a: chlorophyll-a; CHM: Canopy Height Model; CI: Clumpiness Index; cl.: classes; class.: classification; CMFDA: Continuous Monitoring of Forest Disturbance Algorithm; COD_{cr}: chemical oxygen demand; CPL: Core area Percentage of Landscape; CRA: Constrained Redundancy Analysis; CRI: Carotenoid Reflectance Index; CVA: Change Vector Analysis; CWSI: Crop Water Stress Index; DA: Data Assimilation

D

DBH: density at breast height; DCNI: Double-peak Canopy Nitrogen Index; DEM: Digital Elevation Model; DGVI: Derivative Greenness Vegetation Indices; DIM: Digital Intensity Models; DSM: Digital Surface Model; DTM: Digital Terrain Model

E

ECAI: Equivalent Connected Area Index; ED: Euclidean Distance; EL: Edge length; EMMM: Expectation Maximization Mixture Models; EVI: Enhanced Vegetation Index; ExG_M: Excess Green Index

F

fAPAR: fraction of Absorbed Photosynthetically Active Radiation; FBD: Fine-Beam Dual; feat. sel.: feature selection; FVC: Fractional Vegetation Cover

G

GA: Genetic Algorithm; GAM: Generalized Additive Models; GAMLSS: Generalized Additive Models for Location, Scale and Shape; GARP: Genetic Algorithm for Rule-Set Production; GC: Gini Coefficient; GCV: Generalized Cross Validation; GLM: Generalized Linear Models; GMM: Gaussian Mixture Model; GPP: Gross Primary Productivity

H

h-h SR-meter: hand-held spectroradiometer

I

IDWI: Inverse Distance Weighted Interpolation; inv. alg: inversion algorithms; I-T: Information-Theoretic approach

J

JCV: Jack-Knife Cross Validation

L

LAI: Leaf Area Index; LC: Land Cover; LDA: Linear Discriminant Analysis; LDiv: Landscape division; LL R²M: lambda-lambda R² models;

LLSR: Linear Least Square Regression; LogR: Logistic Regression; LPI: Largest Patch Index; LR: Linear Regression; LRA: Linear Regression Analysis; LRM: Linear Regression Models; LSMM: Linear Spectral Mixture Models; LSU: Linear Spectral Unmixing; LSWI: Land Surface Water Index; LU: Land Use

M

m.s.l.: mean sea level; m/date: multi-date; m/res.: multiresolution; m/spectr.: multispectral; m/temp.: multitemporal; MAE: Mean Absolute Error; MANOVA: Multiple Analysis Of Variance; M-C: Monte-Carlo; MCC: Multiscale Curvature Classification; MD: Mahalanobis Distance; MDM: minimum-distance-to-means; MDS: Multidimensional Scaling; MESMA: Multiple Endmember Spectral Mixture Analysis; MFIN: Mean Forest Intensity Normalization; MICA: Material Identification and Characterization Algorithm; MinNF: Minimum Noise Fraction; MLC: Maximum Likelihood Classification; MLLSR: Multivariate Linear Least Square Regression; MLR: Multiple Linear Regression; MLRM: Multiple Linear Regression Models; MLSR: Multiple Least-Square Regression; MMHC: MiraMon's software hybrid classifier; MNF: Maximum Noise Fraction; MPS: Mean Patch Size; MRA: Multiple Regression Analyses; MSN: Most Similar Neighbour; MTMF: Mixture Tuned Matched Filtering Spectral Mixture Analysis

N

NBGLM: Negative Binomial General Linear Models; NBRI: Normalized Burn Ratio Index; NDLI: Normalized Difference Lignin Index; NDLVI: Normalized Difference LiDAR Vegetation Index; NDNI: Normalized Difference Nitrogen Index; NDRE: Normalized Difference Red Edge; nDSM: normalised Digital Surface Model; NDSVI: Normalized Differential Senescent Vegetation Index; NDTI: Normalized Difference Tillage Index; NDVI: Normalized Difference Vegetation Index; NDWI: Normalized Difference Water Index; NH₄-N: ammonia Nitrogen; NIRI: Normalized Infrared Index; nLSU: non-Linear Spectral Unmixing; NN: Nearest Neighbour; NND: Mean nearest neighbour distance; NNI: Nearest Neighbor Imputation; NP: number of patches; NSI: Nitrogen Stress Index; NSM: Normalized Surface Model

O

OA: overall accuracy; OBIA: Object-Based Image Analysis; obj/rule class.: object-oriented rule-based classification; OII: Ozone Injury Index; OIUC: Optimal Iterative Unsupervised Classification; OSAVI: Optimized Soil-Adjusted Vegetation Index

P

PA: producer's accuracy; PAR: Photosynthetically Active Radiation; PC: Patch Cohesion; PCA: Principal Component Analysis; PD: Patch Density; PLSR: Partial Least Square Regression; polarim.: polarimetric; PPI: Pixel Purity Index; PRA: Partial Redundancy Analysis; PRI: Photochemical Reflectance Index; PSCV: patch size coefficient of variance; PVI: Perpendicular Vegetation Index

Q

QDA: Quadratic Discriminant Analysis; QRM: quadratic regression models

R

RDA: Regularized Discriminant Analysis; REIP: Red-Edge Inflection Point; rel.diff.: relative difference; REPI: Red Edge Position Index; RF: Random Forest; RFE: Recursive Feature Elimination; RG: Mean radius of gyration; RGMAP: Refined Gamma Maximum-A-Posteriori (filtering); RGRI: Red Green Ratio Index; RMSE: Root Mean Square Error; RSDP: Relative Spectral Discriminatory Probability; RVoG: random volume over ground

S

s/res.: super-resolution; SAM: Spectral Angle Mapper; SAVI: Soil-Adjusted Vegetation Index; SCM: Spectral Correlation Mapper; sd: standard deviation; SDA: Stepwise Discriminant Analysis; SDD: Secchi Disk Depth; SDDBH: Standard Deviation of Diameters at Breast Heights; SDI: Shannon Diversity Index; segm.: segmentation; SEI: Shannon-Evenness Index; sER: slope adaptive Echo Ratio; SFFS: Sequential Forward Floating Selection; SFLR: Stepwise Forward Logistic

Regression; SFS: Sequential Forward Selection; SG: Savitzky-Golay (filter); SI: Separability Index; SID: Spectral Information Divergence; SLMM: Spectral Linear Mixing Model; SMA: Spectral Mixture Analysis; SMLR: Stepwise Multiple Linear Regression; SMR: Stepwise Multiple Regression; SNA: Spatial Neighborhood Analysis; spat.: spatial (features); spectr.: spectral (features); SRI: Simple Ratio Index; SST: sea-surface temperature; SV: stem volume; SVM: Support Vector Machines; SWI: Shannon-Weaver diversity index

T

TCAI: Tasseled Cap Angle Index; TCT: Tasseled Cap Transformation; text.: texture (features); TMA: Temporal Mixture Analysis; tN: total Nitrogen; tP: total Phosphorous; ts: time series

U

UA: user's accuracy

V

VGPM: Vertically Generalized Production Model; VIF: Variance Inflation Factor; VIP: Variable Importance in Projection; VIT: Vegetation Index Temperature; VTRER: Varying-Time Random Effects Regression

W

WBI: Water Band Index; WCI: Wetland Condition Index; WDRVI: Wide Dynamic Range Vegetation Index

A.2. Tables with methods for CBD headline indicator extraction

A.2.1. Trends in extent, condition and vulnerability of ecosystems, biomes and habitats

Table A.1.: Methods studying different parameters related to the CBD headline indicator measuring trends in extent, condition and vulnerability of ecosystems, biomes and habitats.

RS data	Feature extraction	Mapping	Final product	Best accuracy	Ref.
Forest extent					
ALS	nDSM, sER map	min. height, crown coverage, min. area, min. width	temper. forest detection	96% (2 cl.)	[84]
PALSAR, TM	spectr., text., spat., topogr. features; TCT	RF	trop. forest class.	90% (6 cl.) PALSAR; \approx +3% TM	[80]
PALSAR, TM	polarim., interfer., text. features	SVM	tropical forest class.	85.5% PALSAR + TM (7 cl.)	[83]
ETM+	GIS to define ecoregions; spectr. reflectance	OIUC	temper. late seral forests class.	90.72% (3 cl.)	[70]
TM / ETM+ ts	spectr. reflectance; post-class. map compositing	MLC (pre), max. label (post)	trop. peat swamp forest	86% (4 cl.)	[71]
Hyperion	spectr. reflectance; feat. sel. SDA	ANN, SVM, SAM	trop. forest class.	81% (8 cl.)	[78]
dual-date RSAT-2	polarim. features; SFFS	ensemble SVM	boreal forest class.	69.14% (9 cl.)	[81]
PALSAR	text. features; feat. sel. SVM RFE	SVM	trop. forest class.	69.9% (6 cl.)	[82]
Grassland, savanna, peatland, heathland					
MODIS ts, ETM+	m/res. segm.; EVI, spectr. reflectance, phenol. features; SG filter	RF	dry savanna mapping	94.86% UA, 97.73% PA (12 cl.)	[76]
ASTER	SAVI	MLC, majority 3×3 filter	steppe LU mapping	79% (8 cl.)	[74]
ETM+	growing region segm.; spectr. reflectance	visual interpretation	savanna mapping	71% (6 cl.)	[68]

Continued on next page. . .

Table A.1 – continued

RS data	Feature extraction	Mapping	Final product	Accuracy	Ref.
m/temp. TM	spectr. reflectance, TCT, PCA, veg. indices	MANOVA, SDA, JCV	temper. grassland mapping	70.4% (6 cl.)	[69]
CHRIS	spectr. reflectance	RF, AdaBoost, SVM	Natura 2000 heathland class.	61.8% SVM (10 cl.)	[79]
LC / habitat mapping					
TM, AVNIR-2, PALSAR	text. features	MLC, ANN	trop. rainforest mapping	97.5% AVNIR-2 + PALSAR (8 cl.)	[75]
TM / ETM+	text. features	MLC, <i>k</i> -NN, 4 SVM, MMHC	tropical LC map	up to 96.13% (8 cl.)	[67]
ADS40, MIVIS, ALS	text. features, hillshade modeling, nDSM, SFS feat. reduction	MLC, SAM, SID, post-class. majority filter	LC mapping of heterogeneous landscape	92.57% (17 cl.)	[77]
TM ts	spectr. reflectance; CVA; CD-AL;	SVM	LC update	≈92% (7 cl.)	[72]
ETM+	spectr. reflectance	CART, SVM, MLC	target habitat mapping	88.4% (8 cl.)	[66]
TM / ETM+ ts, ALS, ASTER	segm.; DSM; NDVI; spectr., text. measures	obj/rule class.	EUNIS habitat class.	86.19% (10 cl.)	[47]
m/temp. HRG, ASTER, IRS	spectr. features, multi-level segm.	obj/rule class.	habitat map of Wales	80.7% (19 cl.)	[46]
LISS-III, aerial photos (0.4 m)					
m/temp. QB, WV-2, LiDAR	spat., topol., temp., geometric, context., spectr. features	obj/rule class.	Mediterranean habitat map	78.4% (21 cl.)	[53]
TM	NDVI	image differencing, image ratioing, image regression & CVA	LC/LU ChD	75.5% correct ChD (12 cl.)	[73]
Degradation and deforestation					
TM / ETM+ ts	TCT; temp. segm. and fitting; TCAI	SVM	forest disturbance mapping	95.72% (24 cl.)	[93]
TM / ETM+ ts	TCT Wetness, forestness index, NDVI, NBRI, TCAI	m/temp. RGB color comp. anal.; MDM	wildfire and clearcut harvest disturb. mapping	93% (32 cl.)	[94]

Continued on next page. . .

Table A.1 – continued

RS data	Feature extraction	Mapping	Final product	Accuracy	Ref.
TM / ETM+ ts	CMFDA; NDVI; TCT	threshold-based forest mapping	forest disturbance monitoring	96.7% PA, 95.83% UA; 94% temp. acc.	[95]
PALSAR ts	slope-corrected gamma nought	threshold-based class.	deforestation mapping	87% (5 cl.)	[105]
TM / ETM+ ts	NDVI, NIRI	RF	deforestation estimation	83.3% (6 cl.)	[96]
TM / ETM+ ts	veg. change tracker, NDVI, integrated forest z-score, NBRI	rule-based class.	forest disturbance	around 80% (13 cl.)	[97]
TM / ETM+ ts, MODIS, aerial photos	TCT; Disturbance Index ChD	ISODATA	forest gain and loss mapping	81.67% (3 cl.)	[98]
MSS / TM ts	SLMM; m/date segm.	fuzzy NN; object-level Boolean ChD	deforestation mapping	75% (4 cl.)	[99]
AVHRR ts	reflect. values, NDVI	bagging decision trees	burned area detection	68% PA, 56% UA	[103]
TM / ETM+ ts	spectr., therm., temp., context. features, watershed area, multi-date ChD, region growing, morphological dilation	obj.-based class. tree	burned area mapping	85% PA, 71% UA	[100]
HRG, ETM+	converted brightness, NIR sd and compactness layers	object-based mapping	ecosystem degradation (intactness index)	76.7% Landsat (3 cl.)	[101]
PALSAR ts	MFIN; intensity-based ChD measures; ScanSAR and FBD measure combination	threshold-based class.	tropical deforestation detection	72% detection w. 20% false alarm rate	[106]
MSS / TM / ETM+ ts; ALS	TCT, TimeSync temp. segm., LandTrendr, Landsat disturbance metrics	LRA	forest disturbance history	0.66–0.85 R ² for structure attributes	[376]
AWIFS, MODIS	spectr. reflectances	bagging ANN and Class. tree; region growing	burnt scar mapping	0.72–0.79 <i>k</i> (2 cl.)	[104]
Fragmentation					

Continued on next page. . .

Table A.1 – continued

RS data	Feature extraction	Mapping	Final product	Accuracy	Ref.
MSS / TM	AWMPFD & CPL indices	visual interpretation; post-class. cross-tabulation change analysis	forest fragm. analysis	92.9% LCLU map (7 cl.); different trends in AWMPFD and CPL, whereas other indices remain similar	[110]
TM	indices: NP, PD, LPI, MPS, PSCV, AWMPFD	visual interpretation	marsh fragm. assessment	90% LC map (8 cl.); similar trends to index changes, different scales	[111]
TM	FRAGSTATS indices	supervised class.	Forest fragm. & connectivity change monitoring	83% LC (7 cl.); 93.8% change in connectivity, 0.67–72.8% for fragm. indices	[112]
IKONOS, GE-1, b/w aerial photos	21 FRAGSTATS indices	GLM; object-based class.	trop. forest fragm. assessment	94.8% LC (2 cl.); 18 adjusted pseudo-R ² distance to roads with Shape index	[115]
QB, ASTER, TM	m/level segm.; spectr. reflectances; FRAGSTATS indices	obj/rule class. (QB); pixel-based MLC (ASTER, TM)	tundra mapping and fragm.	80.6% QB (9 cl.); fragm. more obvious in QB class.	[113]
SSat; HRG (both simulated by AISA)	NDVI; variogram analysis; red edge shift	semi-variogram sill and range	fragm.	SSat offers more information for vegetation stress detection	[116]
TM, WiFS	10 FRAGSTATS indices	MLC	cross-scale evaluation of indices	367–6110.5 mean sensitivity to scale for NP, MPS, EL, RG, and NND; 7.3–109.6 for LPI, CI, PC, LDiv, and AgI (more robust to spatial resolution)	[114]
Aerial photos	ECAI	photo interpretation	forest connectivity	2.4% rate of increase in forest connectivity	[117]
Freshwater					
ALS, visible photo	LiDAR Lee filtering, DEM, wetness index	threshold-based class.	temper. wetland inundation	96.3% LiDAR (3 cl.)	[121]
ALS, QB	DEM, CHM, spectr. indices	MLC	temper. upland swamp mapping	98% (boundaries), 70–78% (3 cl.)	[122]
ALS	point cloud parameters & segm., dropout modelling	rule-based class.	river water detection	97%	[123]

Continued on next page. . .

Table A.1 – continued

RS data	Feature extraction	Mapping	Final product	Accuracy	Ref.
airborne optical camera (4 cm)	DEM by 3D point cloud	OBIA rule-based class.	upland swamp mapping	95% (swamp vs eucalypt)	[133]
ETM+, aerial photos	spectr. reflectance	ISODATA, MDM	highland & savannah wetlands class.	up to 83% (9 cl.)	[134]
TM / ETM+, JERS-1	spectr., radar, topogr. features	Bagging class. trees)	wetland mapping	88.6% (2 cl.)	[127]
PALSAR ts, RSAT-2	m/res. segm.; backscatter values	OBIA rule-based class.	trop. wetland class.	81% (5 cl.)	[128]
m/temp. ERS-2, ASAR, ETM+	PCA	LRA	forested wetland hydroperiod mapping	R ² 0.9 soil moisture, 0.88 percent area inundated	[129]
ETM+, MODIS ts	bilinear & bicubic interpolation, s/res. by phase corr. im. registr., halftoning, notch & morphol. filtering	<i>k</i> - & fuzzy <i>c</i> -means	Lake detection & characterization	Errors: 0.15 km ² (area), 1.234 km (perimeter), 0.322 km (length), 0.169 (compactness) MODIS	[135]
Marine and coastal					
ROSI, CASI, MIVIS, IKONOS, QB	spectr. reflectance; MNF, PCA, band averaging	<i>k</i> -means, MLC, SAM	saltmarsh mapping	97.8% ROSIS (5 cl.)	[131]
ALS	DSM, DEM, NSM, DIM; NDLVI	MLC	saltmarsh mapping	91.89% (17 cl.)	[377]
TM, ALI, Hyperion, IKONOS	depth-invariant band extraction	MLC	seagrass mapping	95.9% / 78.94% HYP (3 / 5 cl.)	[132]
ALS	membership of water, intensity and 2D point density	supervised fuzzy classification	water detection	94.5% and 99.1% for two areas	[124]
ALS	bank line extraction	DTM differencing; gradient change	morphological ChD	tidal channel position changes of 55 m identified	[126]
ALS	geometric features, bank line extraction	DTM differencing; ChD of bank lines	morphological ChD	tidal channel position changes identified	[125]

A.2.2. Trends in abundance, distribution and extinction risk of species

Table A.2.: Methods studying different parameters related to the CBD headline indicator measuring trends in abundance, distribution, and extinction risk of species.

RS data	Feature extraction	Mapping	Final product	Accuracy	Ref.
		Alien species			
aerial orthophotos (0.5–1 m)	bi-temporal band ratio, NDVI, text. features	RF	<i>Fallopia japonica</i> (FP) mapping	95.4% OA (9 cl.); 90.3% PA, 98.1% UA for FP	[137]
aerial photo (0.3 m); TM	NDVI; obj. features (color, texture, shape)	pixel-, obj.-based MLC; LRM, QRM	Understory bush honeysuckle mapping	94.9% OA (2 cl.); 91.3% PA, 95.5% UA	[138]
AISA, balloon visible (0.12 m)	MinNF	SAM; LSU	saltmarsh <i>phragmites</i> mapping	90% OA (6 cl.); 93% PA, 96% UA	[139]
m/spectr. aerial photos (25 cm); ALS	segm., NDVI	MLC, obj.-based class.	Invasive woody species mapping	73% PA, 99% UA for <i>Pinus nigra</i>	[140]
HyMap	MinNF; NDVI, NDWI, CAI	LogR; SAM; binary tree; SMA	invasive weed species mapping	63% PA, 75.8% UA for perennial pepperweed; 51.4–69.1% PA, 61.9–89.8% UA for water hyacinth	[148]
QB	spectr. reflectance	MLC	invasive wetland plant mapping	100% PA, 76% UA for <i>Phragmites australis</i>	[143]
ASTER	terrain position cl.; spectr. signatures	ANN, SVM w. Bayesian GIS	invasive shrub <i>Lantana camara</i> mapping	82.9% (4 <i>L. camara</i> cover cl.)	[378]
Hyperion	MinNF	SCM	<i>Phragmites australis</i> mapping	68.8% PA, 61.1% UA	[151]
ETM+; 1.2 m above-ground photos	spectr. reflectance; light intensity, canopy density	MLC; ANN; SMR	Understory <i>Chromolaena odorata</i> properties	R ² 0.86–0.92 for number of flowering stem, flowering branch, etc.	[379]
CASI	PCA; four LSMM	MLC	Yellow starthistle abundance	R ² 0.88 for starthistle cover	[152]
QB; Hyperion	m/res. segm.; landscape pattern metrics; NDVI; TCT; MinNF; PPI	ISODATA; OBIA; LSU, nLSU; ANN	guava abundance mapping	mean root error of 0.00076	[144]

Continued on next page...

Table A.2 – continued

RS data	Feature extraction	Mapping	Final product	Accuracy	Ref.
Hyperion ts	spectr. reflectances	SI threshold	native & invasive species separability	SI > 0.7 (SI < 0.7) for invasive-native in the summer (winter)	[153]
Indigenous species					
Simulated Hyperion by h-h SR-meter	PCA, LL R ² M, SDA, DGVI	discriminant model	savanna mapping	97% (5 cl.)	[154]
HYDICE	spectr. indices; derivative- & absorption- based techniques; SMA	RF	trop. rainforest tree species	around 87.4% (7 species)	[141]
ALS	surface reflectance; Dropout point count	rule-based tree class.	wetland species mapping	82.71% (9 cl.)	[155]
WV-2	manual crown delineation; spectr. reflectance	RF, LDA	temper. forest species discrimination	82.4% (10 cl.)	[145]
CAO-Alpha	segm., spectr. separability measures	LDA, RDA, SVM, ANN, <i>k</i> -NN, QDA	tree species discrimination	73.2% (17 cl.)	[147]
ALS, CASI	DEM, crown segm., BRDF correction; spectr. reflectance; 3D point cloud	stacked SVM	savanna mapping	76.5% (15 species)	[142]
ALS, CAO-Alpha	NDVI; non-metric MDS; topographic variables	stacked SVM; hierarchical clustering; redundancy analysis	savanna plant community composition	76% (15 species)	[149]
HyMap	reflect. & derivative data; Jeffreys-Matusita & ED; SAM; SID; RSDP	single- & multiple-endmember class.	tree species discrimination	71.5% (6 cl.)	[150]
Birds					
AVHRR ts	NDVI; PCA	GAM	distr. modelling of gr. bustard (GB), l. bustard (LB), c. lark (CL)	89.2% for GB; 82% for LB; 81.6% for CL	[158]
SIR-C; TM	inv. alg. for biomass estimation; veg. cover; SNA	GARP	presence modelling for p. warbler (W), c. sparrow (S), red-eyed vireo (V)	84% for W; 85% for S; 75% for V	[167]

Continued on next page...

Table A.2 – continued

RS data	Feature extraction	Mapping	Final product	Accuracy	Ref.
ETM+	NDVI; greenness	LDA; LR; GLM	r. grouse (G) & g. plover (P) abundance	r 0.73 for G; 0.55 for P	[159]
ALS; TM	forest structure variables, topogr. characteristics, vegetation greenness; SDI	MCC; GLM	species richness	R ² 0.318 bird richness	[160]
ALS; IKONOS	veg. structure indices	LR	Dark-eyed Junco and W. Vireo density and occurrence	R ² 0.4	[168]
TM	landscape metrics; crop productivity measures; NDVI	SVM; I-T; LR	bird, butterfly, plant diversity	R ² 0.18 <i>a</i> –, 0.28 <i>b</i> –, 0.3 γ –diversity for birds	[162]
Fishes					
RoxAnn acoustic data; IKONOS	spectr. reflectance; acoustic roughness; in-situ rugosity	unsupervised class.; LR; LogR; NBGLM	reef fish abundance	R ² 0.6– >0.9	[161]
TMI; SeaWiFS;	SST; chl-a; PAR; m.s.l. anomaly	VGPM; piecewise LR	detection of albacore ocean hot spots	R ² 0.79	[176]
ETM+	spectr. reflectance, habitat properties	habitat supervised class.; GAM	SWI model	r 0.87	[174]
MODIS	sea properties	GLM	habitat suitability (HIS) for y. tuna	71.9% of fish catch where HIS>0.5	[163]
IKONOS; acoustic depth sounder	seabed parameters; rugosity index; M-C simulation; SEI	LR	reef fish richness	richness related to evenness for kernels 40-80 m and to rugosity for kernels ≤ 20 m ($p < 0.01$)	[169]
Mammals					
WV2	spectr. reflectance	MLC; ISODATA; <i>k</i> -means; thresholding	whale detection	84.6% detection, 23.7% false positives	[157]
ALS	surface scanner echoes	LogR	habitat suitability mapping for moose	71% (moose/no-moose)	[164]
aerial survey ts; VGT	morphol., topol., spectr. features	SFLR	presence of elephant	74% variance explained	[173]
QB, WV-2, IKONOS	pansharpening; spectr. reflectance	multivariate superv. class.; robust LR	emp. penguin population estimate	4 new breeding colonies & 238,000 breeding pairs found	[166]
TM; QB	spectr. reflectance	rule-based class.	breeding distribution of emp. penguins	10 new breeding sites located;	[165]

Continued on next page...

Table A.2 – continued

RS data	Feature extraction	Mapping	Final product	Accuracy	Ref.
ETM+	spectr. reflectance; NDVI	regression tree analysis	Myanmar's Eld's deer habitat	abundance & % canopy correlation $r = 0.636$	[175]
MODIS	variables: NDVI, FRAGSTATS & topogr. measures, species richness	MRA	Invertebrates butterfly species richness	62% variation explained	[172]
ALS	LiDAR variables	CRA	Spider distribution properties	\bar{R}^2 0.15–0.57 for 6 properties	[170]
ALS	LiDAR variables	CCA; MLRM	forest beetle richness and diversity	26.4% of variance, 23.8% of diversity explained	[171]

A.2.3. Trends in pressures from unsustainable agriculture, forestry, fisheries and aquaculture

Table A.3.: Methods studying different parameters related to the CBD headline indicator measuring trends in pressures from unsustainable agriculture, forestry, fisheries and aquaculture.

RS data	Feature extraction	Mapping	Final product	Accuracy	Ref.
			Unsustainable agriculture		
LISS-II ts	spectr. features	MLC	salinity affected soil mapping	90% LU map (8 cl.)	[178]
TM / ETM+ ts	image segm.; EVI, NDSVI, NDTI, phenol. features	RF	corn and soybean multi-year mapping	90.1% w. spectr., 88.3% w. phenol. same-year (3 cl.); 75.5% w. spectr., 82.3% w. phenol. cross-year (3 cl.)	[184]
DMC Z/I	wetland rel. percentage index; indicator value analysis; non-metric MDS; NDVI	RF	WCI	71% (5 cl.); R^2 0.48 for WCI	[179]
MODIS ts	NDVI, spectr. reflectance, phenol. metrics	SVM	abandoned agriculture mapping	OA 66.9% (4 cl.), UA 56.7%, PA 40.9%	[185]
MODIS ts	NDVI, Time Integrated NDVI	decision tree	irrigated area mapping	R^2 0.91 w. TM map as reference	[180]
TM / ETM+, MODIS	NDVI, EVI, PVI; PCA	RF; thresholding (TM/ETM+); peak method, TMA; hierarch. training (MODIS)	cropping intensity of smallholder farms	R^2 0.71–0.97 TM/ETM+, 0.30–0.97 MODIS	[186]
VEN μ S (VS), Sentinel-2 (S-2) (both simulated by field spectrometer)	spectr. features, NDVI, REIP	PLSR; VIP	LAI of wheat and potato crops	r 0.93 w. VS, 0.92 w. S-2; r 0.91 w. REIP, 0.86 w. NDVI	[187]
DuncanTech; TCAMP	spectr. features; VIT	LR	NSI, CWSI	R^2 0.37–0.41 for NSI	[181]
CASI	spectr. indices; PROSPECT-SAILH model	regression analysis	DCNI	R^2 0.72 for corn N concentration	[182]
REye; GS	NDVI, NDRE, CCCI	regression analysis	Canopy nitrogen percentage of crops	R^2 0.14–0.46 w. GS	[183]

Continued on next page. . .

Table A.3 – continued

RS data	Feature extraction	Mapping	Final product	Accuracy	Ref.
ALS	ALS last pulse; tree-based features; point height metrics	RF	Unsustainable forestry boreal managed forest attributes	R: 0.98 height, 0.89 DBH, 0.96 SV	[189]
TDX, TSX Pol-InSAR	copolarized dual-pol (D-P), single-pol (S-P) data	data inversion, RVoG model	forest height	R ² 0.86 w. D-P, 0.98 w. S-P + DTM, compared with LiDAR reference	[192]
AVNIR-2, HRG ALS; Airborne CIR (0.25 m); AVNIR-2 HRG	spectr., text. features; PCA ALS height percentiles; CIR and AVNIR-2 spectr. & text. features neighbourhood statistics	simple LR, SMLR plot-level MLLSR	forest biomass estimation trop. forest structure	R ² 0.939 R ² : 0.918 SV; 0.774 BA	[195] [200]
IKONOS, ETM+, HRVIR	spectr. features	non-linear regression	hardwood & conif. forest structure LAI in temp. conif. & decid. forest	R ² 0.93 CDIA, DBH, 0.92 height R 0.82–0.88 ETM+	[40] [202]
ALS	laser penetration, height metrics	logarithmic regression; univar. & multiple regression	LAI in pine forest	R ² 0.84	[203]
ALS	Ordinary Kriging, IDWI for DTM & DSM; LiDAR features	MLRM	forest above ground biomass	R ² 0.83	[196]
Simulated GLAS by ALS	Gaussian decomposition	SMLR	forest parameters	R ² 0.76 relief; 0.81 canopy height	[191]
GLAS	SG filter; Sigbeg determination	regression analysis	ragged forest height	R ² 0.73–0.78	[35]
IKONOS	text. features	LR	spruce forest structure: age (A), top height (H), circumference (C), stand density (D), basal area (BA)	R ² 0.82 density, 0.82 circumference, 0.81 age	[41]
BioSAR; Profiling & Scanning ALS	norm. radar cross-section; multiple returns;	Best subsets linear regression	forest biomass	R ² : 0.8 BioSAR + PALS	[197]
HyMap	veg. indices	PLSR	beech forest structure	R ² : 0.62 DBH, 0.36 height, 0.5 density	[193]

Continued on next page. . .

Table A.3 – continued

RS data	Feature extraction	Mapping	Final product	Accuracy	Ref.
WV-2	text. features	SMLR	dryland plantation forest structure	best R^2 : 0.67 SDDBH, 0.54 BA, 0.5 GC	[201]
BioSAR	backscatter values	linear regression	forest biomass	\bar{R}^2 0.77–0.79	[199]
Hyperion	forward MinNF; spectr. reflectance	obj.-based class.; CCA	temper. forest structure	0.973 age, 0.979 height canonical loadings	[194]
TSX Stereo Radargrammetry; ALS	ALS metrics; TSX 3-D coords	NNI; RF	boreal forest structure	RMSE 24.7–31.8% SV, 23.4–29.8% AGB	[198]
TM / ETM+	CCFS; haze correction	ISODATA; 2nd order polyn. regression	AGB in sustain. & unsustain. logging area	98.7% (5 cl.); R^2 0.66	[177]
TM / ETM+ ts	spectr. reflectance	SVM	disturbances in managed forest	94.68–99.4% (2 cl.), 87% detection	[204]
REye ts	MTMF	obj/rule class.	logging trail detection	91.5% (3 cl.)	[205]

A.2.4. Trends in pressures from habitat conversion, pollution, invasive species, climate change, overexploitation and underlying drivers

Table A.4.: Methods studying different parameters related to the CBD headline indicator measuring trends in pressures from habitat conversion, pollution, invasive species, climate change, overexploitation and underlying drivers.

RS data	Feature extraction	Mapping	Final product	Accuracy	Ref.
Climate change					
VGT ts	PVI; earliness index	VTRER	leaf unfolding in dec. broadleaf forest	R^2 0.957–0.975; RMSE \approx 2 days	[207]
MODIS ts	GMM; mean filtering; NDVI	regression analysis	terrestrial biome phenological metrics	R^2 0.42–0.97 (5 metrics), RMSE of onset \leq 1 week for deciduous	[208]
MODIS	NDVI, LSWI, EVI, WDRVI, OSAVI.	double logistic function, LLSR	dec. broadleaf & evergreen needleleaf forest phenology	R^2 0.87 OSAVI (GPP onset), 0.91 WDRVI (GPP offset)	[211]
MODIS	EVI, NDVI, ExG _M	logistic model	dec. forest phenological metrics	MAE 3–14 for NDVI	[209]
TM / ETM+	EVI, NDVI, NDWI, Red-MIR ratio, Thermal-Red-MIR ratio	common sigmoidal models	mixed hardwood forest phenology	Error 11.2 days for full leaf out with EVI	[210]
Pollution					
ASAR	low wind filtering; semi-superv. segm.	regression analysis, adaptive thresholding	oil spill detection	99.93% on subset, 91.7% on rest	[215]
RSAT-1	backscatter; text. features; convolution of texton filters	feed-forward ANN	oil slick delineation	98.22% (2 cl.); 97.74% (3 cl.: oil, clean sea, low wind)	[216]
AVIRIS	MICA	threshold-based mapping	oil marsh mapping	93.4% (2 cl.)	[218]
ERS	geometr., phys., text. features	decision tree forest	oil spill detection	77.4–85% (2 cl.)	[217]
HJ	FVC; scaled NDVI; Dualistic Structure model	linear regression	non-point source pollution	R^2 0.75 TN/TP/NH ₄ -N, 0.23 COD _{cr}	[220]
AVIRIS, CASI	NDVI, SRI, RGRI, PRI, REPI, CRI, ARI, WBI, NDWI, NDNI, NDLI; MinNF	MLC; MLR, stepwise regressions	conif. forest OII	82% (8 cl.); R^2 : 0.59	[221]
OMI	surface-to-column scaling, GEOS-Chem model, CAMx	correlation analysis	urban surface NO ₂ concentrations	R temporal 0.4–0.8; spatial 0.93	[222]

A.2.5. Trends in distribution, condition and sustainability of ecosystem services for equitable human well-being

Table A.5.: Methods studying different parameters related to the CBD headline indicator measuring trends in distribution, condition and sustainability of ecosystem services for equitable human well-being.

RS data	Processing	Mapping	Final product	Accuracy	Ref.
Food provision					
MODIS LAI, EVI, & NDVI	DA; crop growth & canopy reflectance models; GA; SG filter	radiative transfer model; piecewise logistic function	corn yield estimation	rel.diff. corn yield 3.5% LAI + EVI, -0.2% LAI + NDVI	[226]
AVHRR NDVI	fAPAR; AGB; harvest index	CROPSYST model	wheat yield	rel.diff. 3.15%	[227]
MODIS NDVI ts	SG filter	stepwise LR	winter wheat yield	rel.diff. -4.62%	[228]
MODIS ts	NDVI, EVI, LSWI	veg. photosynthesis model; LR	winter wheat-maize GPP	diff. 5.7% wheat, -11% maize; R ² 0.798	[229]
ASAR, MERIS	LAI; variational DA	CERES-Wheat model	wheat yield	rel.diff. 11%	[230]
Provision of raw materials					
ALS	GAMLSS; EMMM; plot-level indices	ridge regression; GCV	eucalyptus forest BA & stand volume (StV)	R ² 0.66–0.89 BA; 0.67–0.85 StV	[231]
GLAS, MODIS	spectr. features; LiDAR waveform variables	MLC, ANN	boreal forest timber volume	93.1% LC (11 cl.); R ² 0.78	[234]
ALS, LISS-III	LiDAR features; spectr. features	stepwise regression	forest stem volume	\bar{R}^2 0.72 ALS + LISS-III	[232]
airborne CIR, ALS, TM	LiDAR 1st & last pulse; CIR variance, TM spectr., PCA, TCT; GA; stepwise selection	RF; ED; MD; MSN	managed mixed forest timber volume (V) & biomass (B)	RMSE 23.27% V, 23.52% B	[233]
Water provision					
TM / ETM+ ts	reflectance values	ISODATA; MLSR	SDD in lakes	R ² 0.71–0.96	[235]
ALI	reflectance values	LR	river estuary water turbidity	R ² 0.9085	[238]
ETM+	reflectance values; panchr. brightness	ISODATA; MLSR	lake & river SDD	R ² 0.77	[236]

Continued on next page. . .

Table A.5 – continued

RS data	Processing	Mapping	Final product	Accuracy	Ref.
ETM+	reflectance values; text. features	regression analysis	chl-a, SDD & turbidity (T)	R^2 0.723 chl-a, 0.54 SDD, 0.57 T	[237]
SeaWiFS	reflectance values; spectr. indices	absorption & backscattering coefficient	open-water estuary SDD	R^2 0.67	[239]
Carbon storage					
AVIRIS	veg. indices; APAR; fAPAR	LRA	carbon (C) & water vapor (WV) fluxes	r −0.986 C, 0.981 WV	[240]
ALS	morphol. filtering; intensity & height metrics	stepwise regression; VIF	AGB, branches (BB) & foliage biomass (FB)	R^2 : 0.7 AGB, 0.67 BB, 0.58 FB	[241]
QB, ASTER	spectr., text. features; TCT	k -NN; SMLR	tundra forest aboveground carbon	r 0.44–0.69 with QB	[242]
Pest control					
QB ts	RGRI; m/spectr. segm.	local maxima filter; threshold-based class.	mountain pine beetle red attack	89–93% true positive	[243]
MODIS	NDVI, EVI, NDWI, NDII; defoliation index	LR	gypsy moth defoliation	R^2 0.769 biomass lost	[244]
AVIRIS	spectr. features	mixed-stepwise LR	emerald ash borer-infested lake region	R^2 0.71 decline	[245]
TM / ETM+, aerial surveys	TCT; LAI, pine stand vigor TCT	regression model	mountain pine beetle-induced mortality	R^2 0.43	[246]

A.2.6. Trends in coverage, condition, representativeness and effectiveness of protected areas and other area-based approaches

Table A.6.: Methods studying different parameters related to the CBD headline indicator measuring trends in coverage, condition, representativeness and effectiveness of protected areas and other area-based approaches.

RS data	Feature extraction	Mapping	Final product	Accuracy	Ref.
		Habitat conservation			
ASTER	NDVI, NDII; climatic & topogr. variables; PRA	MLC; MRA	woody, shrub & tree species richness in temperate forest	92% (4 cl.); R^2 up to 0.5	[249]
AHS-160	spectr. reflectance	LDA w. SFFS; MESMA, class. trees	<i>Calluna</i> age mapping for heathland conservation	$86 \pm 4.2\%$ (3 cl.)	[250]
ALS, CASI	LiDAR-derived height; text. features; inter-band correlation analysis; PCA; FRAGSTATS metrics	MLC	forest condition mapping	81% (5 cl.)	[251]
TSX ts	backscatter features	rule-based class.	swath events in Natura 2000 semi-natural grassland	3 out of 3 detection within 11-day period	[252]
PALSAR	RGMAP filtering	ChD in HV backscatter	mangrove forest habitat degradation	detect pixel with at least 10% change in backscatter	[253]

B. Available data for the study areas

B.1. Ederheide and Ginkelse heide, The Netherlands

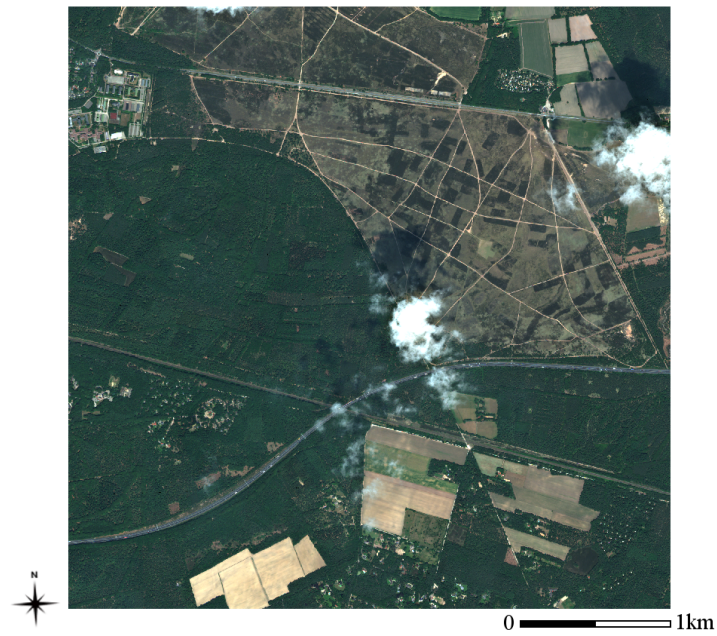


Figure B.1.: The WorldView-2 image for the Dutch study area from June 2011, in true colour.



Figure B.2.: The WorldView-2 image for the Dutch study area from September 2011, in true colour.

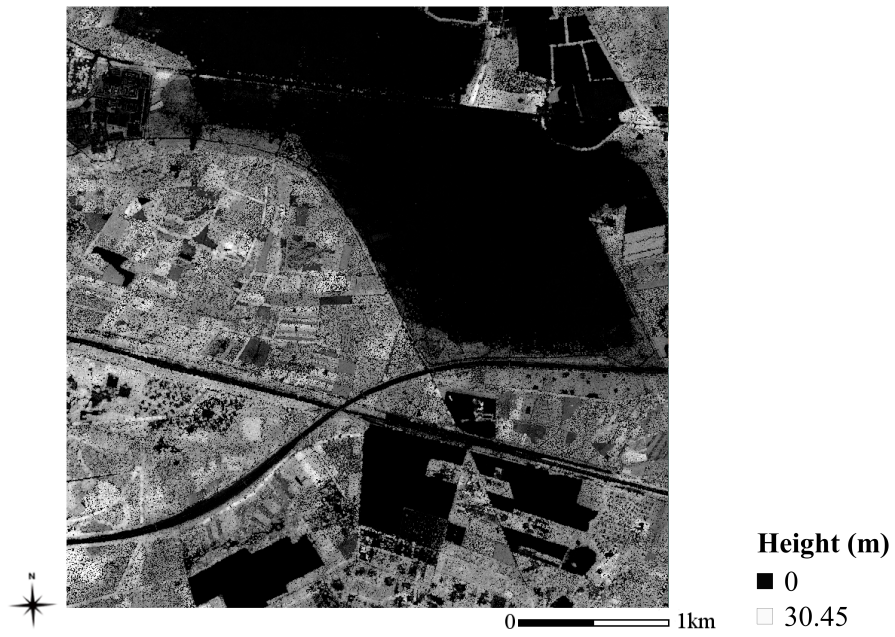


Figure B.3.: The Canopy Height Model for the Dutch study area.

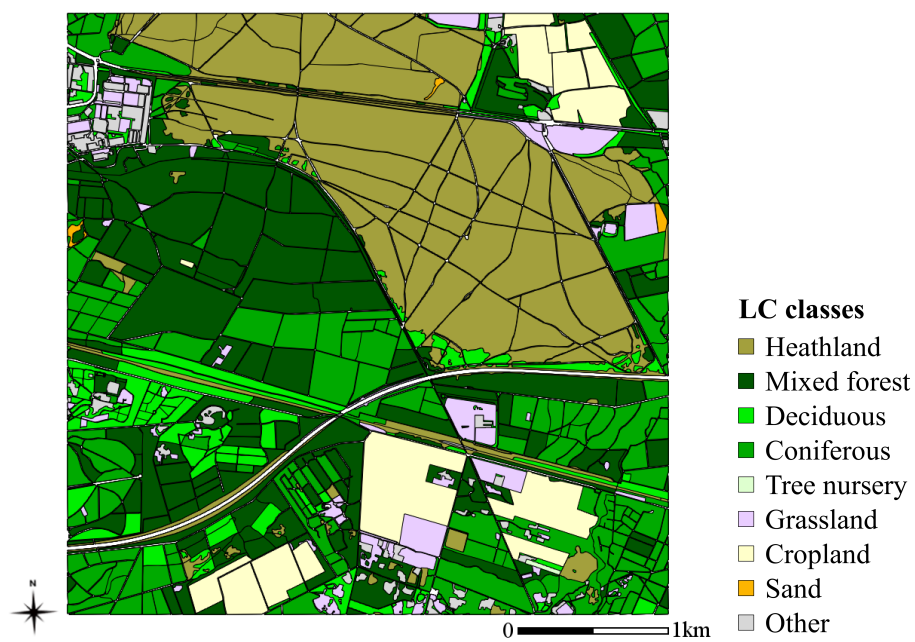


Figure B.4.: The Land Cover map for the Dutch study area.

B.2. Le Cesine, Italy



Figure B.5.: The QuickBird image for Le Cesine study area from June 2009, in true colour.

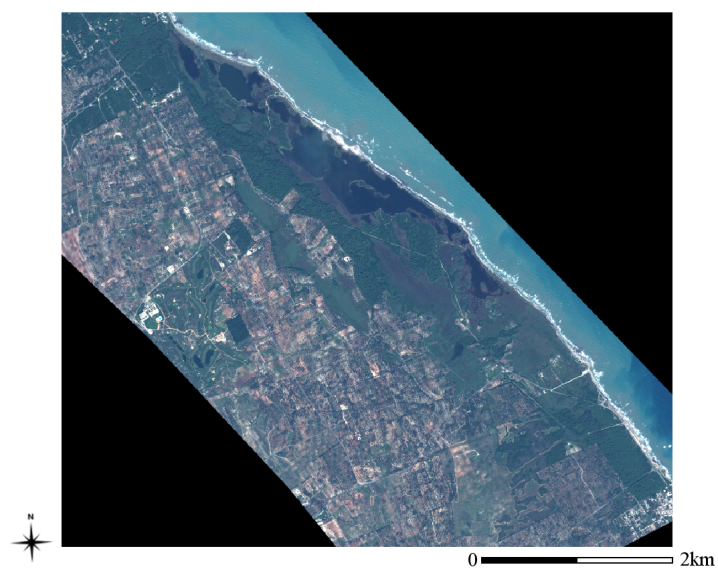
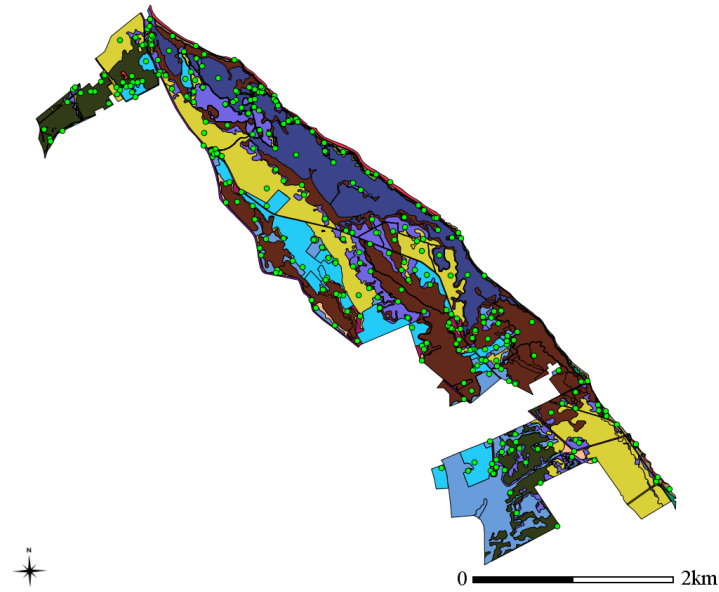


Figure B.6.: The WorldView-2 image for Le Cesine study area from October 2010, in true colour.



LC classes

- A11_A1.A8.A9.W7 (Needleleaved evergreen tree crops - plantation)
- A11_A1.B1.C1.D1.W7.A8.A9.B3 (Large-sized fields of needl. evergr. tree crops - plantation)
- A11_A1.B1.C1.D1.W8.A7.A9.B4 (Medium sized fields of broadleaved evergr. tree crops - orchards)
- A11_A3.A5.B2.C2.D3 (Small sized fields of irrigated non-graminoid crops)
- A12_A1.A4.A10.B3.D1.E1.B9 (Broadl. evergr. medium high thicket)
- A12_A1.A4.A10.B3.D1.E2.B9 (Broadl. deciduous medium high thicket)
- A12_A1.A4.A10.B3.D2.E1.B9 (Needleleaved evergr. medium high thicket)
- A12_A1.A4.A11.B3.D1.E1.B10 (Broadl. evergr. dwarf thicket)
- A12_A2.A5.A10.B4.E5.B12.E7 (Closed annual medium tall forbs)
- A12_A2.A5.A11.B4.E5.B13.E7 (Open annual short forbs)
- A12_A2.A6.A11.B4.E5.B12.E6 (Open perennial medium tall grassland)
- A24_A1.A4.A12.B3.C2.D3.B10 (Aphyllous closed dwarf shrubs on temporarily flooded land)
- A24_A2.A5.A13.B4.C2.E5.B13.E7 (Annual open short forbs on temporarily flooded land)
- A24_A2.A5.A16.B4.C1.E5.A15.B12.E6 (Perennial sparse medium tall forbs on permanently flooded land)
- A24_A2.A6.A12.B4.C2.E5.B11.E6 (Perennial closed tall grassland on tempor. flooded land)
- A24_A2.A6.A12.B4.C2.E5.B12.E6 (Perennial closed medium tall grassland on tempor. flooded land)
- B15_A1.A3.A7.A8 (Paved roads)
- B15_A1.A4.A13.A17 (Scattered urban areas)
- Validation points

Figure B.7.: LCCS map of Le Cesine site and validation points.

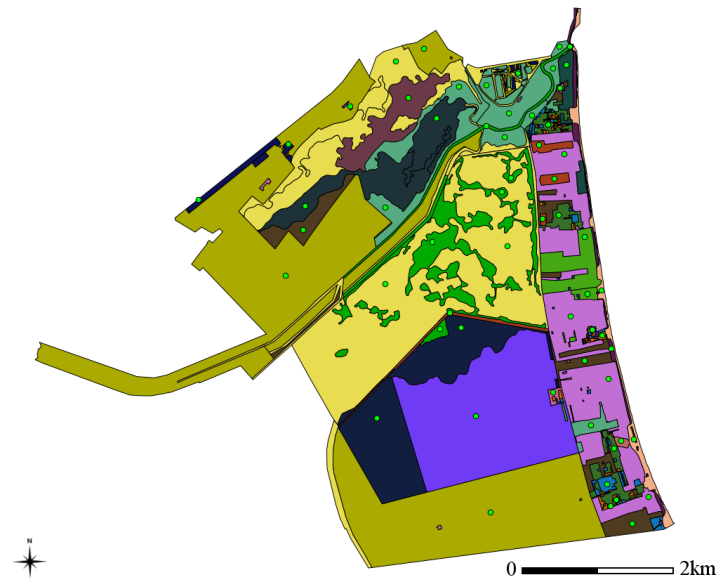
B.3. Lago Salso, Italy



Figure B.8.: The WorldView-2 image for Lago Salso study area from June 2010, in true colour.



Figure B.9.: The WorldView-2 image for Lago Salso study area from February 2011, in true colour.



LC classes

- A11_A1.A8.A9.W7 (Needleleaved evergreen tree crops - plantation)
- A11_A1.B1.C1.D1.W8.A7.A9.B4 (Rainfed broadleaved evergr. tree crops - orchards)
- A11_A1.B1.D1.W7.A7.A9 (Rainfed broadl. evergr. tree crops - plantation)
- A11_A3.A4.B1.B5.C1.D1.D9.B4 (Permanently cropped area graminoid crops)
- A11_A3.B1.B5.C2.D3 (Irrigated herbaceous crops)
- A11_A6.A11 (Vegetated urban area / park)
- A11_A6.A13 (Vegetated urban area / lawn)
- A12_A1.A4.A11.B3.A12.B14 (Open medium to high shrubs)
- A12_A2.A10.B4.XX.E5.B12 (Medium tall herbaceous vegetation)
- A12_A2.A5.A10.B4.XX.E5.B12.E7 (Closed annual medium tall forbs)
- A12_A2.A5.A11.B4.E5.A13.B13.E7 (Open annual short forbs)
- A12_A2.A6.A11.B4.XX.E5.A12.B12.E6 (Open perennial medium tall grassland)
- A24_A1.A4.A12.B3.C2.D3.B10 (Aphyllous closed dwarf shrubs on temporarily flooded land)
- A24_A2.A12.B4.C2.E5 (Mixed closed herbaceous veg. on temp. flooded land)
- A24_A2.A5.A13.B4.C1.E5.A15.B12.E6 (Perenn. open medium tall forbs in perm/ly flooded land)
- A24_A2.A5.A16.B4.C1 (Sparse forbs on permanently flooded land)
- A24_A2.A6.A12.B4.C1.E5.B11.E6 (Perenn. closed tall grassland on perm/ly flooded land)
- A24_A2.A6.A12.B4.C2.E5.B11.E6 (Perenn. closed tall grassland on temp. flooded land)
- B15_A1.A4.A12.A17 (Scattered industrial and/or other area)
- B15_A1.A4.A13.A16 (Low density urban area)
- B15_A1.A4.A13.A17 (Scattered urban area)
- B16_A2.A6 (Loose and shifting sands)
- Validation points

Figure B.10.: LCCS map of Lago Salso site and validation points.